Development of Passive Wireless Humidity Sensors and Dielectric Methodology for A Real-time In-situ Sensing of Disinfectant

by

Jiachen Liu

A dissertation submitted to the Graduate Faculty of
Auburn University
in partial fulfillment of the
requirements for the Degree of
Doctor of Philosophy

Auburn, Alabama
May 7, 2022

Keywords: magnetostrictive particle, wireless sensors, water-sensitive materials, dielectric, disinfectant

Approved by

Zhongyang Cheng, Chair, Professor of Materials Engineering
Thorsten Knappenberger, Associate Professor of Crop Soil and Environmental Sciences
Pengyu Chen, Associate Professor of Materials Engineering
Siyuan Dai, Assistant Professor of Materials Engineering

Abstract

Many agricultural sensors, which play a critical role in smart and precision agriculture, are used to provide real-time sensing information for better control of agricultural production and saving of freshwater. There are preharvest and postharvest processes in agricultural production. In preharvest, soil water sensors are heavily used to detect soil water in vast crop farmland, which requires a wireless sensing feature and large numbers of distributions of the sensors. In postharvest, a huge amount of fresh produce is disinfected by disinfection and wash processes to ensure food safety before being sold in the supermarket, which requires an in-situ real-time monitor of the disinfectant. Based on these two needs, we developed two passive wireless sensor platforms to detect soil water for the preharvest process and new dielectric sensing and analyzing methodology to monitor the disinfectant for the postharvest process.

First, a wireless sensor platform, i.e., a magnetostrictive particle (MSP) sensor coated by a layer of the water-sensitive polymer was developed. The polymer-MSP sensor was a low-cost passive wireless freestanding sensor to detect humidity, which had the potential to be used to in-situ wirelessly monitor soil water in the soil. Moreover, two water-sensitive polymers were coated on the MSP sensor platform to measure their overall humidity sensing performances. Cellulose nanofiber (CNF), which was an environmental-friendly material, was used to develop the polymer-MSP humidity sensor. Another water-sensitive polymer, polyvinyl alcohol (PVA), which was originally vulnerable to water, by crosslinking, turned out to be water-resistant without losing its water-sensitive capability. An issue came out that, as the polymer gained water resistance by crosslinking, the water-sensitive ability was gradually

decreased. To obtain water-resistance capability while retaining its high water sensitivity, a fundamental study to optimize the crosslinking ratio for the PVA was conducted.

Second, a high dielectric permittivity ceramic was discovered to make a humidity capacitance sensor, due to that the sensor had a unique humidity sensing feature and a potential to be used to develop an inductance-capacitance (LC) resonant sensor to in-situ wirelessly monitor soil water in the soil.

Third, dielectric sensing and analyzing methodology to in-situ real-time monitor the disinfectant was developed. This research determined a characteristic frequency, which was changing with the disinfectant concentration in the water. As this dielectric methodology had many advantages, such as in-situ real-time detection, low-cost, and simple handling, over other sensing technologies, it had the potential to be used in the disinfection and wash processes of fresh produce production. Water quality influence on sensing of the disinfectant concentration was studied. Moreover, the influence of contamination from sand/soil on dielectric sensing was also studied.

Acknowledgments

I would like to express my deepest and sincere appreciation to my advisor, Prof. Dr. Zhongyang Cheng, for his guidance, support, care, and help during my Ph.D. program at Wilmore Laboratories at Auburn University. I would like to emphasize that his influence on me is very helpful to my upcoming career regarding scientific knowledge and thought. I want to thank Dr. Thorsten Knappenberger, Dr. Pengyu Chen, and Dr. Siyuan Dai for being on my Ph.D. committee and giving me ideas and suggestions. I would like to thank Dr. Zhihua Jiang for serving as my university reader to help me improve the quality of my dissertation writing. Thanks to Steven Moore and Cheryl Rhodes for their help at Wilmore Laboratories.

I want to thank Dr. Dongye Zhao for his help in my life and study at Auburn University.

I would like to express my love and gratitude to my wife, my parents, and many of my relatives for their mental support and encouragement which inspire me to move forward.

I want to thank my group members: Dr. Xu Lu, Dr. Patrick Bass, Dr. Yang Tong, Dr. Hossein Talebinezhad, Dr. Liangxi Li, Dr. Yuzhe Liu, Dr. Farrukh Najmi, Yancen Cai, Wei Yi, Weiye Wang, Jialiang Shen, Jindong Wei, Haoran Wang, Yaqub Babatunde Adediji, for offering me support and help. I am delighted to study, discuss, and make progress together with them.

Thanks also go to all my friends at Wilmore Laboratories and other departments at Auburn University: Dr. Lang Zhou, Dr. Anqin Zhang, Dr. Yan Chen, Dr. Eunji Lee, Dr. Songtao Du, Dr. Jianguo Xi, Dr. Pu Deng, Dr. Yixuan Wu, Dr. Mahesh Parit, Dr. Jaesik Yoon, Dr. Yuzhe Sun, Dr. Jiacheng He, Wen Yang, Doohee Lee, Jingfan Yang, Houshang Yin, Chuanyu Wang.

Thank you to everyone that has helped me during my life at Auburn University!

Table of Contents

List of Figures

List of Tables

List of Abbreviations

AA	Ascorbic acid
BTO	Barium titanate
CNF	Cellulose nanofiber
D.I.	Deionized
DSC	Differential scanning calorimetry
EP	Electrode polarization
FDR	Frequency domain reflectometry
FE-SEM	Field emission scanning electron microscopy
FTIR	Fourier Transform Infrared Spectroscopy
GA	Glutaraldehyde
GPR	Ground-penetrating radar
HClO	hypochlorous acid
LC	Inductance-capacitance
MSP	Magnetostrictive particle
NaClO	Sodium hypochlorite
NCs	Nanocarbon tubes
PEO	Polyethylene oxide
PPM	Parts per million
PVA	Polyvinyl alcohol
RF	Resonant frequency
RF_0	Base resonant frequency
ΔRF	Delta resonant frequency
ΔRF_{sat}	Saturated delta resonant frequency

RH	Relative humidity
SiO_2	Silicon dioxide
SPS	Spark plasma sintering
TDR	Time-domain reflectometry

Chapter 1 Introduction and research objectives

1.1 Agriculture and water

According to statistics, agricultural production is the largest consumer of fresh water, accounting for about 70% of the fresh water supply worldwide [1,2]. Many agricultural sensors, which play a critical role in smart and precision agriculture, are used to provide real-time sensing information for better control of agricultural productions [3-5]. Agricultural productions involve both preharvest and postharvest processes. In preharvest, soil water sensors are heavily used to detect the soil water content in vast crop farmland [6]. The sensors are distributed in the soil at different depths of the farmland to obtain detailed soil water data at all depths, where a wireless detection capability of the sensors is required. The aim is to help manage the crop growth with saving of irrigation water and beneficial to an improved harvest. In postharvest, a huge amount of fresh produce, such as spinach, lettuce, tomatoes, et.al., is disinfected by disinfection and wash processes before being sold in the supermarket each day. During the disinfection and wash processes, the sensors to detect the disinfectant concentration are required to increase the disinfection efficiency and enhance the food safety of the disinfected fresh produce (i.e., avoid/minimize foodborne illness outbreaks related to fresh produce) [7]. In summary, the sensors for smart and precision agriculture are heavily in need for both preharvest agriculture and postharvest agriculture to promote food production efficiency, food safety, and saving of fresh water.

1.2 Soil water sensors

1.2.1 Soil water content sensors

Soil water content sensor is to measure/detect soil water content, such as time-domain reflectometry (TDR), frequency domain reflectometry (FDR), ground-penetrating radar (GPR), neutron scattering, gamma attenuation, etc. TDR can be used to detect soil water content based on the time delay on reflected waveforms due to the interaction between transmitted electromagnetic waves and the water content in the soil. A schematic image of the measurement of volumetric soil water content by TDR is shown in Figure 1.1. When the water content increases, the time delay on the reflected waveform increases. TDR has a fast detection speed which can achieve real-time sensing and it is more accurate than the FDR method that the influence of soil texture and salt content is smaller than that of the FDR method [5,8-10]. However, TDR is costly as a high-frequency pulse signal is required to improve the accuracy, which usually requires expensive devices. Whereas, FDR, which is based on frequency domain analysis, is less costly than TDR so that more data points can be recorded for a given area of the field. Both TDR and FDR measurements need to either use long wires to connect the probe to an outside interrogator or datalogger. Nowadays, a wireless detection requirement of the sensor has been raised. There are three reasons: 1. A battery, which is considered a pollution source, needs to be embedded in the sensor as a power module and placed in the soil. 2. Many TDR/FDT probes need time to be placed in the soil carefully and properly, which is time-consuming. 3. For the currently used TDR/FDR, the gaps between the probes and soil may generate large errors affecting the sensing accuracy of the soil water content. Recently, interestingly, a radar-based method, i.e., the GPR method, can detect soil water content of large geographical areas [11]. It measures dielectric permittivity from either reflected wave velocity, ground wave velocity, or surface reflection coefficient. It is a non-invasive measurement that can be used to detect soil water content for a large area of subsurface ground. The disadvantage of GPR is that it is inconvenient to obtain valid interpretations due to the surface morphology of the ground and the signal attenuation influence of saline soils on the detection result. Neutron scattering and gamma attenuation always have safety concerns that greatly limit their agricultural applications [12,13]. Gamma attenuation is a relatively accurate measurement method for soil water content. However, it cannot be used in real applications due to its risk of radiation. In summary, each soil water content sensor has its advantages and disadvantages concerning the cost, the sensing accuracy, the unique sensing features (such as the wireless sensing feature), and the influence factors.

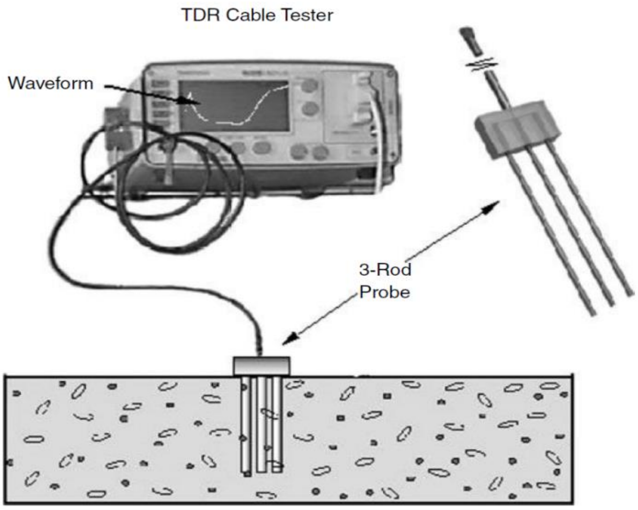

Figure 1.1 TDR cable tester, which shows the waveform, with a three-rod probe embedded vertically in the surface layer of soil to detect volumetric soil water content. S.B. Jones, et. al. [8].

1.2.2 Soil water potential sensors

The soil water potential sensor, which defines the ability of the soil to absorb water, is used to measure the matric potential of the soil in the unit of pressure (-1500 kPa ~ 0 Pa) rather than the volumetric soil water content [14-16]. Some values of the soil water potential are important for the management of crop growth. The soil water potential of -33 kPa is the field capacity, which is defined as the amount of soil moisture or water content held in the soil after excess water has drained away and the rate of downward movement has decreased [17]. The soil water potential of -1500 kPa is the wilting point, which is defined as the minimum amount of water in the soil that the plant requires not to wilt [18]. Atmospheric water potential is much more negative and a typical value for air is -100 MPa, which is not possible to be found in the case of the soil.

Figure 1.2(a) shows a commonly used electrical resistance sensor containing water absorption material, such as fiberglass or gypsum, with a known relation between its resistance and soil matric potential [14]. Some relations between the resistance of the materials and matric potentials are measured by some researchers, as shown in Figure 1.2(b). However, this method still suffers from a small detection range. Moreover, in relatively dry soil conditions and water flooded soil conditions, it might be beyond the measurement scope of the electrical resistance sensor. Furthermore, it is required to either use long wires to connect the probe to an outside reader or to use a battery as the sensor’s power module to obtain a wireless detection ability, However, placing long wires in the fields for many sensors is inconvenient and the use of a battery can cause a severe pollution issue in the soil.

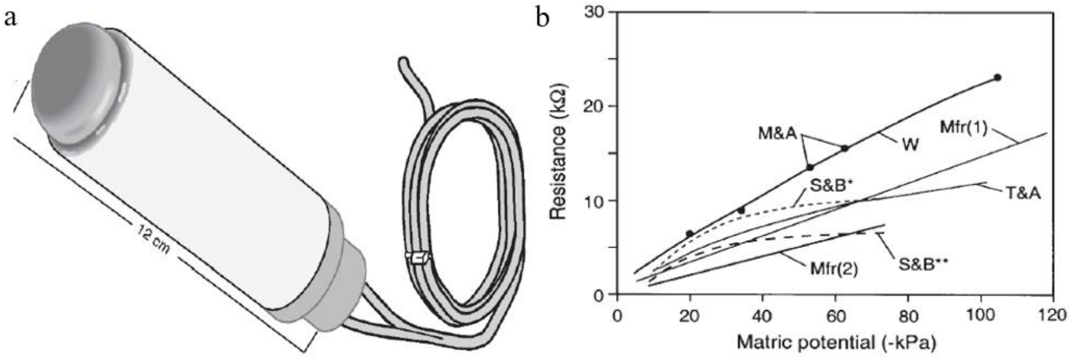

Figure 1.2 Electrical resistance matric potential sensor containing water absorption material with known relation between resistance and matric potential (a), and some relations between the resistance of different materials and matric potentials tested by some researchers (b). B.R. Scanlon, et. al. [14].

The fundamental of the humidity sensor is the same as the water potential sensor. The humidity sensor measures the humidity in the soil and the relative humidity has a direct relationship with the soil water potential, which can be described by Kelvin Equation [19]:

$$\psi = \frac{RT\rho_w}{M_w} \cdot \ln{(RH)} \qquad (1\text{-}1)$$

where ψ is soil water potential (MPa); R is gas constant, which is about 8.314 J/(K•mol); T is the absolute temperature (K); ρ_w is the density of water, which is normally 1 g/cm^3; M_w is the molecular weight of water (g/mol).

Table 1.1 Comparison between the soil water potential and RH.

Water potential	-100 MPa	-83.18 MPa	-6924 kPa	-1500 kPa	-33 kPa
Relative humidity (RH)	47.68%	54%	95%	98.90%	99.98%

From calculations by Kelvin Equation, Table 1.1 lists some values of the soil water potential and their corresponding RH for an intuitive comparison between the soil water potential and RH.

The benefit of the humidity sensor is that, similar to the water potential sensor, it can ignore the influence of soil type/constituent on water absorption ability and is directly related to the water absorption ability of the soil. The humidity sensors in agricultural applications require that they should be resistant to water immersion and their detection range should be wide, normally from certain relative humidity (RH) to 100% RH [20,21]. Most of the humidity sensors used in agriculture are resistance and capacitance sensors [22,23]. These sensors are required to either use long wires to connect the probe to an outside reader or to use a battery as a power module of the sensor to enable a wireless detection capability. However, the use of the battery is considered a severe pollution source in the soil. Therefore, the development of a passive wireless humidity sensor is an alternative and promising approach to achieving inexpensive wireless sensing of the humidity without introducing any environmental hazards.

1.3 Disinfectant sensors

1.3.1 Application of the disinfectant sensors

Commercial chlorine-based disinfectant, such as sodium hypochlorite (NaClO), is currently used during the disinfection of fresh produce [24,25]. However, an essential issue occurs that the disinfection concentration is always fluctuating during the disinfection process and subsequent wash process. The dynamic fluctuation of the disinfectant and the effectiveness of the disinfection of the fresh produce is dependent on several variables, such as the disinfectant concentration, disinfection and wash times, and quality of the water.

Moreover, the fluctuation of the disinfectant concentration results in serious problems. A lower disinfectant concentration results in a lower disinfection efficiency, which is not acceptable for the safety requirement. On the contrary, if the disinfectant concentration is too high, unnecessary disinfectants will be released, which causes a waste of the disinfectant and an environmental problem. Moreover, if the residual of the disinfectant is retained in the fresh produce, it is also harmful to human health. Therefore, the introduction of a disinfectant sensor control system is an inevitable approach to facilitate an instant sensing and precise adjustment of disinfectant concentration during the disinfection process and wash process of the fresh produce.

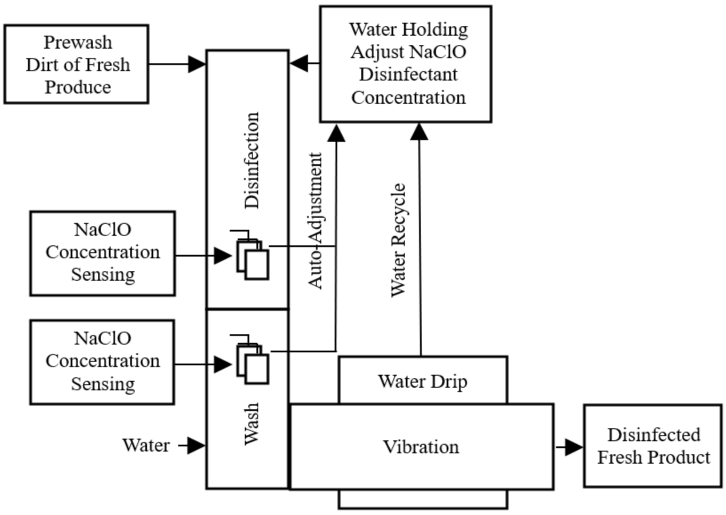

Figure 1.3 Schematic illustration of the disinfection process and wash process of the fresh produce along with sensing of the NaClO disinfectant concentration and precise adjustment system of the NaClO disinfectant concentration to meet the safety requirement of the fresh produce.

Figure 1.3 shows the scheme of the disinfection process and the sensing and precise adjustment system of the NaClO disinfectant concentration. The key to the disinfection process contains the disinfection step by stir and calm wash steps by water injection. The disinfection step aims to disinfect the fresh produce by adding NaClO and agitating. The calm wash step aims to wash the fresh produce and get rid of the disinfectant residuals by adding tap water. The sensors can be placed in both two steps to detect the concentration of NaClO disinfectant in water to obtain feedback and precisely adjust the NaClO disinfectant concentration during the disinfection step and ensure the NaClO concentration is diluted to meet the safety requirement after the wash step of the fresh produce.

1.3.2 Reagent based methods for disinfectant sensing

Reagent-based methods of assessing water quality involve titrimetric methods, such as colorimetric, luminescent, and fluorescent methods [26-35]. Colorimetric methods are those that produce a change in the color of a solution, the intensity of which corresponds to the quantity of the presence of chlorine or indicates the endpoint in a titration [26-28]. For example, as shown in Figure 1.4, a colorimetric assay can be used for chlorine detection based on the anti-dissolution of MnO_2 nanosheets. The comparison of absorption spectra of the MnO_2 nanosheets, the mixture of MnO_2 nanosheets and ascorbic acid (AA), and the presence of chlorine in MnO_2 are exhibited in the figure. When AA is mixed and consumed by chlorine, the concentration of AA decreases, which greatly inhibits the redox reaction between MnO_2 nanosheets and AA. Therefore, MnO_2 nanosheets cannot be dissolved and the color of the solution changes from colorless to yellow with the increase of the chlorine concentration. Luminescent methods produce light where the intensity is used as an indicator of the residual chlorine [29-31].

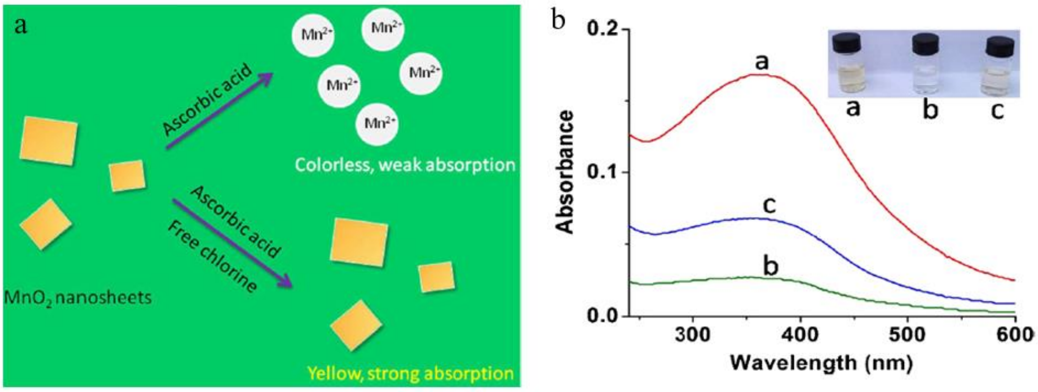

Figure 1.4 Schematic illustration of the colorimetric assay for chlorine-based anti-dissolution of MnO_2 nanosheets (a) and the chlorine influence on absorption spectra (b). H. Yu, et. al. [28].

Fluorescent methods measure the re-emission of incident electromagnetic radiation [32-35]. For example, as shown in Figure 1.5, the emission spectra of AuNCs in the presence of varying HClO concentrations are exhibited. Most colorimetric methods can be interfered with by temperature, pH, and different substances, such as oxidants, metal ions, and organic compounds. However, reagent methods have some drawbacks. For all reagent-based methods, trained staff are typically required to carry out the procedures. Moreover, the reagents are often unstable or toxic and the samples cannot be retested after analysis. In summary, these reagent-based methods cannot provide real-time sensing and are not suitable to be used in disinfectant and wash processes of fresh produce. Moreover, they have errors of as large as 10% and most methods have narrow concentration detection ranges (0.2 ppm - 2 ppm).

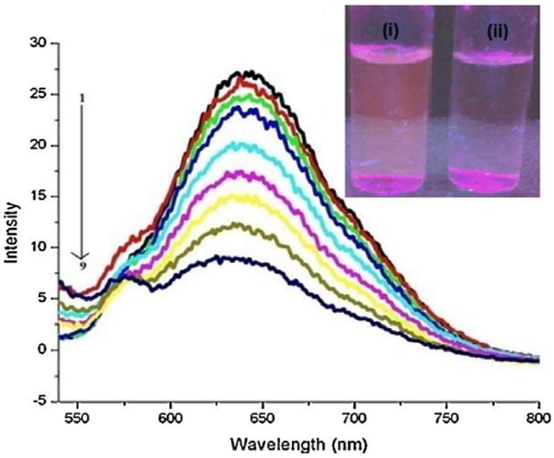

Figure 1.5 Emission spectra of AuNCs in the presence of varying HClO concentrations from 1 to 9 shown in the figure - 0, 0.34, 0.69, 1.72, 3.44, 6.89, 10.33, 13.77 and 17.21. The photo shows the fluorescence of the AuNCs in the absence (i), and presence (ii) of HClO under a hand-held UV lamp with 365 nm light. C.L. Gopu, et. al. [32].

1.3.3 Electrochemical sensors for disinfectant sensing

The mechanism of electrochemical sensors is based on amperometric detection of the disinfectant which is resulted from oxidation-reduction reactions of the disinfectant. They are commercially available sensors for continuous disinfectant sensing [36,37]. There are several manufacturers, for instance, Analytical Technology, Electro-Chemical Devices, Pulse Instruments, et al. For the research of electrochemical sensors, the study has been focused on the detection of hypochlorite [38]. As shown in Figure 1.6, the schemes of ampere vs sweeping voltage divided by Ag/AgCl measured voltage at different hypochlorite concentrations are exhibited. In recent years, different materials were studied to increase the durability and corrosion resistance of the electrodes/probes. For example, gold thin-film microelectrodes, multi-walled carbon nanotube electrodes, epoxy nanocomposite sensors with CuO nanoparticles, boron-doped diamond sensor, and gold-graphite chemical-resistive sensor were studied [38-44]. Although these commercially available electrochemical sensors could detect the disinfectant concentration, however, they have several limitations while being used for a rapid/real-time sensing of the disinfectant to support the feedback system for accurate control of the disinfectant concentration during the disinfection and wash processes of fresh produce: 1) the response time is long (normally 0.5~3 min) due to the time to reach the equilibrium state of the chemical reaction, which probably could not meet the requirement of real-time sensing of the disinfectant; 2) relatively high cost and frequently regular maintenance due to the degradation of electrodes and biofouling on the electrodes which is resulted from the forming of the oxide layer on platinum electrodes and potentially being aggravated by the presence of some organics [44-46].

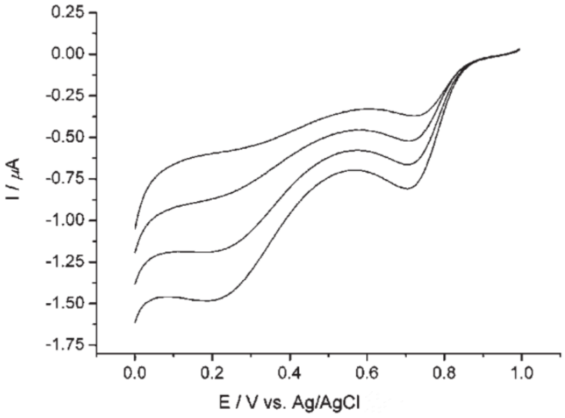

Figure 1.6 Schemes of ampere vs sweeping voltage divided by Ag/AgCl measured voltage at hypochlorite concentrations of 0.68, 1, 1.32, and 1.58 μM/L, respectively at constant pH of 7. O. Ordeig, et. al. [38].

1.4 Research objectives

1.4.1 Research objective 1

The goal of this research is to develop a wireless sensor platform - a magnetostrictive particle (MSP) sensor coated by a layer of water-sensitive polymer. The polymer-MSP sensor is a low-cost passive wireless freestanding sensor to detect humidity, which has the potential to be used to in-situ wirelessly monitor soil water in the soil in different depths of the farmland.

Two water-sensitive polymers will be coated on the MSP sensor platform to measure their overall humidity sensing performances. CNF, which is an environmental-friendly material, will be used to develop the polymer-MSP humidity sensor. Another water-sensitive polymer, polyvinyl alcohol (PVA), which is originally vulnerable to water, by crosslinking, turns out to be water-resistant without losing its water-sensitive capability. An issue comes out that as the polymer gains water resistance by crosslinking, the water-sensitive ability is gradually decreasing. To obtain water-resistance capability while retaining its high water sensitivity, a fundamental study to optimize the crosslinking ratio for the PVA will be conducted.

A newly found high dielectric permittivity humidity capacitor/sensor based on core-shell BTO-SiO_2 ceramics will be studied, due to that, it has superior comprehensive properties and the potential to be used to develop a passive LC wireless humidity resonant sensor to in-situ wirelessly monitor soil water in the soil.

1.4.2 Research objective 2

The goal of this research is to develop new dielectric sensing and analyzing methodology to in-situ real-time monitor the disinfectant in the water. This research will study the dielectric permittivity vs frequency spectrum and determine a characteristic frequency, which changes with the disinfectant concentration in the water. This methodology will provide a new way to detect the disinfectant concentration.

Due to that this dielectric sensing method has many advantages, such as time-saving, low-cost, simple handling, and in-situ detection, over other sensing technologies, it has the potential to be used in the disinfection and wash processes of fresh produce production.

Water quality influence on sensing of the disinfectant concentration will be studied. Moreover, the influence of contamination from sand/soil containing organic matters on the dielectric spectrum of the water will also be studied.

1.5 Background of passive wireless sensor platforms

1.5.1 Passive wireless sensor platform based on the MSP

1.5.1.1 Principle and characteristics of the MSP

Magnetostrictive particle (MSP) is amorphous ferromagnetic alloy particles. Under an external magnetic field, the dimension of the MSP changes due to its magnetostrictive effect corresponding to the external magnetic field. Under an alternative magnetic field, the MSP undergoes a corresponding oscillation with a shape change which is resulted in a mechanical vibration with a characteristic resonant frequency. This mechanical vibration causes the emission of magnetic flux from the MSP that is measured by pick-up coils. Figure 1.7 shows the configuration of an MSP sensor, which is a rectangular free-standing MSP strip with the length, width, and thickness of L, w, and t, respectively. Typically, the length (L) of the sensor is bigger than the width (w) and much bigger than the thickness (t). As the length direction is the biggest in all dimensions of the MSP sensor, the dominant vibration occurs along the length direction. Thus, the longitudinal resonant frequency can be excited and detected [47]. The MSP can be used as the transducer of the sensor by detecting its resonant frequency. Therefore, the MSP can be detected wirelessly without any physical connection to it.

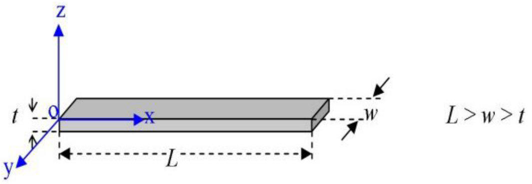

Figure 1.7 Dimension of the MSP sensor.

As shown in Figure 1.7, the fundamental longitudinal resonant frequency of the MSP sensor is given in Eq. (1-1) in the medium of the air and Eq. (1-2) in the medium of low viscosity liquids [48]:

$$f_n = \frac{1}{2L}\sqrt{\frac{E}{\rho(1-\upsilon)}} \cong f_{vac} \quad \text{(in the air)} \qquad (1\text{-}1)$$

$$f_n = f_{vac} - \frac{\sqrt{\eta \rho_{liq} f_{vac}/\pi}}{2\rho t} \quad \text{(in viscous liquids)} \qquad (1\text{-}2)$$

where, f_n is the resonant frequency of the sensor at its nth resonance mode, while f_{vac} is the associated resonant frequency in a vacuum; E is Young's modulus of elasticity; ρ and υ are the density, and the Poisson's ratio of the sensor material, respectively; ρ_{liq} and η are the density and viscosity of the liquid, respectively.

If a small mass Δm, such as pathogens, is added onto the sensor surface, the additional mass corresponds to an increased density of the sensor, resulting in a decrease in the sensor's resonant frequency. Therefore, the mass sensitivity (S_m) of an MSP bio-detection sensor can be expressed in Eq. (1-3):

$$S_m = \frac{\Delta f}{\Delta m} \approx -\frac{1}{2}\frac{f_0}{M} = -\frac{1}{4L^2wt}\sqrt{\frac{E}{\rho^3(1-\upsilon^2)}} \qquad (1\text{-}3)$$

where Δf is the resonant frequency change; M is the mass of the original sensor; L, w, and t are the length, width, and thickness of the sensor, respectively.

The negative sign in Eq. (1-3) implies the decrease of the resonant frequency when the mass load is added to the sensor surface. Therefore, the mass load added to the MSP sensor can be quantitatively determined by measuring a shift of the resonant frequency.

1.5.1.2 Passive wireless MSP sensors

As shown in Figure 1.8, MSP sensors can be used to wirelessly measure the magnetic field, force, and other target analytes, such as pathogens, while coating a sensing layer onto the surface of the MSP [49,50].

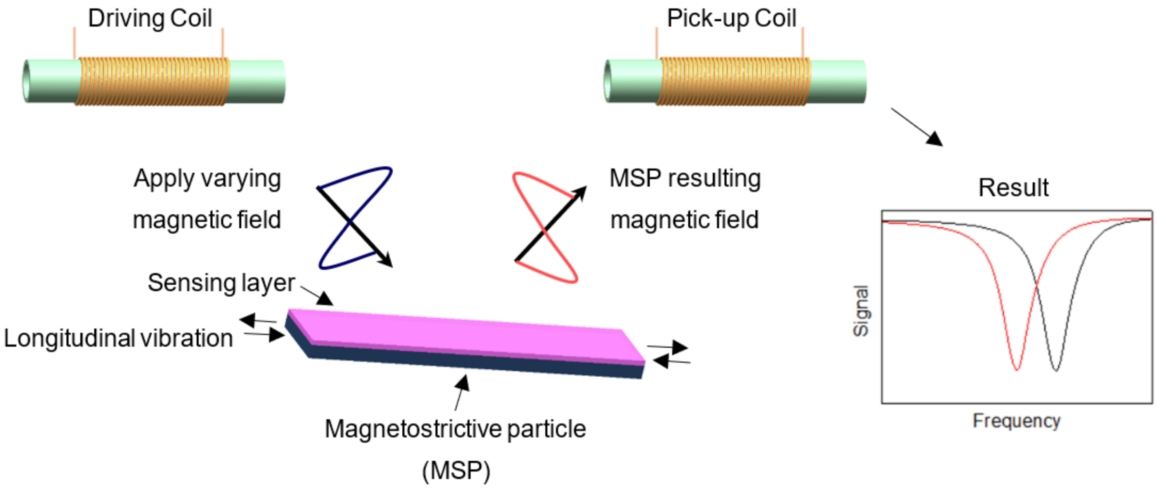

Figure 1.8 Schematic image of the wireless sensing of an MSP sensor and the sensing resonant frequency peak obtained by the pick-up coils.

Based on the characteristic of the detection through magnetic field/flux, the MSP sensors have the unique advantage because they do not require on-board power or any wires physically connected to the sensor, which enables the sensor to be detected wirelessly and remotely.

In recent years, passive wireless MSP biosensors were developed enabling biosensing using homemade coils to pick up the resonant frequency of the sensor [51]. As shown in Figure 1.9(a), the solenoid coils winded on a glass core as detector coils were placed over the MSP biosensors to measure their resonant frequency [52]. The ME biosensors were located under the coils and on the tomato surface during the entire sensing procedure. An oscillating magnetic field produced out of the coils actuates a longitudinal vibration of the biosensor. The resultant magnetic flux created by the biosensor was then immediately picked up by the same coils, and the shift of the resonant frequency could be measured, as shown in Figure 1.9(b) [53].

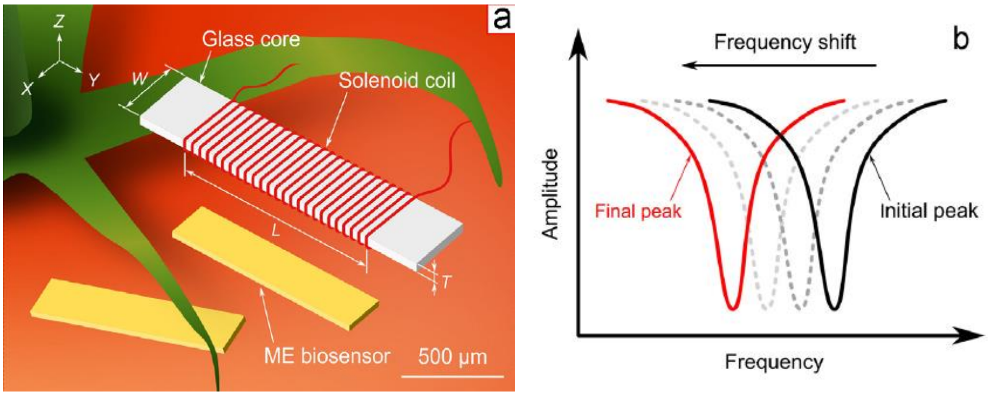

Figure 1.9 Scheme of solenoid coils on a glass core to wirelessly pick up the resonant frequency of the MSP sensor (a) and resonant peak shifts with respect to the condition change of the analyte (b). Y Chai, et. al. [53].

Another configuration of passive wireless detection method for biosensing was developed and is currently used to conduct research, as shown in Figure 1.10. A planar detection coil manufactured by microfabrication and electrodeposition methods was used to wirelessly generate magnetic flux interrogate with the vibrated MSP biosensor, resulting in the determination of the resonant frequency of the sensor and quantitative measurement of the bacteria [54-58].

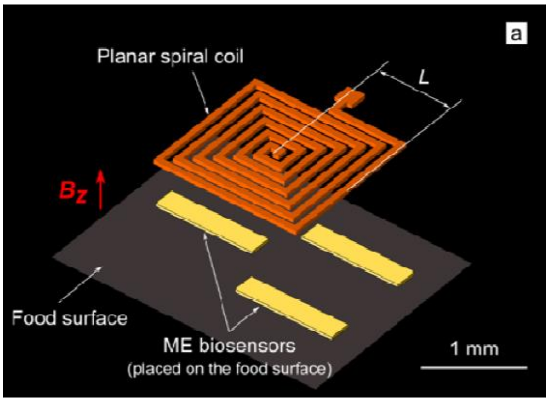

Figure 1.10 Scheme of the planar detection coil to wirelessly pick up the resonant frequency of the MSP sensor. Y Chai, et. al. [55].

MSP sensor could be coated with humidity-sensitive thin films of porous TiO_2 ceramics to make passive and wireless humidity sensors interrogated with the pick-up coils [59]. However, the porous TiO_2-MSP sensor suffered from a very small sensitivity that only a 130 Hz difference in resonant frequency was obtained for the entire humidity detection range from the lowest humidity to the highest humidity, as shown in Figure 1.11. This small sensitivity was probably due to the small mass ratio of water absorption of the porous TiO_2 film, which limited the application of the sensor to the real scenario.

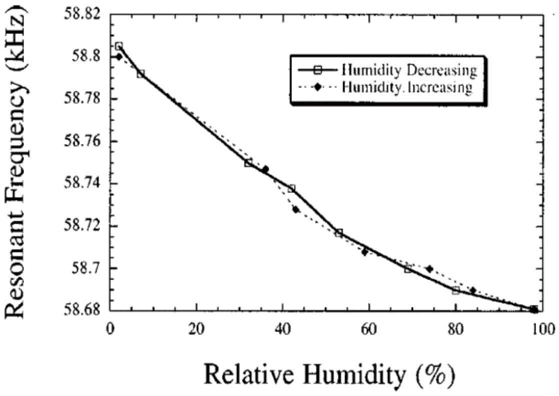

Figure 1.11 Scheme of the resonant frequency vs relative humidity of the TiO_2 porous ceramics-MSP humidity sensor. C.A. Grimes, et. al. [59].

In summary, the MSP sensor is a low-cost sensing platform to achieve an in-situ detection on an analyte through mass loading onto the sensor surface as well as a passive wireless detection method by using pick-up coils, Hence, the MSP sensor platform is a promising sensing approach to be further studied to develop some new humidity sensors with high humidity sensitivity for a real application scenario.

1.5.2 Wireless sensor based on passive LC resonator

1.5.2.1 Principle of passive LC resonant sensor

The main advantage of a passive inductance-capacitance (LC) resonant sensor is its wireless sensing capability [60,61]. The operation principle and equivalent circuit of the passive LC resonant sensor interrogated with a detector made of the inductors/coils are shown in Figure 1.12 [62].

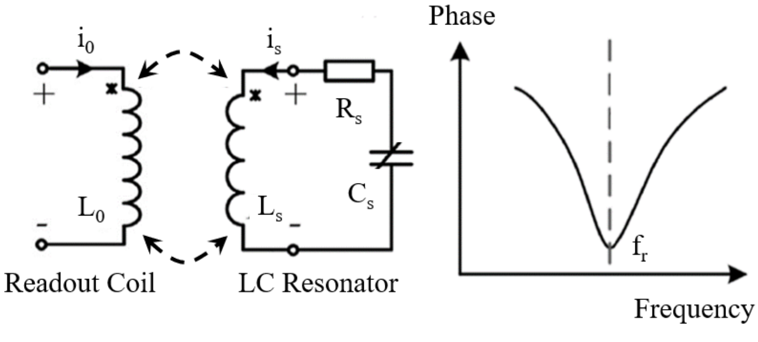

Figure 1.12 Principle and equations for the wireless interrogating system containing a wireless passive LC resonant sensor and readout coil. Phase peak frequency, which determines the resonant frequency of the LC resonant sensor, shifts with a change of capacitance (C_s). Q.A. Huang, et. al. [62].

A passive LC resonant sensor is typically constructed from a spiral inductor and a resistor connected with a sensing capacitor, forming a resonant LC tank. The capacitor changes in response to the substance of the sensing interest, resulting in a shift in its resonant frequency observed at the peak of the frequency spectrum. To wirelessly interrogate the passive LC resonant sensor, readout coils/inductors are magnetically coupled with the passive LC resonant sensor. The resonant frequency of the sensor can be detected by monitoring the impedance or input return loss of the readout coils/inductor [63].

1.5.2.2 Dielectric capacitive ceramics sensor

Based on the illustration in the last section, the dielectric capacitive sensors play a key role in the sensing of the analyte. Hence, this section focuses on a brief introduction to the dielectric capacitive sensor.

The dielectric capacitive sensor detects the capacitance change resulting from a physical or chemical change of dielectric properties (i.e., dielectric permittivity, loss, etc.) of the dielectric sensing material interacting with the analyte, such as gases, humidity, and other chemicals [64]. Therefore, the properties of the dielectric sensing material.

In the dielectric capacitive sensor, the dielectric sensing ceramics, which determine the performance of the dielectric capacitive sensor, are commonly used dielectric sensing materials [65-69]. Gas sensors based on dielectric ceramics have been studied to detect different gases, such as O_2, CO, CO_2, H_2, CH_4, NH_3, SO_2, et.al. [65-72]. The mechanism of these sensors was based on the change of dielectric properties of the ceramics due to the grain surface reaction with the gases. Many studies found that some doping atoms in the ceramics could improve the sensitivity of the gas sensors [73,74].

Capacitive ceramics humidity sensors were also studied in recent years [75,76]. The mechanism of the capacitive ceramics humidity sensors is the change of the dielectric constant of the sensing ceramics with RH change [77]. It is worth noting that among the sensors with various device structures, capacitive dielectric ceramics sensors are competitive in the market (about 75% of the humidity sensor market) due to the simple manufacturing process, ease of miniaturization, high stability, and low cost [78,79]. Moreover, capacitive humidity sensors commonly have low power consumption and large output signals [80,81]. Generally, when the frequency increases, the electric field direction changes fast, and, however, the polarization of the water cannot catch up with the changing speed of the electric field direction, resulting in a decrease in the dielectric permittivity and capacitance [82]. For the capacitive ceramics humidity sensors, more dielectric composite materials need to be studied to improve the characteristics of the dielectric permittivity spectrums, increase humidity sensitivity and discover humidity sensing mechanisms influencing the dielectric permittivity change of the dielectric material when interacted with the water molecules.

Chapter 2 Polymer-MSP-Based Wireless Humidity Sensors

The polymer-MSP sensors have a promising potential to be massively used/distributed on the farmlands and can be placed at different depths of the ground/soil, where the humidity in different depths can be wirelessly detected by a handheld device/gun. The vision is schematically shown in Figure 2.1. The (bare) MSP sensors, in a size of about 1 inch (2.5 cm) with the same passively and wirelessly detecting feature, are currently and massively placed in the wearing/coats in shopping malls for anti-theft purposes [83]. The wireless detection distance of the MSP sensor has been proved to be more than 1 meter, and theoretically, to be more than several meters when detected/tested by a frequency domain instead of a time domain. Therefore, the polymer-MSP humidity sensors based on the same wirelessly detecting mechanism are probably applicable to be massively used on the farmlands at different depths of the soil.

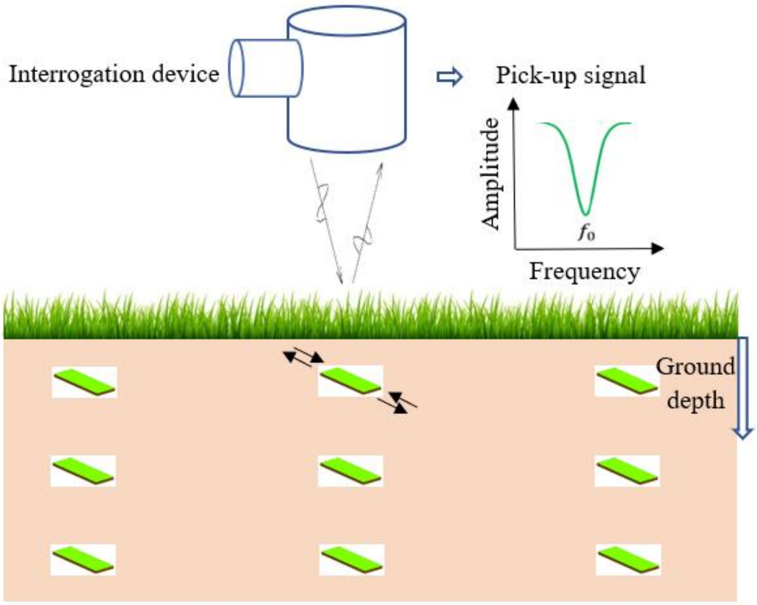

Figure 2.1 A schematic vision of the sensors covered by plastic packaging distributed in the farmlands and placed at different depths of the soil.

In this Chapter, new wireless humidity sensors are developed by using a newly developed sensor platform, i.e., magnetostrictive particle (MSP). A layer of the water-sensitive polymer is coated on the MSP as the sensing element. The wireless polymer-MSP sensors are low-cost and freestanding small-sized sensors to monitor humidity, which are designed for precision agriculture, i.e., in-situ monitoring soil water.

Comparisons of humidity sensing features, such as humidity responses at different humidity levels, and the influence of the thickness of the polymer layer, among CNF-MSP, PVA-MSP, and crosslinked PVA-MSP humidity sensors will be studied. The sensitivity, response time and long-time stability, water-resistant capability, and temperature coefficient of the polymer-MSP sensors will also be systematically studied.

2.1 Sensing principle and characterization method

2.1.1 Polymer-MSP humidity sensor

As has been introduced in Section 1.5.1, MSP in very small sizes can be used as a transducer of the sensor. Under an AC magnetic field, the MSP undergoes a corresponding oscillation having its resonant frequency (RF) which depends on the dimension and physical properties of the MSP. The mechanical oscillation of the MSP causes an emission of magnetic flux that can be measured/detected by a pick-up coil. Hence, the RF of the MSP can be detected wirelessly and passively without any physical connection to the MSP [47.51].

The sensing mechanism of the MSP depends on mass loading onto the surface of the MSP. Specifically, the additional mass attached to the MSP can be considered as a density increase of the MSP, resulting in a decrease of the RF of the MSP, as has been exhibited in Eq. (1-1) in Section 1.5.1 [84].

Based on the sensing mechanism of the mass loading onto the MSP, new wireless humidity sensors can be developed by using the MSP as the transducer and a water-sensitive polymer layer coated on the MSP as the sensing element. As shown in Figure 2.2, when the humidity in the environment changes, the water-sensitive polymer layer absorbs/desorbs water molecules from the humid environment. This water mass-load change results in a change in the RF of the MSP. By monitoring the RF change of the MSP, the relative humidity (RH) of the environment can be wirelessly detected.

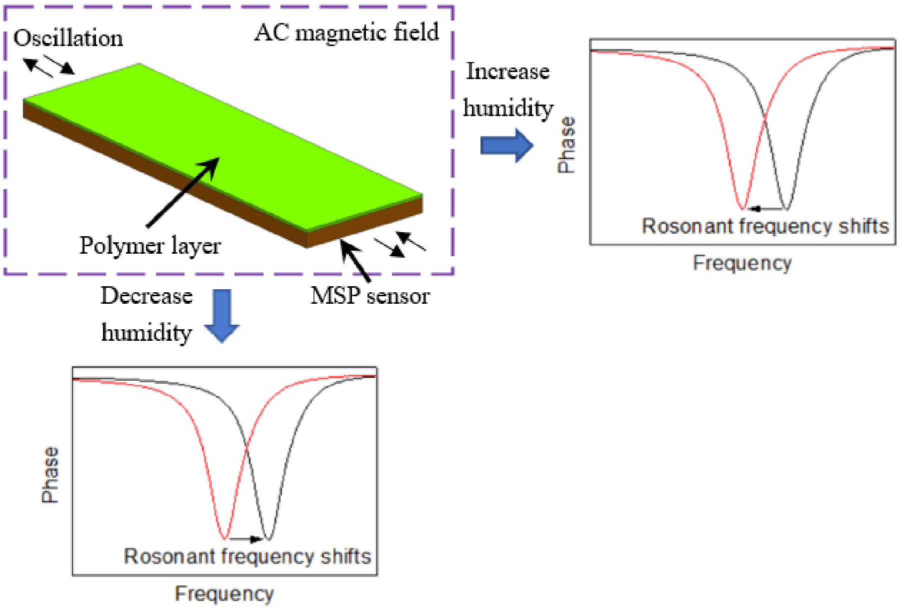

Figure 2.2 Polymer-MSP sensor platform and the humidity sensing principle.

2.1.2 Influencing factors of humidity sensitivity

The sensitivity (i.e., the change of RF corresponding to the change of RH) of the wireless polymer-MSP humidity sensor mainly depends on three aspects, the sensitivity of the MSP (i.e., the dimension of the MSP), the thickness of the water-sensitive polymer layer (and the same length and width of the MSP), and water absorption/desorption ability of the water-sensitive polymer [53,59]. Due to a requirement of the dimension of the MSP to ensure its long wireless detection distance which has been illustrated, the water absorption/desorption ability of the water-sensitive polymer is a key factor in achieving the high sensitivity of the polymer-MSP humidity sensor. Therefore, two different water-sensitive polymers with high water-sensitive ability are selected to develop new polymer-MSP humidity sensors, respectively.

2.1.3 Characterization

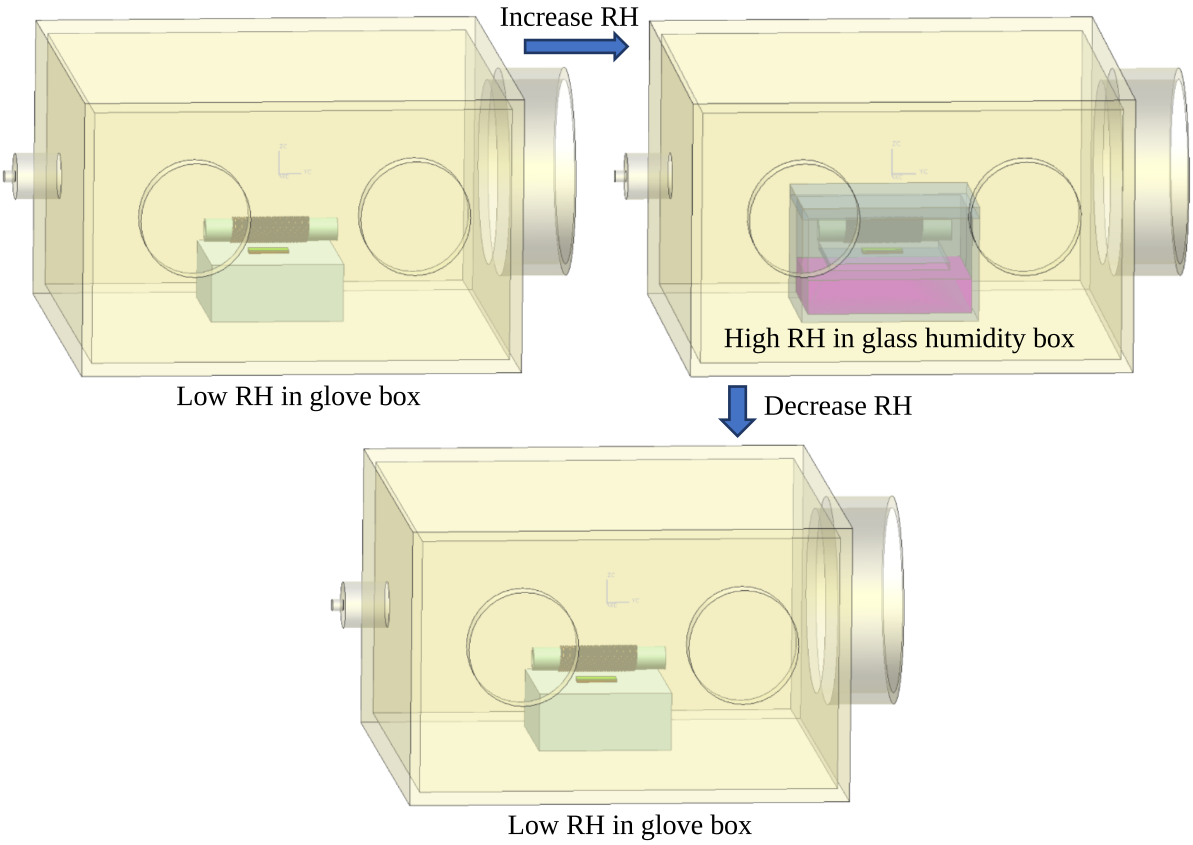

Figure 2.3 Schematic illustration of the humidity sensor placed in the humidity environments controlled by the glove box with low humidity and the glass box containing the saturated salt solution for a generation of the high humidity.

As shown in Figure 2.3, stable humidity conditions are generated by the saturated salt solutions in the glass humidity boxes, respectively. The stable humidity levels generated by the saturated salts are listed in Table 2.1 [85]. Outside the glass humidity boxes, a big glove box is maintaining a stable humidity of 54% RH. The polymer-MSP sensor is placed into and out of the glass humidity boxes for measurements under a humidity cycle between the low humidity of 54% RH and high humidity levels generated in the glass humidity boxes.

Table 2.1 Saturated salt solutions used to generate stable RH at room temperature (20℃) [85].

Temperature\Saturated salt	NaBr	$CuCl_2$	NaCl	KCl	KNO_3
20℃	59.1%	69.1%	75.5%	85.1%	94.6%

Homemade coils are used and connected to a precision impedance analyzer (Agilent 4294A) for wirelessly interrogating with the polymer-MSP humidity sensor placed in the big glove box, as shown in Figure 2.3. The impedance analyzer is used to detect the RF of the wireless humidity sensor by recording the frequency of the peak point (i.e., the minimum point) of the phase angle versus frequency spectrum, as shown in Figure 2.2.

2.1.4 Sensing data analyzing method

To study the humidity response of the polymer-MSP wireless humidity sensor, it is necessary to further analyze the RF corresponding to the humidity change. It should be mentioned that due to the feature of the experimental set-up shown in Figure 2.3, the humidity box containing the saturated salt solution takes time to generate the designed humidity at its saturated level. The increase of the humidity is relatively slower than the decrease of the humidity. However, the decrease of the humidity from a high humidity level (generated by a saturated salt solution) to the low humidity of 54% RH can be considered an immediate change in the humidity environment. Therefore, as shown in Figure 2.4, the RF response during the humidity decrease process can be used for further analysis to reflect the real sensor response.

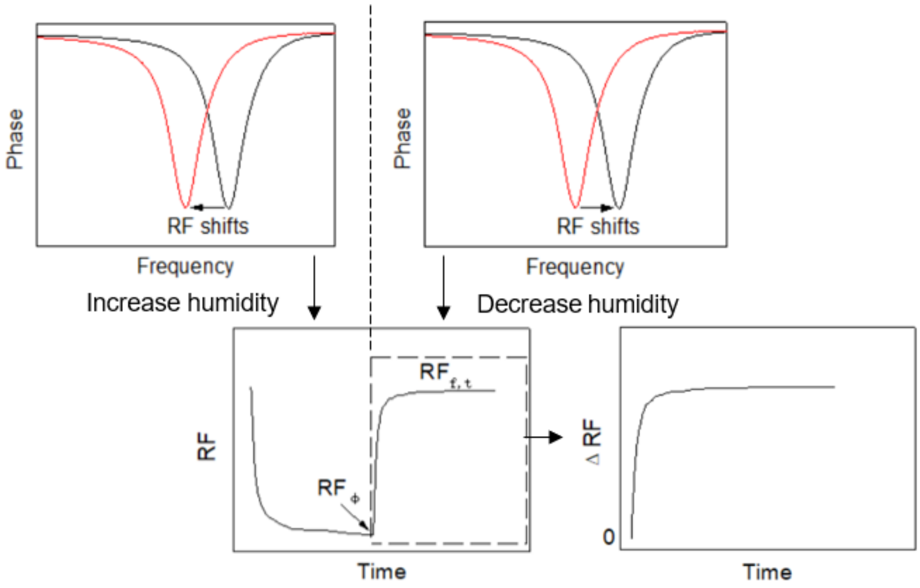

Figure 2.4 Resonant frequency (RF) of the polymer-MSP humidity sensor obtained from the phase peak changes corresponding to one humidity cycle (increase and decrease the humidity) and illustration to calculate the delta resonant frequency (ΔRF) from the RF versus time plot during the humidity decreasing process.

Hence, an important variable, delta resonant frequency (ΔRF), when the humidity is decreased from a high humidity level to low humidity of 54% RH, can be used to analyze the sensor response corresponding to the humidity change. The ΔRF can be calculated by Eq. (2-1):

$$\Delta RF(t) = RF_{f,t} - RF_{\varphi} \qquad (2\text{-}1)$$

where ΔRF(t) is the delta resonant frequency (Hz) with respect to time, which reveals the difference between the RF at a saturated high humidity level to the RF at the low humidity level of 54% RH with respect to time; $RF_{f,t}$ is the RF (changing with time until saturation) at the low humidity level of 54% RH; RF_{φ} is the RF at a high humidity level (when the sensor response is saturated).

2.2 Experiment procedures

2.2.1 MSP preparation

A commercially available magnetostrictive material, Metglas™ 2826MB ribbon, was chosen to fabricate the MSP sensors. Metglas™ 2826MB ribbon was cut into rectangular sensor strips in size of 13.5 mm × 4.5 mm using Disco Automatic Dicing Saw 3220. The rectangular MSP sensors were cleaned in acetone and methanol, successively, by ultrasonic treatment. The MSP sensors were immediately dried with nitrogen gas and heat-treated in a vacuum oven at 220 °C for 2 h releasing residual stress.

2.2.2 CNF coating on the MSP platform

CNF used in this study was obtained in a gel form (Lot no-U31, grade-91% fines) and a CNF suspension was prepared [86]. 2 mL 7.5 wt.% CNF suspension and 0.5 mL 10 wt.% PVA solution were mixed and stirred for 1 h to prepare a uniform CNF and PVA (3:1 in wt. ratio) suspension. The solutions with 50 µL were spin-coated on the sensor platforms (13.5 mm × 4.5 mm) with different rotation speeds in the range from 800 to 3000 r/min for 20 sec, followed by an oven-dry (Isotemp Oven by Fisher Scientific) at 70°C to obtain a CNF coating layer with different thicknesses. The thicknesses of the CNF layers for the sensors were measured by a thickness meter. The CNF-MSP sensors prepared were used for the measurements under the humidity cycle.

2.2.3 Preparation of the crosslinked PVA films with different crosslinking ratios

PVA fine powders, which have a molecular weight (M_w) of 146,000~186,000 and 98% hydrolyzation, were purchased from SIGMA-Aldrich. 9×5 mL 8 wt.% PVA aqueous solutions were prepared at the temperature of 95℃ stirring for 4 h. For a purpose of optimization of the crosslinking density of the crosslinked PVA film, different amounts of glutaraldehyde (GA) in 50 wt.% were added to the PVA aqueous solutions and the ratios of the newly prepared mixture of GA and PVA were shown in Table 2.2. Diluted hydrochloric acid was added to the solution to adjust the Ph value of the solution to 3.0.

Table 2.2 Molar ratio and weight ratio of GA/PVA to spin coat the crosslinked PVA films.

Molar ratio of GA/PVA	0:1	4:1	8:1	16:1	33:1	83:1	208:1	416:1	832:1
Weight ratio of GA/PVA	0:1	1:400	1:200	1:100	1:50	1:20	1:8	1:4	1:2

The films were cast using different GA/PVA ratios of solutions prepared by spin coating with a low speed of 500 r/min on big glass slides (75 mm × 50 mm). They were dried in an oven (Isotemp Oven by Fisher Scientific) at 70℃ for drying and crosslinking. For the solution with each GA/PVA ratio, six films were prepared. The crosslinked PVA films were rinsed in deionized (D.I.) water and dried in the oven at 70℃. The crosslinked PVA films were prepared by peeling off from the big glass slides.

2.2.4 Measurement of remaining mass and weight gain of the crosslinked PVA films

A study on the determination of the GA/PVA ratio regarding the performance of the crosslinked PVA films was conducted. To evaluate the percentage of weight gain of the crosslinked PVA films under a high humidity of 95% RH, films were placed from dry condition to 95% RH for 3 days to ensure humidity equilibrium along the thickness of the films was reached and the weight of the films was immediately measured. To evaluate the water-resistance of the film, the crosslinked PVA films were completely immersed in D.I. water for three times 12 h immersion and dried after each water immersion. The remaining mass of the films for each time of water immersion was measured when the films were dried in a vacuum furnace.

2.2.5 FTIR measurement of the crosslinked PVA films

For verification of the occurrence of the crosslinking reaction of the PVA, Fourier transform infrared spectroscopy (FTIR) measurements on three PVA films with different crosslinking GA/PVA ratios (0:1, 1:100, 1:20 in wt. ratio) were conducted, respectively, by a Thermo Scientific iS-50 FTIR with an ATR attachment that enabling the films to be directly tested.

2.2.6 DSC test of the crosslinked PVA films

Differential scanning calorimetry (DSC) tests of the crosslinked PVA films with different GA/PVA ratios were conducted on a DSC 250 provided by TA Instruments. DSC specimens in weight of 8 mg were prepared for each test.

2.2.7 Crosslinked PVA and pure PVA coatings on the MSP platform

The MSP sensor platform in the dimension of 13.5 mm × 4.5 mm × 30 µm (the same platform size as that to prepare the CNF-MSP sensor) was used as the substrate for coating the crosslinked PVA layer. The same PVA fine powders (M_w=146,000~186,000, 98% hydrolyzation) were used to prepare the solution. Two equal volumes of 4 mL 8 wt.% PVA aqueous solution was prepared at the temperature of 95℃ stirring for 4 h. One volume of the solution (in pure PVA) was ready for coating. Another volume of the solution was mixed with 6.4 μL 50 wt.% GA to prepare GA/PVA solution in a weight ratio of 1:100. Diluted hydrochloric acid was also added to the GA/PVA solution to adjust the Ph value of the solution to 3.0. The two solutions (pure PVA and crosslinked PVA) were spin-coated on one surface/side of the MSP sensors with different rotation speeds ranging from 900 to 3500 r/min for 20 sec, respectively, to obtain different thicknesses of the PVA layers. Then, they were oven-dried at 70℃. The pure PVA-MSP sensors were prepared. For sensors coated with the crosslinked PVA layers, a rinse in D.I. water and a drying process in the oven at 70℃ were followed, consecutively. The crosslinked PVA-MSP sensors were prepared.

2.2.8 SEM surface morphology observation

JEOL 7000F field emission scanning electron microscopy (FE-SEM) was used to observe the surface morphology of the crosslinked PVA film which was coated on the MSP sensor platform. Moreover, the thicknesses of the PVA layers for the sensors were measured by a thickness meter.

2.2.9 Temperature-dependent sensor response measurement

A (bare) MSP sensor and a crosslinked PVA-MSP humidity sensor in the same dimensions of the MSP (13.5mm×4.5mm×30μm) were used for the humidity response measurements at different temperatures. At various temperature conditions ranging from 10℃ to 40℃

generated by a heater in the big glove box, the humidity sensors were placed from one humidity box with low humidity (about 54% RH) to another humidity box with high humidity (about 85% RH), respectively, in the big glove box to obtain one humidity cycle. The two humidity boxes were all placed in the big glove box with a constant humidity of 54% RH. The characterization process has been illustrated in Section 2.1.3 - Characterization.

2.3 CNF-MSP humidity sensor

Several organic water-sensitive elements have high water sensitivity, such as polyethylene oxide (PEO), chitosan, et. al [87-89]. However, by the pre-verification experiments conducted in our lab, PEO suffers from a small humidity sensing range and very low sensing stability as its structure can be easily damaged during water absorption in high humidity conditions. Moreover, chitosan suffers from a large humidity sensing hysteresis since chitosan is difficult to desorb water molecules while decreasing humidity.

Among all the organic water-sensitive elements, CNF is considered one of the promising water-sensitive elements [90]. CNF is a natural organic material composed of cellulose fibers in nano-size with a high length-to-width ratio [91,92]. The fiber width of the CNF is in the range of 5 to 20 nm and their length is in micrometer [93,94]. Due to the vast numbers of hydroxyl groups of the backbone of the nano-cellulose and the nano-porous fibric structure, CNF has some superior characteristics, such as a high water sensitivity, very low humidity hysteresis, high humidity cycle stability, and unique insolubility to water [95]. Moreover, CNF is also an environmentally friendly material, which can be degraded in the environment in years, hence, is suitable in the application of agriculture where large numbers of sensors are required for the farmland [96]. According to the overall beneficial characteristics of the

CNF, in this research, the CNF is used as the water-sensitive element to develop a novel CNF-MSP humidity sensor.

As shown in Figure 2.5, a thin layer of CNF is uniformly coated on the MSP sensor platform to develop the CNF-MSP sensor. When the humidity in the environment changes, vast numbers of hydroxy groups of the CNF absorb/desorb water molecules from the environment, bonding/debonding the hydrogen bonds with water molecules, which results in a change in the resonant frequency (RF) of the MSP due to the mass-load change caused by the absorption/desorption of water by the CNF layer. Based on the relationship between the mass and the RF of the sensor, which has been illustrated in Eq. (1-3) in chapter 1, the RF of the sensor can be continuously measured corresponding to the change in the environment.

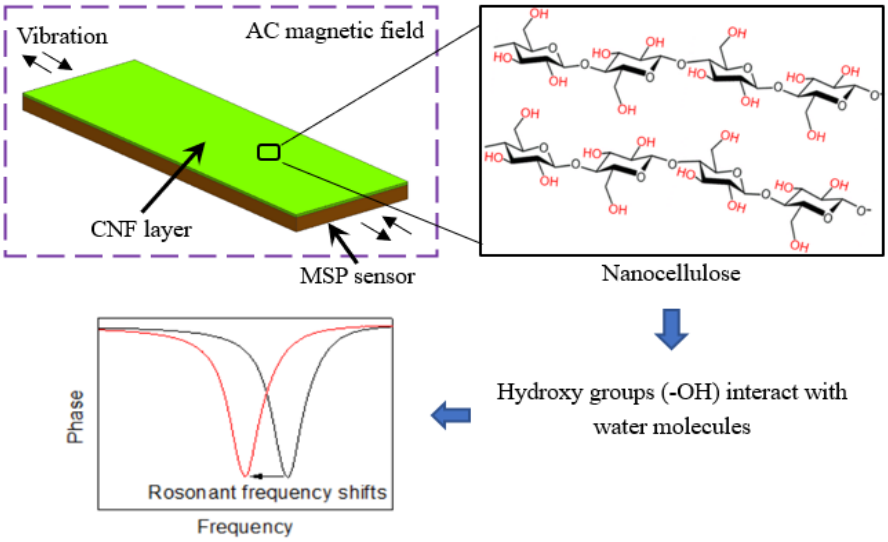

Figure 2.5 Cellulose nanofiber (CNF)-MSP sensor and the humidity sensing principle.

2.3.1 Sensor responses at different humidity levels

The humidity responses of a sensor with a 5.9 μm CNF layer are shown in Figure 2.6. Figure 2.6(a) shows one humidity cycle between different high humidity levels and low humidity of 54% RH and the corresponding RF vs time plots in different humidity cycles under different high humidity levels, respectively. For each test with a high RH, it shows that the RF significantly decreases with increasing humidity and eventually reaches a saturated value, and then increases with decreasing humidity and reaches a saturated value at the low humidity, which is the same as the initial RF at the beginning of the test.

After the calculation by Eq. (2-1) from the data points in Figure 2.6(a), Figure 2.6(b) shows the ΔRF vs time results for the sensors with a 5.9 μm CNF layer when the humidity is immediately decreased from different high humidity levels to the low humidity of 54% RH.

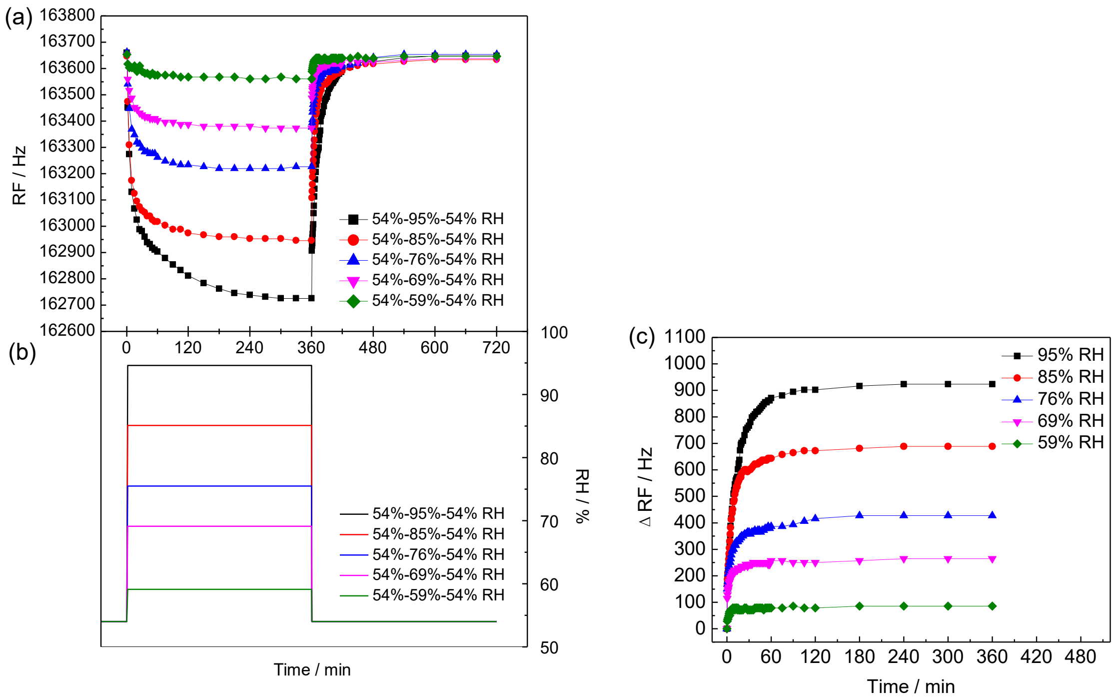

Figure 2.6 Resonant frequency responses of the CNF-MSP sensor with 5.9 μm CNF layer under different humidity levels. (a) Resonant frequency (RF) vs time plots; and (b) corresponding relative humidity (RH) vs time plots in one humidity cycle; (c) delta resonant frequency (ΔRF) vs time plots when humidity is decreased to 54% RH.

A classic model describing the mass diffusion is used to fit the humidity response (i.e., ΔRF) of the newly developed polymer-MSP humidity sensor, which is as follows:

$$\Delta RF = \Delta RF_{sat} \cdot [1 - \exp(-At)] \qquad (2\text{-}2)$$

where ΔRF is delta resonant frequency (Hz); t is time (min); ΔRF_{sat} is saturated delta resonant frequency (Hz), which is a constant at a humidity testing level; A is a constant at a humidity testing level.

Reorganize the terms of Eq. (2-2) and take logarithm on both sides:

$$\ln\left(1 - \frac{\Delta RF}{\Delta RF_{sat}}\right) = -At \qquad (2\text{-}3)$$

The data points of $\ln(1-\Delta RF/\Delta RF_{sat})$ vs time of the CNF-MSP sensor when the humidity is decreased are shown in Figure 2.7(a). However, the data points are not following a linear relationship, and hence, cannot be fitted by Eq. (2-3). An alternative fitting method is used to fit just the linear portion of the data. Besides, it is noted that, in Eq. (2-3), ΔRF_{sat} is difficult to accurately calculate as it is in the group of the fitting constant, $\ln(1-\Delta RF/\Delta RF_{sat})$. Therefore, to observe the influence of ΔRF_{sat}, three different ΔRF_{sat} values are used to fit the linear portion in Figure 2.7(a). As a result, the fittings are almost the same by using the three different ΔRF_{sat} values, which reveals that the variation of ΔRF_{sat} will not affect much of the fitting result and any suitable ΔRF_{sat} value can be used for the linear fitting to determine the fitting constant (A). After the determination of A, the fitting curve by Eq. (2-2) is plotted in Figure 2.7(c). However, the fitting curve of ΔRF when the humidity is decreased is somewhat slower than/deviates from those of the tested data points. The fitting curve also has a delayed turning point after the sharp changing stage of ΔRF in the beginning and has a higher ΔRF value than the tested data points after reaching the turning point. Therefore, this classic model is not very suitable to fit the time-dependent humidity response of the crosslinked PVA-MSP sensor.

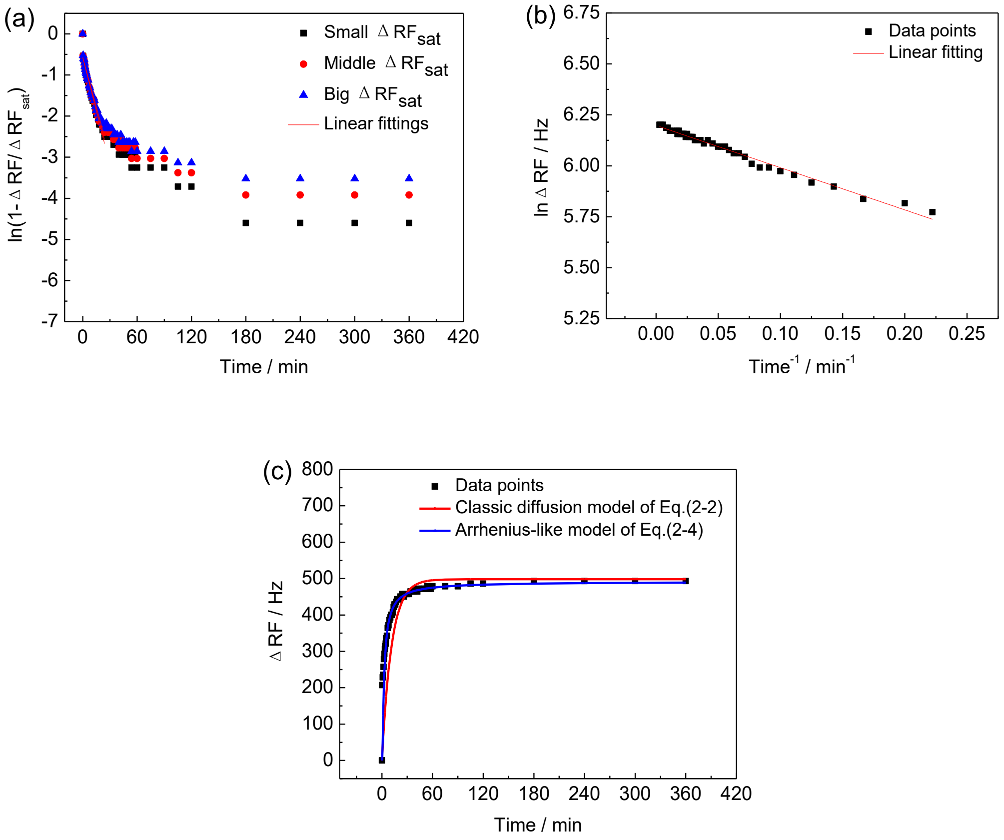

Figure 2.7 Schematics of the fittings of the data points of the CNF-MSP sensor when humidity is decreased. (a) Ln(1-$\Delta RF/\Delta RF_{sat}$) vs time and linear fittings of the linear part (first 28 data points) by three different ΔRF_{sat} values; (b) linear fitting of the data points of logarithm delta resonant frequency (lnΔRF) vs time^{-1} (min^{-1}); (c) different fitting methods to fit the data points of delta resonant frequency (ΔRF) vs time.

An Arrhenius-like equation can be used to fit the tested data points of the ΔRF versus the time of the humidity sensor, which is exhibited in Eq. (2-4):

$$\Delta \mathrm{RF} = \Delta RF_{sat} \cdot \exp\left(-\frac{B}{t}\right) \qquad (2\text{-}4)$$

where B is a constant at a humidity testing level.

Take the logarithm on both sides of Eq. (2-4) and reorganize the terms:

$$\ln(\Delta \mathrm{RF}) = \ln(\Delta RF_{sat}) - \frac{B}{t} \quad \text{(2-5)}$$

As shown in Figure 2.7(b), the data points of the logarithm ΔRF vs time^{-1} (min^{-1}) of the CNF-MSP sensor show a linear relationship and are fitted by Eq. (2-4) when the humidity is decreased. As shown in Figure 2.7(c), the fitting result of the ΔRF vs time by Eq. (2-4) can better describe the tested data points than that of the fitting result by Eq. (2-2), implying that the Arrhenius-like Eq. (2-4) is very suitable to be used to describe the time-dependent humidity response of the newly developed polymer-MSP-based humidity sensor.

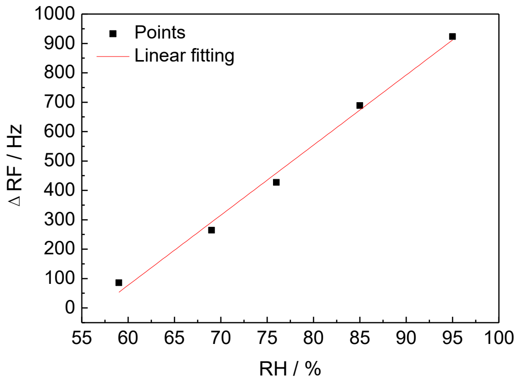

Figure 2.8 Calculated data points of saturated delta resonant frequency (ΔRF_{sat}) vs RH and their linear fitting.

The values of the saturated delta resonant frequency (ΔRF_{sat}) are 85.8, 264.5, 427.1, 688.3, and 923.5 Hz, when humidity decreases from 59%, 69%, 76%, 85%, 95% RH, to 54% RH, respectively. As shown in Figure 2.8, it is found that the ΔRF_{sat} of the sensor with a 5.9 μm CNF layer is close to linearly dependent on RH. The coefficient of determination (R^2) of the linear fitting is 0.991. The sensitivity of 23.8 Hz/%RH for the sensor with a 5.9 μm CNF layer is obtained from the slope of the linear fitting. Besides, the analysis of the response times of the sensors with different thicknesses of the CNF layer will be studied in the next Section.

2.3.2 Sensor responses in different thicknesses of CNF layer

The responses, i.e., the RF, of the sensors with different thicknesses (1.9~9 μm) of the CNF layer tested in the same humidity range between 54% and 85% RH are shown in Figure 2.9. Figure 2.9(a) shows the RF versus time plots in one humidity cycle for different thicknesses of the CNF layer.

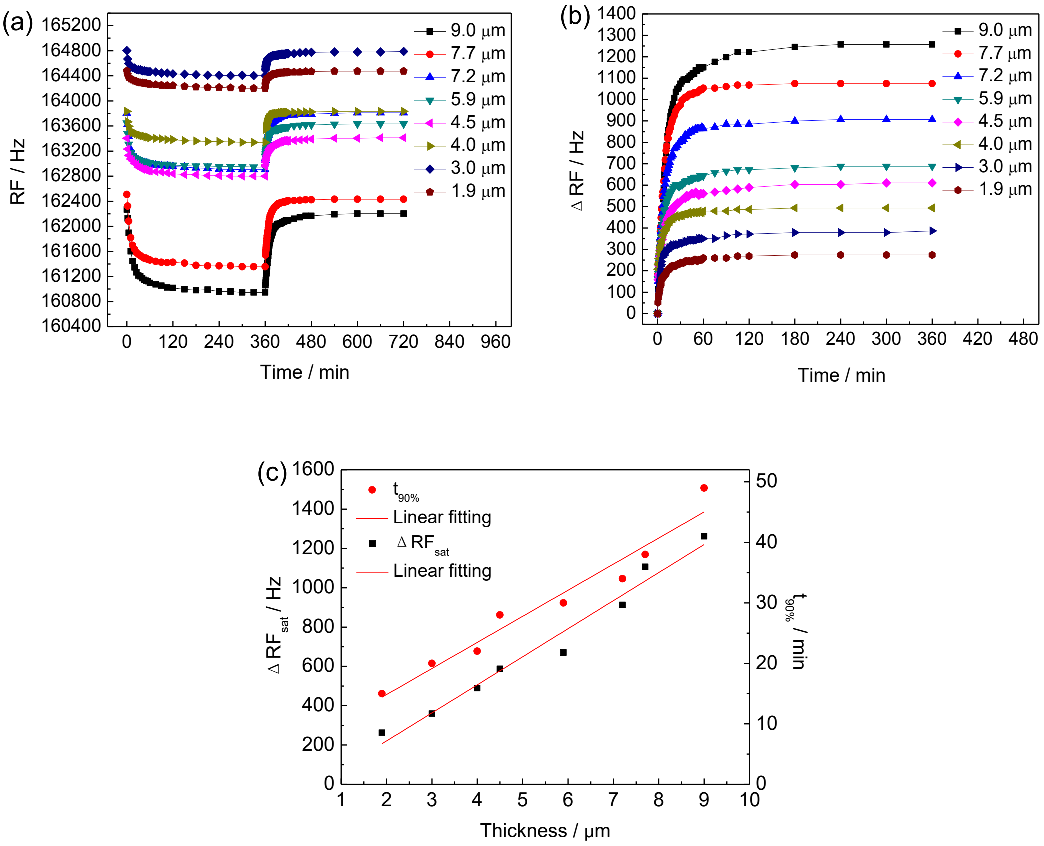

Figure 2.9 Resonant frequency responses of the sensors with different thicknesses (1.9~9 μm) of CNF layers tested in the same humidity range between 54% and 85% RH. (a) Resonant frequency vs time plots in one humidity cycle; (b) delta resonant frequency (ΔRF) vs time

plots when decreasing humidity; (c) saturated delta resonant frequency (ΔRF_{sat}) of the MSP sensor and the response time ($t_{90\%}$) vs the thickness of the CNF layer, respectively.

In this study, the RFs of the sensors at 54% RH are in the range of 162 kHz to 165 kHz, as shown in Table 2.3. Table 2.3 reveals that, with the increase of the thickness of the CNF layer, the increased CNF mass, which is loaded onto the MSP sensor, decreases the RF of the sensor. Moreover, from Figure 2.9(a), all the sensors with different thicknesses of the CNF layers exhibit consistent responses. That is, the RF decreases with increasing RH and increases with decreasing RH. The ΔRF of the sensors with different thicknesses of the CNF layer are calculated by Eq. (2-4) when RH decreases from 85% to 54%. As has been illustrated in Figure 2.4 in Section 2.1.4, the ΔRF versus time plots, which can reflect the response of the CNF-MSP sensors, are shown in Figure 2.9(b). With decreasing RH, the ΔRF rapidly changes and finally reaches a constant value. After linear fittings by Eq. (2-5) on the data points of the logarithm ΔRF versus time^{-1} (min^{-1}), the saturated delta resonant frequency (ΔRF_{sat}) of the sensors with different CNF layers can be obtained. The values of ΔRF_{sat} and the fitting constant B for the sensors with different thicknesses of the CNF layers are listed in Table 2.3, which implies that both the values of ΔRF_{sat} and B decrease with the decrease of the thickness of the CNF layer, respectively. As shown in Figure 2.9(c), it is observed that the ΔRF_{sat} of the MSP-based sensor is linearly dependent on the thickness of the CNF layer. The coefficient of determination (R^2) of the linear fitting is 0.973. By the linear fitting, ΔRF_{sat} per unit thickness of the CNF layer is 137.6 Hz/μm. It is a parameter to select the suitable thickness of the CNF layer, which can determine the humidity sensitivity of the CNF-MSP sensor.

Table 2.3 Base resonant frequencies (RF_0) of the CNF-MSP sensors with different thicknesses of the CNF layers at 54% RH and saturated delta resonant frequency (ΔRF_{sat}) when humidity decreases from 85% RH to 54% RH and linear fitting constant (B) fitted by Eq. (2-4).

Thickness of the CNF	9.0	7.7	7.2	5.9	4.5	4.0	3.0	1.9
RF_0 / Hz	162268	162509	163803	163647	163405	163831	164803	164480
ΔRF_{sat} / Hz	1262	1106	912	670	587	489	359	262
B	5.82	4.29	4.08	3.01	3.32	2.07	2.21	3.13

Response time is usually used to reflect the response speed of the humidity sensors. The response time of a humidity sensor is defined as: the time to reach 90% of the ΔRF_{sat} of the sensor with respect to an immediate humidity change.

After the fittings by Eq. (2-4), the ΔRF_{sat} at different times for the sensors with different thicknesses of the CNF layer is shown in Figure 2.9(c). It reveals that the response time of the sensors is more than a few minutes long and is linearly increased as the thickness of the CNF layer increases. Since the microstructure of the CNF layer consists of CNF nanofibers, the response time for water molecules to penetrate through the CNF nanofibers during water absorption/desorption is controlled by the bonding and penetration speeds of the CNF nanofibers. It is preferable that the response time of the sensor can be minimized by reducing the thickness of the CNF layer. On the other side, a large ΔRF_{sat}, which contributes to high sensitivity, is also required by increasing the thickness of the CNF layer. For instance, to obtain a response time of about 19 min, a sensitivity of 12.3 Hz/%RH is obtained for the sensor with a 3 μm CNF layer. To obtain a response time of about 15 min, a sensitivity of 7.9 Hz/%RH is obtained for the sensor with a 2 μm CNF layer.

2.3.3 Long-time stability of the CNF-MSP humidity sensor

The long-time stability of the sensor is tested for 7 days. The humidity testing results of the sensor with a 3 μm CNF layer are shown in Figure 2.10. RFs of the sensor in 7 diurnal cycle humidity tests between 54% and 85% RH are plotted in Figure 2.10(a). Moreover, the ΔRFs of the sensor when RH increases and decreases in 7 diurnal cycles are calculated by Eq. (2-4). As a result, the stability of the sensor in 7 humidity cycles when RH is increased and decreased is shown in Figure 2.10(b). A little random fluctuation of the ΔRF_{sat} can be observed for the processes of both increasing and decreasing humidity. It is found that the fluctuations of the ΔRF_{sat} for either increasing or decreasing humidity are less than ±50 Hz. It reveals that, with a sensitivity of 12.3 Hz/%RH, the sensor is possible to detect humidity with an accuracy of about ±4% RH. Although the CNF is considered a non-soluble water-sensitive element, the PVA, which is mixed and filled in the space of CNF fibers in a small amount to improve the physical attachment of the CNF layer to the MSP sensor platform, can probably be dissolved in water. The possible reason for the high fluctuation of the tested results might be related to the partial dissolution of the PVA chains in the CNF layer while absorbing water molecules at high humidity. Moreover, stresses that are generated between the CNF layer and the MSP sensor platform during the humidity test might be another reason, which will be further discussed in Section 2.4.8. But it seems that these two possible influencing reasons are reversible among cycles and not accumulated over time.

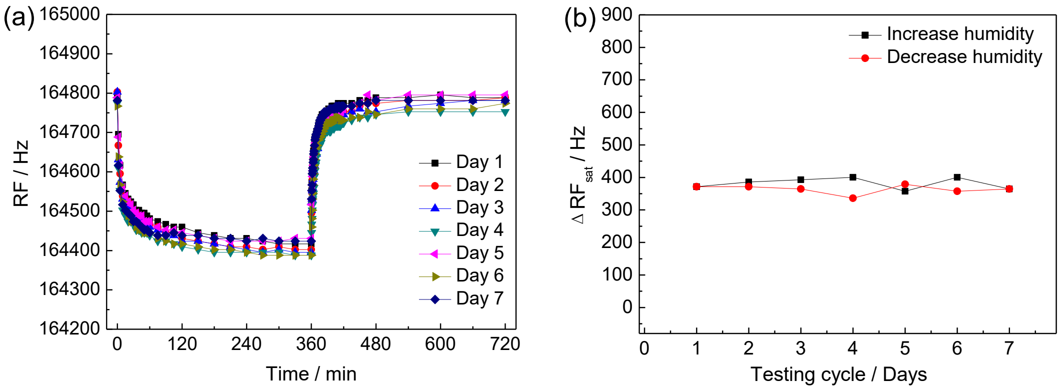

Figure 2.10 Long-time stability of the CNF-MSP sensor with 3 μm CNF layer in 7 days with 54%-85%-54% RH cycle. (a) The resonant frequency (RF) of the sensor for 7-cycle humidity tests in 7 days; (b) comparison of the saturated delta resonant frequencies (ΔRF_{sat}) of the sensor for both increasing and decreasing humidity.

2.4 Crosslinked PVA-MSP humidity sensor

As shown in Figure 2.11, a crosslinked PVA thin layer, which is used as the water-sensitive element, is coated on the MSP sensor platform. As shown in Figure 2.12, the crosslinking reaction occurred between GA and PVA to form a network structure. It is known that PVA contains huge numbers of hydroxy groups. These hydroxy groups absorb/desorb water molecules in the environment, forming hydrogen bonds with water molecules. As a result, PVA changes its mass with respect to the humidity variation in the environment [97,98]. Similar to the humidity sensing mechanism of the CNF-MSP sensor, as the PVA layer is tightly attached to the MSP sensor platform, the overall mass of the sensor changes with the variation of humidity so that the humidity can be continuously measured from the ΔRF of the sensor. In summary, the MSP sensor platform coated with a humidity-sensitive element, i.e., crosslinked PVA layer, can be used as a water-mass-based sensor for the irrigation process in agriculture applications.

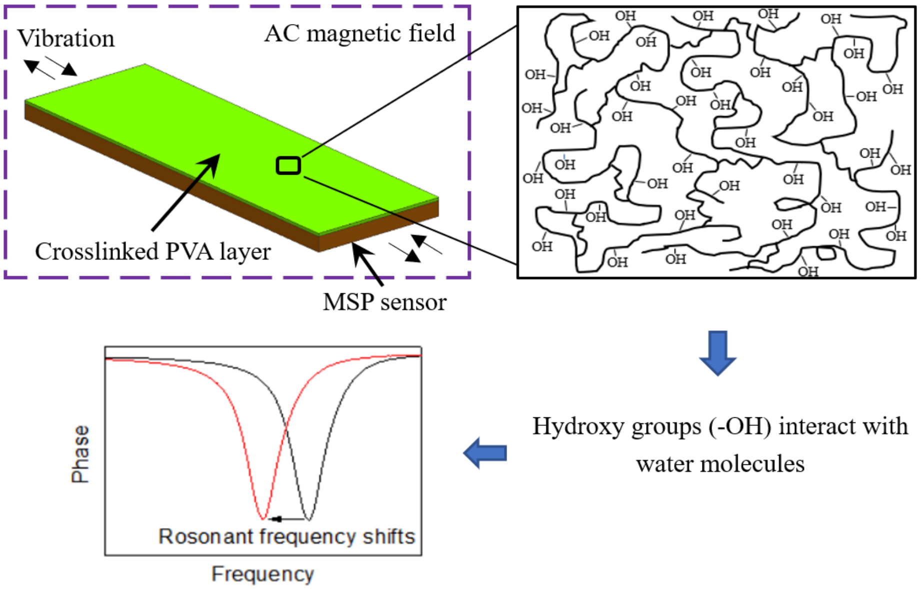

Figure 2.11 Crosslinked PVA-MSP humidity sensor and the humidity sensing principle.

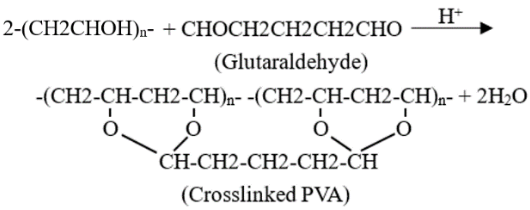

$$2\text{-}(CH2CHOH)_n\text{-} + CHOCH2CH2CH2CHO \xrightarrow{H^+}$$
$$\text{(Glutaraldehyde)}$$
$$\text{-}(CH2\text{-}\underset{|}{CH}\text{-}CH2\text{-}\underset{|}{CH})_n\text{-}\ \text{-}(CH2\text{-}\underset{|}{CH}\text{-}CH2\text{-}\underset{|}{CH})_n\text{-} + 2H_2O$$
$$O\quad O\qquad O\quad O$$
$$CH\text{-}CH2\text{-}CH2\text{-}CH2\text{-}CH$$
$$\text{(Crosslinked PVA)}$$

Figure 2.12 Crosslinking reaction formula between PVA and glutaraldehyde (GA) to form a crosslinked PVA network.

2.4.1 Crosslinking characterized by determination of PVA/GA ratio

PVA is considered a very promising humidity sensing element, due to its high water absorption ratio (higher than CNF), large humidity sensing range, fast sensing response, and high stability [97,99]. Therefore, using PVA as the water-sensitive element can improve both the sensitivity and response time of the MSP-based humidity sensor, compared with the newly developed CNF-MSP sensor. However, the major drawback is that PVA alone could not withstand water immersion as the sensor might be directly exposed to water during irrigation. By crosslinking, the PVA film was modified to obtain water resistance capability [100,101]. An issue comes out that as PVA gains water-resistant capability by crosslinking, considerable numbers of hydroxy groups in PVA are grafted, hence, humidity sensing sensitivity would decrease. Therefore, a systematic study was first carried out to optimize the ratio of PVA to the crosslinker, glutaraldehyde (GA), to obtain a crosslinked PVA film while maintaining a high humidity sensing sensitivity. Second, the influence of different humidity, and different thicknesses of the crosslinked PVA layer on the sensing response of the crosslinked PVA-MSP sensors, and their comparison with the (pure) PVA-MSP sensors without crosslinking of PVA were studied, respectively. Third, the long-time stability and water resistance of the crosslinked PVA-MSP humidity sensor were analyzed, respectively.

2.4.1.1 Remaining mass and weight gain of the crosslinked PVA films

Figure 2.13 shows the crosslinked PVA remaining mass while the PVA film is water immersed for 24 hours followed immediately by the oven-dry (two times of 12 h water immersion and dry processes) and the weight gain of the PVA film under humidity of 95% RH respect to the film in dry condition. Table 2.4 reveals that the remaining mass of the crosslinked PVA films prepared by different crosslinking ratios of GA: PVA after water immersion for 24 h is retained without further loss of the mass except for the remaining mass of pure PVA film (GA: PVA = 0:1).

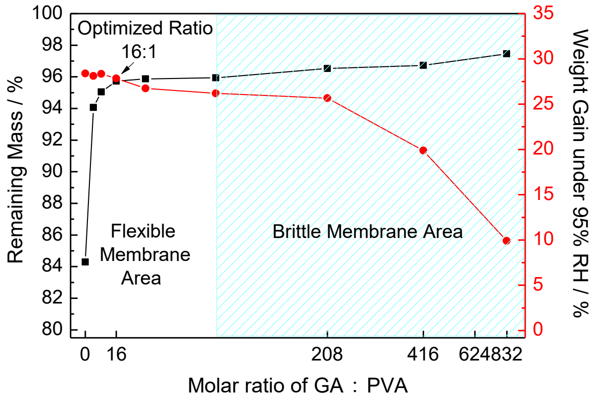

Figure 2.13 Percentage of average remaining mass of the crosslinked PVA films prepared by the different molar ratio of GA: PVA after water immersion for 24 h (12 h + 12 h) and percentage of weight gain of the films under humidity of 95% RH.

Table 2.4 The remaining mass of the crosslinked PVA films prepared by different crosslinking ratios of the crosslinker, GA: PVA after water immersion for one time of 12 h and the second time of another 12 h.

Weight ratio of GA and PVA	Molar ratio of GA and PVA	Mass before tests	Remaining mass after 1st 12 h water immersion		Remaining mass after 2nd 12 h water immersion		Remaining mass after 3rd 12 h water immersion
		(mg)	(mg)	(%)	(mg)	(%)	(%)
0:1	0:1	98.7	86.5	86.4	85.1	84.2	83.3
		88.6	76.2		73.7		
		88.3	75.6		73.5		
1:400	4:1	84.8	80.1	94.5	79.7	94.1	94.0
		71.6	67.7		67.4		
		83.1	78.4		78.2		
1:200	8:1	65.1	61.9	95.1	61.8	95.0	95.0
		61.7	58.7		58.7		

		72.9	69.3		69.3		
1:100	16:1	55.6	53.4	95.9	53.3	95.7	95.7
		86.2	82.4		82.4		
		68.7	65.9		65.8		
1:50	33:1	65.8	63	95.9	62.9	95.9	95.9
		69.7	66.9		66.9		
		68.1	65.4		65.4		
1:20	83:1	76.3	73.7	96.0	73.6	96.0	96.0
		74.4	71.2		71.2		
		98	93.8		93.8		
1:8	208:1	75.2	72.6	96.6	72.5	96.5	96.5
		75.8	73.6		73.6		
		82.1	78.9		78.9		
1:4	416:1	90.4	87.3	96.8	87.2	96.8	96.8
		45.9	44.5		44.5		
		68.6	66.5		66.5		
1:2	830:1	32.4	31.6	97.5	31.6	97.5	97.5
		57	55.7		55.6		
		44.1	42.9		42.9		

From Figure 2.13, the remaining mass of the PVA film after water immersion of 24 h and the immediate drying process firstly increases dramatically with increasing molar ratio of GA: PVA. The reason is that, as the crosslinker, GA, increases, films are crosslinked by forming a network, gaining a water-resistant capability for the PVA film and preventing its weight loss during water immersion. However, the plot of the mass that remained after water immersion is nearly flattened and is increased very slowly when the molar ratio of GA: PVA is higher than 16:1. The reason is that, as the crosslinker, GA, increases, a crosslinked PVA network is formed and only small numbers of non-crosslinked segments of PVA are removed from the PVA film by water immersion. In contrast, as shown in Figure 2.13 and Table 2.5, the weight gain of the PVA film under humidity of 95% RH slightly decreases at first with an increasing molar ratio of GA: PVA, due to that the hydroxy groups are slightly consumed from crosslinking reactions with GA and sufficient numbers of hydroxy groups are still existed to contribute to humidity sensing. When the molar ratio of GA: PVA is higher than 208:1, the weight gain of the crosslinked PVA film under humidity of 95% RH significantly decreases, as the crosslinking density is very high and fewer hydroxy groups are existed in the PVA film to form hydrogen bonds with water molecules [99,100]. It should be mentioned that when the crosslinking density increases, more hydroxy groups are consumed to form the crosslinking points between the adjacent PVA chains and there should be fewer water-molecule bonding sites in the PVA, resulting in a fast decrease in the water weight gain of the crosslinked PVA film with increasing the crosslinking density. However, the water weight gain only decreases very slightly with increasing the crosslinking density. This interesting phenomenon will be discussed in Section 2.4.1.3 when analyzing DSC plots of the crosslinked PVA films. Besides, when the molar ratio of GA: PVA is higher than 103:1, the crosslinked PVA film gets brittle and even crumpled, losing its physical adhesion capability to the substrate, i.e., the MSP sensor platform. The brittle film obtained from the high molar ratio of GA: PVA is shown by the blue color area in Figure 2.13. In summary, an optimized molar ratio of GA: PVA is from 16:1 (1:100 in weight ratio) to 33: 1 (1:50 in weight ratio), where theoretically a PVA chain has from 16 to 33 crosslinking points connected to other PVA chains. In this crosslinking density range, a strong water resistance, and a good film adhesion (to the MSP sensor platform) can be obtained for the manufacture of the crosslinked PVA-MSP humidity sensors while a superior humidity sensing/water absorption capability is also retained.

Table 2.5 Percentage of water weight gain of the crosslinked PVA films from dry condition prepared by the different molar ratio of the crosslinker, GA: PVA under humidity of 95% RH.

Weight ratio of GA and PVA	0:1	1:400	1:200	1:100	1:50	1:20	1:8	1:4	1:2
Molar ratio of GA and PVA	0:1	4:1	8:1	16:1	33:1	83:1	208:1	416:1	830:1
Water weight gain / wt.%	28.3	28.1	28.3	27.8	26.7	26.2	25.7	19.9	9.9

2.4.1.2 FTIR analysis

To further verify the occurrence of the crosslinking reaction of the PVA, FTIR transmittance spectrums of three PVA films with different GA/PVA wt. ratios (0:1, 1:100, 1:20) are measured and analyzed. As shown in Table 2.6 and Figure 2.14(a), the transmittance peaks of different stretching and bending vibrations are identified. A broad peak is observed at a wavenumber of about 3282 to 3292 cm^{-1} for all three samples, which implies a stretching vibration of O-H (hydroxyl group). It reveals the existence of -OH groups on the backbone of PVA [101-104]. A sharp peak can be observed at 2940 cm^{-1} for all three samples, which implies sp^3 C-H stretching vibration [101,103]. As is widely known, sp^3 C-H bonds largely exist in alcohol-like structures, such as PVA. In the fingerprint region below 1500 cm^{-1}, there are four major peaks. A peak at 1417 cm^{-1} implies a bending vibration of sp^3 C-H. A peak at 1328 cm^{-1} implies a bending vibration of the -CH$_3$ group. A peak at 1087 cm^{-1} represents a stretching vibration of C-O. It is another piece of evidence of the existence of the hydroxyl group which has been verified at the vibration peak from 3282 to 3292 cm^{-1}. A peak at 839 cm^{-1} implies a bending vibration of sp^2 C-H. Moreover, small peaks at a wavenumber of 965 cm^{-1} can be observed for the PVA samples with GA/PVA wt. ratios of 1:100 and 1:20, however, could not be observed for the pure PVA sample. The vibration peak at 965 cm^{-1} is probably evidence of the formation of acetal rings (C-O-C stretching) from the acetal reaction [104].

Table 2.6 Transmittance peaks of different stretching and bending vibrations.

Bond	O-H	C-H	C-H	$-CH_3$	C-O	C-O-C	C-H
Vibration mode	Stretch	sp^3 stretch	sp^3 bend	Bend	Stretch	Stretch	sp^2 bend
Vibration peak / cm^{-1}	3282-3292	2940	1417	1328	1087	965	839

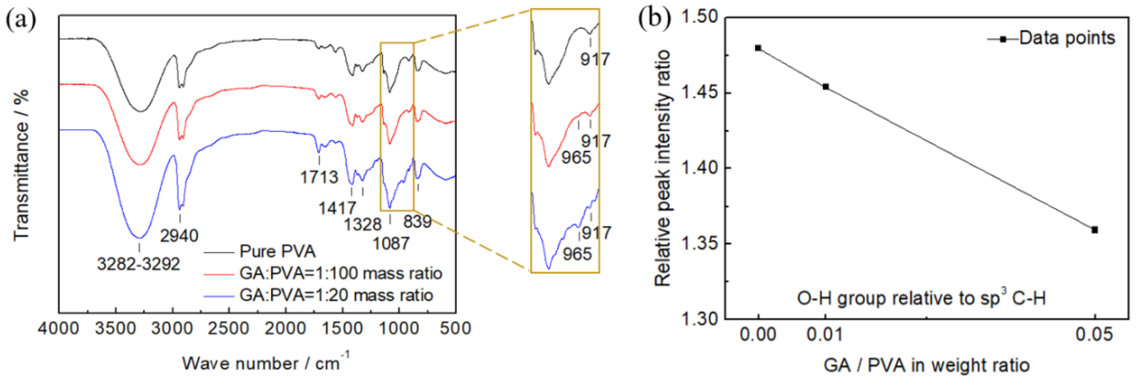

Figure 2.14 FTIR transmittance spectrums of PVA films with different GA/PVA wt. ratios (a); and relative peak intensity of stretch vibration of O-H (hydroxyl group) to the peak intensity of the stretch vibration of sp^3 C-H vs. GA/PVA in wt. ratio (b).

The peak intensity of sp^3 C-H bonds has always been used as the reference peak intensity to analyze and determine the relative amount of the other bonds in the material, owing to its stability before and after the crosslinking reaction [102,103,105]. Therefore, a relative analysis of the peak intensity of the O-H stretch vibration to the peak intensity of the sp^3 C-H stretch vibration vs. GA/PVA wt. the ratio is conducted. As shown in Figure 2.14(b), the relative peak intensity of the O-H stretch vibration (-OH group) proportionally decreases with increasing GA/PVA wt. ratio. As the reaction formula is shown in Figure 2.12, twice the molar number of -OH is consumed during the crosslinking reaction between GA and PVA. Therefore, it is another piece of evidence supporting the occurrence of the crosslinking reaction between GA and PVA to form a crosslinked PVA film.

2.4.1.3 DSC analysis

DSC plots of the pure PVA film (GA: PVA= 0:1) and the crosslinked PVA films with different molar ratios of GA/PVA are shown in Figure 2.15. For the pure PVA without crosslinking, the endothermic peak at 223.1℃ implies the melting temperature of the crystalline PVA. The area of the endothermic peak of the pure PVA, which implies the latent heat (per unit mass), is large (53.77 $J{\bullet}g^{-1}$) compared with those of the crosslinked PVA, as shown in Table 2.7. Hence, the crystallinity is high in pure PVA film. Moreover, with the increasing molar ratio of GA/PVA, the melting temperature of the endothermic peak decreases, and the peak area/latent heat also decreases. It reveals that the crystallinity of the crosslinked PVA film decreases with the increase of the crosslinking density, but small crystals can still be formed in local areas of the long PVA chains in the crosslinked PVA film. In these cases, the crosslinked PVA film is still very flexible and has good adhesion to the substrate. As has been described in Section 2.4.1.1, when the molar ratio of GA/PVA increases, more hydroxy groups are consumed to form the crosslinking points between the adjacent PVA chains and there should be fewer water-molecule bonding sites in the PVA, resulting in a fast decrease of the water weight gain of the crosslinked PVA film with increasing the molar ratio of GA/PVA. However, the water weight gain only decreases very slightly with increasing the molar ratio of GA/PVA. This phenomenon can be explained by analyzing the DSC plots. That is, the crystallinity of the crosslinked PVA decreases with increasing the molar ratio of GA/PVA, releasing substantial numbers of the PVA chains in an amorphous state instead of the crystals. These released PVA chains in the amorphous state contain the hydroxy groups, contributing to the absorption of the water molecules. Therefore, the consumption of the hydroxy groups by the crosslinking reaction and the release of the amorphous PVA chains with the hydroxy groups somehow cancel out mostly with each other, resulting in a very slight decrease of the humidity sensitivity (implied by the weight gain of the crosslinked PVA film) with increasing molar ratio of GA/PVA in a wide range which is clearly shown in Figure 2.15. Eventually, the endothermic peak of the crosslinked PVA vanishes in the molar ratio of 208:1, which reveals that the crosslinking density is so high that even small crystals could not be formed in local areas of the long PVA chains. However, as has been illustrated in Figure 2.15, by observation, the crosslinked PVA film with this high crosslinking density coated on the substrate is highly crumpled.

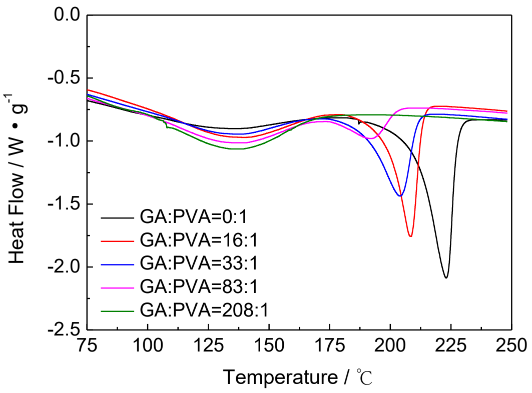

Figure 2.15 DSC plots of the pure PVA film (GA: PVA = 0:1) and the crosslinked PVA films with different molar ratios of GA/PVA.

Table 2.7 Melting temperature (T_m), melting temperature change (ΔT_m), and latent heat (ΔH) of the crosslinked PVA films with different weight/molar ratios of GA: PVA obtained from the analysis of their exothermic peaks (0:1 implies pure PVA).

Weight ratio of GA and PVA	0:1	1:100	1:50	1:20	1:8
Molar ratio of GA and PVA	0:1	16:1	33:1	83:1	208:1
T_m / °C	223.1	208.7	204.2	192.6	/
ΔT_m / °C	/	14.4	18.9	30.5	/
ΔH / $J \cdot g^{-1}$	53.77	40.01	32.59	11.07	/

2.4.2 SEM surface morphology of the crosslinked PVA layer coated on the MSP

SEM surface morphology of the crosslinked PVA layer coated on the MSP sensor platform is shown in Figure 2.16. In magnification of ×600, its surface is smooth without observable defects, such as crumpled surfaces or micro-holes. It seems that the crosslinking density might have a little fluctuation in the PVA film as observed in the SEM image. The reason might be that the crosslinking reaction occurs successively in each local area to form the crosslinked PVA film.

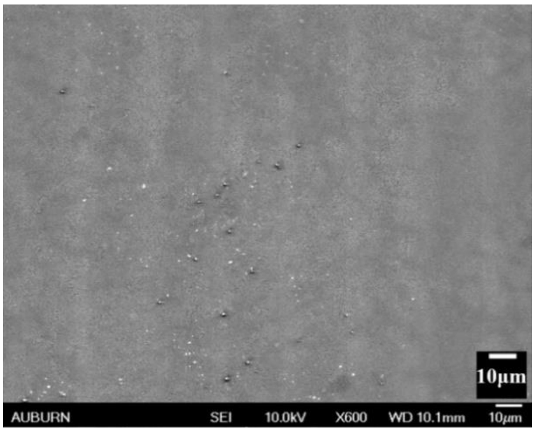

Figure 2.16 SEM surface morphology of the crosslinked PVA film coated on the MSP sensor platform.

2.4.3 Responses of the crosslinked PVA-MSP and the PVA-MSP humidity sensors at different humidity levels

The humidity responses of the sensors with the crosslinked PVA layers in thicknesses of 3 μm and 4 μm are shown in Figure 2.17. Figures 2.17(a), 2.17(c) show one humidity cycle between different high humidity levels and low humidity of 54% RH and the corresponding RF vs time plots in different humidity cycles under different high humidity levels, respectively.

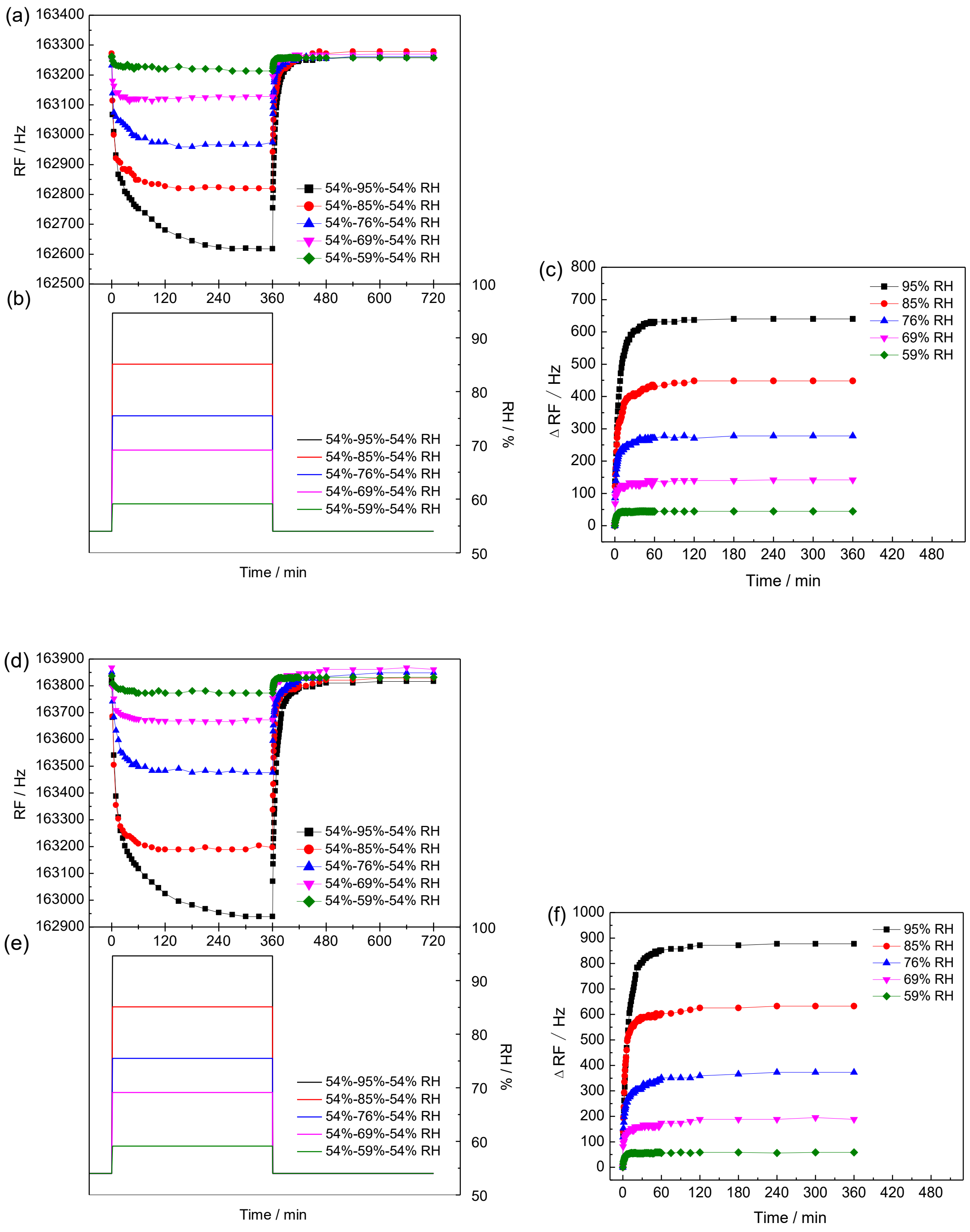

Figure 2.17 Resonant frequency responses of the sensors with 3 μm and 4 μm crosslinked PVA layers under different humidity levels, respectively. (a) Resonant frequency (RF) vs time plots; and (b) corresponding relative humidity (RH) vs time plots of the sensor with 3 μm crosslinked PVA layer in one humidity cycle; (c) delta resonant frequency (ΔRF) vs time

plots of the sensor with 3 μm crosslinked PVA layer when the humidity is decreased to 54% RH; (d) RH vs time plots; and (e) corresponding RH vs time plots of the sensor with 4 μm crosslinked PVA layer in one humidity cycle; (f) ΔRF vs time plots of the sensor with 4 μm crosslinked PVA layer when the humidity is decreased to 54% RH.

Similar to the responses of the CNF-PVA humidity sensor, for each test of a high RH, the RF of the crosslinked PVA-MSP sensor significantly decreases with increasing humidity and eventually reaches a saturated value and then, increases with decreasing humidity and reaches a saturated value at low frequency. It is found that the RF finally goes back to the initial RF at the beginning of the test for each humidity cycle. Besides, as has been illustrated in Section 2.1.4, to study the response time and calculate the ΔRF of the crosslinked PVA-MSP sensor, it is necessary to further analyze the response of the sensor in the humidity decreasing process. To analyze the performance of the humidity responses of the crosslinked PVA-MSP sensors with the crosslinked PVA layers in thicknesses of 3 μm and 4 μm, it is necessary to further analyze the RF data and calculate the ΔRF by Eq. (2-4) in the humidity decreasing process of the humidity cycle exhibited in Figures 2.17(b), 2.17(e). The ΔRF versus time plots of the sensors are shown in Figures 2.17(c), 2.17(f) respectively.

The data points of $\ln(1-\Delta RF/\Delta RF_{sat})$ vs time of the crosslinked PVA-MSP sensor when the humidity is decreased are shown in Figure 2.18(a). However, the data points are not following a linear relationship, and hence, cannot be fitted by Eq. (2-3). An alternative fitting method is used to fit just the linear portion of the data. After the determination of A, the fitting curve by Eq. (2-2) is plotted in Figure 2.18(c). However, when the humidity is decreased, the fitting curve of ΔRF somewhat deviates from those of the tested data points. Therefore, this classic model is not very suitable to fit the time-dependent humidity response of the crosslinked PVA-MSP sensor.

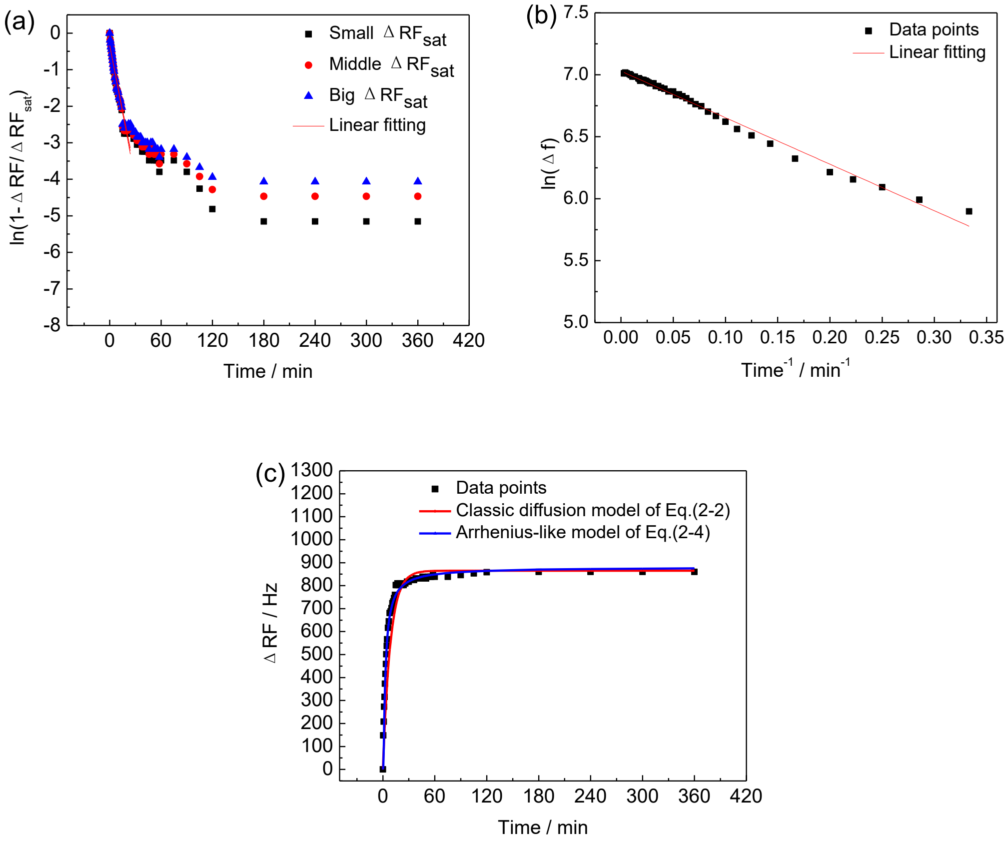

Figure 2.18 Schematics of the fittings of the data points of the crosslinked PVA-MSP sensor when humidity is decreased. (a) Ln(1-ΔRF/ΔRF$_{sat}$) vs time and linear fittings of the linear part (first 28 data points) by three different ΔRF$_{sat}$ values; (b) linear fitting of the data points of logarithm delta resonant frequency (lnΔRF) vs time^{-1} (min^{-1}); (c) different fitting methods to fit the data points of delta resonant frequency (ΔRF) vs time.

Arrhenius-like Eq. (2-4) and Eq. (2-5) are used to fit the data points of the ΔRF vs time and the logarithm ΔRF vs time^{-1} (min^{-1}), respectively, as shown in Figure 2.18. From Figure

2.18(b), the linear fitting result by Eq. (2-5) can be observed, which is acceptable. As shown in Figure 2.18(c), the fitting result by Eq. (2-4) can better describe the tested data points than that of the fitting result by Eq. (2-2), implying that the Arrhenius-like Eq. (2-4) is very suitable to be used to describe the time-dependent humidity response of the newly developed crosslinked PVA-MSP sensor.

The average values of the ΔRF_{sat} for five-cycle tests of the sensor with a 4 μm crosslinked PVA layer is 58.6, 187.9, 372.6, 632.5, 887.3 Hz, when humidity decreases from 59%, 69%, 76%, 85%, 95% RH, to 54% RH, respectively. The average values of the ΔRF_{sat} for five-cycle tests of the sensor with a 3 μm crosslinked PVA layer is 43.4, 142.3, 278.1, 448.6, 639.9 Hz, when humidity decreases from 59%, 69%, 76%, 85%, 95% RH to 54% RH, respectively. It is found that the ΔRF_{sat} of the sensors with 3 μm and 4 μm crosslinked PVA layers are close to linearly dependent on RH, respectively, as shown in Figure 2.19. The coefficients of determination (R^2) of the linear fittings for the sensors with 3 μm and 4 μm crosslinked PVA layers are 0.993 and 0.991, respectively. The sensitivity of 17.0 Hz/%RH and 23.6 Hz/%RH of the sensor with 3 μm and 4 μm crosslinked PVA layers, respectively, are obtained from the slops of the linear fittings in Figure 2.19. It has also been tested and analyzed that the standard deviation for five tests is less than 20 Hz. Besides, the analysis of the response times of the sensors with different thicknesses of the crosslinked PVA layer will be studied in the next Section.

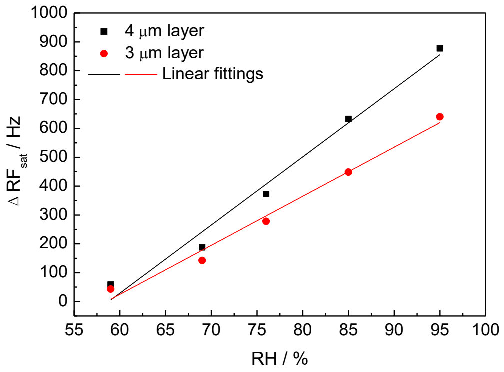

Figure 2.19 Calculated data points of saturated delta resonant frequency ($\Delta RF_{sat,\,i}$, i=1,2) of the sensor with 3 μm and 4 μm crosslinked PVA layers vs relative humidity (RH) and their linear fittings.

The humidity responses of the sensor with a 4.7 μm PVA layer without crosslinking (i.e., pure PVA layer) are shown in Figure 2.20. Figures 2.20(a), 2.20(b) show one humidity cycle between different high humidity levels and low humidity of 54% RH and the corresponding RF vs time plots in different humidity cycles under different high humidity levels, respectively. The RF of the PVA-MSP sensor significantly decreases with increasing humidity and eventually reaches a saturated value and then, increases with decreasing humidity and reaches a saturated value at low frequency. The RF finally goes back to the initial RF at the beginning of the test for each humidity cycle. Figure 2.20(c) shows the ΔRF vs time plots for the sensor with a 4.7 μm PVA layer, which are calculated by Eq. (2-4) from the data plots in Figure 2.20(a), when decreasing humidity from different high humidity levels to the low humidity of 54% RH. After linear fittings by Eq. (2-5) on the data points of the logarithm ΔRF vs time^{-1} (min^{-1}), the average values of the ΔRF_{sat} are calculated to be 86.0, 265.2, 465.7, 758.9, 1044.1 Hz, when humidity decreases from 59%, 69%, 76%, 85%, 95%

RH, to 54% RH, respectively. It is observed that the ΔRF_{sat} of the sensor with a 4.7 μm PVA layer is close to linearly dependent on RH, as shown in Figure 2.20(d). The coefficient of determination (R^2) of the linear fitting for the sensor is 0.992. The sensitivity of 27.4 Hz/%RH of the PVA-MSP sensor with a 4.7 μm PVA layer is obtained from the fitting plot. It has also been tested and analyzed that the standard deviation for five tests is less than 20 Hz. Besides, the analysis of the response times of the sensors with different thicknesses of the (pure) PVA layer will be studied in the next Section.

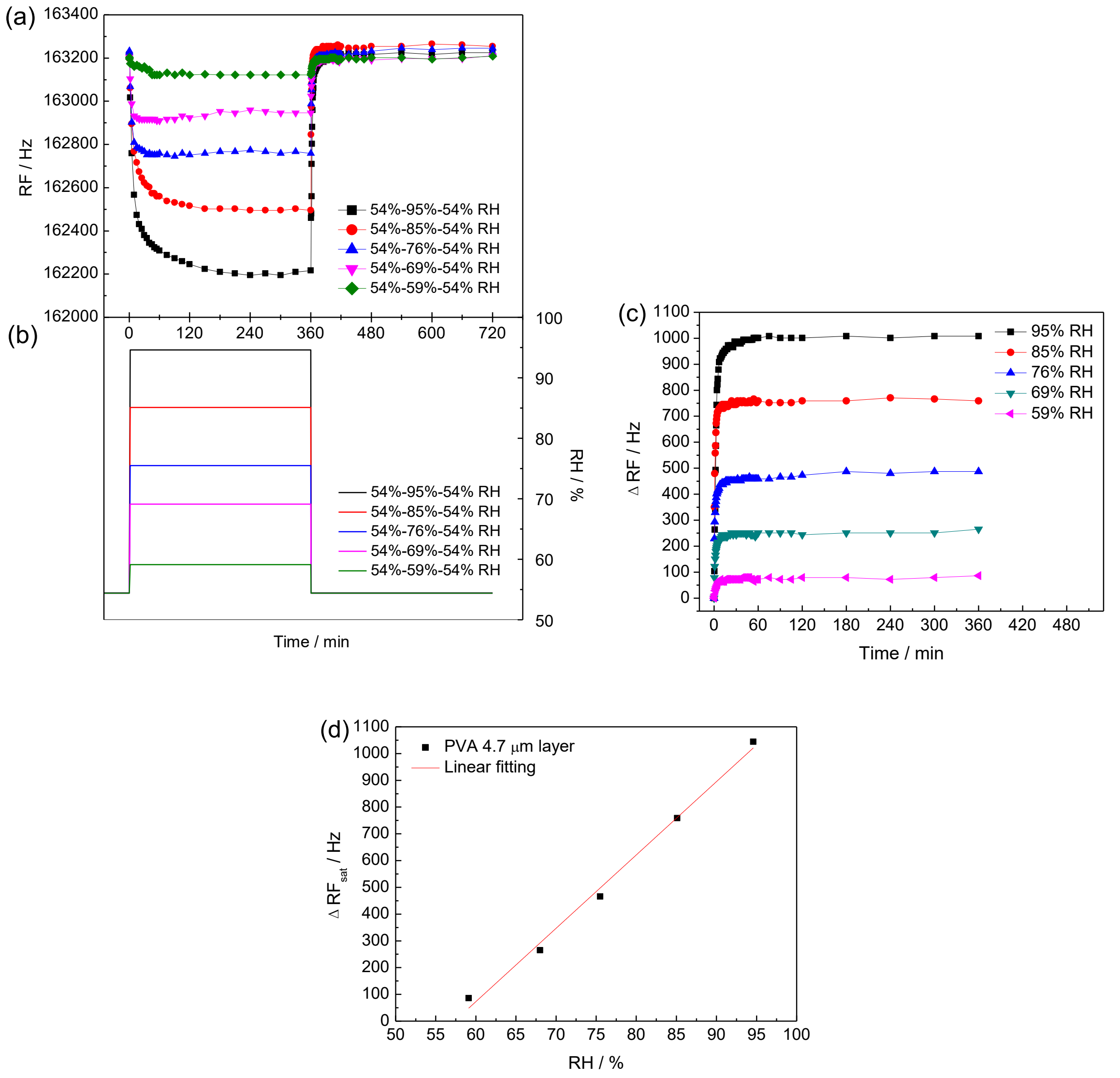

Figure 2.20 Resonant frequency responses of the sensor with a 4.7 μm PVA layer without

crosslinking under different humidity levels. (a) Resonant frequency (RF) vs time plots; and (b) corresponding relative humidity (RH) vs time plots in one humidity cycle; (c) delta resonant frequency (ΔRF) vs time plots when humidity is decreased; (d) Saturated delta resonant frequency (ΔRF_{sat}) vs relative humidity (RH).

2.4.4 Sensor responses at different thicknesses of the crosslinked PVA and pure PVA layers

The RF responses of the sensors with different thicknesses (2.2~10 μm) of the crosslinked PVA layer are also investigated, as shown in Figure 2.21. Figure 2.21(a) shows the RF vs time plots in one humidity cycle for different thicknesses of the PVA layer. In this study, the RFs of the sensors at 54% RH are in the range of 160 kHz to 164 kHz, as shown in Table 2.8. All the sensors exhibit consistent responses that the RFs decrease with increasing RH and increase with decreasing RH. The ΔRF vs time plots of the sensors with different thicknesses of the PVA layer when RH is decreased from 85% to 54% are calculated by Eq. (2-4) from the data plots of Figure 2.21(a) and shown in Figure 2.21(b). With decreasing RH, the ΔRF rapidly changes and finally reaches a constant (i.e., saturated) value. Furthermore, the values of the ΔRF_{sat} and the fitting constant B in the linear fitting Eq. (2-5) for the sensors with different thicknesses of the crosslinked PVA layers are listed in Table 2.8, which implies that both the values of ΔRF_{sat} and B roughly decrease with the decrease of the thickness of the crosslinked PVA layer, respectively.

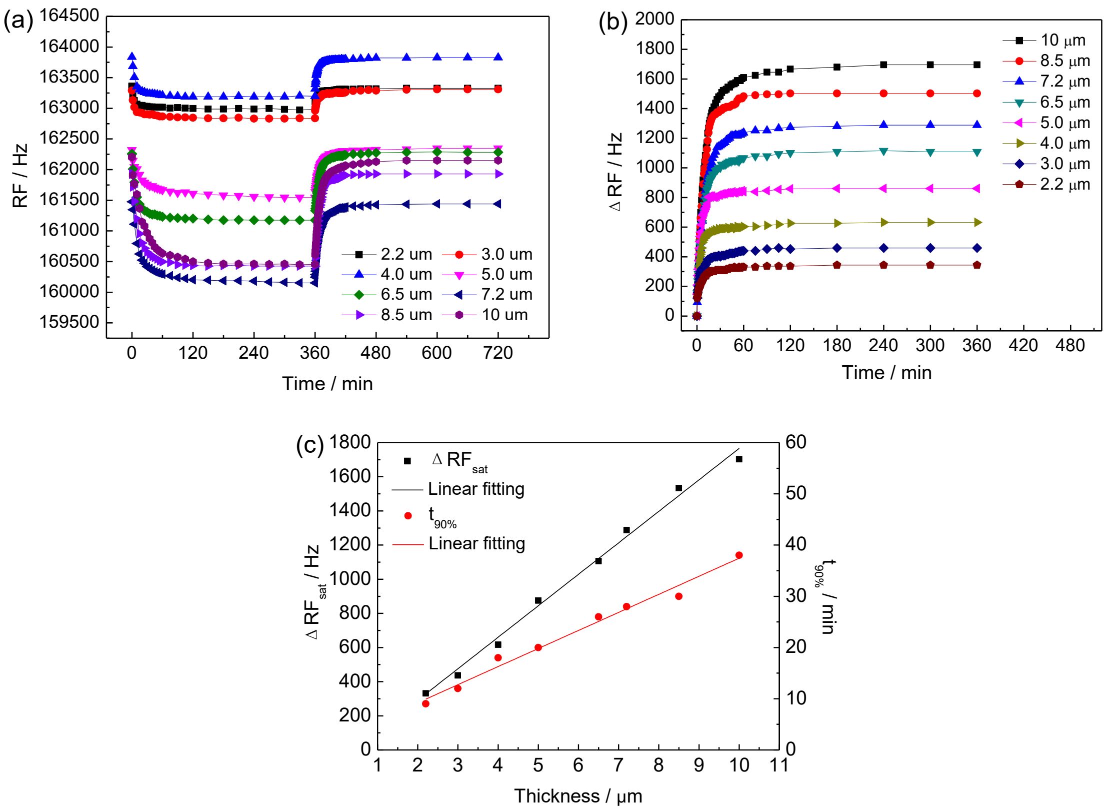

Figure 2.21 Resonant frequency responses of the sensors with different thicknesses (2.2~10 μm) of the crosslinked PVA layer tested in the same humidity range between 54% and 85% RH. (a) Resonant frequency (RF) vs time plots in one humidity cycle; (b) delta resonant frequency (ΔRF) vs time plots when decreasing humidity; (c) saturated delta resonant frequency (ΔRF_{sat}) of the MSP sensor and the response time ($t_{90\%}$) vs the thickness of the crosslinked PVA layer, respectively.

It is found that the ΔRF_{sat} of the MSP sensor is linearly dependent on the thickness of the PVA layer, as shown in Figure 2.21(c). The coefficient of determination (R^2) of the linear fitting is 0.998. By the linear fitting, the ratio of the ΔRF_{sat} over the thickness is 183.74 Hz/μm for the tested humidity level, which is, besides the parameters of the MSP sensor platform, one of the influencing parameters to control the humidity sensitivity of the crosslinked PVA-MSP sensor.

Table 2.8 Base resonant frequencies (RF_0) of the crosslinked PVA-MSP sensors with different thicknesses of the crosslinked PVA layers at 54% RH and saturated delta resonant frequency (ΔRF_{sat}) when humidity decreases from 85% RH to 54% RH and linear fitting constant (B) fitted by Eq. (2-4).

Thickness of the crosslinked PVA	10.0	8.5	7.2	6.5	5.0	4.0	3.0	2.2
RF_0 / Hz	163354	163289	163836	162320	162253	161476	161924	162205
ΔRF_{sat} / Hz	1703	1534	1288	1106	875	616	436	331
B	4.07	3.87	4.34	3.53	2.19	1.64	1.80	1.88

The RF responses at different times of the sensors with different thicknesses of the polymer layer are also shown in Figure 2.21(c). It reveals that the response time of the sensors is more than a few minutes long and is linearly increased as the thickness of the PVA layer is increased. Since a three-dimensional network is formed by crosslinking of the PVA chains, the network structure hinders the diffusion of the water molecules and it takes time for the water molecules to penetrate through the PVA layer during the water absorption/desorption process. Therefore, the response time of the sensors is long and increases with the thickness of the PVA layer. It is preferable that the response time of the sensor can be shortened by reducing the thickness of the PVA layer. On the contrary, a large ΔRF_{sat}, which contributes to high sensitivity, is required by increasing the thickness of the PVA layer. For instance, to obtain a response time of about 12.9 min, a sensitivity of 15.5

Hz/%RH is obtained for the sensor with a 3 μm PVA layer. Moreover, to obtain a response time of about 9.8 min, a sensitivity of 9.5 Hz/%RH is obtained for the sensor with a 2 μm PVA layer. For agriculture applications, it is necessary to select a good match of the response time and humidity sensitivity. The response time should be no more than 10 min to achieve a fast-sensing response. Therefore, a preferable thickness range of the crosslinked PVA layer is probably from 2 um to 3 um.

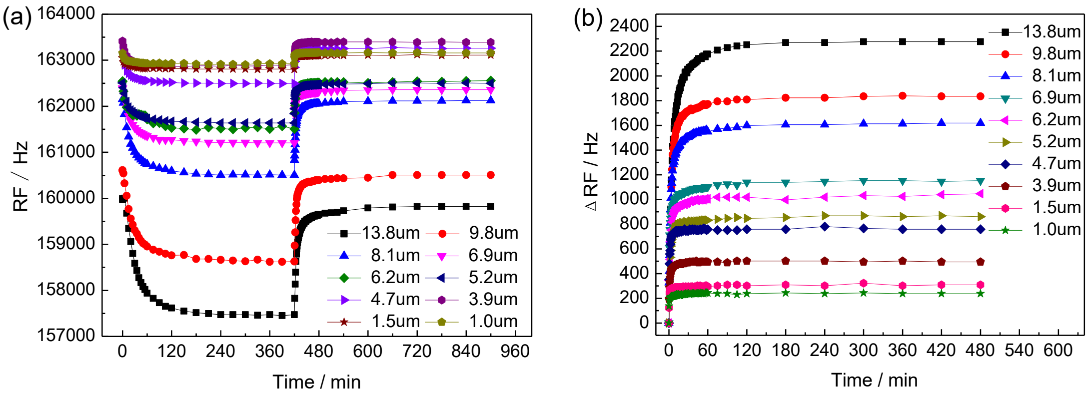

Figure 2.22 Resonant frequency responses of the sensors with different thicknesses from 1 μm to13.8 μm of the (pure) PVA layers. (a) Resonant frequency (RF) vs time plots in one cycle humidity test; and (b) delta resonant frequency (ΔRF) vs time plots when decreasing humidity.

The RF responses of the sensors with different thicknesses (1~13.8 μm) of the PVA layer without crosslinking are also analyzed, as shown in Figure 2.22. Figure 2.22(a) shows the RF vs time plots in one humidity cycle for different thicknesses of the PVA layer. In this study, the RFs of the sensors at 54% RH are in the range of 160 kHz to 164 kHz, as shown in Table 2.9. All the sensors exhibit consistent responses that the RFs decrease with increasing RH and increase with decreasing RH. The ΔRF vs time plots of the sensors with different thicknesses of the PVA layers, when RH is decreased from 85% to 54%, are calculated by Eq. (2-4) from the data plots of Figure 2.22(a) and shown in Figure 2.22(b). With decreasing RH, the RF rapidly changes and finally reaches a constant value.

Table 2.9 Base resonant frequencies (RF_0) of the (pure) PVA-MSP sensors with different thicknesses of the (pure) PVA layers at 54% RH and saturated delta resonant frequency (ΔRF_{sat}) when humidity decreases from 85% RH to 54% RH and linear fitting constant (B) fitted by Eq. (2-4).

Thickness of PVA	13.8	9.8	8.1	6.9	6.2	5.2	4.7	3.9	1.5	1.0
RF_0 / Hz	159965	160598	162153	162389	162546	162505	163196	163419	163046	163153
ΔRF_{sat} / Hz	2276	1834	1618	1152	1046	860	759	495	308	237
B	2.06	1.79	1.50	0.68	1.16	0.99	0.46	0.59	0.22	0.29

The values of ΔRF_{sat} and the fitting constant B in the linear fitting Eq. (2-5) for the sensors with different thicknesses of the PVA layers are fitted and listed in Table 2.9, which implies that both the values of ΔRF_{sat} and B roughly decrease with the decrease of the thickness of the PVA layer, respectively. It is observed that the ΔRF_{sat} of the sensor is linearly dependent on the thickness of the PVA layer, as shown in Figure 2.23(a) and Table 2.9. It is also found that the fitting slopes of the ΔRF with respect to the thickness of the polymer layer for both crosslinked and non-crosslinked PVA-MSP sensors are very close/identical, which means the sensitivities are close to the same value. It is a parameter to select the suitable thickness of the

CNF layer, which can determine the humidity sensitivity of the CNF-MSP sensor. Therefore, the PVA crosslinking cannot influence the sensitivity of the sensors. This is due to that the crosslinking density is too small to consume many of the hydroxy groups in the PVA backbones, which does not influence hydroxy groups in huge numbers to bond with water molecules. Moreover, by crosslinking, some amorphous PVA chains are released from the PVA crystal, as observed from the DSC results in Section 2.4.1.3, which contributes to the humidity sensitivity and partially cancels out the sensitivity decreasing mechanism from the consumption of some hydroxy groups in the PVA by crosslinking. In comparison, the sensitivity of the sensors with the CNF layer (i.e., 137.6 Hz/μm) is much lower than those of the sensors with the PVA layer and crosslinked PVA layer (i.e., 173.1 Hz/μm and 183.7 Hz/μm), respectively, which verifies the PVA has better humidity sensitivity than the CNF as a water sensitive element. However, as shown in Figure 2.23(b), the response times ($t_{90\%}$) of the sensors, which exhibit linear relationships with the thickness of the polymers (i.e., CNF, PVA, crosslink PVA) having the coefficient of determination (R^2) of the linear fittings of 0.944, 0.973, 0.982, respectively, show that the crosslinking of PVA prolongs the response time by a factor of about 2 compared with those of the sensors with non-crosslinked PVA layer. The reason is that the crosslinking reaction of GA and PVA increases the density of the PVA film, resulting in a delayed diffusion/penetration of water molecules through the PVA layer. However, the response time of the sensors with the crosslinked PVA layer is much shorter than those of the sensors with the CNF layer. In summary, the sensors with the crosslinked PVA layer have better humidity sensitivity/sensing performance than those CNF-based sensors in both the humidity response and response time.

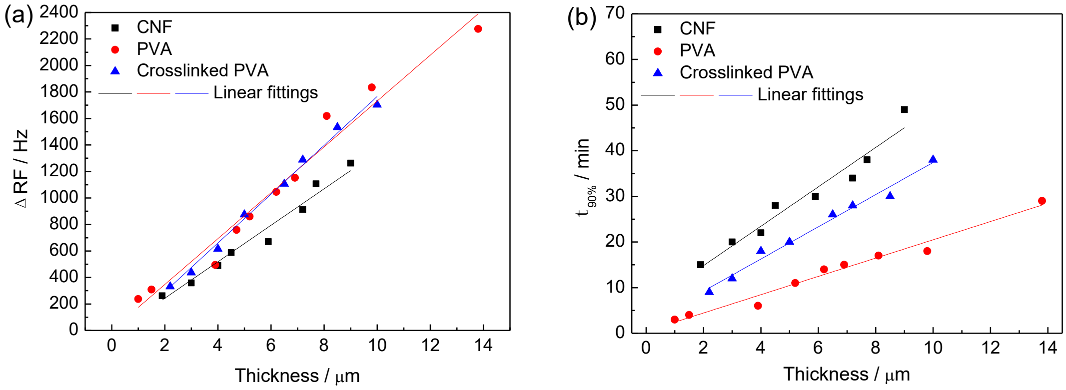

Figure 2.23 Comparisons of the sensors with different polymer layers (CNF/pure PVA/crosslinked PVA layers) in different thicknesses. (a) Relation between the saturated delta resonant frequency (ΔRF_{sat}) of the sensors (with CNF/PVA/crosslinked PVA layer) and the thickness of the polymer layers, respectively; (b) Relation between the response time ($t_{90\%-i}$, i=1,2,3) of the sensors (with CNF/PVA/crosslinked PVA layer) and the thickness of the polymer layers, respectively.

2.4.5 Long-time stability of the crosslinked PVA-MSP humidity sensor

The long-time stability of the sensor has been tested for a period of 20 days under the same humidity cycle of 54%-85%-54% every day. The monitored humidity response of the PVA-MSP sensors with a 4 μm crosslinked PVA layer is shown in Figure 2.24. Resonant frequency (RF) of the sensor in 20 diurnal cycle humidity tests between 54% and 85% RH are depicted in Figure 2.24(a). Moreover, the ΔRF of the sensor when RH increases and decreases in 20 diurnal humidity cycles are calculated by Eq. (2-4). As a result, the stability of the sensor in 20 cycles when RH is increased and decreased is shown in Figure 2.24(b). The ΔRF_{sat} tested for 20 days is almost identical with very little random fluctuation. Furthermore, it is found that the fluctuation of the ΔRF_{sat} in either increasing or decreasing humidity is less than ±30

Hz, which reveals that such a sensor is possible to detect humidity with an accuracy of no more than ±2% RH. The reason for the fluctuation of the tested results might be related to stresses that are generated between the PVA layer and the MSP sensor. It seems that those stresses are reversible in each cycle and not accumulated over time. In summary, the good stability of the crosslinked PVA-MSP sensor in the 20-day test has been verified.

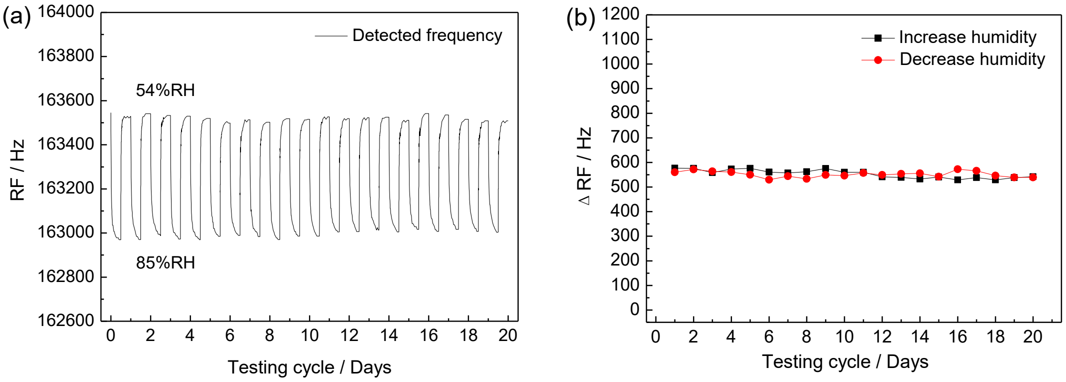

Figure 2.24 Long-time stability of the PVA-MSP sensor with 4 μm crosslinked PVA layer in a 20-day test under the same humidity cycle of 54%-85%-54% RH every day. (a) The resonant frequency (RF) of the sensor for 20-cycle humidity tests in 20 days; (b) comparison of the saturated delta resonant frequency (ΔRF_{sat}) of the sensor tested in 20 days for both increasing and decreasing humidity.

The long-time stability of the sensor has been tested for a period of 12 days under the same humidity cycle of 54%-85%-54% every day. The humidity response testing results of the sensor with a 4.4 μm non-crosslinked PVA layer are shown in Figure 2.25. RF of the sensor in 12 diurnal cycle humidity tests between 54% and 85% RH are depicted in Figure 2.25(a). Moreover, the ΔRF of the sensor when RH increases and decreases in 12 diurnal cycles is calculated by Eq. (2-4). As a result, the stability of the sensor in 12 cycles when RH is increased and decreased is shown in Figure 2.25(b). The ΔRF_{sat} is almost identical with a little random fluctuation. Furthermore, it is found that the fluctuation of the ΔRF_{sat} in either increasing or decreasing humidity is less than ±55 Hz, which reveals that such a sensor is possible to detect humidity with an accuracy of no more than ±3.5% RH. The main reason for the fluctuation of the tested results might be related to the partial dissolution of the non-crosslinked PVA chains in PVA film while absorbing water molecules at high humidity. Moreover, stresses that are generated between the PVA layer and the MSP sensor platform during the humidity test might be another reason. It seems that these two possible influencing reasons are reversible among cycles and not accumulated over time. In comparison, as shown in Figures 2.24(b), 2.25(b), the humidity sensing stability of the sensor with the crosslinked PVA layer is better than that of the sensor with the pure PVA layer. Among all the three MSP sensors (i.e., CNF/PVA/crosslinked PVA-MSP sensor), the crosslinked PVA-MSP sensor has the best long-term stability.

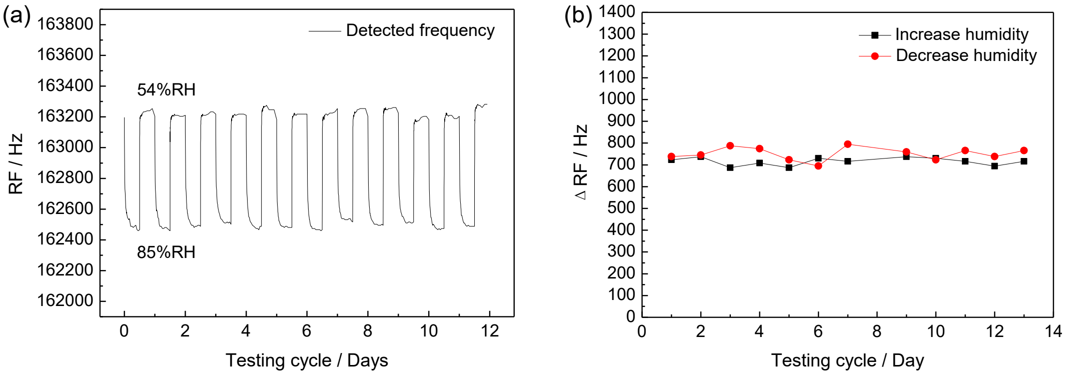

Figure 2.25 Long-time stability of the PVA-MSP sensor with 4.4 μm non-crosslinked PVA layer in a 12-day test under the same humidity cycle of 54%-85%-54% RH every day. (a) The resonant frequency (RF) of the sensor for 12-cycle humidity tests in 12 days; (b) comparison of the saturated delta resonant frequency (ΔRF_{sat}) of the sensor for both increasing and

decreasing humidity.

2.4.6 Water resistance of the crosslinked PVA-MSP humidity sensor

Water-resistant capability is important for humidity sensors. If the water immersion of the sensor causes dissolution or damage to the PVA layer, a false signal and unexpected RF change can be introduced. The water-resistant capability experiments on the crosslinked PVA-MSP sensor with a 5 μm crosslinked PVA layer is conducted, as shown in Figure 2.26. It is found that the RF response of the sensor after being immersed in water for six hours is consistent with that of the original sensor without water immersion. This good stability can be attributed to the network structure of the PVA film and its considerable flexibility and tight adhesion to the sensor platform. Therefore, based on the water resistance of the crosslinked PVA, it shows that the crosslinked PVA-MSP sensor can work in an environment that might experience direct water immersion and still provide reliable humidity measurement results.

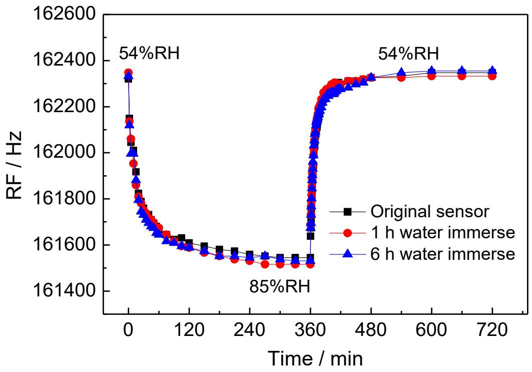

Figure 2.26 Resonant frequency (RF) vs time plots of one humidity cycle (54%-85%-54% RH) for the (original) crosslinked PVA sensor and the sensor immersed in water for 1 h and 6 h, respectively.

2.4.7 Temperature dependence of the crosslinked PVA-MSP humidity sensor

The humidity sensing characteristics of different kinds of humidity sensors can be affected by temperature [106]. Therefore, a temperature influence on the RF response of the newly developed humidity sensor should be considered, and a temperature coefficient should be measured and determined for compensation of the humidity sensing.

Both the characteristics of the crosslinked PVA layer and the MSP sensor can be influenced by temperature. On one hand, the water-bonding ability of hydroxy groups of the water-sensitive PVA can be influenced by the temperature. The RF of the MSP sensor is also affected by temperature according to thermodynamics.

In agriculture applications, a typical temperature fluctuation range in the soil is about from 5 ℃ to 40 ℃. Therefore, the crosslinked PVA-MSP sensor was tested at different temperatures from 5 ℃ to 40 ℃ to characterize the temperature influence on the RF and the sensitivity. The temperature testing range has been determined based on the data on the fluctuation of the soil temperature [107,108].

Table 2.10 Standard relative humidity (RH) generated by two saturated salt solutions at various temperatures.

Saturated salt solution	Temperature / ℃	RH / %	ΔRH between two humidity levels / %
$Mg(NO_3)_2$	10	57.4	/
	20	54.4	
	30	51.4	
	40	48.4	
KCl	10	86.8	29.4
	20	85.1	30.7
	30	83.6	32.2
	40	82.3	33.9

As shown in Table 2.10, due to the different humidity generated at different temperatures in the humidity boxes, the tested results of the crosslinked PVA-MSP sensor undergo a humidity correction to get the same humidity levels to calculate the temperature coefficient. That is, to correct the RF of the sensors at various temperatures to the same (low and high) humidity levels generated in the humidity boxes at 20℃, as illustrated in Table 2.11.

Table 2.11 RH corrected resonant frequency (RF) and the corresponding saturated delta resonant frequency (ΔRF_{sat}) of the crosslinked PVA-MSP humidity sensor at various temperatures.

Temperature / ℃	ΔRH / %	ΔRF per 1% RH	Modified RF at low RH of 54.4% / Hz	Modified RF at high RH of 85.1% / Hz	ΔRF_{sat} obtained from the fittings / Hz
10	29.4	15.11	163311	162879	463.77
20	30.7	14.80	163290	162838	454.41
30	32.2	14.03	163272	162786	430.59
40	33.9	13.18	163243	162743	404.62

After the humidity correction, Figure 2.27(a) shows the temperature dependence of the crosslinked PVA-MSP sensor with a 3 μm PVA layer on the RF tested at two humidity levels of 54% RH (low RH) and 85% RH (high RH), respectively. A bare MSP sensor is also tested at different temperatures for comparison. As a lack of water absorption element, PVA, of the bare MSP sensor, the same RF is shown at any humidity levels at each tested temperature. It is found that its RF decreases with increasing temperature with a temperature coefficient of 8.08 Hz/℃. In comparison, the crosslinked PVA-MSP sensor with a 3 μm PVA layer has a lower RF than that of the bare MSP sensor at each tested temperature, due to the PVA mass loading on the sensor. It is shown that the RF of the crosslinked PVA-MSP sensor also decreases with increasing temperature at two tested humidity levels, respectively. However, the temperature coefficients (shown by the fitting slopes) of the sensor, which are 2.21 Hz/°C, and 4.58 Hz/°C, at two tested humidity levels, 54% RH, and 85% RH, respectively, are both smaller than that of the (bare) MSP sensor. By further analysis, as shown in Figure 2.27(b), the ΔRF_{sat} of the crosslinked PVA-MSP sensor tested between two humidity levels of 54% and 85% RH has a little temperature dependence with a temperature coefficient of about 2.01 Hz/°C. The reason is probably that the water bonding ability of hydroxy groups of the crosslinked PVA is also influenced by temperature, and interestingly, the temperature influence on the temperature coefficient of the crosslinked PVA counteracts that of the temperature influence of the MSP sensor. With these two counteracting effects, the temperature coefficient of the crosslinked PVA-MSP sensor has a relatively small temperature coefficient.

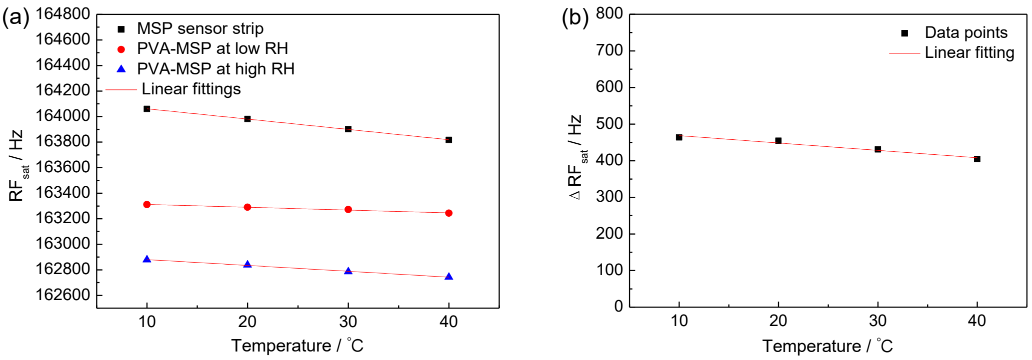

Figure 2.27 Fitting plots of the data after the humidity correction for various temperatures (i.e., correct the humidity to that generated at 20°C) to determine the temperature coefficients. (a) The temperature (T) dependence of the crosslinked PVA-MSP sensor with a 3 μm PVA layer on the saturated resonant frequency (RF_{sat}) tested at two humidity levels of 54% RH (low RH) and 85% RH (high RH), respectively. A bare MSP sensor is also tested at different

temperatures for a comparison; (b) temperature (T) dependence of the crosslinked PVA-MSP sensor on the saturated delta resonant frequency (ΔRF_{sat}) tested between humidity levels of 54% and 85% RH.

2.4.8 Comparison of sensitivity between theoretical calculation and experimental results

For humidity detection, the sensitivity (S_H) of the crosslinked PVA-MSP humidity sensor is defined as the ΔRF_{sat} of the sensor for each percentage (1%) of RH change. Based on Eq. (1-3) in Chapter 1.3.1, based on the size of the MSP sensor and water mass absorbed by the PVA layer loaded on the sensor platform, a sensitivity prediction of the crosslinked PVA-MSP sensor can be derived in Eq. (2-6):

$$S_H = S_m \cdot \Delta m_H = S_m \cdot m_{PVA} \cdot |\delta| = S_m \cdot L \cdot w \cdot h_{PVA} \cdot \rho_{PVA} \cdot |\delta| = -\frac{h_{PVA} \cdot \rho_{PVA} \cdot |\delta|}{4Lp} \sqrt{\frac{E}{\rho^3(1-\upsilon^2)}} \quad (m << M) \quad (2\text{-}6)$$

where, M is the mass of the (original) MSP sensor; L, w, and p are the length, width, and thickness of the sensor, respectively. Δm_H is the water mass absorbed/desorbed by the PVA layer when RH varies by 1%; m_{PVA} is the dry mass of the PVA layer. L_{PVA} and w_{PVA} are the length and width of the PVA layer, respectively, which are equal to the length and width of the MSP sensor, respectively; h_{PVA} is the thickness of the dry PVA layer; ρ_0 is the density of the PVA; δ is the water absorption/desorption mass ratio of the PVA when RH varies by 1%.

Some relations can be calculated as follows:

$$\delta_{total} = \delta \cdot \Delta H \quad (2\text{-}7)$$

$$\Delta m_{total} = \Delta m_H \cdot \Delta H \quad (2\text{-}8)$$

$$\Delta RF_{total} = S_H \cdot \Delta H \quad (2\text{-}9)$$

where, δ_{total} is the total water absorption mass ratio of the PVA layer when humidity increases from 54% RH to 95% RH, which can be experimentally determined (as shown in Table 2.5); ΔH is the value of humidity difference, which is from 54% to 95% RH; Δm_{total} is the total water mass absorbed by the PVA layer when humidity increases from 54% RH to 95% RH; ΔRF_{total} is the saturated resonant frequency of the PVA-MSP humidity sensor when humidity increases from 54% RH to 95% RH.

Table 2.12 The parameters of the MSP sensor.

Material	L / m	W / m	p / m	E / Pa	ρ / kg/m^3	υ	M / g	RF$_0$ / Hz
2826MB	1.35×10^{-2}	4.5×10^{-3}	3×10^{-5}	1.1×10^{11}	7.9×10^{3}	0.5	14.4×10^{-3}	160×10^{3}

The material (2826MB) parameters and the dimensions of the MSP sensors are listed in Table 2.12. The humidity sensitivity (S_H) of the PVA-MSP humidity sensors with different thicknesses of the PVA layers is calculated and listed in Table 2.13. First, the mass sensitivity can be calculated (5.54 Hz/μg) from some parameters of PVA in Eq. (2-6). Second, the ΔRF_{total} of the sensor with different thicknesses of the PVA layer when humidity increases from 54% RH to 95% RH (41% RH difference) can also be calculated, which is shown in Table 2.13 and Figure 2.28. The calculated ΔRF_{total} ranges from 119 Hz for the sensor with a 1 μm PVA layer to 2382 Hz for the sensor with a 20 μm PVA layer, which is listed in Table 2.13.

Table 2.13 Calculated sensitivity (S_H) of the PVA-MSP humidity sensor with different thicknesses of the PVA layers. For the PVA layers, L=13.5 mm, w=4.5mm. For humidity tests, ΔH=41, which is obtained from 54% RH to 95% RH (41% RH difference). The density of PVA, ρ_{PVA}, is 1250 kg/m^3. δ_{total} value of 28.3% (at 95% RH) can be obtained from Table 2.5. The mass sensitivity in Eq. (2-6) can be calculated (5.54 Hz/μg).

h_{PVA} / μm	m_{PVA} / μg	Δm_{total} / μg	Δm_H / μg/1%RH	S_H / Hz/1%RH	ΔRF_{total} / Hz	ΔRF_H / Hz/1%RH
1	76	21.5	0.53	2.93	119	2.9
2	152	43.0	1.06	5.87	238	5.9
3	228	64.5	1.59	8.8	357	8.8
4	304	86.0	2.12	11.74	476	11.7
5	380	107.5	2.65	14.67	595	14.7
6	456	128.9	3.17	17.6	715	17.6
7	532	150.4	3.70	20.53	834	20.5
8	608	171.9	4.23	23.46	953	23.5
9	683	193.4	4.76	26.4	1072	26.4
10	759	214.9	5.29	29.33	1191	29.3
11	835	236.4	5.82	32.27	1310	32.3
12	911	257.9	6.35	35.2	1429	35.2
13	987	279.4	6.88	38.14	1548	38.1
14	1063	300.9	7.41	41.07	1667	41.1
15	1139	322.4	7.94	44.01	1786	44.0
16	1215	343.8	8.46	46.93	1906	46.9
17	1291	365.3	9.00	49.86	2025	49.9
18	1367	386.8	9.53	52.8	2144	52.8
19	1443	408.3	10.06	55.73	2263	55.7

20	1519	429.8	10.59	58.67	2382	58.7

Figure 2.28 shows the comparison of the ΔRF_{sat} between the humidity testing results of the sensors with different thicknesses of the PVA layers at the humidity of 85% and 95% RH, respectively, and the calculation results at the humidity of 95% RH. It can be found that the ΔRF_{sat} and humidity sensitivity (implied by the slopes in the figure) from experiment testing results at 95% RH (in blue fitting) are much higher than those from calculated results (in green fitting). The reason for the large deviation of the humidity sensitivity is possibly due to that, at different humidity levels, the stress and strain on the MSP sensor are induced by Young's modulus change of the PVA layer/film coated on the sensor. With increasing humidity from 54% RH to 95% RH, the stress and strain gradually increase due to a decrease of Young's modulus and a stretch of the PVA layer relative to the rigid MSP sensor with a large Young's modulus. This Young's modulus difference probably contributes to the decrease of the RF of the sensor. As evidence, a slight bending curve of the MSP sensor can be observed while increasing humidity from 54% RH to 95% RH, which supports the assumption that the stress and strain occur between the PVA layer and the MSP sensor while humidity changes.

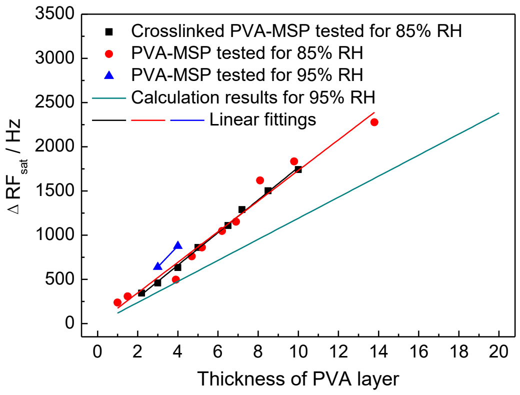

Figure 2.28 Comparison of the saturated delta resonant frequencies (ΔRF_{sat}) between the humidity testing results of the sensors with different thicknesses of the PVA layer at the humidity of 85% and 95% RH, respectively, and the calculated results at 95% RH.

2.5 Conclusions

1. A novel low-cost, in-situ, wireless sensor platform - MSP sensor with a dimension of 13.5 mm × 4.5 mm × 30 μm coated by a thin layer of water-sensitive polymers, CNF, and crosslinked PVA, respectively, was developed.
2. Crosslinked PVA-MSP humidity sensors were developed, which had both water-resistant capability and high humidity sensing sensitivity. A fundamental study was carried out to optimize the GA/PVA ratio to obtain the crosslinked PVA film with the best match of water-resistant capability and water absorption ability. The optimized molar ratio of GA: PVA is in the range of 16:1 to 83:1.
3. The sensors with crosslinked PVA layers in different thicknesses were tested under humidity ranging from 54% to 100%. It was found that the sensor signal, i.e., the resonant frequency of the sensor, is linearly dependent on RH. Moreover, the change in the resonant frequency of the sensor is also linearly dependent on the thickness of the PVA layer.
4. The sensitivity of the sensors with the crosslinked PVA layer was almost the same as those of the sensors with the non-crosslinked PVA layer, but much higher than those of the sensors with the CNF layer. The response time of the sensors with the crosslinked PVA layer was longer than those of the sensor with the non-crosslinked PVA layer but shorter than those of the sensors with the CNF layer.

5. The long-time stability of the sensor with the crosslinked PVA layer was improved compared with those of the sensors with the non-crosslinked PVA layer and with the CNF layer.

6. Good stability was obtained during a 20-day test. The humidity response of the sensor after water immersion was consistent with that of the original sensor without water immersion, indicating that the sensor can work in an environment that was directly exposed to water.

Chapter 3 Wireless Humidity Sensor Based on High Dielectric Permittivity Ceramics

In this chapter, another wireless sensor, a type of passive sensor based on an inductance-capacitance (LC) resonator is introduced by using high permittivity ceramics which is designed for precision agriculture, i.e., in-situ monitoring soil water.

Like the polymer-MSP wireless humidity sensors developed in Chapter 2, the LC resonant sensor can also be used as a wirelessly and passively detected humidity sensor with a compact/small size. Therefore, the passive LC resonant sensor has a promising potential to be massively used/distributed on the farmlands in soil, where the humidity in different positions in the farmlands can be wirelessly detected by a handheld device.

The key sensing module in the wireless LC resonator platform is the capacitor. The dielectric material used in the capacitor and the electrodes-configuration of the capacitor play important roles in the humidity sensing performance of the wireless LC resonant sensor. Therefore, in this chapter, the study focuses on the humidity sensing performance (at different frequencies) of the main sensing module, i.e., a newly found high permittivity core-shell BTO-SiO_2 ceramics humidity capacitor/sensor (coated) with flat surface electrodes. Long-time stability of the ceramics sensor has been conducted. The probable soil influence on the humidity sensing of the ceramics sensor at different frequencies has been theoretically analyzed and experimentally verified.

3.1 Sensing principles

3.1.1 Principle of wireless LC resonant humidity sensor

The principle of the interrogating system of an LC wireless resonant sensor is shown in Figure 3.1. An LC wireless resonant sensor is typically made of a spiral inductor connected to a (sensing) capacitor, forming a resonant LC tank [61]. The capacitance of the capacitor changes in response to the detecting substance of interest, such as the humidity. The capacitance variation of the capacitor results in a change in the resonant frequency of the LC resonant sensor. To wirelessly interrogate the LC resonant sensor, readout coils are magnetically coupled with the LC resonant sensor. The resonant frequency (RF) of the sensor can be obtained at the peak point of the phase spectrum which can be picked up by the readout coils. The relation between the RF of the LC wireless resonant sensor and the capacitance of the capacitor/sensor is given in Eq. (3-1) [62].

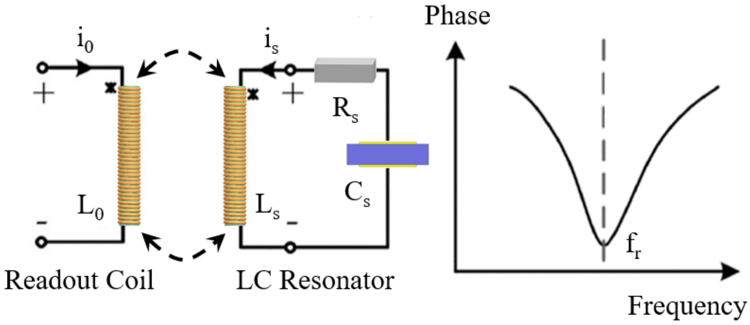

Figure 3.1 Principle of the wirelessly interrogating system of an LC resonator/resonant sensor containing a wireless passive LC resonant sensor and readout coils. The peak frequency of the phase, which determines the detected resonant frequency (f_0), which varies with the change of the capacitance (C_s) of the capacitor sensor. In the figure, L_0, i_0, L_s, and i_s, are the inductance and the current of the readout coils, and the inductance and the current of the LC resonant sensor, respectively; f_r is the resonant frequency of the LC resonant sensor.

$$f_s = \frac{1}{2\pi\sqrt{L_s C_s}} \qquad (3\text{-}1)$$

where f_s is the resonant frequency (RF) of the LC resonant sensor system. L_s, C_s, and R_s are the inductance, capacitance, and resistance of the LC resonant sensor, respectively.

The quality factor, Q, is a parameter that describes the resonance behavior of an underdamped harmonic resonator. In the figure, it implies the sharpness of the phase peak. A high Q is preferred to have a more accurate reading and sense. Eq. (3-2) is given as follows [62]:

$$Q = \frac{1}{R_S}\sqrt{\frac{L_S}{C_S}} \qquad (3\text{-}2)$$

3.1.2 Dielectric humidity sensor with parallel plate electrodes

For the wireless LC resonant sensor designed, the capacitor (C_s shown in Figure 3.1) is the essential component/sensing module to detect the substance of interest, such as the humidity. The dielectric properties (such as dielectric permittivity) of the dielectric material (i.e., measured as the capacitor, C_s) change with the humidity change due to the absorption and desorption of the water molecules of the dielectric (sensing) material from the humid environment.

For a capacitor with parallel plate electrodes, as shown in Figure 3.2, the electric field line is uniformly and parallelly distributed through the dielectric sensing material. The dielectric permittivity of the dielectric sensing material has a direct relationship with the capacitance of the capacitor. The parallel plate electrodes model is expressed in Eq. (3-3).

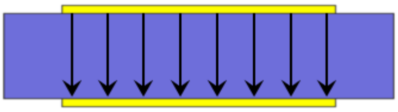

Figure 3.2 A capacitor with parallel plate electrodes and the electric field.

$$C = \varepsilon_0\varepsilon_r \cdot \frac{S}{d} \qquad (3\text{-}3)$$

where S is the area of the parallel plate electrode of the capacitor; d is the vertical distance of the parallel plate electrodes.

From Eq. (3-3), the dielectric permittivity of the dielectric material is directly related to the capacitance of the sensor/capacitor. Hence, the permittivity of the dielectric material significantly influences the humidity sensing of the capacitor. A fundamental study needs to be done to select a candidate dielectric material and a configuration of the capacitor with a preferable overall humidity sensing performance.

The requirements of the dielectric material are as follows: (1) the humidity sensing response should be high; (2) the response time should be fast; (3) the capacitor should not be influenced by the surrounding substances, especially, the soil, other than the sensing of the interest, i.e., the humidity; (4) the dielectric loss should be relatively low to decrease the detecting signal loss at a frequency range for use; (5) the dielectric material used for the capacitor should have some features for agriculture applications, such as long-time stability, and water-resistant capability.

For a capacitor with parallel plate electrodes for the sensing of the humidity, the major drawback is that the response time is very long due to that the humid air needs a long-time to penetrate through the entire thickness of the dielectric material between the parallel plate electrodes. Therefore, the capacitor with parallel plate electrodes is not suitable for the sensor used in agriculture applications where a fast/instant sensing response is required.

3.1.3 Dielectric humidity sensor with flat surface electrodes and its effective permittivity equation

Due to that, the capacitor based on the dielectric material with parallel plate electrodes is not applicable to realize a fast response of humidity sensing in the application of agriculture, an alternative capacitor based on the dielectric material with flat surface electrodes is developed, as shown in Figure 3.3.

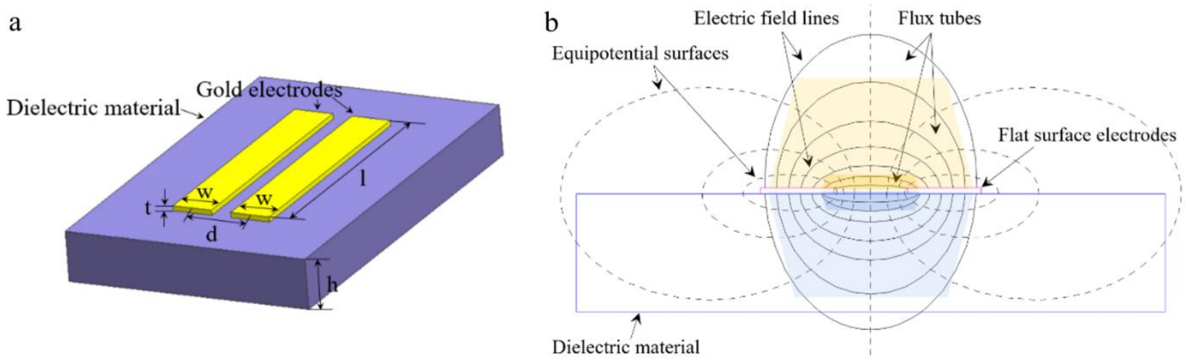

Figure 3.3 (a) Rectangular surface electrodes/conductors located apart at a distance, d, on the top of a dielectric material with a thickness, h, and relative dielectric permittivity, ε_r; and (b) its cross-section view and electric field lines generated from the electrodes/conductors, equipotential surfaces, and flux tubes implying that the same contribution of the capacitance for unit flux tube [109].

The configuration of the capacitor with flat surface electrodes is different from the one with parallel plate electrodes. The electromagnetic field connecting the two rectangular flat surface electrodes non-uniformly passes through both the dielectric material and the surrounding environment. First, as shown in Figure 3.3(b), a high-density electromagnetic field and large numbers of flux tubes are distributed in a very thin layer of the dielectric material close to the flat surface electrodes [109]. Based on the electric field mapping principle, that is, no matter whether the size is big or small, the unit flux tube contributes the same capacitance [109]. It is concluded that the smaller the flux tubes, the more contribution to the capacitance of the capacitor. Therefore, the sensing response (i.e., the capacitance) is largely determined by a very thin layer of the dielectric material close to the flat surface electrodes, as shown in Figure 3.3(b). Therefore, by this electrode configuration, it takes a very short time for the humid air to pass through the very thin layer of the dielectric material close to the surface electrodes. The response time of the sensor can be dramatically improved/shortened, which is the most beneficial feature to be used in agricultural applications. Second, differently, the dielectric permittivity of the capacitor with flat surface electrodes is determined not only by the dielectric permittivity of the dielectric material but also partially by the dielectric permittivity of the surrounding environment (such as the soil in which the sensor is placed). As a result, it is necessary to calculate the effective permittivity of the capacitor/sensor with flat surface electrodes, $\varepsilon_{r(eff)}$, instead of solely the permittivity of the dielectric material, for a detailed study of the influence of its dielectric property spectrums on the humidity sensing. Eq. (3-4) can be used to determine the effective permittivity of the capacitor with rectangular flat surface electrodes coated on a dielectric material (such as dielectric ceramics), as shown in Figure 3.3 [109]:

$$\varepsilon_{r(eff)} = \frac{C \cdot ln(\frac{\pi(d-w)}{w+t}+1)}{\pi \varepsilon_0 l}, \text{ when } h \geqslant t \qquad (3\text{-}4)$$

where d is the distance between the rectangular conductor electrodes' middle positions (m); l, w, and t denote the length, width, and thickness of the conductor electrodes (m), respectively; h is the thickness of the dielectric material (m) with a relative dielectric permittivity of ε_r; the device is surrounded by air with a relative dielectric permittivity of 1.

Eq. (3-4) is a classic equation that has long derivation procedures by using many assumptions and methods based on electromagnetic theories. It is derived in detail as follows:

The electric field intensity of an infinite line of (positive) charge is given below [109]:

$$E_r = \frac{\rho_L}{2\pi\varepsilon R} \qquad (3\text{-}5)$$

where ρ_L is uniform charge density per unit length (C/m); R is the distance between a point experiencing an electric field and an infinite line of charge (m); ε is the dielectric permittivity of the medium ($\varepsilon = \varepsilon_0\varepsilon_r$, ε_r=8.85×10^{-12} F/m).

As shown in Figure 3.4, the potential difference V_{21} between two points at radial distances R_2, and R_1, from the infinite line of charge is the work per unit charge required to transport a positive charge from P_1 to P_2. Assume that $R_2 > R_1$. This potential difference is given by the line integral of E_r from P_2 to P_1, the potential at P_1 being higher than at P_2 if the line of charge is positive. The following is the equation:

$$V_{21} = -\int_{R_2}^{R_1} E_r dR = \frac{\rho_L}{2\pi\varepsilon}\int_{R_1}^{R_2}\frac{dR}{R} = \frac{\rho_L}{2\pi\varepsilon} ln\frac{R_2}{R_1} \qquad (3\text{-}6)$$

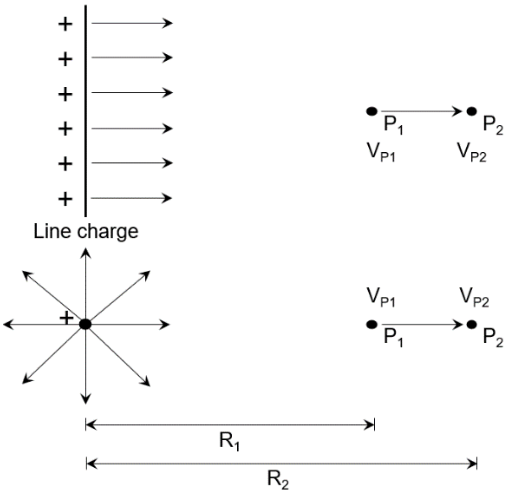

Figure 3.4 Schematic diagram of the potential difference between two points, P_1, and P_2, at radial distances, R_2, and R_1, from the infinite line of positive charge.

To derive the equation to calculate the permittivity from the capacitance of two flat surface electrodes coated on a dielectric material/medium, it is necessary to derive it from the simplest case of two infinite lines of charge in a medium.

As shown in Figure 3.5, two infinite parallel lines of charge are separated by the distance of 2S. Assume that the linear charge density of the two lines is equal but of opposite sign. The electric field at a point P, distant R_1 from the negative line and R_2 from the positive line, is then the vector sum of the field of each line taken alone.

Let the origin of the coordinates in Figure 3.5 be the reference for potential. Imagine that only the positively charged line is present. From Eq. (3-6), the potential difference between P and the origin is [110]:

$$V_+ = \frac{\rho_L}{2\pi\varepsilon} ln \frac{S}{R_2} \qquad (3\text{-}7)$$

Similarly, for the negatively charged line:

$$V_- = -\frac{\rho_L}{2\pi\varepsilon} ln \frac{S}{R_1} \qquad (3\text{-}8)$$

With both lines present the total potential difference V between P and the origin is the sum of Eq. (3-7) and Eq. (3-8):

$$V = V_+ + V_- = \frac{\rho_L}{2\pi\varepsilon} ln \frac{R_1}{R_2} \qquad (3\text{-}9)$$

If V in Eq. (3-9) is a constant, thus, Eq. (3-9) is the equation of an equipotential line. The form of the equipotential line will be more apparent if Eq. (3-9) is transformed to Eq. (3-10) and Eq. (3-11):

$$ln \frac{R_1}{R_2} = \frac{2\pi\varepsilon V}{\rho_L} \qquad (3\text{-}10)$$

$$\frac{R_1}{R_2} = e^{2\pi\varepsilon V/\rho_L} \qquad (3\text{-}11)$$

Since $2\pi\varepsilon V/\rho_L$ is a constant for any equipotential line, the right side of Eq. (3-11) is a constant K:

$$e^{2\pi\varepsilon V/\rho_L} = K \qquad (3\text{-}12)$$

$$R_1 = KR_2 \qquad (3\text{-}13)$$

The coordinates of the point P in Figure 3.5 are (x,y), thus, $R_1 = \sqrt{(S+x)^2 + y^2}$ and $R_2 = \sqrt{(S-x)^2 + y^2}$. Substituting the values of R_1 and R_2 to Eq. (3-13), after squaring and rearranging:

$$x^2 - 2xS\frac{K^2+1}{K^2-1} + S^2 + y^2 = 0 \qquad (3\text{-}14)$$

Rearrange by mathematics:

$$(x - S\frac{K^2+1}{K^2-1})^2 + y^2 = (\frac{2KS}{K^2-1})^2 \qquad (3\text{-}15)$$

where x, y = coordinates of the point on a circle; H = x coordinate of the center of the circle; r = radius of the circle.

As shown in Figure 3.5, it is obvious that the equipotential curve passing through P (x, y) is a circle with a radius of r and a center on the x-axis:

$$r = \frac{2KS}{K^2-1} \qquad (3\text{-}16)$$

$$H = S\frac{K^2+1}{K^2-1} \qquad (3\text{-}17)$$

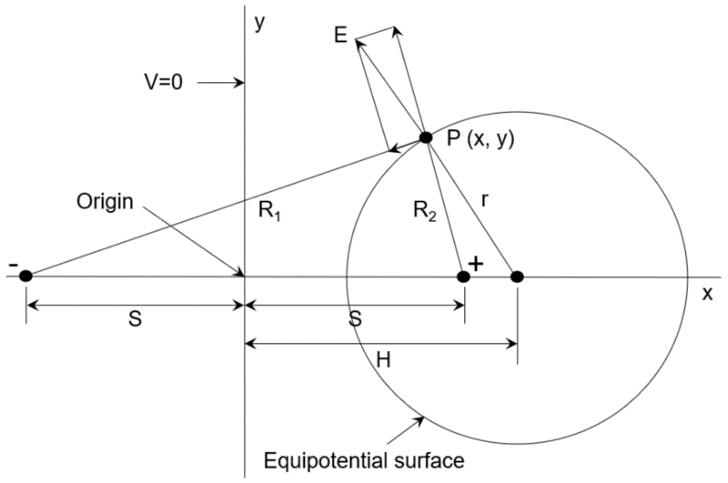

Figure 3.5 Cross-sectional view of two lines of charge separated by the distance of 2S.

An equipotential line of radius r with center at (H, 0) is shown in Figure 3.6. As K increases, corresponding to larger equipotentials, r approaches zero and H approaches S, so that the equipotentials are smaller circles with their centers more nearly at the line of charge.

This is illustrated by the additional equipotential circles in Figure 3.6. The potential is 0 along the y axis. That is, V = 0 at x = 0. Thus, the plane x = 0 is the reference plane for potential.

The discussion of two infinite lines of charge can be easily extended to the case of an infinite line consisting of two paralleled current-carrying wires, i.e., two conducting wires. Under static conditions, much can be learned about its properties from a consideration of its behavior. Let a fixed potential difference be applied between the conductors so that the charge per unit length of each conductor is ρ_L.

The surface of the wires is equipotential, and therefore, an equipotential circle in Figure 3.6 will coincide with the wire surface. Thus, the heavy circles of radius r_0 and center-to-center spacing 2H can represent the two wires. The field and potential distributions external to the wire surfaces are the same as if the field were produced by two infinitesimally thin lines of charge with a spacing of 2S. The field inside the wires is, of course, 0, and the potential is the same as on the surface. The charge is not uniformly distributed on the wire surface but has a higher density on the adjacent sides of the conductors.

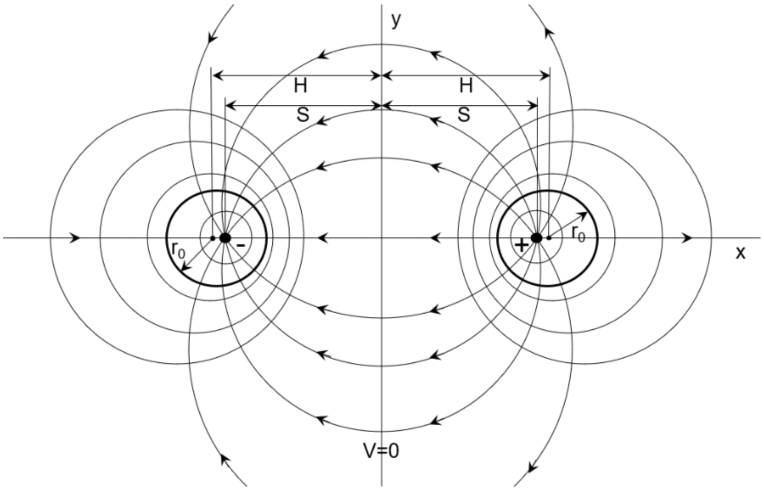

Figure 3.6 Field and equipotential surfaces around two infinite paralleled lines of charge/two infinite conductor lines.

The potential difference V_c between one of the conductor wires and a point midway between them is [110]:

$$V_c = \frac{\rho_L}{2\pi\varepsilon} lnK \qquad (3\text{-}18)$$

The value of K can be expressed in terms of the radius of the wires, r_0, and half center-to-center spacing H by eliminating s from Eq. (3-16) and Eq. (3-17) and solving for K:

$$K = \frac{H}{r_0} + \sqrt{\frac{H^2}{r_0^2} - 1} \qquad (3\text{-}19)$$

The potential difference, V_{2c}, between the two conductor wires is:

$$V_{2c} = 2V_c = \frac{\rho_L}{\pi\varepsilon} \ln\left(\frac{H}{r_0} + \sqrt{\frac{H^2}{r_0^2} - 1}\right) \qquad (3\text{-}20)$$

To find the capacitance per unit length, C/l, of the two-conductor wires we take the ratio of the charge per unit length on one conductor to the difference of potential between the conductors:

$$\frac{C}{l} = \frac{\rho_L}{V_{2c}} = \frac{\pi\varepsilon}{\ln\left(\frac{H}{r_0} + \sqrt{\frac{H^2}{r_0^2} - 1}\right)} \qquad (3\text{-}21)$$

where H is half (conductor) center-to-center spacing (m); r_0 is the radius of the conductor (m).

The equation is transformed to:

$$\frac{C}{l} = \frac{\rho_L}{V_{2c}} = \frac{\pi\varepsilon_r\varepsilon_0}{\ln\left\{\frac{H}{r_0}\left[1 + \sqrt{1 - \left(\frac{r_0}{H}\right)^2}\right]\right\}} \qquad (3\text{-}22)$$

When $\frac{r_0}{H} \ll 1$, the equation is transformed to [109]:

$$\frac{C}{l} \approx \frac{\pi\varepsilon_{r(eff)}\varepsilon_0}{\ln\left(\frac{2H}{r_0}\right)} \qquad (3\text{-}23)$$

Figure 3.7 shows the comparison of flux plots of the one-quadrant approximate field distribution of both two circular conductors/wires and two elliptical conductors which are very similar to the case of the two flat conductors/electrodes. According to a similarity of the distribution of the equal potential surfaces and the flux tubes (proposed in the electric field mapping method) among the circular conductors/wires, the two elliptical conductors, and the flat surface conductors/electrodes, it is approximated that both the circular conductors/wires and the two elliptical conductors can be used to simulate the case of the two flat surface conductors/electrodes [109]. By making the perimeter of the round conductors equal to that of the rectangular conductors with the distance of the middle points of the conductors, d, the equal surface areas per unit length of the two geometries have a relation [109]:

$$Perimeter = 2\pi r_0 = 2(w+t) \qquad (3\text{-}24)$$

$$r_0 = \frac{w+t}{\pi} \qquad (3\text{-}25)$$

Substituting r_0 obtained in Eq. (3-25) into Eq. (3-23), where 2H = d for the case of the flat rectangular conductors:

$$\frac{C}{l} \approx \frac{\pi \varepsilon_{r(eff)} \varepsilon_0}{\ln\left(\frac{\pi \cdot d}{w+t}\right)}, \text{ for } \frac{w+t}{\pi H} \ll 1 \qquad (3\text{-}26)$$

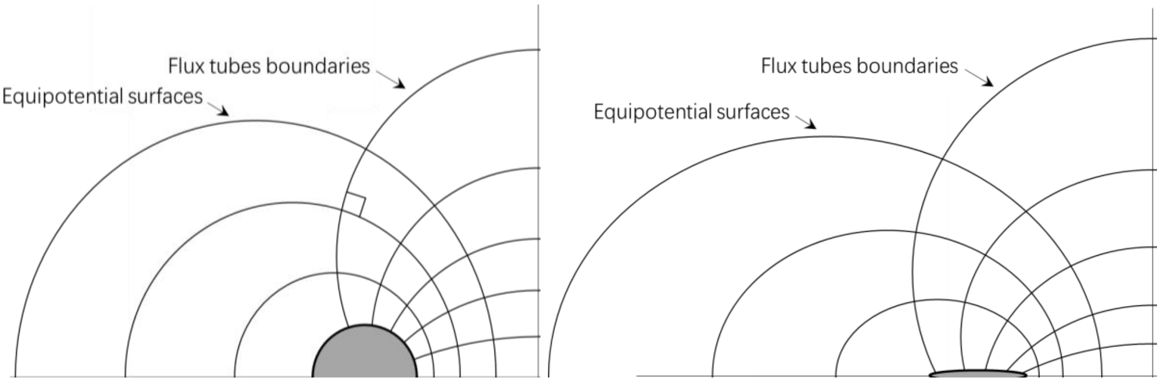

Figure 3.7 Comparison of flux plots of the one-quadrant approximate field distribution for both two circular conductors/wires and two elliptical conductors which are very similar to the case of the two flat electrodes/conductors.

The limitations of Eq. (3-26) are illustrated if we let d = w. The equation is not valid when the conductors are (very close to) touching. Adding a correction factor, Δ, to d so that we can get infinite capacitance when d = w:

$$\frac{C}{l} \approx \frac{\pi \varepsilon_{r(eff)} \varepsilon_0}{\ln\left(\frac{\pi(d+\Delta)}{w+t}\right)}, \text{ for } \frac{2(w+t)}{\pi d} \ll 1 \qquad (3\text{-}27)$$

For infinite capacitance per unit length, when d = w:

$$[\ln\left(\frac{\pi(w+\Delta)}{w+t}\right)] = 0 \qquad (3\text{-}28)$$

This implies that:

$$\left(\frac{\pi(w+\Delta)}{w+t}\right) = 1 \qquad (3\text{-}29)$$

Thus, Δ is:

$$\Delta = \frac{w+t}{\pi} - w \qquad (3\text{-}30)$$

Substituting Δ into Eq. (3-27):

$$\frac{C}{l} \approx \frac{\pi \varepsilon_{r(eff)} \varepsilon_0}{\ln\left(\frac{\pi(d-w)}{w+t}+1\right)} \qquad (3\text{-}31)$$

Eq. (3-31) can be rearranged to get Eq. (3-4) for a determination of the effective permittivity, $\varepsilon_{r(eff)}$, of the dielectric ceramics sensor/capacitor, coated with rectangular flat surface electrodes.

As the effective permittivity of the ceramics sensor/capacitor has been calculated by Eq. (3-4), the soil influence on the effective permittivity of the humidity sensor will be discussed using the empirical equations in the next section.

3.1.4 Theoretical analysis of soil influence on humidity sensing of the dielectric ceramics sensor

There is a relationship between the real permittivity of the dielectric material and the effective permittivity of the capacitor/sensor made of the dielectric material and the rectangular flat surface electrodes. Interestingly, a problem has been raised that whether the humidity sensing performance is influenced by the surrounding medium, such as the soils replacing the medium of the air. The issue is discussed as follows:

According to the Gauss theorem, if the rectangular flat electrodes/conductors are all surrounded by one (infinite) medium (such as the dielectric material) with a dielectric permittivity of ε_r, the effective permittivity, $\varepsilon_{r(eff)}$, has a relation [109]:

$$\varepsilon_{r(eff)} \approx \varepsilon_{r(medium)} \qquad (3\text{-}32)$$

In this study, the rectangular flat electrodes are coated on the surface of the dielectric material, as shown in Figure 3.3, and the ratio of the distance of the middle positions of the electrodes, d, to the thickness of the dielectric material h, is close to 1 (i.e., $d \approx h$), the relation can be expressed by Eq. (3-32) [109]:

$$\varepsilon_{r(eff)} \approx (\varepsilon_{r(medium)}+\varepsilon_{r(diel)})/2 \qquad (3\text{-}33)$$

where $\varepsilon_{r(diel)}$ is the dielectric permittivity of the dielectric material.

When the medium is the air, the effective permittivity of the sensor/capacitor exposed in the air, $\varepsilon_{r(eff,\ air)}$, can be expressed as follows:

$$\varepsilon_{r(eff,\ air)} \approx (\varepsilon_{r(air)}+\varepsilon_{r(diel)})/2 \approx (1+\varepsilon_{r(diel)})/2 \qquad (3\text{-}34)$$

where $\varepsilon_{r(air)}$ is the dielectric permittivity of the air.

When the medium is the soil with the dielectric permittivity of about 3~7 (which will be experimentally determined in Section 3.4.1) in a certain frequency range, the equation to express the effective permittivity of the sensor covered by the soil can be expressed as follows:

$$\varepsilon_{r(eff,\ soil)} \approx (3\sim 7+\varepsilon_{r(diel)})/2 \text{ in a wide frequency range} \qquad (3\text{-}35)$$

From Eq. (3-35), it can be found that, if the dielectric permittivity, $\varepsilon_{r(diel)}$, of the dielectric material of the capacitor/sensor is a large value, for example, about 10^4~10^5 [111,112], obviously:

$$\varepsilon_{r(\mathrm{eff,\ air})} \approx (1+\varepsilon_{r(\mathrm{diel})})/2 \approx \varepsilon_{r(\mathrm{eff,\ soil})} \approx (3\sim7+\varepsilon_{r(\mathrm{diel})})/2 \approx 10^4\sim10^5 \quad (3\text{-}36)$$

From Eq. (3-36), it reveals that, in the cases of either surrounded by the medium of the air or by the medium of the soils, the effective permittivity (and measured capacitance) of the sensor coated by the flat surface electrodes is the same, due to the very low permittivity of both the air and the soils compared to the high dielectric permittivity of the dielectric material. Therefore, the effective permittivity spectrums of the sensor/capacitor with the flat surface electrodes can be used to make the sensing module of the LC wireless resonant humidity sensor in agricultural applications where the sensor is covered by the soils. A verification experiment will be conducted at different humidity levels based on this theoretical analysis later in this chapter.

3.1.5 Dielectric humidity sensor based on high permittivity BTO-SiO_2 ceramics

To be used as humidity sensors, dielectric ceramics have several good advantages, such as high humidity sensitivity, long-time stability, and water-resistant capability due to their dielectric sensing features, rigidity, and structural integrity [75,113].

As has been illustrated, to obtain a humidity sensing capacitor without the influence of the soils in agricultural applications, a humidity sensing dielectric material with a high dielectric permittivity is preferred to be used. It has been reported that SiO_2-coated BTO ceramics sintered by spark plasma sintering (SPS) can be used to densify the sample and obtain a high dielectric permittivity up to 2×10^5 at 10 kHz with a very low dielectric loss [111]. In our group, we also observed a high dielectric permittivity of the SiO_2-coated BTO ceramics sintered by SPS [112]. Hence, the core-shell BTO-SiO_2 ceramics can be used as the high dielectric permittivity material to get rid of the influence of the permittivity contributed by the soils.

An interesting finding in our group is that a high permittivity core-shell BTO-SiO_2 ceramics has a large humidity response of about one order increase of the dielectric permittivity from low humidity to high humidity at a low-frequency range. Therefore, it is a promising candidate for the dielectric material to be used as the humidity sensing capacitor to make the sensing module of the LC wireless resonant humidity sensor. However, conversely, a decrease in the dielectric permittivity of the humidity sensing response from low humidity to high humidity can be observed at a high-frequency range. Thus, between the low-frequency range and the high-frequency range, interestingly, at one frequency, the permittivity neither increases nor decreases (i.e., retains the same permittivity). Interestingly, the phenomenon of the BTO-SiO_2 ceramics humidity sensor illustrated above has not been reported and the reason behind is not clear, it raises a major motivation to study and report the humidity sensor/capacitor based on the core-shell BTO-SiO_2 ceramics. Detailed illustrations and discussions of this finding will be followed in the coming sections. In summary, a fundamental study of the high dielectric permittivity core-shell BTO-SiO_2 ceramics humidity capacitor/sensor is very important for the development of the passive wireless LC resonant humidity sensor in the application of agriculture, which needs to be detailly studied and reported.

3.2 Experiment procedures

3.2.1 Preparation of the BTO-SiO_2 ceramics humidity sensor

Barium titanate (BTO) powders in the diameter of 140 nm were coated with silicon dioxide

(SiO_2) using atomic layer deposition. The core-shell BTO-SiO_2 nano-powders were sintered at 1050 °C for 5 min at 50 MPa using a direct current sintering furnace. Samples were heated at a rate of 100 °C/min to 950°C and held for two minutes and then heated at a rate of 50 °C/min to 1050°C to avoid overshooting the final temperature. The BTO-SiO_2 nanocomposite ceramics tablets which were sintered were in the size of Φ20 mm × 5 mm, as shown in Figure 3.8. The sintered tablets were cut into pieces in thicknesses of about 900~1100 μm by the wafering blade (with a diamond-metal bond) in the dimension of 152 mm × 0.51 mm × 12.7 mm. After the cutting, the specimens were grounded and polished to obtain flat surfaces with good surface roughness. Two flat rectangular gold electrodes were sputtered on one side of the polished specimens, respectively. A specimen/capacitor with a surface area of about 18 mm^2 and a thickness of about 1100 μm with two rectangular electrodes in size of 3 × 1 mm and a 150 μm uniform gap between the rectangular electrodes was manufactured.

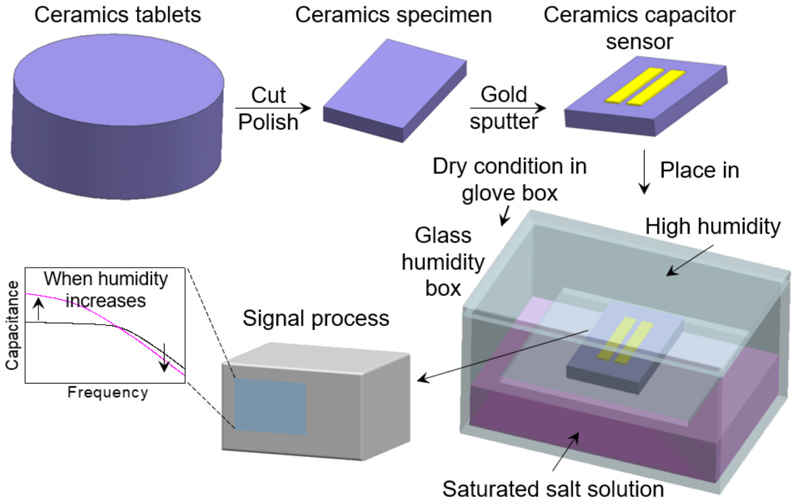

Figure 3.8 Schematics of the experiment procedures to measure the dielectric spectrums of the ceramics capacitor sensor at various humidity levels. The low humidity is maintained with inlet dry air in the glove box and the high humidity levels are generated in the humidity

boxes with different saturated salt solutions.

3.2.2 Characterization of the ceramics humidity sensor

As shown in Figure 3.8, the humidity sensing ceramics specimen was placed into the glove box with inlet dry air at a humidity of lower than 8% RH, which was considered the dry condition having the same dielectric permittivity as the oven-dried specimen. At room temperature (20℃), the capacitance and dielectric loss of the sensors were measured by a precision impedance analyzer (Agilent 4294A) with 16034H 1m text fixture, which was connected to the sensing specimen by two wires. C_p and D measurement function in the precision impedance analyzer was used to record the capacitance and dielectric loss of the sensor. The measured frequency range is from 100 Hz to 1 MHz. After the measurements, Eq. (3-4) was used to calculate the effective permittivity of the sensor with flat surface electrodes. Different saturated salts were contained in each sealed box, providing different humidity levels, which were shown in Table 3.1. By carefully bringing the testing stage with the specimen into/out of the humidity box to provide high humidity and dry conditions, the humidity testing cycle could be processed.

Table 3.1 Different humidity levels generated by different saturated salt solutions [85].

Temperature\Saturated salt	$MgCl_2$	K_2CO_3	NaBr	$CuCl_2$	NaCl	KCl
20℃	33.1%	43.2%	59.1%	69.4%	75.5%	85.1%

3.2.3 Experiment procedures of soil influence on the ceramics humidity sensor

A ceramics specimen/sensor with a thickness of about 900 μm and two rectangular flat surface electrodes in size of 3 × 1 mm with a 150 μm uniform gap between electrodes was used for the humidity measurements when placed in the air, sand, and top soil, respectively. The ceramics sensor was completed covered by the sand or top soil and tested at both dry conditions and 85% RH. The characterization procedures were the same as those illustrated in Section 3.2.2. After the measurement, Eq. (3-4) (i.e., the rectangular flat surface electrode model) was used to calculate the effective permittivity of the sensor with flat surface electrodes.

3.2.4 Characterization of the dielectric properties of different soils

As shown in Figure 3.9, three different types of soils, i.e., sand, top soil, and lake soil, were prepared for dielectric measurements. The particle size is no more than 1 mm for the sand and 500 μm for the soils. The top soil contains organic matters for planting purposes, in contrast, the lake soil does not contain much.

Figure 3.9 Three different types of soils prepared for dielectric measurements.

To make a probe/capacitor to measure the dielectric properties of the soils, a pair of paralleled copper electrodes/sheets in size of 13 cm × 9 cm was fixed (by double-sided tape) onto a pair of paralleled thick glass plates which were placed on a glass stage, as shown in

Figures 3.10(a), 3-19(b). The distance of the copper electrodes was 4 mm. Two cables connected the electrodes and the precision impedance analyzer (4294A). Besides, two thick plastic plates were placed/fixed on the glass stage and vertically contacted the paralleled glass plates. The aim was to hold the soils between the electrodes.

After the calibration, as shown in Figures 3.10(c), 3.10(d), 3.10(e), 3.10(f), three types of soils were filled in the gap between the electrodes to measure their dielectric properties (by Cp-D function) at different frequencies from 100 Hz to 1 MHz. After the measurements, Eq. (3-3) (i.e., the parallel plate electrode model) was used to calculate the real permittivity of the soils.

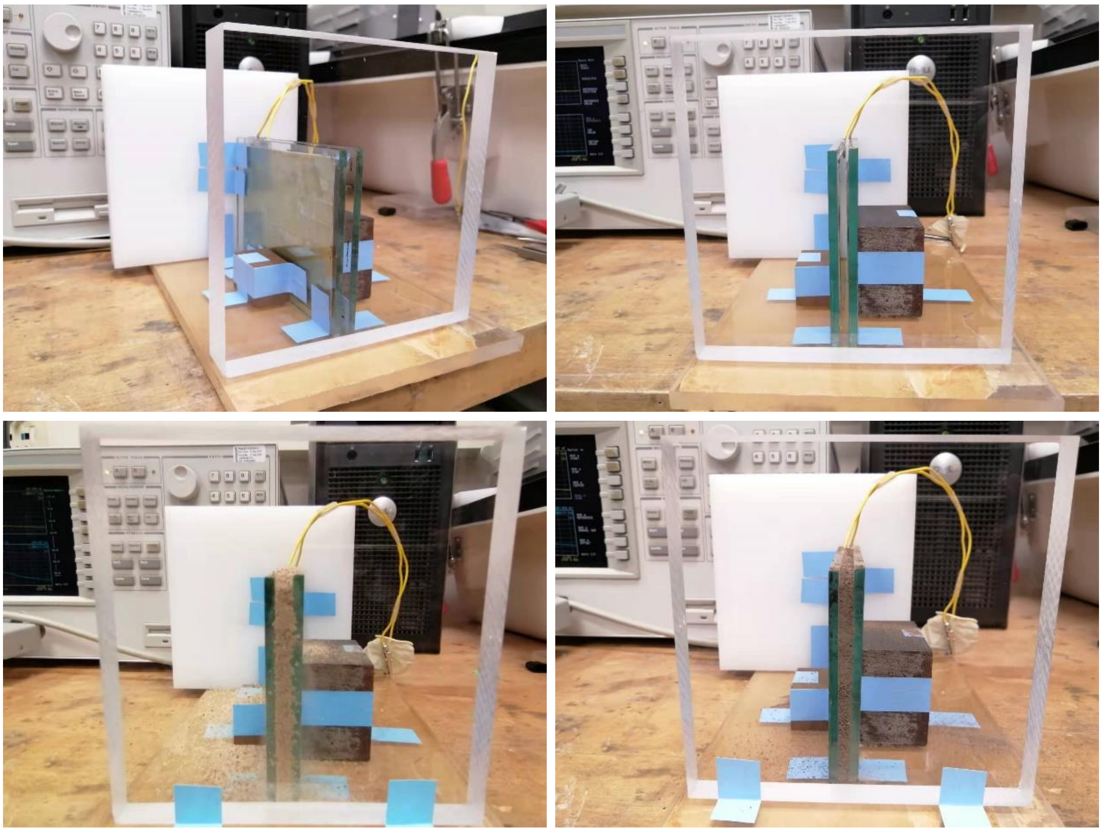

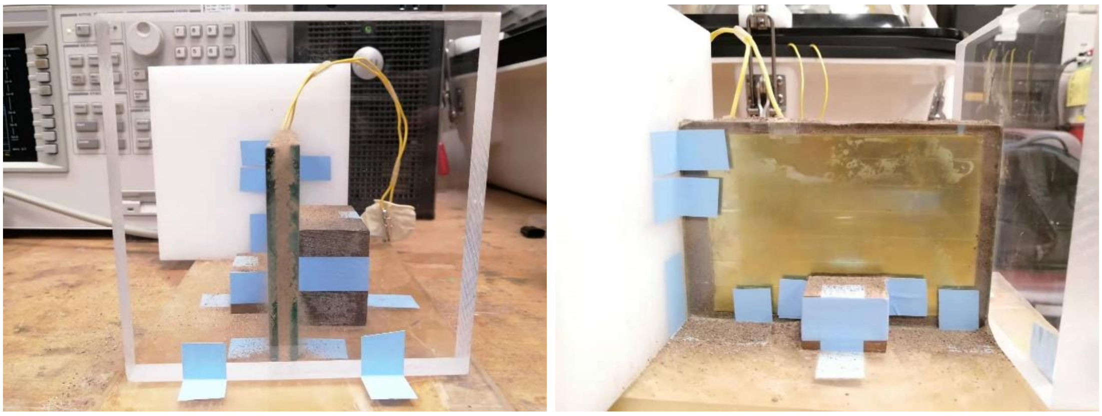

Figure 3.10 Different view directions of the paralleled copper capacitor to measure permittivity/dielectric loss vs frequency spectrums of the three different types of soils. (a) oblique view and (b) front view to measure permittivity of air for calibration; (c) front view to measure the sand; (d) front view to measure the topsoil; (e) front view to measure the lake soil; (f) side view to measure the lake soil.

3.3 Humidity testing results of high dielectric permittivity ceramics sensor with flat surface electrodes

3.3.1 Effective permittivity and loss responses of the ceramics sensor at different humidity levels

Figure 3.11 shows the effective permittivity and dielectric loss vs frequency spectrums of the specimen/sensor with surface electrodes when increasing and decreasing humidity in the humidity range between dry condition and 85% RH. At dry condition, as shown in the black line in Figure 3.11(a), with increasing frequency, permittivity gradually decreases at low frequency and then, dramatically decreases at high frequency. From Figure 3.11(b), with increasing frequency, loss at the dry condition in the black line decreases at low frequency and then, increases at high frequency. From Figure 3.11(a), when humidity increases from dry condition to 85% RH, permittivity increases at a frequency lower than 20 kHz, however, slightly decreases at a frequency higher than 20 kHz. Moreover, more than one order of the permittivity increase at 100 Hz, and about one order of the permittivity increase at 1 kHz can be obtained. A reverse trend on the permittivity spectrum is found when humidity decreases from 85% to dry condition, as shown in Figure 3.11(c). From Figure 3.11(b), when humidity increases, loss decreases at low frequency and increases at high frequency, which implies that the loss spectrum shifts to a low frequency. When the humidity decreases, a reverse trend on the loss spectrum can be found, as shown in Figure 3.11(d).

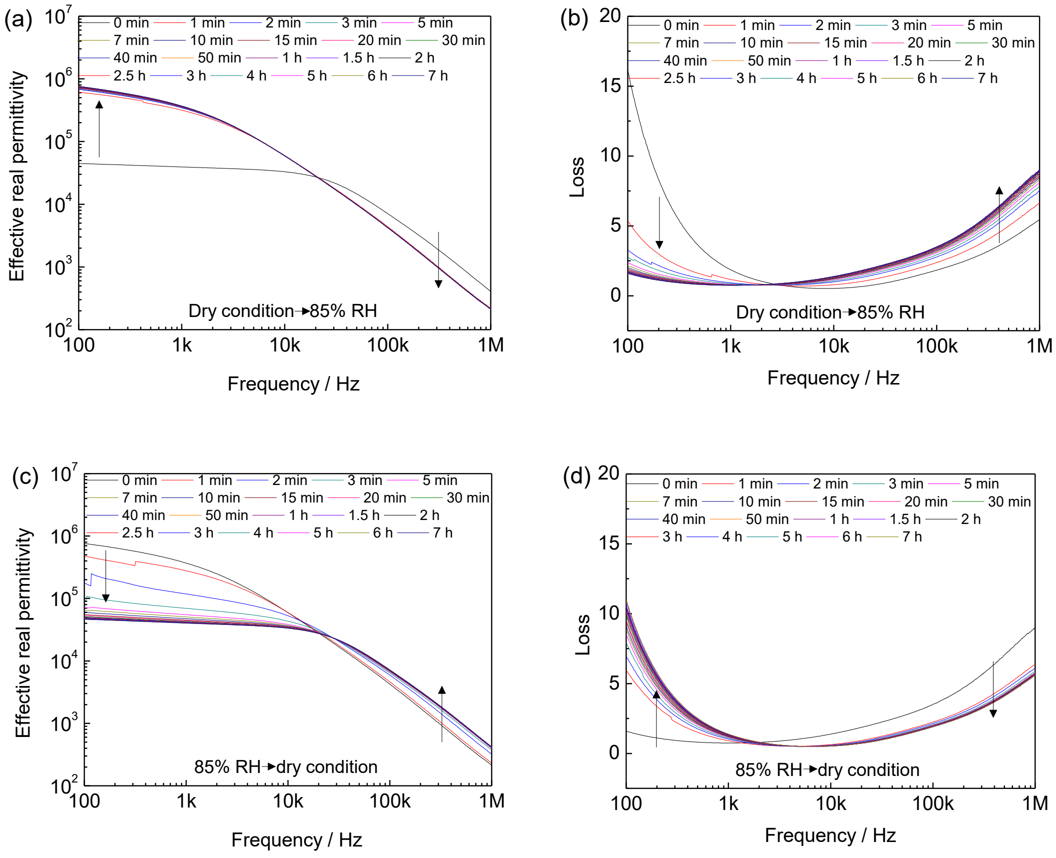

Figure 3.11 Effective permittivity/dielectric loss vs frequency spectrums of the sample with surface electrodes when increasing humidity from dry condition to 85% RH (a)/(b); and decreasing humidity from 85% RH to dry condition (c)/(d).

Besides, from Figures 3.11(a), 3.11(c), between the low-frequency range and the high-frequency range, interestingly, at one frequency, the permittivity neither increases nor decreases (i.e., retains the same permittivity). This phenomenon found in the BTO-SiO_2 ceramics humidity sensor has not been reported and the reason behind is not clear. However, this fixed permittivity point at a certain middle frequency probably could be used for calibration of the sensor at different temperatures.

Typically, some reports about other ceramics humidity sensors reveal that the mechanism behind the total capacitance and the dielectric permittivity of the (CCTO, for example) ceramics sensor corresponding to the humidity response can be explained as follows [114,115]. When relative humidity changes, the amount of the water molecules absorbed/desorbed by the ceramics sensor changes. The grain boundaries between the adjacent grains might have their grain boundary potential barriers which place a key role to influence the grain boundary capacitance [114]. The water molecules bonded in the grain boundaries vary at different relative humidity (RH) levels. Hence, the total capacitance and the dielectric permittivity of the sensor change with the variation of the grain boundary potential barrier capacitance [114,115]. When the grain size is small and the amount of the grain boundaries is large, the influence of the grain boundary capacitance on the total capacitance of the sensor is large. This mechanism may play an important role to influence (increasing/decreasing) the total capacitance, hence, influencing the dielectric permittivity as well as the dielectric loss of the sensor at the entire frequency spectrum.

However, in this study, the permittivity spectrums of the ceramics sensor show a different changing trend with the humidity change compared to the typical humidity sensing mechanism of the ceramics sensor. It is found that the permittivity spectrum is not increased or decreased at the entire frequency spectrum when increasing or decreasing the humidity. Thus, the explanation discussed in the last paragraph is probably not suitable to explain the phenomenon observed in Figures 3.11(a), 3.11(c). However, the humidity influencing mechanism of this core-shell BTO-SiO_2 ceramics humidity capacitor/sensor is not clear, which requires further study.

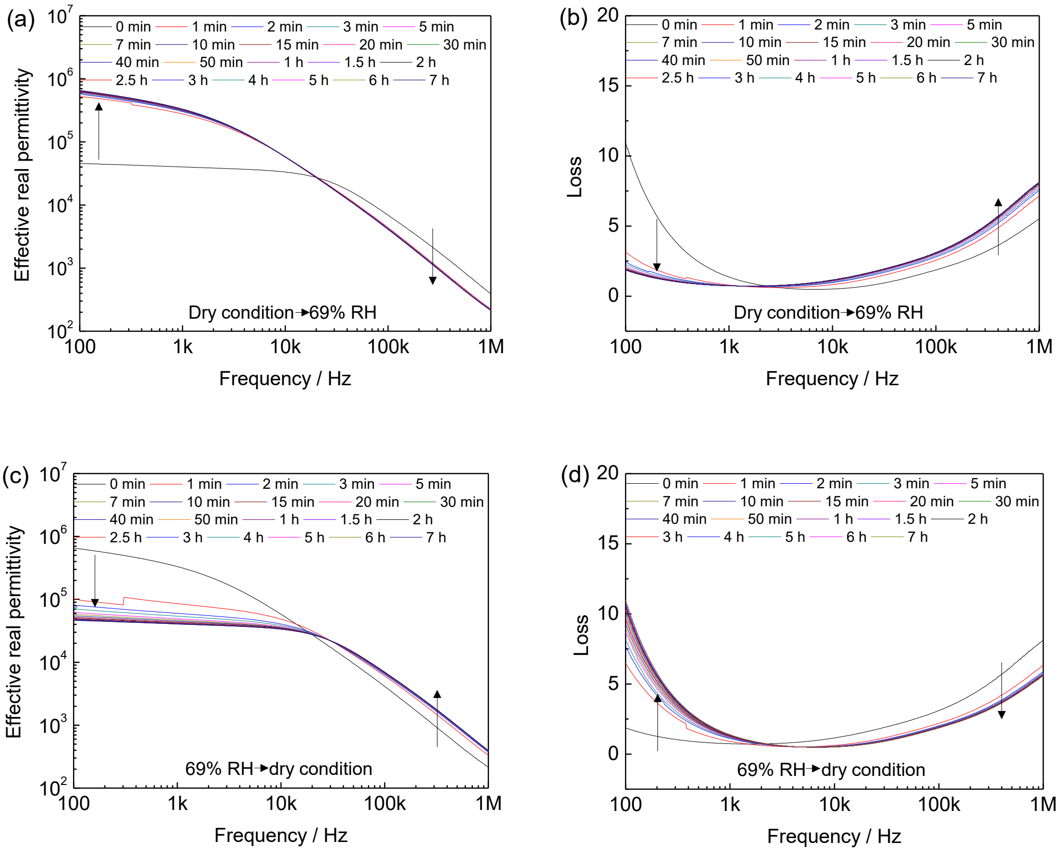

Figure 3.12 Effective permittivity/dielectric loss vs frequency spectrums of the sample with surface electrodes when increasing humidity from dry condition to 69% RH (a)/(b); and decreasing humidity from 69% RH to dry condition (c)/(d).

Figure 3.12 shows effective permittivity and dielectric loss vs frequency spectrums of the sample when increasing and decreasing humidity in the humidity range between dry condition and 69% RH. Similar to the humidity response of the sensor between dry condition and 85% RH, as shown in Figure 3.12(a), when humidity increases from dry condition to 69% RH, permittivity increases at a frequency lower than 20 kHz, however, slightly decreases at a frequency higher than 20 kHz. A reverse trend on the permittivity spectrum can be found when humidity decreases from 69% to dry condition, as shown in Figure 3.10(c). From Figure 3.12(b), when humidity increases, loss decreases at low frequency and increases at high frequency, which also implies that the loss spectrum shifts to a low frequency. A reverse trend on the loss spectrum can be found when humidity decreases, as shown in Figure 3.12(d). By comparison among the permittivity and loss spectrums between Figure 3.12 and Figure 3.11, the humidity response of the specimen measured between dry condition and the humidity of 69% RH is similar to that measured between dry condition and the high humidity of 85% RH. However, comparing Figure 3.12 and Figure 3.11, permittivity and loss responses tested between dry condition and 69% RH are smaller than those tested at the high humidity of 85% RH, which is resulted from a smaller amount of water vapor absorbed by the sample at the lower humidity of 69% RH than that at the high humidity of 85% RH.

Figure 3.13 shows effective permittivity and dielectric loss vs frequency spectrums of the specimen when increasing and decreasing humidity in the humidity range between dry condition and 43% RH. Similar to the humidity response of the sensor between dry condition and 69/85% RH, as shown in Figure 3.13(a), when humidity increases from dry condition to 43% RH, permittivity increases at a frequency lower than 20 kHz, but slightly decreases at a frequency higher than 20 kHz. A reverse trend on the permittivity spectrum can be found when humidity decreases from 43% to dry condition, as shown in Figure 3.13(c). From Figure 3.13(b), when humidity increases, loss decreases at low frequency and increases at high frequency, which implies that the loss spectrum shifts to a low frequency. A reverse trend on the loss spectrum can be found when humidity decreases, as shown in Figure 3.13(d).

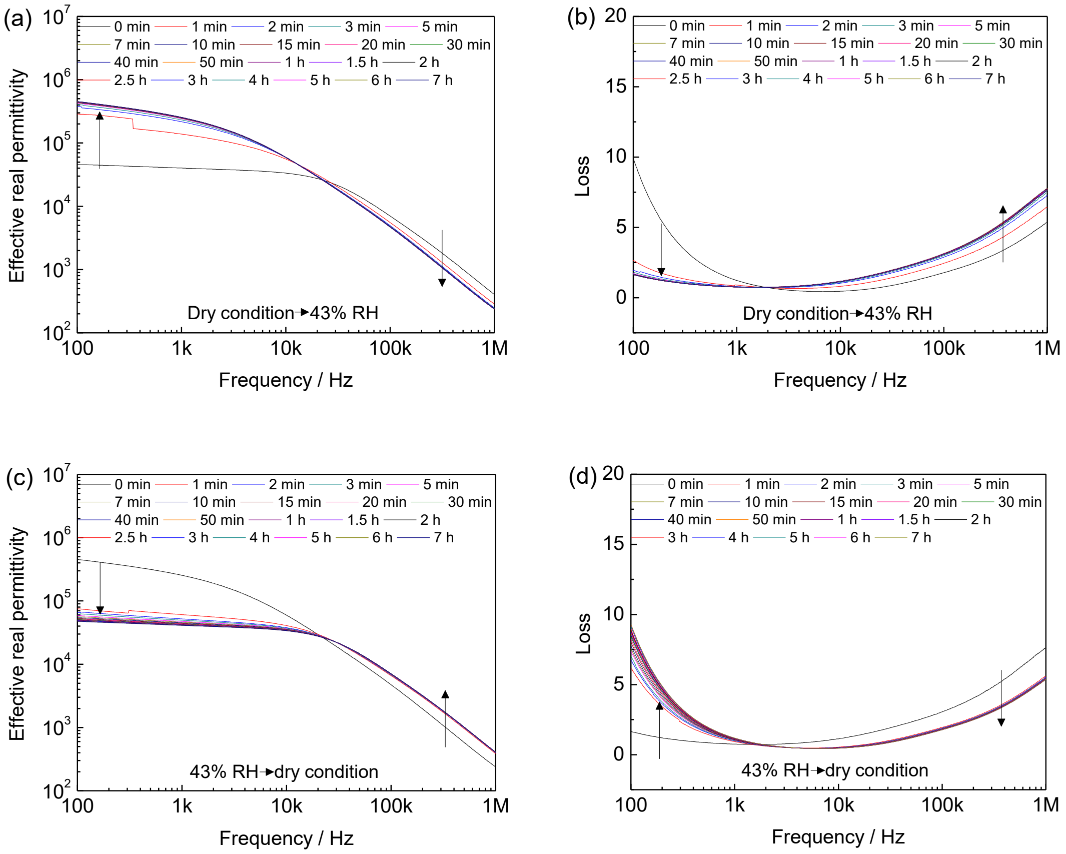

Figure 3.13 Effective permittivity/dielectric loss vs frequency spectrums of the sample with surface electrodes when increasing humidity from dry condition to 43% RH (a)/(b); and decreasing humidity from 43% RH to dry condition (c)/(d).

By comparison among the permittivity and loss spectrums in Figure 3.11, Figure 3.12, and Figure 3.13, it is concluded that the humidity response of the sample measured between dry condition and the humidity of 43% RH is very similar to that measured between dry condition and the high humidity of 69/85% RH. However, comparing Figure 3.11, Figure 3.12, and Figure 3.13, in the low-frequency range, permittivity and loss responses tested between dry condition and 43% RH are much smaller than those tested at 69% RH and 85% RH, which implies that the water vapor absorbed by the grain boundaries of the sample at the humidity of 43% RH is much smaller than those at the humidity of 69% RH and 85% RH.

Figure 3.14 shows effective permittivity vs time plots of the sample with surface electrodes of one-cycle humidity tests in different humidity testing levels from 85% RH to 43% RH at selected frequencies from 100 Hz to 100 kHz. From Figures 3.14(a), 3.14(c), 3.14(e), 3.14(g), 3.14(i), in each humidity testing level, high permittivity is obtained, in order of 10^5, and permittivity increases when increasing humidity and decreases when decreasing humidity at low frequencies of 100 Hz to 3 kHz. As shown in Figures 3.14(b), 3.14(d), 3.14(f), 3.14(h), and 3.14(j), at the high frequency of 100 kHz, permittivity is very low, in order of 10^3, and permittivity decreases slightly when increasing humidity and increases when decreasing humidity which shows a reverse trend compared with the permittivity at low frequencies. Moreover, it is observed that, in one humidity cycle, the permittivity of the sample goes back to the initial value at all analyzed frequencies. Besides, from Figures 3.14(a), 3.14(c), 3.14(e), 3.14(g), and 3.14(i), at low frequencies, permittivity response gradually decreases when the humidity testing level decreases from 85% RH to 43% RH. However, from Figures 3.14(b), 3.14(d), 3.14(f), 3.14(h), 3.14(j), at the high frequency of 100 kHz, permittivity response does not vary much in different humidity testing levels. It is also confirmed that, in one humidity cycle, permittivity and loss of the sample go back to the initial value in all tested high humidity levels.

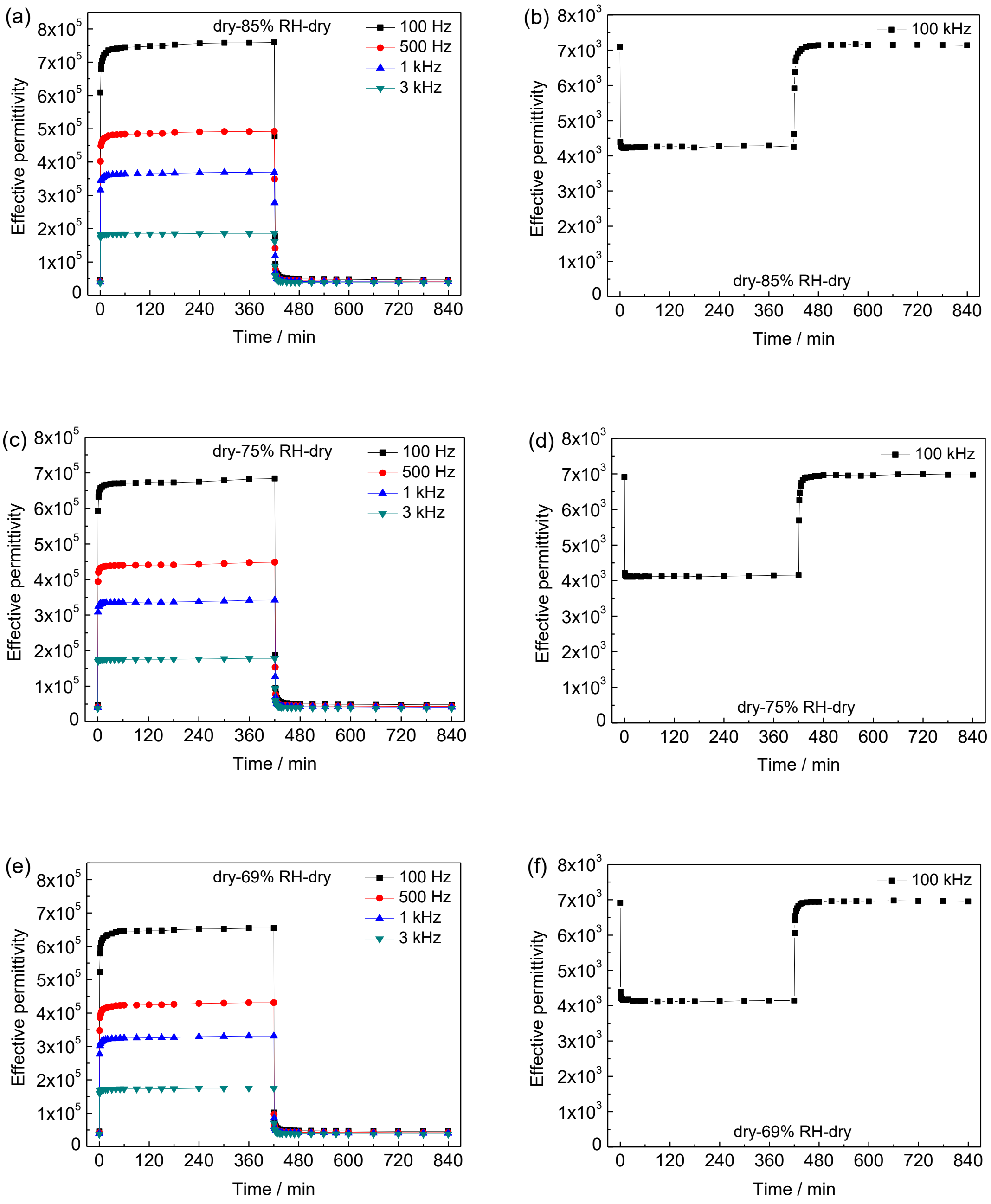

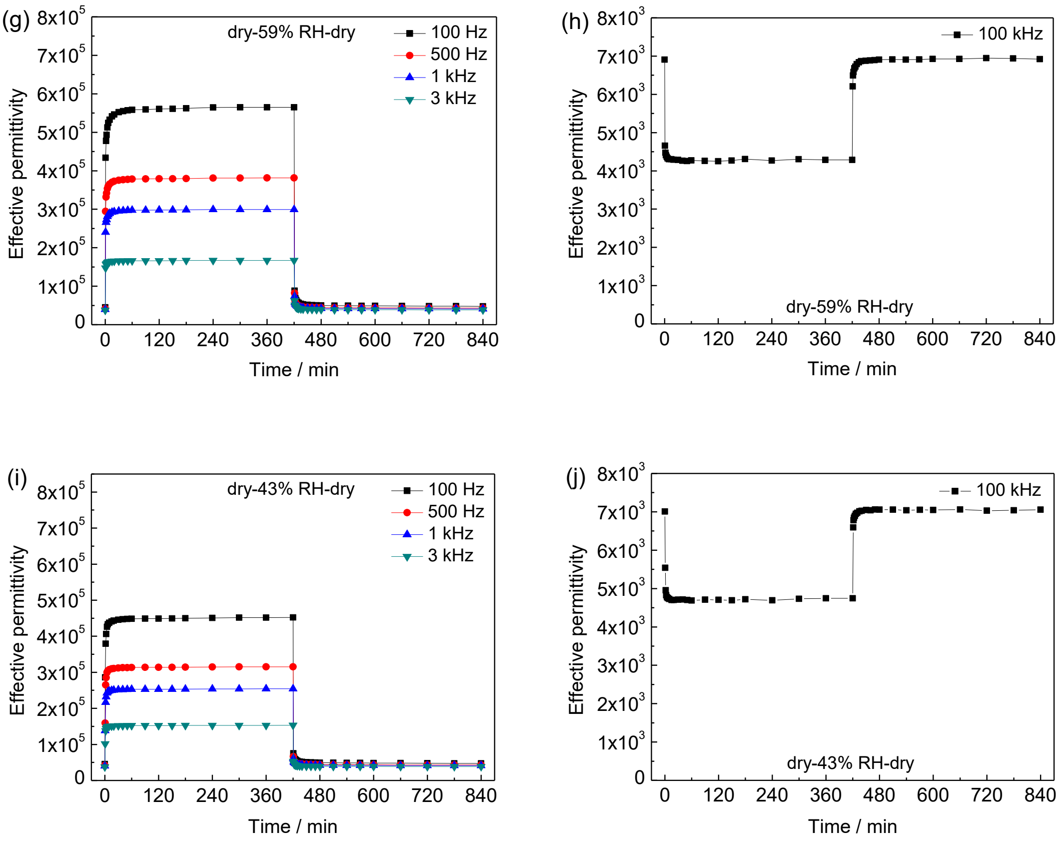

Figure 3.14 Effective permittivity vs time plots of the sample with surface electrodes at selected frequencies of 100, 500, 1k, 3k, and 100k Hz at different humidity testing levels. (a) at 100 - 3k Hz and 85% RH; (b) at 100 - 3 k Hz and 85% RH; (c) at 100 - 3k Hz and 75% RH; (d) at 100 - 3 k Hz and 75% RH; (e) at 100 - 3k Hz and 85% RH; (f) at 100 - 3 k Hz and 85% RH; (g) at 100 - 3k Hz and 85% RH; (h) at 100 - 3 k Hz and 85% RH; (i) at 100 - 3k Hz and 85% RH; (j) at 100 - 3 k Hz and 85% RH.

Figure 3.15 shows one cycle of effective permittivity and dielectric loss vs time plots of the sample with surface electrodes in different humidity testing levels at selected frequencies of 100 Hz - 100 kHz. From Figures 3.15(a), 3.15(c), 3.15(e), 3.15(g), at each selected low frequency (100 Hz - 3 kHz), permittivity increases when increasing humidity and decreases when decreasing humidity in different humidity testing levels. Moreover, permittivity response increases with increasing humidity. However, from Figure 3.15(i), at the high frequency of 100 kHz, permittivity decreases when increasing humidity and increases when decreasing humidity in different humidity testing levels. From Figures 3.15(b), 3.15(d), 3.15(f), 3.15(h), at selected frequencies of 100 Hz, 500 Hz, and 1 kHz, loss decreases when increasing humidity and increases when decreasing humidity. Moreover, at selected frequencies of 100 Hz, 500 Hz, and 1 kHz, loss barely differs much in different humidity testing levels. However, from Figures 3.15(h), and 3.15(j), at selected frequencies of 3 kHz and 100 kHz, loss increases with increasing humidity and decreases with decreasing humidity. Moreover, the loss has a clear distribution in different humidity testing levels. Besides, from Figure 3.15, in one humidity cycle, permittivity and loss of the sample go back to the initial value at all analyzed frequencies.

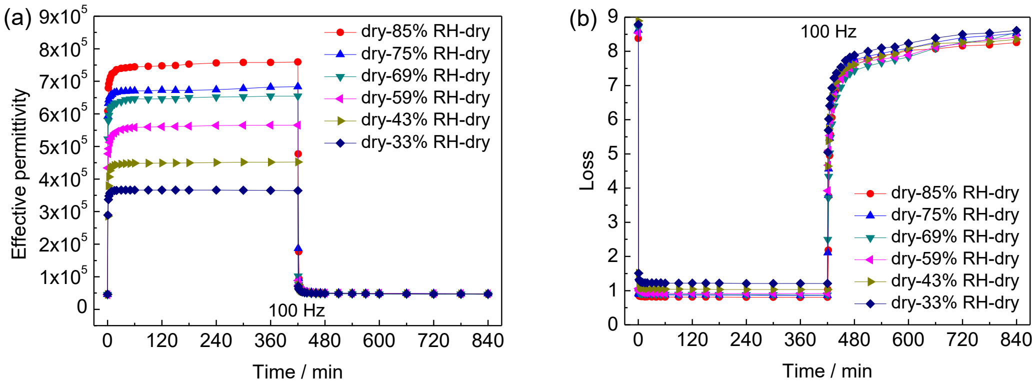

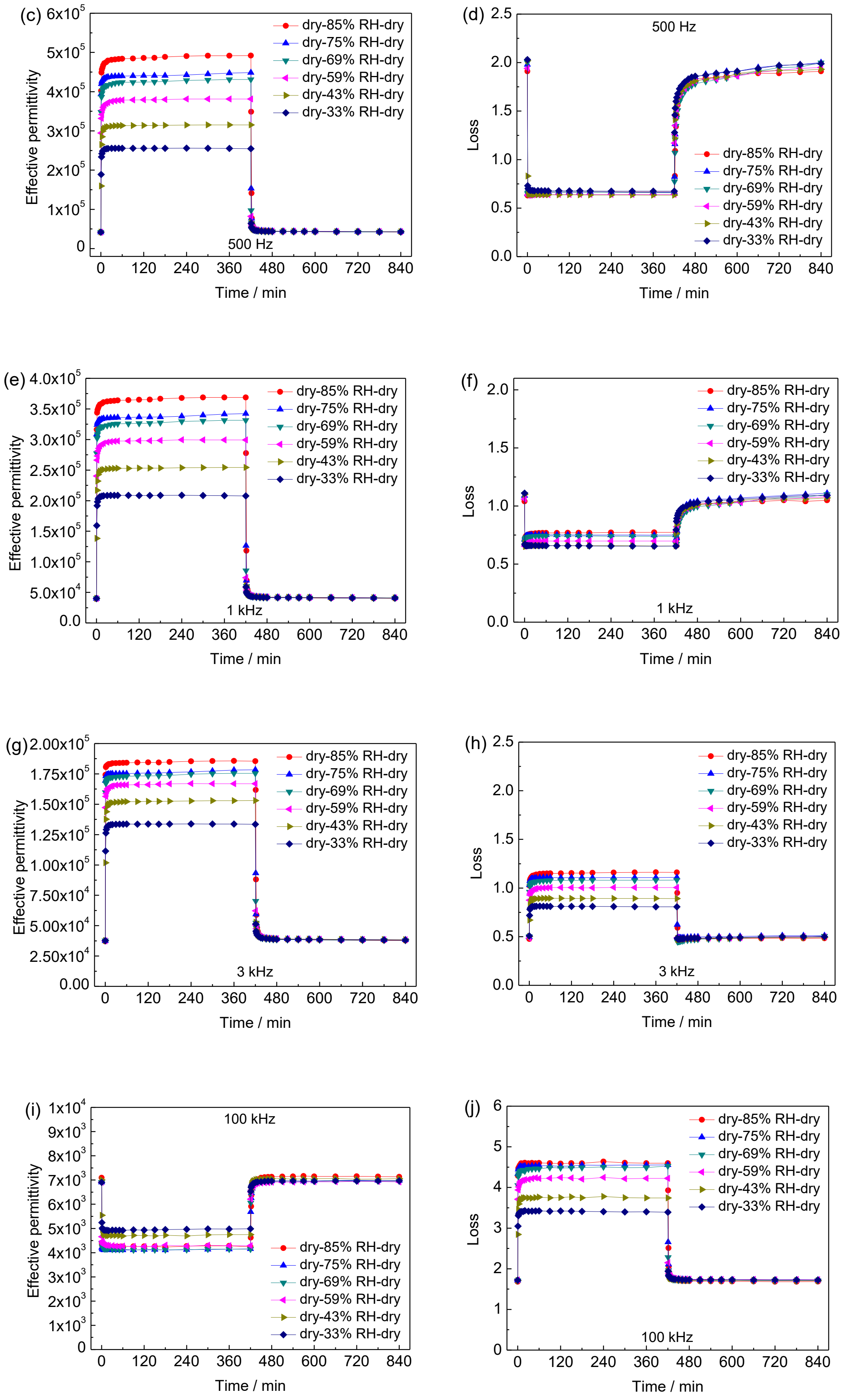
(c)
Effective permittivity
6x10^5
5x10^5
4x10^5
3x10^5
2x10^5
1x10^5
0
500 Hz
Time / min
0 120 240 360 480 600 720 840
dry-85% RH-dry
dry-75% RH-dry
dry-69% RH-dry
dry-59% RH-dry
dry-43% RH-dry
dry-33% RH-dry
(d)
Loss
2.5 2.0 1.5 1.0 0.5 0.0
500 Hz
Time / min
0 120 240 360 480 600 720 840
dry-85% RH-dry
dry-75% RH-dry
dry-69% RH-dry
dry-59% RH-dry
dry-43% RH-dry
dry-33% RH-dry
(e)
Effective permittivity
4.0x10^5
3.5x10^5
3.0x10^5
2.5x10^5
2.0x10^5
1.5x10^5
1.0x10^5
5.0x10^4
0.0
1 kHz
Time / min
0 120 240 360 480 600 720 840
dry-85% RH-dry
dry-75% RH-dry
dry-69% RH-dry
dry-59% RH-dry
dry-43% RH-dry
dry-33% RH-dry
(f)
Loss
2.0 1.5 1.0 0.5 0.0
1 kHz
Time / min
0 120 240 360 480 600 720 840
dry-85% RH-dry
dry-75% RH-dry
dry-69% RH-dry
dry-59% RH-dry
dry-43% RH-dry
dry-33% RH-dry
(g)
Effective permittivity
2.00x10^5
1.75x10^5
1.50x10^5
1.25x10^5
1.00x10^5
7.50x10^4
5.00x10^4
2.50x10^4
0.00
3 kHz
Time / min
0 120 240 360 480 600 720 840
dry-85% RH-dry
dry-75% RH-dry
dry-69% RH-dry
dry-59% RH-dry
dry-43% RH-dry
dry-33% RH-dry
(h)
Loss
2.5 2.0 1.5 1.0 0.5 0.0
3 kHz
Time / min
0 120 240 360 480 600 720 840
dry-85% RH-dry
dry-75% RH-dry
dry-69% RH-dry
dry-59% RH-dry
dry-43% RH-dry
dry-33% RH-dry
(i)
Effective permittivity
1x10^4
9x10^3
8x10^3
7x10^3
6x10^3
5x10^3
4x10^3
3x10^3
2x10^3
1x10^3
0
100 kHz
Time / min
0 120 240 360 480 600 720 840
dry-85% RH-dry
dry-75% RH-dry
dry-69% RH-dry
dry-59% RH-dry
dry-43% RH-dry
dry-33% RH-dry
(j)
Loss
6 5 4 3 2 1 0
100 kHz
Time / min
0 120 240 360 480 600 720 840
dry-85% RH-dry
dry-75% RH-dry
dry-69% RH-dry
dry-59% RH-dry
dry-43% RH-dry
dry-33% RH-dry

Figure 3.15 Effective permittivity/dielectric loss vs time plots of the sample with surface electrodes at different humidity testing levels from 85% RH to 33% RH at selected frequencies. (a) permittivity at 100 Hz; and (b) loss at 100 Hz; (c) permittivity at 500 Hz and (d) loss at 500 Hz; (e) permittivity at 1 kHz and (f) loss at 1 kHz; (g) permittivity at 3 kHz and (h) loss at 3 kHz; (i) permittivity at 100 kHz and (j) loss at 100 kHz.

The study aims to find a suitable humidity sensing frequency of the sensor to achieve a balance between sensitivity and loss while high sensitivity with low loss is preferred. Figure 3.16 shows delta effective permittivity vs relative humidity results of the sample at selected frequencies from 100 Hz to 100 kHz which are calculated from the humidity testing results in Figures 3.15(a), 3.15(c), 3.15(e), 3.15(g), 3.15(i). For the humidity sensor, linear relationships between the delta effective permittivity and relative humidity (RH) are found at selected frequencies from 100 Hz to 100 kHz, respectively, as shown in Figure 3.16(a), 3.16(b), 3.16(c), 3.16(d), 3.16(e). Moreover, as shown in Table 3.2, in the humidity testing range from dry condition to 85% RH, when increasing frequency, humidity sensitivity decreases from 7555 Hz/%RH at the low frequency of 100 Hz to 17.6 Hz/%RH at the high frequency of 100 kHz. And the calculated values of percentage sensitivity to effective permittivity at dry conditions show a similar decreasing trend when increasing frequency. Further, a frequency range with a low loss of the sensor is preferred to be used due to a small energy degradation, which is essential for the ceramics to develop a passive wireless LC resonant humidity sensor.

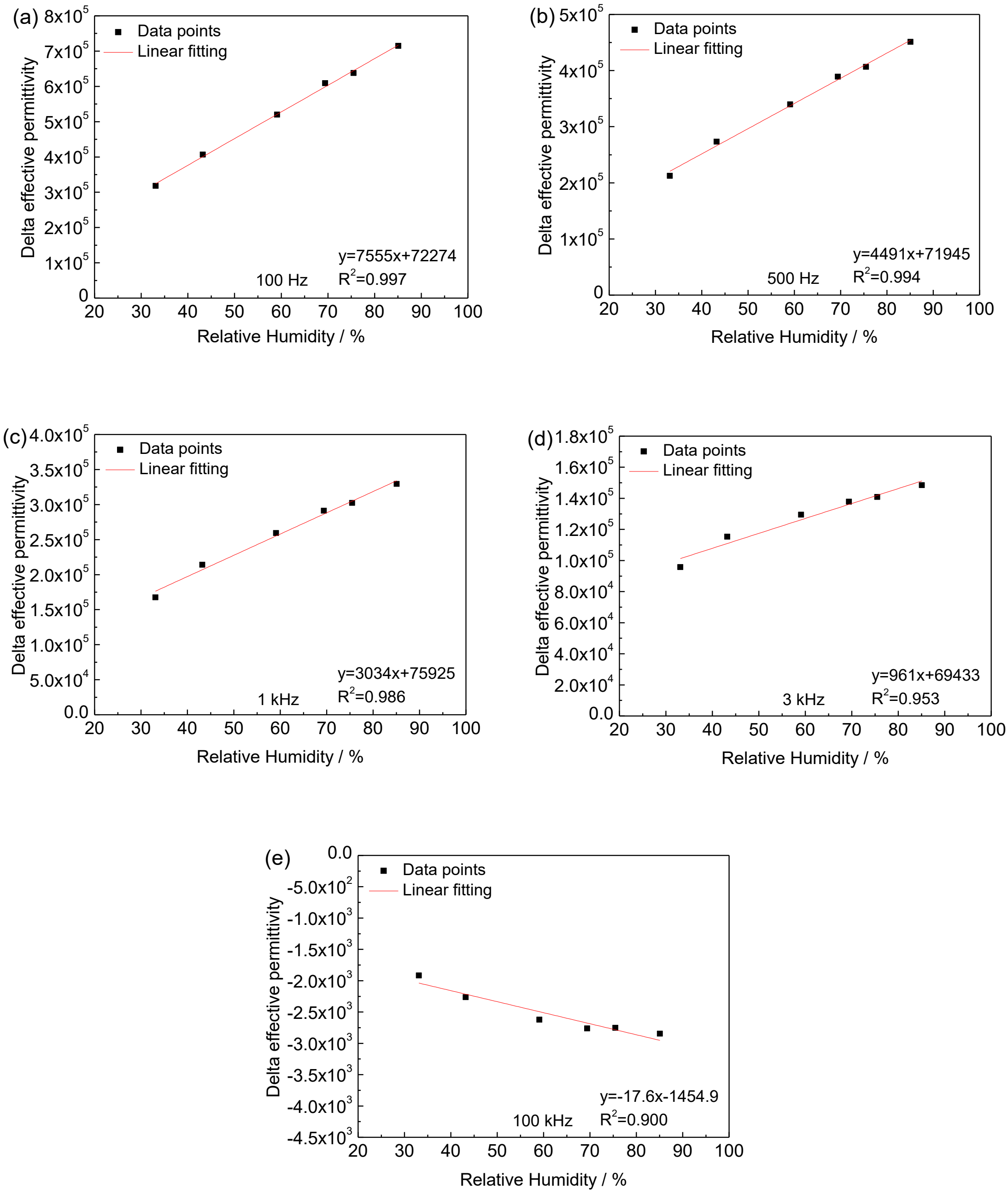

Figure 3.16 Delta effective permittivity vs relative humidity of the sample with surface electrodes and linear fittings at selected frequencies. (a) 100 Hz; (b) 500 Hz; (c) 1 kHz; (d) 3 kHz; (e) 100 kHz.

Loss ranges between the humidity range of dry condition and 85% RH at selected frequencies are shown in Table 3.2, which reveals that low loss ranges can be chosen at the frequency of 500 Hz to 3 kHz. Besides, it reveals that the coefficient of determination, R^2, of the linear fittings decreases with increasing frequency. Therefore, better prediction results of the fitting curves can be obtained at the low frequencies of 100 Hz, 500 Hz, and 1 kHz. In summary, the low-frequency range from 500 Hz to 1 kHz is a preferable candidate range enabling the sensor to have a better overall humidity sensing performance with high sensitivity and low loss.

Table 3.2 Humidity sensitivity and loss at different frequencies.

Frequency / Hz	100	500	1 k	3 k	100 k
Effective permittivity at dry condition	44651	40939	39353	37045	7092
Sensitivity / 1/% RH	7555	4491	3034	961	17.6
Percentage sensitivity respect to effective permittivity at dry condition / 1/% RH	16.9%	11.0%	7.7%	2.6%	0.25%
Loss between dry condition and 85% RH	0.80~8.38	0.67~1.91	0.77~1.04	0.48~1.16	1.68~4.60

3.3.2 Long-time stability of the ceramics humidity sensor

Dielectric ceramics sensor, such as the sensor, is supposed to have good humidity sensitivity, long-time stability, and water-resistant capability, due to its high dielectric permittivity, ceramics rigidity, and structural integrity. Long-time stability is the most important property for the potential applications of humidity sensors. Figure 3.17 shows effective permittivity and dielectric loss vs time plots of the sensor with surface electrodes after about 66-day 33-cycle long-time stability tests in humidity range between dry condition and 85% RH at selected frequencies. As shown in Figure 3.17(a), 3.17(c), 3.17(e), 3.17(g), effective permittivity plots of 33 humidity cycles are exhibited at frequencies of 100 Hz, 500 Hz, 1 kHz, and 3 kHz, respectively. The first 10 humidity cycles reveal a gradual increase of the permittivity response and the last 23 humidity cycles clearly show stable permittivity responses with a small random fluctuation. The same clear trend also can be observed in Figure 3.18(a), which shows the delta effective permittivity of the sensor during long-time stability tests when increasing/decreasing humidity at the frequencies of 100 Hz, 500 Hz, 1 kHz, and 3 kHz. Similarly, as shown in Figure 3.17(b), 3.17(d), 3.17(f), 3.17(h), loss plots of the humidity cycles at frequencies of 100 Hz, 500 Hz, 1 kHz, and 3 kHz also show a gradual decrease of the permittivity response in the first 10 humidity cycles and a stable loss response with a small random fluctuation in the last 23 humidity cycles. The same clear trend can also be observed in Figures 3.18(b), 3.18(c), which show the delta loss of the sensor during long-time stability tests when increasing/decreasing humidity at the same selected frequencies. However, at the frequency of 100 kHz, both permittivity and loss plots show an unclear trend, and the fluctuations of the humidity responses of permittivity and loss are large compared to the total responses. A similar trend is also found in Figures 3.18(d), 3.18(e). Comparing all the permittivity plots and delta permittivity results in Figures 3.17, 3.18, respectively, the humidity responses of the sensor decrease with increasing frequency from 100 Hz to 100 kHz. However, the loss responses of the sensor first decrease from 100 Hz to 1 kHz, and then, increase from 1 kHz to 100 kHz, due to the shift in frequency of the loss spectrum. Besides, comparing the permittivity and loss responses during the last 23 humidity cycles, the stability of the permittivity responses is much better than those of the loss responses. Therefore, permittivity should be primarily used for humidity sensing. In summary, the humidity sensor has a humidity sensing hysteresis in the first 10 humidity cycles, however, after 10 humidity cycles, the sensor reveals a preferable humidity cycle stability during long-time stability tests. The humidity sensor should be pretreated by 10 humidity cycles in 20 days to get rid of its humidity sensing hysteresis where high stability of humidity sensing can be developed.

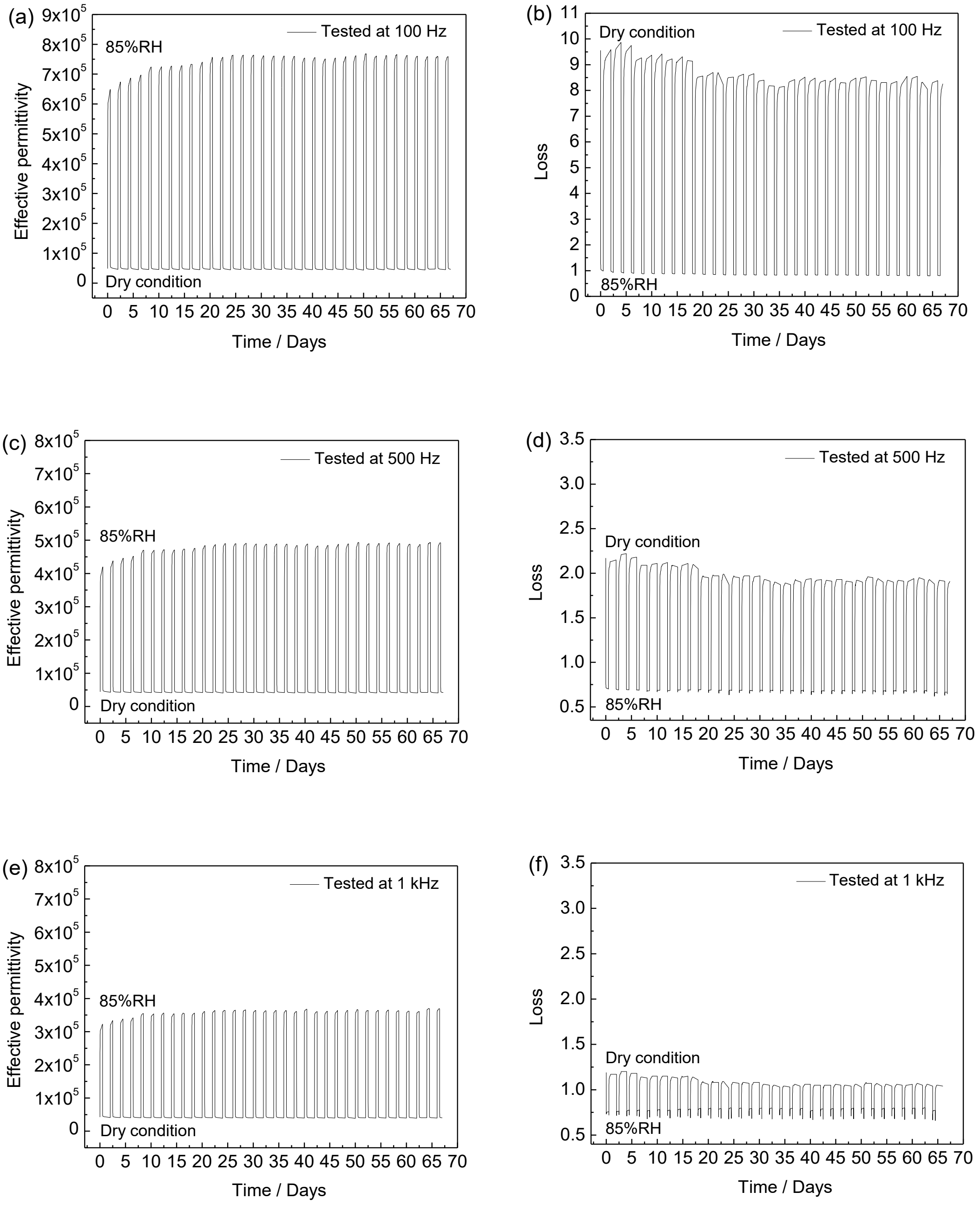

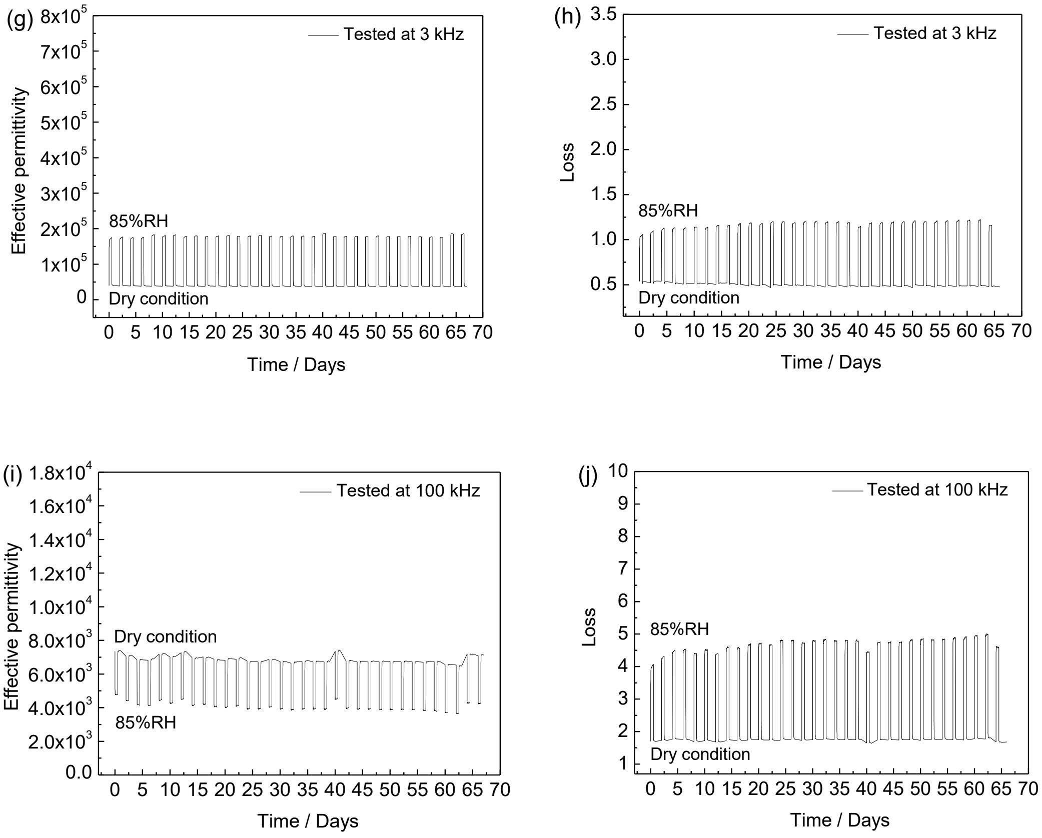

Figure 3.17 Effective permittivity/dielectric loss responses of the sensor of long-time stability tests in humidity range between dry condition and 85% RH at selected frequencies. One humidity cycle is tested in two days. (a) permittivity at 100 Hz; (b) loss at 100 Hz; (c) permittivity at 500 Hz; (d) loss at 500 Hz; (e) permittivity at 1 kHz; (f) loss at 1 kHz; (g) permittivity at 3 kHz; (h) loss at 3 kHz; (i) permittivity at 100 kHz; (j) loss at 100 kHz.

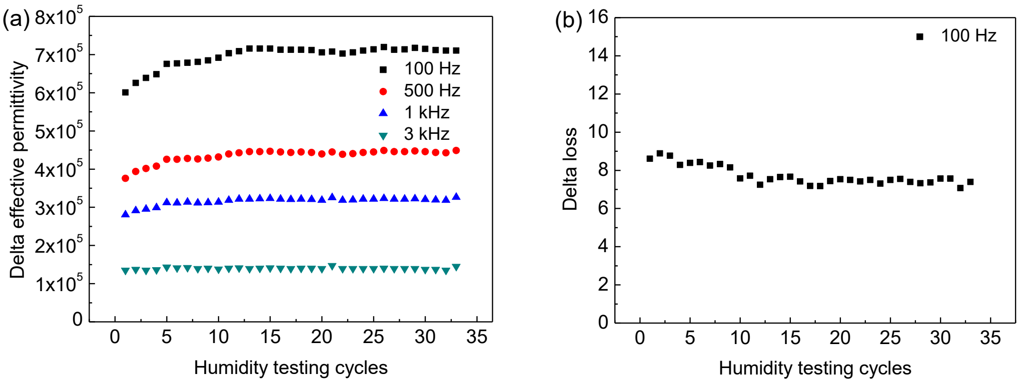

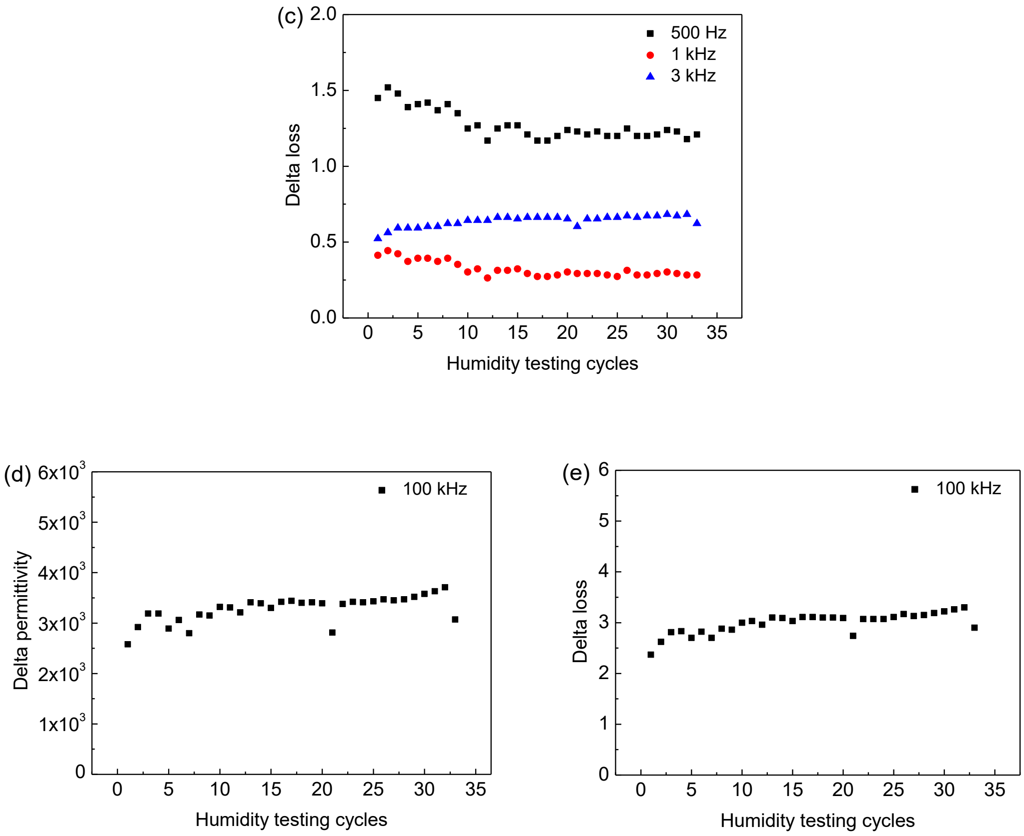

Figure 3.18 Comparison of the delta effective permittivity of the sensor and delta dielectric loss when increasing/decreasing humidity during long-time stability tests at selected frequencies. (a) delta permittivity at 100 Hz, 500 Hz, 1 kHz, 3 kHz; (b) delta loss at 100 Hz; (c) delta loss at 500 Hz, 1 kHz, 3 kHz; (c) delta permittivity at 100 kHz; (d) delta loss at 100 kHz.

3.4 Influences of soils on humidity sensing of high dielectric permittivity ceramics humidity sensor with flat surface electrodes

In agriculture applications, the sensor is supposed to be placed in the soil in the fields. When the sensor with flat surface electrodes is covered by the soil instead of exposed to the air, it might be possible that the effective permittivity spectrum has a little variation, due to that the soil and air have different dielectric permittivity and the electromagnetic waves generated by the capacitor sensor not only pass through the dielectric ceramics material but also pass through the soil or the air.

However, in Section 3.1.4, it has been theoretically proposed in Eq. (3-36) that wherever surrounded by the air or the soils, the effective permittivity (and the measured capacitance) of the sensor with flat surface electrodes is the same/identical, due to the very low permittivity of both the air and the soils compared to the high dielectric permittivity of the dielectric material. Therefore, it is important to experimentally verify this theoretical conclusion.

3.4.1 Dielectric properties of the ceramics humidity sensor with flat surface electrodes in soils

As shown in Figure 3.19(a), the results show that whenever the sensor is exposed to air or placed in/covered by the sand and the top soil, effective permittivity spectrums show identical results in both dry condition and 85% RH, respectively, and from Figure 3.19(b), the identical loss spectrums are also observed in both dry condition and 85% RH, respectively.

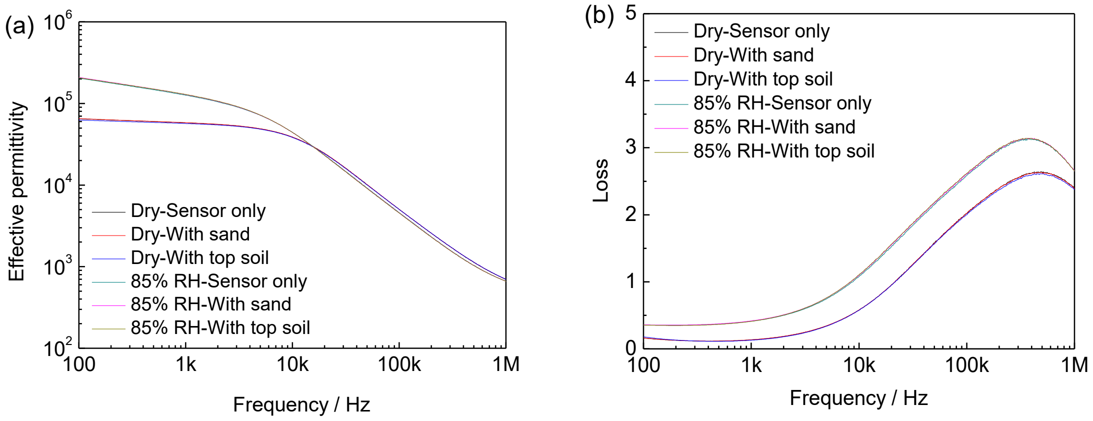

Figure 3.19 Effective permittivity (a) / dielectric loss (b) vs frequency spectrums of the sensor free-standing in the air, covered by the sand, and covered by the top soil at both dry condition and 85% RH.

Figure 3.20 shows, at five selected frequencies, a detailed comparison of dielectric properties on the sensor merely exposed in air, covered by the sand, and covered by the top soil in both dry condition and 85% RH, respectively. For the sensor placed in/covered by three soils in 85% RH, both permittivity and loss at different frequencies exhibit identical values, which implies replacing air with sand or soil has no observable influence on the dielectric properties of the sensor, as shown in Figures 3.20(a), 3.20(b), 3.20(c), 3.20(d). For the sensor placed in all three soils in dry condition, permittivity and loss at different frequencies show almost identical values, which again reveals replacing air with sand or soil has almost no influence on the dielectric properties of the sensor. In summary, based on the verification experiments, it is concluded that, in different humidity conditions, the soils covered on the sensor would not influence the humidity sensing of the sensor, which has been proposed by Eq. (3-36) in Section 3.1.4.

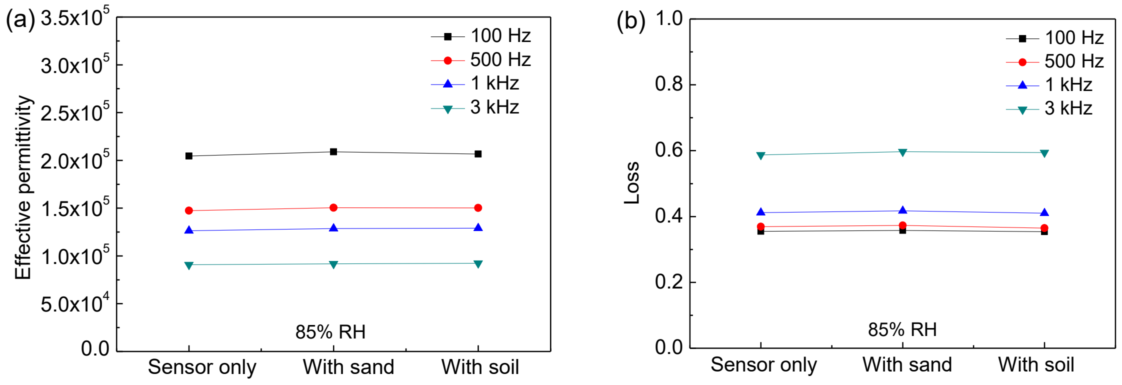

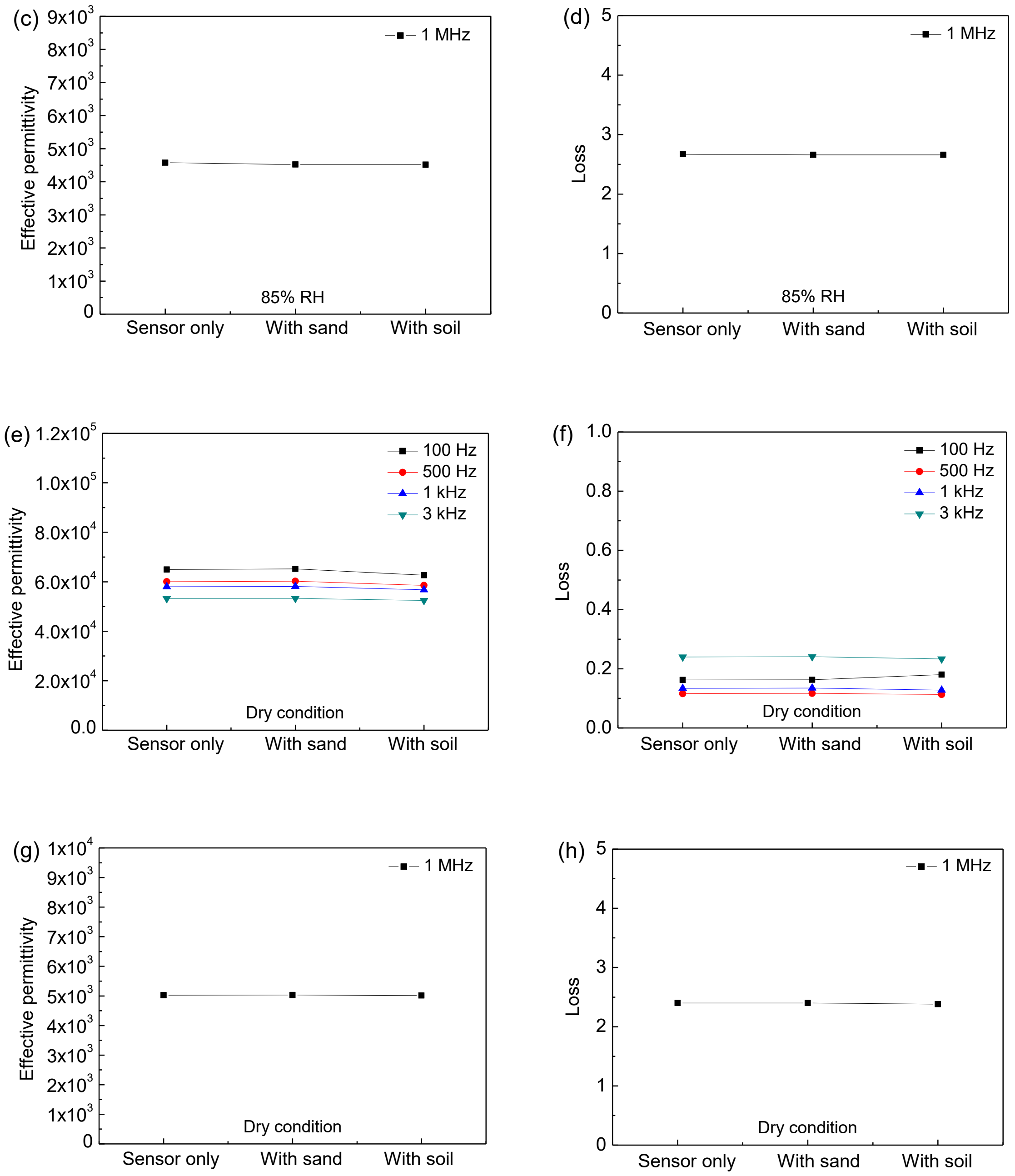

Figure 3.20 Effective permittivity (a) / dielectric loss (b) comparisons among the sensor placed in the air, covered by the sand, and covered by the top soil at different frequencies in both dry condition and 85% RH, respectively. (a) permittivity at 100 - 3k Hz in 85% RH; (b) loss at 100 - 3k Hz in 85% RH; (c) permittivity at 100 kHz in 85% RH; (d) loss at 100 kHz in 85% RH; (e) permittivity at 100 - 3k Hz in dry condition; (f) loss at 100 - 3k Hz in dry condition; (g) permittivity at 100 kHz in dry condition; (h) loss at 100 kHz in dry condition.

3.4.2 Dielectric spectrums of soils and discussions of soil influences on humidity sensing of the high dielectric permittivity ceramics sensor

In the last section, an interesting and useful conclusion has been discovered that the soils covered on the sensor with flat surface electrodes would not influence on humidity sensing of the sensor. To better support the theoretical calculations proposed in Eq. (3-36) in Section 3.1.4, it is necessary to measure the permittivity spectrums of different soils in a wide frequency range.

Before the soil influence measurements, air capacitance has been measured for a purpose of calibration, which is about 41 pF at the low frequency of 100 Hz and 40.3 pF at the high frequency of 1 MHz. By calculation from an equation for the paralleled electrodes, the permittivity is very close to 1, which is the theoretical permittivity of air, as shown in Figure 3.21(a).

Figure 3.21 shows the real permittivity and dielectric loss vs frequency spectrums of air, sand, top soil, and lake soil. For the sand and the two soils, both permittivity and loss decrease with increasing frequency. At the low frequency of 100 Hz, the permittivity of the sand is the largest, probably due to a high content of quartz in the sand. Lake soil has the lowest permittivity among the three soils at 100 Hz. When frequency increases to about 50 kHz, the permittivity of the three soils is around 4 to 5 and decreases very slowly. At the frequency of 1 MHz, the permittivity of the three soils approaches the same value of about 4, which is the intrinsic permittivity of soil. At the low frequency of 100 Hz, the loss of the sand is also the largest, followed by the topsoil and the lake soil. Interestingly, at a frequency of around 3 kHz, a relaxation peak of the sand is observed. It is probably due to a high content of quartz in the sand. At about 40 kHz, the loss of the topsoil starts to be larger than that of the sand, due to a larger decreasing rate of loss of the sand than that of the topsoil. The loss of the lake soil is the lowest at all tested frequency ranges. At the high frequency of 1 MHz, the loss of each soil reaches the lowest values of about 0.06 to 0.18.

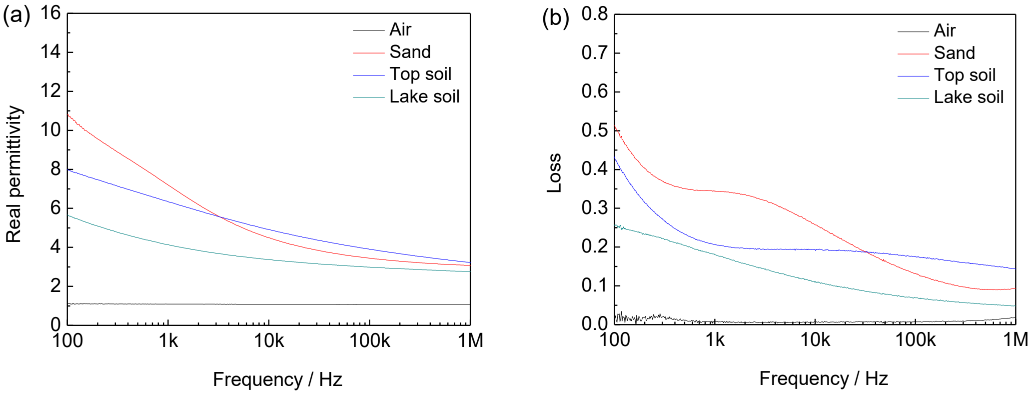

Figure 3.21 Real permittivity (a) / dielectric loss (b) vs frequency spectrums of air, the sand, the topsoil, and the lake soil.

Real/undisturbed soils are more condensed than the loosed soils. Therefore, the compressed soils should have different dielectric property values/spectrums. Figure 3.22 shows the real permittivity and dielectric loss of the sand and the two soils before and after the soil compression process. Both permittivity and loss increase after compression at each measured frequency from 100 Hz to 1 MHz. The reason is that compressed soil has a larger percentage of the soil and a smaller percentage of air between each soil particle. Therefore, compressed soils reveal much closer dielectric properties to the real situation than those of the loosed soils before compression and should be used as the real dielectric properties of the soils. The permittivity values of the compressed soils in the measured frequency range will be used in the following discussion to explain the reason why the medium change would not influence the effective permittivity of the sensor.

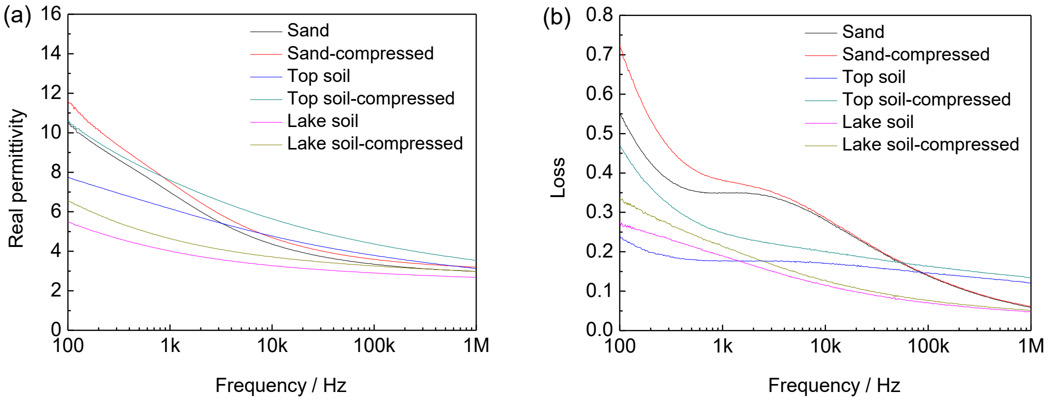

Figure 3.22 Real permittivity (a) / dielectric loss (b) vs frequency spectrums of the sand, the topsoil, and the lake soil before and after compression on the soils.

By analysis of the data from Figure 3.22, percentage increase spectrums of real permittivity and loss of the three soils during compression are calculated, as shown in Figure 3.23. The percentage increases of permittivity and loss of the three soils decrease with increasing frequency. Both permittivity and loss of the topsoil have a higher percentage increase than the other two soils in the low-frequency range. The reason is probably that the topsoil contains larger content of organic matters in an irregular shape and hence, has a much larger compression ratio than the sand and the lake soil. At the high-frequency range, the percentage increase of the permittivity and loss of the three soils reach almost constants, except for the permittivity of the topsoil. It is concluded that compression on the soils has a stable percentage influence on the permittivity and loss in the high-frequency range, however, in the low-frequency range, the magnitude of the influence on the permittivity and loss decreases with increasing frequency.

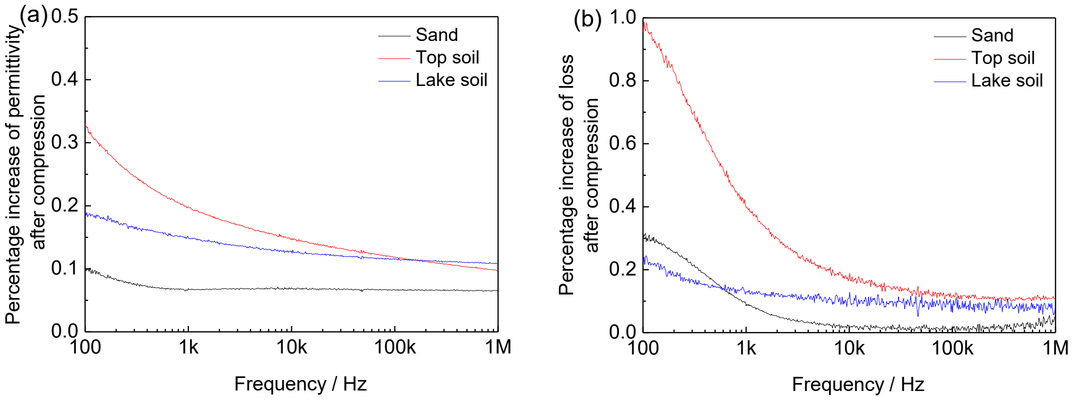

Figure 3.23 Percentage increase (0.1=10%) vs frequency spectrums of real permittivity (a) / dielectric loss (b) of the sand, the topsoil, and the lake soil during compression.

3.5 Conclusions

1. A high dielectric permittivity core-shell BTO-SiO_2 ceramics humidity sensor was developed. The sensor based on capacitance/effective permittivity change corresponding to humidity change has the potential to be used to develop a passive wireless LC humidity resonant sensor to be used in agricultural applications.

2. For the humidity sensor, a linear relationship between the delta permittivity and relative humidity is obtained at different frequencies, respectively. It also has a fast response time of three minutes and a wide detection range from dry condition to 85% RH.

3. The optimized measurement frequency range of the sensor is from 500 Hz to 1 kHz, where a balance of high humidity sensitivity and relatively low loss can be achieved.

4. The permittivity of the ceramic sensor increases in the low-frequency range and decreases in the high-frequency range when the humidity increases. At a certain unique frequency, the permittivity remains unchanged, and hence, this unique frequency could be used for temperature calibration.

5. The ceramics sensor has a long-time humidity testing stability after 10 humidity-cycle treatments in 20 days to eliminate its hysteresis characteristic.

6. It is theoretically analyzed and experimentally verified that the ceramics sensor with flat surface electrodes can be used without any influence from the soils at any frequency in the tested humidity range.

Chapter 4 Dielectric Methodology for Real-time In-situ Disinfectant Sensing in Water

In this study, new dielectric sensing and analyzing methodology was developed to rapidly in-situ detect disinfectants in the water. This dielectric sensing method has many advantages, such as real-time detection, inexpensive, and simple handling over other sensing technologies, such as the reagent method and electrochemical method [26-46,116,117]. The relationship between frequency-dependent dielectric permittivity and the concentration of a common type of disinfectant, NaClO, prepared in four different qualities of the waters in a concentration range from 0 to 200 PPM (parts per million) will be measured and analyzed in the frequency range from 100 Hz to 4 MHz. A changeable electrode distance of the probe and an even wider frequency testing range from 0.1 Hz to 4 MHz will be used for the disinfectant measurements to fundamentally study the dielectric properties of the disinfectants. The newly developed methodology to detect the disinfectant concentration is based on the determination of a characteristic frequency where relaxation of the disinfectant ions occurs in the water and the permittivity of the disinfectant decreases to a constant value of almost the same as that of the pure water in the high frequency. A direct linear relationship will be found between the characteristic frequency and the disinfectant concentration. Moreover, repeatability measurements of different concentrations of the disinfectants and soil influence on the disinfectant sensing will also be studied.

4.1 Experiment procedure

The disinfectant, NaClO, was added in water to make aqueous solutions in different concentrations in the range from 0 to 200 PPM, i.e., 0, 5, 10, 15, 20, 25, 30, 40, 50, 60, 70, 80, 100, 125, 150, 175, 200 PPM. The chemical of the NaClO disinfectant is a 2.5% (w/v) solution provided by LabChem Inc. Four different qualities of water were used to prepare the NaClO aqueous solutions. They were tap water, Nestle bottled water, Dasani bottled water, and deionized (D.I.) water. The prepared disinfectant solutions were placed into glass beakers for the dielectric measurements.

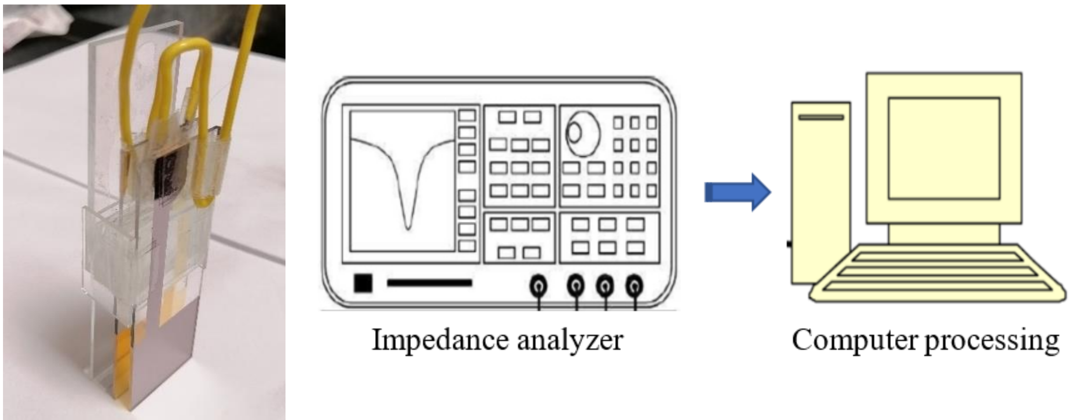

Figure 4.1 Picture of the sputtered Au/Cr/glass electrodes as the probe for dielectric sensing on the NaClO disinfectant concentration in the water (a), and schematics of the precision impedance analyzer and the computer to measure, transform and record the capacitance (C_p) and dielectric loss (D) spectrums (b).

As shown in Figure 4.1(a), a pair of paralleled gold electrodes sputtered on the glass slides (200 nm Au / 5 nm Cr / 1 mm glass) in the dimension of 25 mm × 25 mm with a constant distance of 3 mm was used as the probe. The gold electrodes of the probe were connected to the precision impedance analyzer (Agilent 4294A), respectively, as shown in Figure 4.1(b) and Figure 4.2. The probe was completely immersed in the NaClO disinfectant in the glass beaker, as shown in Figure 4.2. The impedance of the NaClO disinfectant in different concentrations prepared by four the water in four different qualities was measured by the impedance analyzer in the frequency ranging from 100 Hz to 4 MHz. The impedance spectrums were calculated and transformed to capacitance (C_p) and dielectric loss (D) by the precision impedance analyzer and recorded on the computer.

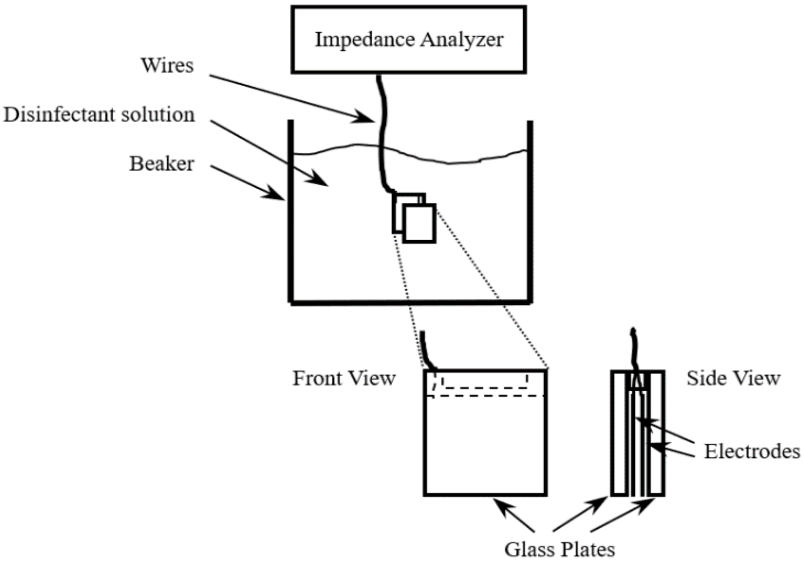

Figure 4.2 Schematic of the dielectric sensing system for real-time in-situ measurement of the dielectric spectrums of the NaClO disinfectant solutions prepared by the waters.

A modified probe with a changeable electrode distance consisting of the same Au/Cr/glass electrodes (200 nm Au / 5 nm Cr / 1 mm glass) in the dimension of 25 mm × 25 mm (as mentioned in the last paragraph) paralleled with each other was developed. The electrode distances of the probe of 2 mm, 3 mm, 4 mm, and 5 mm were used. The precision impedance analyzer (Agilent 4294A) and the low-frequency impedance analyzer (Solartron 1260) were used to connect to the probe, respectively, for the dielectric measurements. By using these two impedance analyzers, a wide frequency measurement range (0.1 Hz - 4 MHz) was covered. The probe was completely immersed in the NaClO disinfectant in the glass beaker, as shown in Figure 4.2. The impedance of the NaClO disinfectants in different concentrations (i.e., 0, 5, 25, 50, 100, 200 PPM) prepared by the tap water was measured by the probe in four different electrode distances in a wide frequency range from 0.1 Hz to 4 MHz, respectively. The impedance spectrums were calculated and transformed to capacitance (C_p) and dielectric loss (D) by the precision impedance analyzer and recorded on the computer.

The probe with the paralleled Au/Cr/glass electrodes (200 nm Au / 5 nm Cr / 1 mm glass) in the dimension of 25 mm × 25 mm with a constant distance of 3 mm was used. The precision impedance analyzer (Agilent 4294A) was used for the dielectric measurements, which were connected to the probe. Five-time repeatability tests of the impedance of the NaClO disinfectants in different concentrations (0, 5, 25, 50, 100, 200 PPM) prepared by the tap water were conducted in the frequency range from 100 Hz to 4 MHz. The impedance spectrums were calculated and transformed to capacitance (C_p) and dielectric loss (D) by the impedance analyzers and recorded on the computer.

Figure 4.3 The tap water mixed with different masses of sand and topsoil containing organic matters. (a) The mass of 0.05g, 0.5g, and 5g of the sand (on the top) and the topsoil (on the bottom) are shown from the left to the right, respectively; (b) the tap water (200 mL) is mixed with the sand (on the top) and the topsoil (on the bottom) in mixing ratios (w/v) of 0.025%, 0.25%, and 2.5%, respectively.

Experiments of the sand/topsoil influence on the dielectric spectrums of the tap water were conducted. As shown in Figure 4.3, the sand and topsoil containing organic matters were weighed in the mass of 0.05 g, 0.5 g, and 5 g, respectively. 200 mL tap water was prepared to be mixed with each mass of the sand/topsoil by 10 min stir and 10 min precipitation, respectively. The mixing ratios (w/v) of the sand/topsoil and the tap water were 0.025%, 0.25%, and 2.5%, respectively. After precipitation, the mixed solutions were placed in glass beakers for dielectric measurements by using the probe with an electrode distance of 3 mm. The probe was connected to the precision impedance analyzer (Agilent 4294A).

4.2 Description of the dielectric sensing and analyzing methodology

The permittivity of pure water is about 80, owing to the water molecules having dipole moment and the polarization ability of the water can be observed under AC electric field. The ionic dipoles in the disinfectant solution change their orientation (reorient) under AC electric field at low frequencies, resulting in a high capacitance/dielectric permittivity which can be detected by the probe with the paralleled electrodes connecting to an electronic analyzing device, such as an impedance analyzer. Due to the difference in the permittivity spectrums of the disinfectant in different concentrations prepared by the water, it can be used to detect the chemicals, such as the disinfectant, as shown in Figure 4.4.

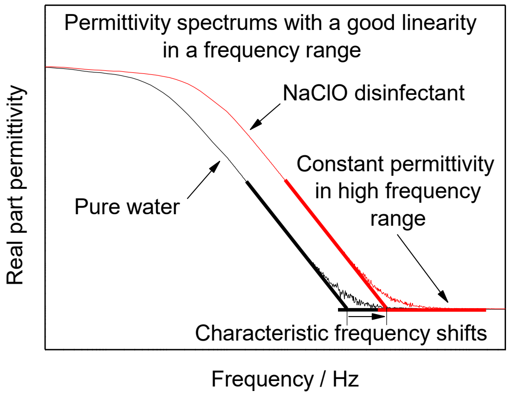

Figure 4.4 Schematic description of the dielectric sensing and analyzing methodology based on the frequency dependence of the real part permittivity of the disinfectants in different concentrations.

It has been noted that a US patent has a visional claim of a dielectric sensing method to detect the chemical concentration in a dielectric liquid. That is, the real permittivity has a close to a linear relationship with the chemical concentration in a dielectric liquid, such as a disinfectant in water [118].

However, this method has two major issues which cannot be handled/solved by this US patent. First, this US patent visionary claims that the real permittivity of the dielectric liquid has a linear relationship with the concentration of the chemical. But based on our measurement and analyzed results, as shown in Figure 4.5 and Figure 4.6, the permittivity of the disinfectants versus disinfectant concentration has a (close to) linear relationship at a certain middle frequency range and could not be applicable at either low-frequency or high-frequency ranges. This confirmatory analysis is contradictory to the application to the whole frequency range claimed by the patent [118]. It can be observed in Figure 4.6 that, at the low-frequency range (lower than 37 Hz), the permittivity has a close to a linear relationship with the concentration at first, and then, gradually saturate at high concentration. At the high-frequency range (1 kHz - 400 kHz), the permittivity has a close to saturated status with the concentration at first, and then, changes to a linear relationship with the concentration. Only in the middle frequency range, the permittivity has a close to a linear relationship with the concentration.

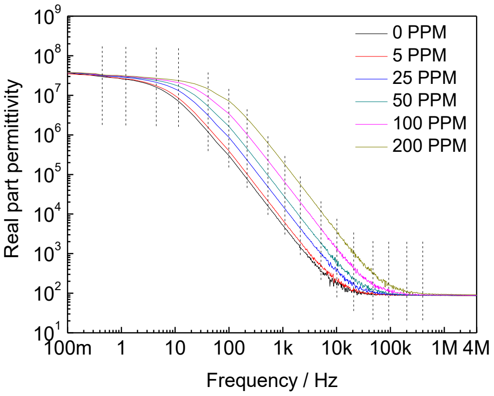

Figure 4.5 Dielectric real permittivity spectrums of the disinfectants (0-200 PPM) measured by a paralleled electrode probe at a wide frequency range from 0.1 Hz to 4 MHz. Based on the vision of the dielectric liquid detection method at a single frequency illustrated by a US patent [118], at some selected frequencies, real part permittivity measured at different concentrations is analyzed, where the analyzed results are shown in the next figure.

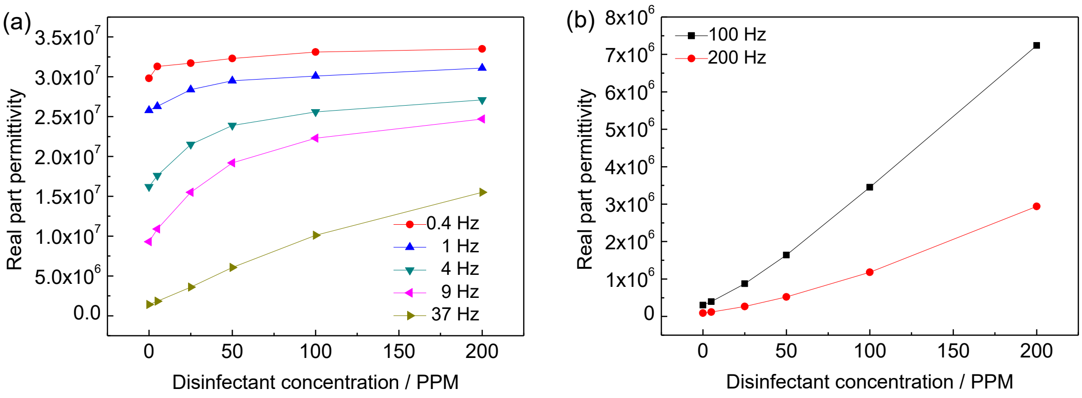

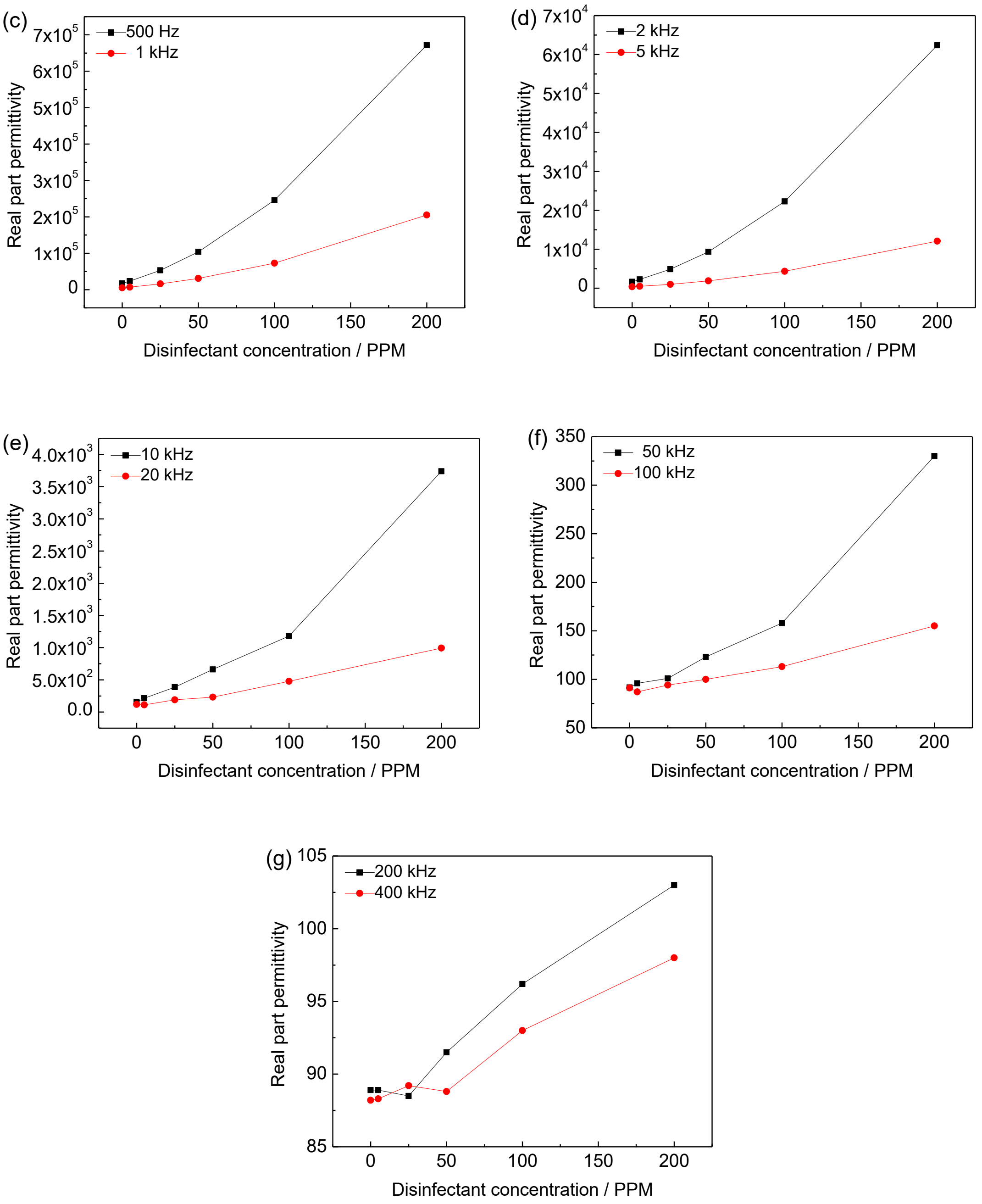

Figure 4.6 Dielectric real permittivity spectrums of the disinfectants (0-200 PPM) measured by a paralleled electrode probe at a wide frequency range from 0.1 Hz to 4 MHz. Based on the vision of the dielectric liquid detection method at a single frequency illustrated by the US patent [118], at some selected frequencies, the relationship between real part permittivity and disinfectant concentration measured at different selected frequencies from 0.1 Hz to 400 kHz, which is the visional method to detect the chemical concentration at a selected frequency

illustrated by the US patent [118]. (a) Permittivity at 0.4 Hz to 37 Hz; (b) permittivity at 100 Hz to 200 Hz; (c) permittivity at 500 Hz to 1 kHz; (d) permittivity at 2 kHz to 5 kHz; (e) permittivity at 10 kHz to 20 kHz; (f) permittivity at 50 kHz to 100 kHz; (g) permittivity at 200 kHz to 400 kHz.

Second, a mixing of a substance, such as air bubbles or soils (having a very low permittivity) in the disinfectant/water would result in a false reading of the chemical concentration due to a decrease of the entire permittivity spectrum while mixing with the low permittivity substances [118]. Hence, how the issues could be eliminated by our newly developed approach will be discussed in Section 4.7. In summary, this dielectric method described in the previous patent could not be used to have a reasonable/satisfactory result to detect the chemicals, for example, the disinfectant. A detailed analysis of the sensing of the disinfectant will be discussed later.

To solve the above issues illustrated, according to the characteristics of the dielectric permittivity spectrums of the disinfectants (prepared by the water) in various concentrations, as shown in Figure 4.4, new dielectric sensing and analyzing methodology is proposed, where the illustrated issues can be properly solved. For the disinfectants in different concentrations, the permittivity decreases with the frequency increases until the permittivity decreases to a constant at a certain frequency of about 10 kHz to 100 kHz. This frequency is defined as the characteristic frequency (at the characteristic point) of the aqueous solution prepared by a certain quality of water in a certain concentration of the disinfectant.

Interestingly, in the low-frequency range, the permittivity decreases with increasing frequency in a linear relationship by their logarithm scales. The permittivity at a relatively high frequency, where a constant permittivity value is obtained, is the base permittivity of the disinfectant. This constant permittivity value is very close to the pure water permittivity in a constant value of about 80. Above all, as shown in Figure 4.4, it is revealed that the characteristic frequency can be calculated by the intersection of the two lines (the linear/straight line at the low frequency and the horizontal line of a constant permittivity at the high frequency). These two lines are the extension line of the linear fitting curve of the logarithm real permittivity vs logarithm frequency and the extension line of the constant of the permittivity value at the high-frequency range, respectively.

4.3 Dielectric spectrums of the disinfectants prepared by different qualities of water and the relation between the characteristic frequency and disinfectant concentration

4.3.1 Dielectric spectrums of the disinfectants prepared by different qualities of water

Figure 4.7 shows the frequency dependences of the real dielectric permittivity of the NaClO disinfectants prepared by four waters in different qualities and their correspondent dielectric loss. For each water measured at low frequency, when the NaClO concentration increases, the real permittivity increases. For each disinfectant and each water prepared, when frequency increases, dielectric permittivity decreases. A linear relation between the permittivity and frequency is observed in the frequency range from about 100 Hz to 1 kHz in the tested NaClO concentrations prepared by the tap water, Nestle bottled water, and Dasani bottled water. The disinfectants prepared with D.I. water also show linear relations between the permittivity and frequency in the frequency range from about 100 Hz to 1 kHz in most of the tested NaClO concentrations except for the pure D.I. water (0 PPM). When the permittivity decreases to a constant value of about 80, i.e., the base permittivity of the water, the characteristic frequency of the NaClO disinfectant can be obtained, which is from 10 kHz for the three pure waters (i.e., the tap water, Nestle bottled water, and Dasani bottled water) to 100 kHz for the NaClO disinfectants in 200 PPM. It is observed that water quality influences the dielectric permittivity and the characteristic frequency at the same disinfectant concentration, especially for the D.I. water. Dasani bottled water and Nestle bottled waters in 0 PPM, which are known for their high quality with less residual ions, exhibit lower real permittivity compared with the permittivity of the tap water. However, for all disinfectants, as the frequency increases, the permittivity is very rough when the permittivity decreases to close to the base permittivity that the characteristic frequency could not be directly determined on the permittivity spectrums. However, at a high disinfectant concentration, the real permittivity prepared by the four waters is almost identical.

From Figure 4.8, the dielectric loss vs frequency spectrums show a loss peak for each NaClO concentration and each prepared water, which implies a significant relaxation of Na^+ and ClO^- in water at about the same characteristic frequency observed from the permittivity spectrums in Figure 4.7. It also can be observed that the loss peak increases with increasing NaClO concentration for each water, which reveals that the characteristic frequency increases with increasing NaClO concentration and is identical to the results obtained from the permittivity spectrums. It should be mentioned that the highly rough loss peaks are probably caused by the very small phase angle detected by the impedance analyzer, which reveals a close to pure resistance state is developed in this frequency range.

As is briefly mentioned in the last section, by analyzing the real permittivity and loss spectrums, the mechanism might be that the ionic dipoles in the disinfectant solution change their orientation (reorient) under AC electric field at low frequencies which results in a high real dielectric permittivity detected by the probe with the paralleled electrodes. However, the thermal vibration of the water molecules counter-reacts with the reorientation of the ionic dipoles in the solution at room temperature. When the frequency of the AC electric field increases, the time to form the ionic dipoles decreases, and the water molecules' counter-reacting effect to disorientate against the reoriented ionic dipoles under the electric field grows and begins to dominate. Therefore, the real permittivity of the disinfectant solution decreases with increasing frequency. At a middle frequency where the permittivity decreases to constant values close to that of the pure water, the relaxation of the reorientation of the ionic dipoles occurs, which implies the frequency is fast enough to eliminate the contribution of the reorientation of the ionic dipoles in the dielectric (disinfectant) solution. The constant permittivity at a relatively high-frequency range for the disinfectants in different concentrations reveals the first issue of the previous patent, that is, at one chosen frequency in the entire frequency range, the chemical concentration corresponding to the dielectric permittivity of the chemical solution probably is not a correct description [118]. Moreover, the loss spectrums also show a similar relaxation process where high loss peaks are observed (in Figure 4.8).

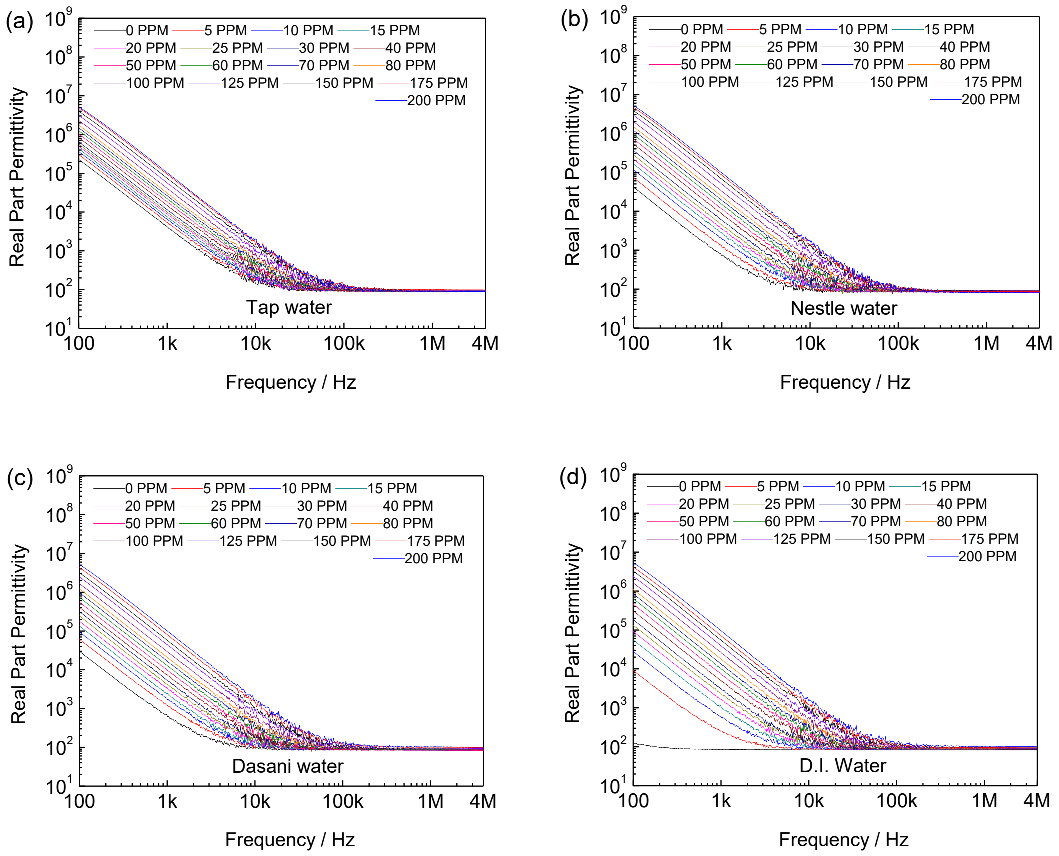

Figure 4.7 Frequency dependences of the real part dielectric permittivity of the NaClO disinfectant solutions prepared by different qualities of water. (a) Tap water; (b) Nestle bottled water; (c) Dasani bottled water; (d) D.I. water.

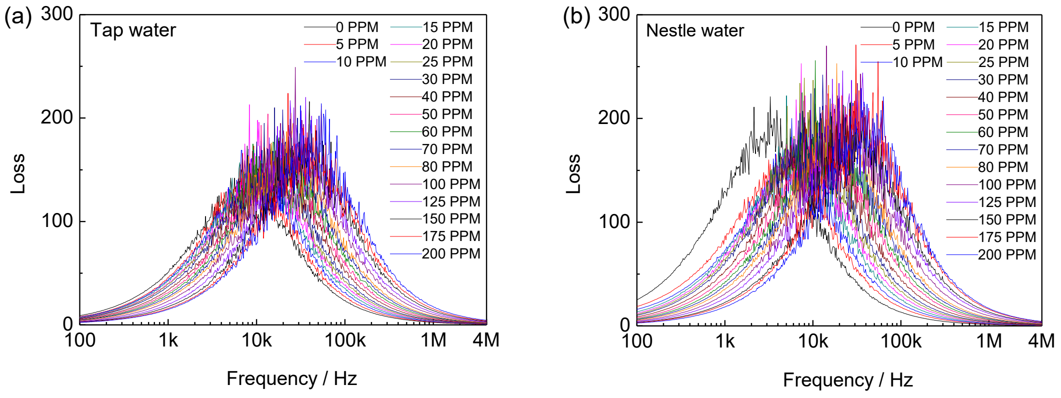

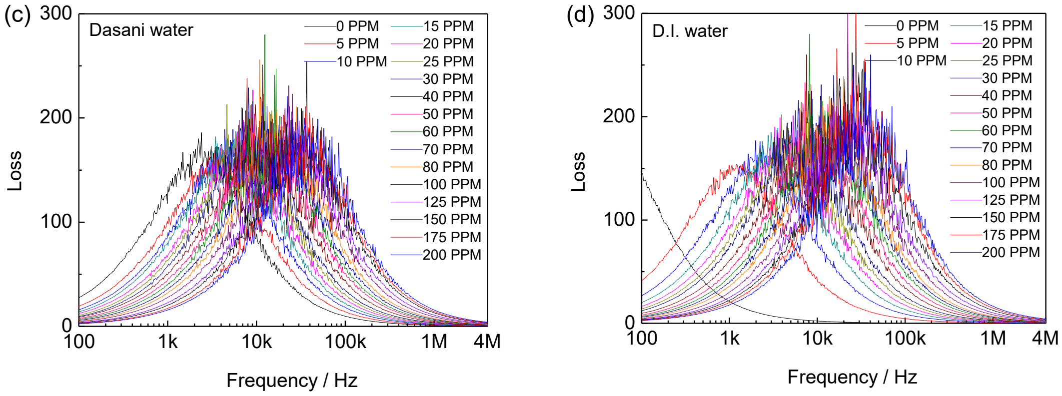

Figure 4.8 Frequency dependences of the dielectric loss of the NaClO disinfectant solutions prepared by different qualities of water. (a) Tap water; (b) Nestle bottled water; (c) Dasani bottled water; (d) D.I. water.

Imaginary dielectric permittivity spectrums of the NaClO disinfectants prepared by different qualities of water are shown in Figure 4.9. The imaginary permittivity decreases with increasing frequency for all disinfectants prepared in different waters. Moreover, all the imaginary spectrums show the linear relationships between the logarithm imaginary permittivity and the logarithm frequency. Further, the imaginary permittivity increases with increasing the concentration of the disinfectant. Besides, the imaginary permittivity spectrums are also different for different qualities of the waters due to different concentrations of the residue ions in the waters. Hence, the imaginary permittivity could also be used for sensing the disinfectant at some selected frequencies.

It is known that the imaginary permittivity spectrums are related to the conductivity which is caused by the disassociation of the NaClO disinfectant into Na^+ and ClO^- in the water. Specifically, the disassociated ions in the water are accelerated under AC testing voltage in a direction parallel to the AC electric field, however, they collide with the thermal vibrated water molecules and lose speed, which results in a suppression of the ions to move and attach to the electrode for the reading of the impedance analyzer. Only small numbers of the ions attach to the electrode and contribute to the increase of the imaginary permittivity/conductivity. As shown in Figure 4.10(a), the conductivity increases with increasing disinfectant concentration. Hence, the phenomenon is ion concentration-dependent. The reason is probably that, as the NaClO disinfectant concentration increases, more ions are accelerated under the AC testing voltage and there is more chance for the ions to attach to the electrodes to contribute to the conductivity. Figure 4.10(b) reveals the residual ions that existed in the pure waters in different water qualities also influence the conductivity. Therefore, considering both the water quality and the added disinfectant, the classical conductivity linear equation to describe the behavior of the non-ideal conduction of the disinfectants is shown below:

$$\sigma_{total} = \sigma_{residual} + \sigma_{dis} = N_{residual} \cdot \mu_{residual} \cdot e_{residual} + N_{dis} \cdot \mu_{dis} \cdot e_{dis} \qquad (4\text{-}1)$$

where σ_{totle} is the total conductivity of the disinfectant; $\sigma_{residual}$ is the residual conductivity of the pure water; σ_{dis} is the conductivity of the NaClO disinfectant with the disassociated ions of Na^+ and ClO^-; $N_{residual}$ is the number of the residual ions in the pure water; $\mu_{residual}$ is the average mobility of the residual ions in the pure water; $e_{residual}$ is the average charge of the residual ions in the pure water; N_{dis} is the number of pairs of Na^+ and ClO^- in the disinfectant; μ_{dis} is the mobility of a pair of Na^+ and ClO^- in the disinfectant; e_{dis} is the charge of the ions for a pair of Na^+ and ClO^- in the disinfectant.

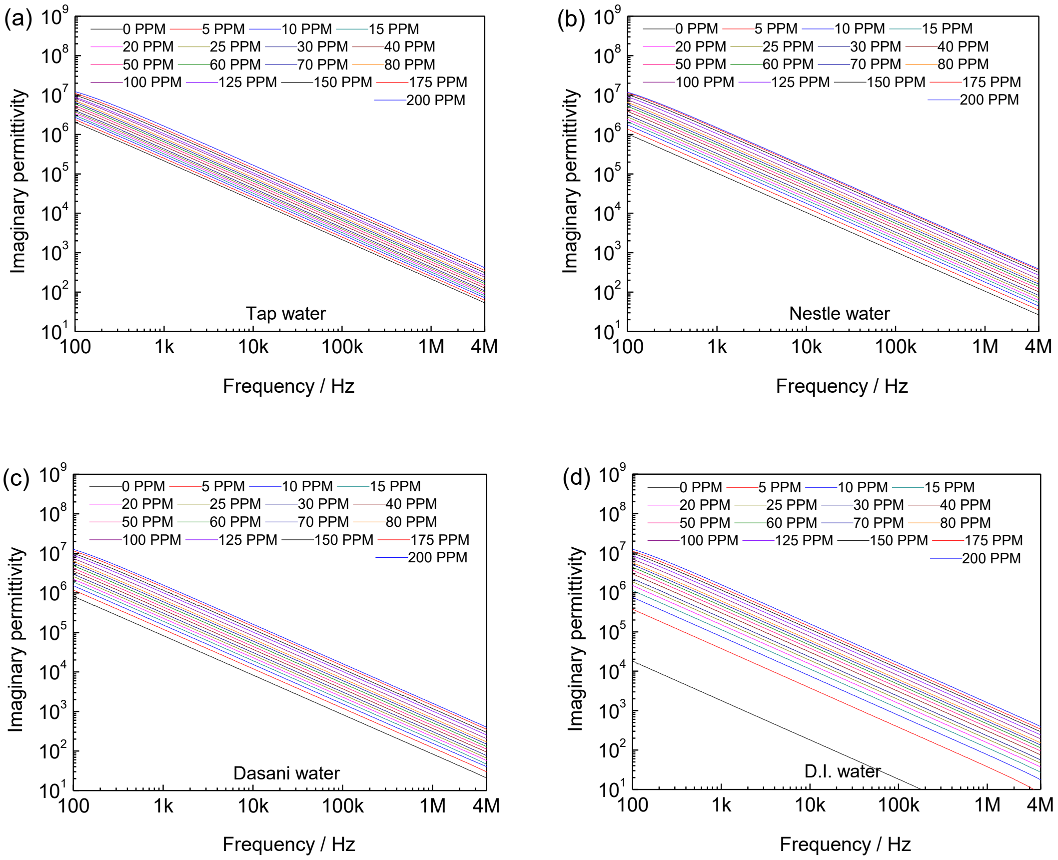

Figure 4.9 Frequency dependences of the imaginary part dielectric permittivity of the NaClO disinfectant solutions prepared by different qualities of water. (a) Tap water; (b) Nestle bottled water; (c) Dasani bottled water; (d) D.I. water.

Interestingly, the conductivity almost remains the same at different frequencies, except for a little decrease at the frequency lower than 500 Hz and a sharp decrease for the D.I. water at the frequency higher than 1 MHz. The mechanism of the sharp decrease for the D.I. water at high frequency is unclear. It reveals that the conductivity of the disinfectants is almost independent of the testing frequency in the wide frequency range from 500 Hz to 1 MHz, whereas, the real permittivity, which implies the dielectric property of the disinfectant, is highly dependent on the testing frequency, especially in the low-frequency range. By observation at different frequencies, although there are the conductivities at different disinfectant concentrations, the trend of the real permittivity spectrum changing with the disinfectant concentration is different from the trends of the conductivity and the imaginary permittivity. Therefore, the dielectric behavior and the conductivity of the disinfectant are two physical mechanisms that existed simultaneously under AC testing voltage.

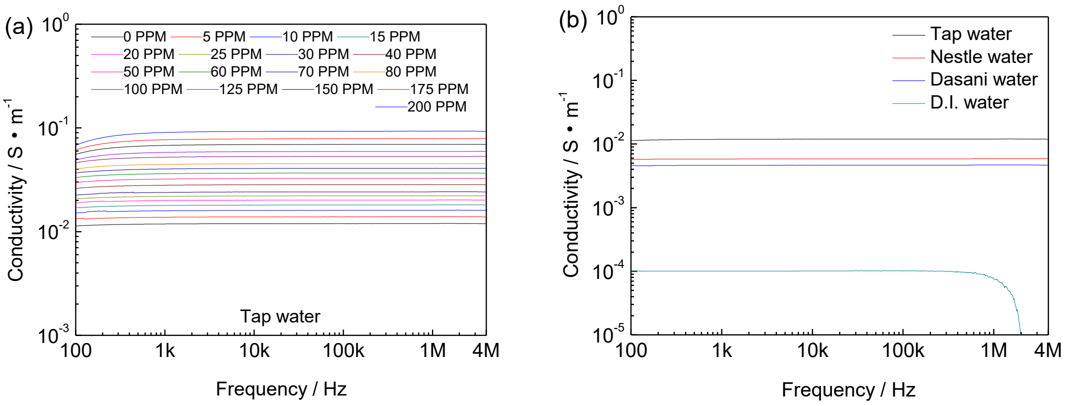

Figure 4.10 Comparison of the frequency dependences of the conductivity. (a) Comparison of different concentrations prepared by the tap water; (b) comparison of four pure waters (0 PPM).

4.3.2 The relation between the characteristic frequency and disinfectant concentration

To calculate the characteristic frequency of the disinfectants in different concentrations prepared by different waters, real permittivity spectrums in Figure 4.7 are used. However, the linearity of the real permittivity spectrums at the whole low-frequency range seems not all consistent. Hence, an investigation is conducted to find the linear range of the logarithm real permittivity vs the logarithm frequency spectrums by calculating the differential of the logarithm real permittivity on the logarithm frequency. The calculated differential spectrums of the disinfectants in some concentrations prepared by four waters are shown in Figures 4.11, 4.12, 4.13, 4.14, respectively. A common trend of the spectrums is observed and the average values between the fluctuated spectrums are plotted in black lines. At a low-frequency range and a high-frequency range, two constant values can be found, respectively. The constant at the low-frequency range shows the linear range of the logarithm real permittivity vs the logarithm frequency spectrums. The constant at the high-frequency range shows the (constant) real permittivity of the water at high frequency. Table 4.1 summarizes the linear ranges of the logarithm real permittivity vs logarithm frequency spectrums of the disinfectants in different concentrations prepared by four waters. Interestingly, the logarithm real permittivity of the disinfectants has a common linear range, however, the logarithm frequency does not. It seems that, at different disinfectant concentrations, the real permittivity spectrums are shifted in the direction of the frequency axis. In summary, the (common) linear fitting range for all disinfectant concentrations and all waters can be determined from 3.90 to 4.65.

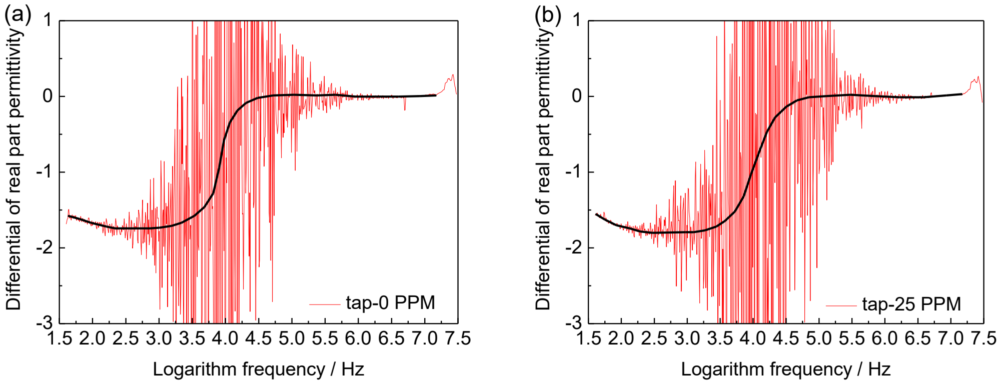

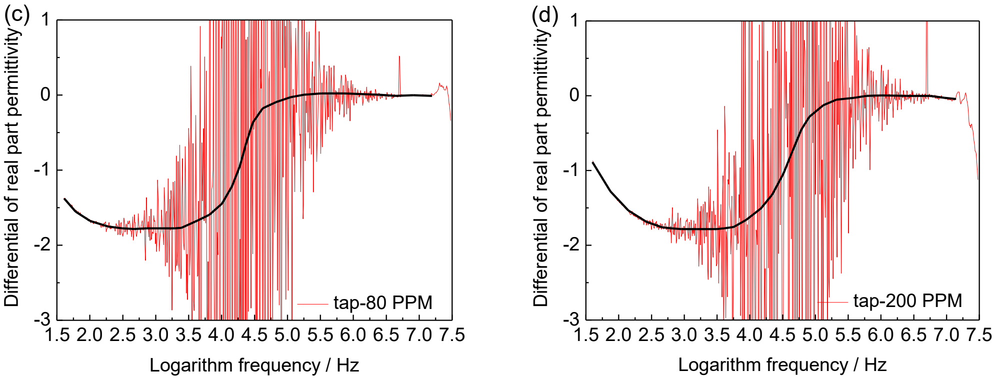

Figure 4.11 The differential of logarithm real part permittivity vs logarithm frequency spectrums of the disinfectants prepared by the tap water. The black lines show the average spectrums between the fluctuated spectrums and the constant ranges of the average values at low frequencies reveal the linear fitting range of the logarithm permittivity spectrums. (a) 0 PPM; (b) 25 PPM; (c) 80 PPM; (d) 200 PPM.

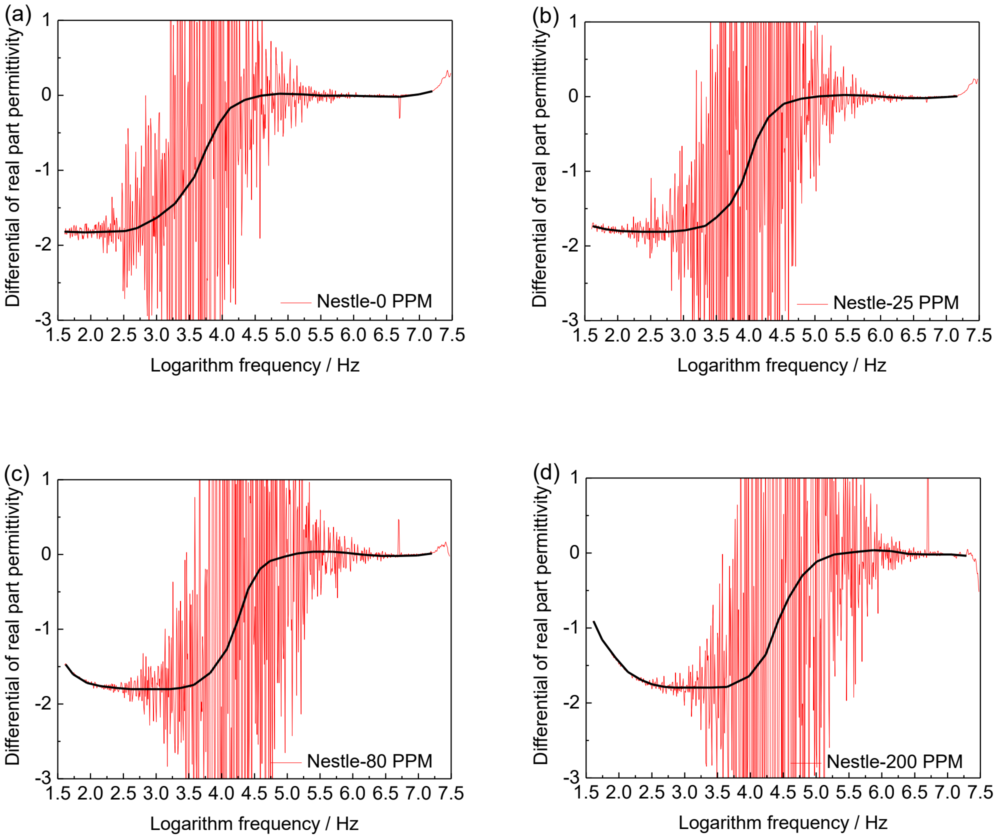

Figure 4.12 The differential of logarithm real part permittivity vs logarithm frequency spectrums of the disinfectants prepared by the Nestle bottled water. The black lines show the average spectrums between the fluctuated spectrums and the constant ranges of the average values at low frequencies reveal the linear fitting range of the logarithm permittivity spectrums. (a) 0 PPM; (b) 25 PPM; (c) 80 PPM; (d) 200 PPM.

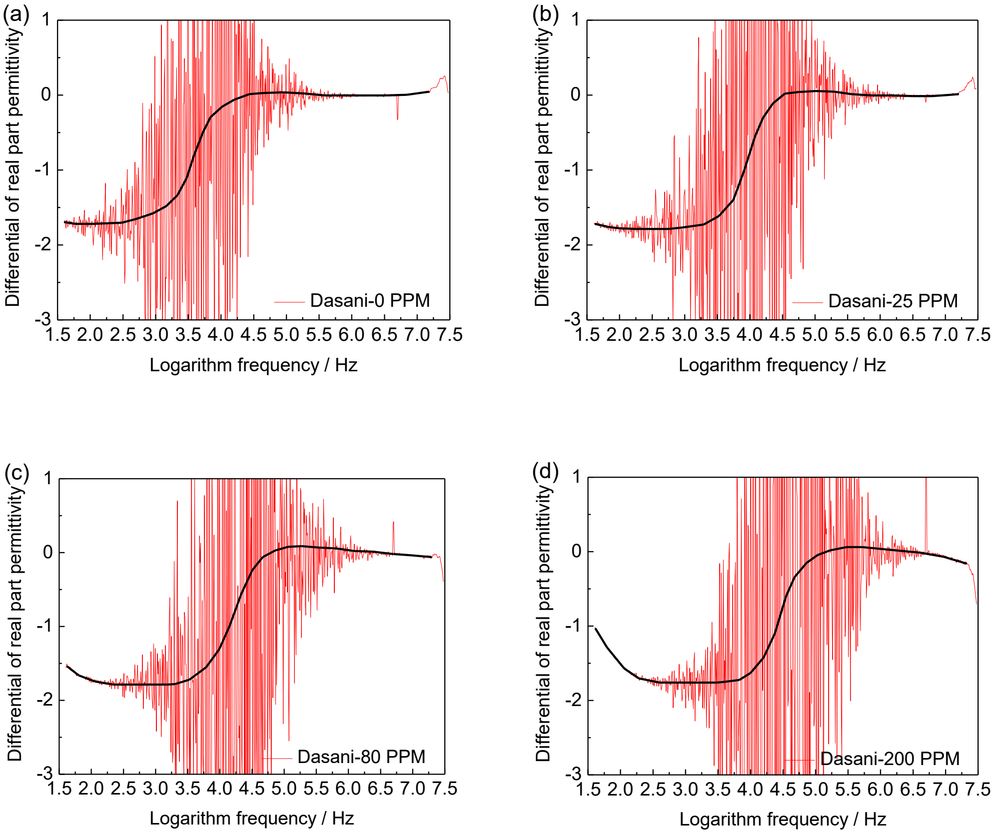

Figure 4.13 The differential of logarithm real part permittivity vs logarithm frequency spectrums of the disinfectants prepared by the Dasani bottled water. The black lines show the average spectrums between the fluctuated spectrums and the constant ranges of the average values at low frequencies reveal the linear fitting range of the logarithm permittivity spectrums. (a) 0 PPM; (b) 25 PPM; (c) 80 PPM; (d) 200 PPM.

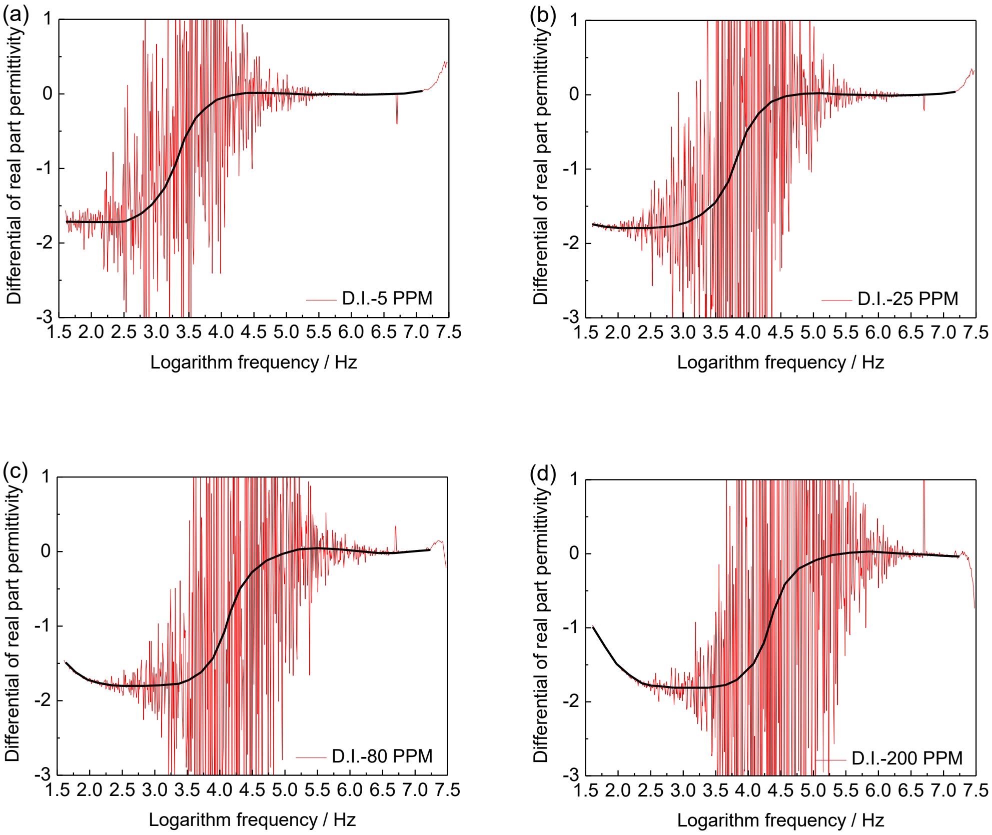

Figure 4.14 The differential of logarithm real part permittivity vs logarithm frequency spectrums of the disinfectants prepared by the D.I. water. The black lines show the average spectrums between the fluctuated spectrums and the constant ranges of the average values at low frequencies reveal the linear fitting range of the logarithm permittivity spectrums. (a) 5 PPM; (b) 25 PPM; (c) 80 PPM; (d) 200 PPM.

Table 4.1 The linear ranges of the logarithm real permittivity vs logarithm frequency spectrums of the different NaClO concentrations prepared by four waters. Both linear frequency ranges and linear permittivity ranges are listed. f is frequency, and ε_r is relative real permittivity.

	D.I. water				Tap water				Nestle water				Dasani water			
Conc./ppm	Log f / Hz		Log ε_r		Log f / Hz		Log ε_r		Log f / Hz		Log ε_r		Log f / Hz		Log ε_r	
	From	To	From	To	From	To	From	To	From	To	From	To	From	To	From	To
0	/	/	/	/	2.34	2.90	4.77	3.80	1.60	2.46	5.29	3.74	1.77	2.42	4.87	3.75
5	1.60	2.43	4.65	3.22	2.35	2.92	4.88	3.88	1.83	2.58	5.15	3.79	1.81	2.56	5.11	3.81
10	1.76	2.47	4.87	3.61	2.43	3.00	4.81	3.80	1.97	2.67	5.08	3.83	1.88	2.65	5.19	3.85
15	1.82	2.52	5.06	3.81	2.44	3.03	4.86	3.84	2.08	2.75	5.03	3.83	1.94	2.73	5.24	3.85
20	1.89	2.62	5.15	3.85	2.46	3.05	4.90	3.88	2.20	2.84	4.96	3.84	1.99	2.81	5.27	3.86
25	1.98	2.70	5.16	3.88	2.48	3.08	4.90	3.86	2.37	2.89	4.77	3.83	2.07	2.89	5.26	3.83
30	2.06	2.78	5.15	3.87	2.50	3.12	4.93	3.86	2.40	2.95	4.82	3.83	2.12	2.94	5.29	3.85
40	2.13	2.91	5.25	3.86	2.52	3.17	5.00	3.88	2.43	3.04	4.92	3.85	2.18	3.01	5.29	3.84
50	2.21	3.01	5.28	3.85	2.54	3.24	5.07	3.87	2.46	3.13	5.00	3.84	2.23	3.07	5.34	3.87
60	2.30	3.08	5.27	3.86	2.57	3.28	5.11	3.87	2.50	3.19	5.05	3.85	2.27	3.14	5.39	3.87
70	2.36	3.14	5.29	3.86	2.59	3.32	5.14	3.85	2.55	3.24	5.07	3.86	2.30	3.20	5.45	3.88
80	2.41	3.22	5.32	3.85	2.61	3.36	5.17	3.87	2.60	3.30	5.09	3.83	2.38	3.25	5.42	3.89
100	2.48	3.31	5.35	3.86	2.67	3.42	5.18	3.88	2.63	3.38	5.18	3.85	2.43	3.34	5.47	3.88
125	2.56	3.39	5.39	3.88	2.75	3.48	5.19	3.88	2.66	3.47	5.28	3.85	2.52	3.43	5.49	3.89
150	2.64	3.47	5.39	3.88	2.81	3.52	5.19	3.90	2.71	3.52	5.35	3.89	2.60	3.51	5.47	3.87
175	2.71	3.53	5.38	3.87	2.89	3.59	5.14	3.89	2.77	3.59	5.35	3.89	2.68	3.57	5.47	3.89
200	2.78	3.60	5.39	3.87	2.96	3.68	5.16	3.89	2.88	3.66	5.28	3.86	2.75	3.62	5.46	3.89
Log permittivity range	3.88 ~ 4.65				3.90 ~ 4.77				3.89 ~ 4.77				3.89 ~ 4.87			
The range for all waters	3.90 ~ 4.65															

Figure 4.15 shows the linear fittings of the linear portion of the real permittivity spectrums of the disinfectants prepared by four waters, respectively. The linear fitting equations and the fitting constants of the disinfectants prepared by four waters are shown in Eq. (4-2) and Tables 4.2, 4.3, 4.4, and 4.5. The constant permittivity at high frequency is also listed in the tables. Therefore, following the calculating method illustrated in Figure 4.4 in Section 4.2, the characteristic frequencies of the disinfectants in different concentrations prepared by four waters are calculated from the linear fittings of the linear portion of the logarithm real permittivity spectrums at low frequency and the constant real permittivity at high frequency.

$$lg\varepsilon_{r(water\ type,conc)} = A_{0(water\ type,conc)} + A_{1(water\ type,conc)} \times lgFre_{(water\ type,conc)} \qquad (4\text{-}2)$$

where $\varepsilon_{r\,(water\ type,conc)}$ is permittivity at high frequency (nearly a constant value close to 80) for each concentration and each water, thus, $\lg\varepsilon_{r(water\ type,conc)}$ is close to a constant value for each concentration and each water; $A_{0\ (water\ type,conc)}$ is the intercept value at a concentration of NaClO disinfectant prepared by a water type; $A_{1\ (water\ type,conc)}$ is the slope value at a concentration of NaClO disinfectant prepared by a water type; $Fre_{\ (water\ type,conc)}$ is the characteristic frequency at a concentration of NaClO disinfectant prepared by a water type.

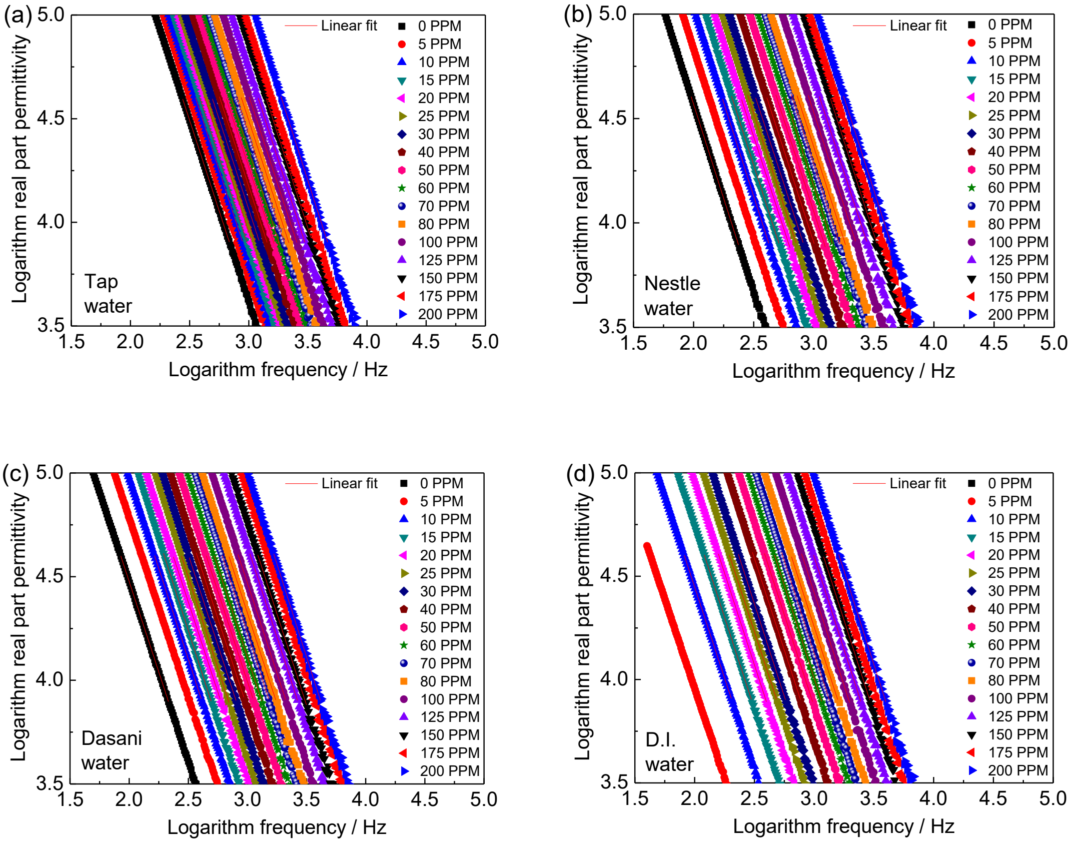

Figure 4.15 Linear fittings of the data points of the logarithm real permittivity vs logarithm frequency of the NaClO disinfectant solutions in different concentrations prepared by four waters. The linear fitting range is from the permittivity of 3.90 to 4.65. (a) Tap water; (b) Nestle bottled water; (c) Dasani bottled water; (d) D.I. water.

Table 4.2 Linear fitting parameters for the measured data points of logarithm real part permittivity vs frequency (100 Hz ~ 1 kHz) for the NaClO disinfectant solutions in different concentrations from 0 PPM to 200 PPM prepared by the tap water.

Conc. / PPM	A_0 (Tap, conc)	A_1 (Tap, conc)	Residual sum of squares	ε'_r (Tap, conc)	Log_{10} Fre (Tap, conc)	Fre (Tap, conc)
0	8.863	-1.748	0.000162	88.82	3.955	9019
5	8.943	-1.734	0.000850	89.20	4.033	10795
10	9.069	-1.752	0.000601	89.71	4.062	11527
15	9.115	-1.745	0.000581	89.66	4.104	12713
20	9.193	-1.747	0.000554	90.14	4.142	13869
25	9.216	-1.738	0.000733	90.01	4.178	15052
30	9.274	-1.737	0.000479	90.22	4.213	16343
40	9.404	-1.744	0.000615	91.05	4.270	18618
50	9.456	-1.730	0.000830	91.33	4.333	21546
60	9.532	-1.729	0.001240	92.19	4.377	23827
70	9.633	-1.737	0.001060	91.93	4.415	26010
80	9.715	-1.741	0.000932	93.54	4.448	28035
100	9.838	-1.742	0.001050	92.85	4.517	32893
125	10.031	-1.764	0.000913	83.83	4.597	39543
150	10.190	-1.777	0.001290	84.79	4.650	44691
175	10.247	-1.768	0.001940	85.20	4.704	50637
200	10.439	-1.782	0.002030	88.62	4.765	58156

Table 4.3 Linear fitting parameters for the measured data points of logarithm real part permittivity vs frequency (100 Hz ~ 1 kHz) for the NaClO disinfectant solutions in different concentrations from 0 PPM to 200 PPM prepared by Nestle bottled water.

Conc. / PPM	A_0 (Nes, conc)	A_1 (Nes, conc)	Residual sum of squares	ε'_r (Nes, conc)	Log_{10} Fre (Nes, conc)	Fre (Nes, conc)
0	8.172	-1.801	0.002890	83.62	3.469	2945
5	8.452	-1.809	0.001420	84.11	3.609	4065
10	8.609	-1.792	0.001220	84.84	3.727	5336
15	8.741	-1.785	0.001390	84.90	3.816	6541
20	8.820	-1.763	0.000929	85.83	3.907	8070
25	8.919	-1.758	0.000345	86.72	3.971	9352
30	9.022	-1.757	0.000482	87.40	4.029	10691
40	9.226	-1.773	0.000218	87.61	4.108	12832
50	9.367	-1.771	0.000162	89.69	4.187	15372
60	9.511	-1.778	0.000143	91.07	4.247	17646
70	9.635	-1.785	0.000089	91.88	4.297	19837
80	9.684	-1.773	0.000052	90.17	4.358	22809
100	9.853	-1.775	0.000049	94.05	4.440	27554
125	9.972	-1.762	0.000060	96.17	4.534	34225
150	10.230	-1.795	0.000071	101.38	4.580	38045
175	10.315	-1.793	0.000154	98.30	4.642	43867

200	10.409	-1.786	0.000219	102.55	4.701	50205

Table 4.4 Linear fitting parameters for the measured data points of logarithm real part permittivity vs frequency (100 Hz ~ 1 kHz) for the NaClO disinfectant solutions in different concentrations from 0 PPM to 200 PPM prepared by Dasani bottled water.

Conc. / PPM	A_0 (Das, conc)	A_1 (Das, conc)	Residual sum of squares	ε'_r (Das, conc)	Log_{10} Fre (Das, conc)	Fre (Das, conc)
0	7.963	-1.743	0.001890	84.37	3.463	2904
5	8.260	-1.737	0.001230	84.88	3.646	4423
10	8.483	-1.753	0.000602	83.35	3.744	5549
15	8.670	-1.772	0.000633	85.84	3.802	6345
20	8.726	-1.740	0.000518	85.64	3.905	8041
25	8.883	-1.754	0.000619	86.84	3.958	9088
30	8.969	-1.745	0.000409	87.41	4.027	10637
40	9.057	-1.730	0.000278	84.02	4.122	13239
50	9.218	-1.742	0.000163	83.27	4.190	15488
60	9.341	-1.744	0.000118	87.72	4.243	17493
70	9.491	-1.755	0.000185	88.66	4.298	19861
80	9.580	-1.752	0.000073	89.17	4.355	22629
100	9.684	-1.738	0.000046	89.36	4.448	28049
125	9.920	-1.758	0.000036	93.68	4.522	33242
150	10.041	-1.760	0.000043	90.61	4.592	39072
175	10.246	-1.779	0.000072	99.40	4.636	43278
200	10.379	-1.791	0.000127	101.44	4.676	47448

Table 4.5 Linear fitting parameters for the measured data points of logarithm real part permittivity vs frequency (100 Hz ~ 1 kHz) for the NaClO disinfectant solutions in different concentrations from 0 PPM to 200 PPM prepared by D.I. water.

Conc. / PPM	A_0 (D.I., conc)	A_1 (D.I., conc)	Residual sum of squares	ε'_r (D.I., conc)	Log_{10} Fre (D.I., conc)	Fre (D.I., conc)
0	/	/	0.002130	82.77	0	100
5	7.426	-1.734	0.005540	83.55	3.174	1493
10	7.965	-1.758	0.002540	83.89	3.436	2727
15	8.292	-1.773	0.001370	84.26	3.590	3894
20	8.516	-1.778	0.000967	84.87	3.705	5074
25	8.650	-1.767	0.000671	85.18	3.802	6343
30	8.834	-1.787	0.000748	85.84	3.861	7268
40	9.014	-1.771	0.000548	86.90	3.995	9878
50	9.209	-1.780	0.000275	88.09	4.081	12060
60	9.399	-1.797	0.000206	89.00	4.144	13948
70	9.492	-1.788	0.000114	90.32	4.215	16394
80	9.617	-1.787	0.000090	89.30	4.289	19470
100	9.791	-1.790	0.000037	91.29	4.374	23662

125	9.974	-1.793	0.000063	92.34	4.466	29221
150	10.124	-1.796	0.000086	94.48	4.538	34475
175	10.269	-1.805	0.000124	94.62	4.594	39236
200	10.404	-1.809	0.000156	101.77	4.642	43830

Figure 4.16 and the last column of Tables 4.2, 4.3, 4.4, and 4.5, show the calculated characteristic frequency vs the disinfectant concentration prepared by four waters. The linear relationships between the characteristic frequency and the (NaClO) disinfectant concentration prepared by four waters can be found in Figure 4.16(a). The data points are fitted by the linear fittings of Eq. (4-3), Eq. (4-4), Eq. (4-5), and Eq. (4-6) for the disinfectants prepared by four waters are also shown in Figure 4.16(a). Due to the different concentrations of the residual ions, the intercepts of the linear fittings of the characteristic frequencies of the different qualities of the waters are different. To further observe the slight difference of the slopes of four waters, the characteristic frequencies of the disinfectants prepared by each water are subtracted by the intercept of each pure water (0 PPM), respectively, hence, the new calculated delta characteristic frequencies of the disinfectants prepared by each water are shifted to the same start point (i.e., the delta characteristic frequency of 0) for each water, as shown in Figure 4.16(b). It is found that the slopes of the four waters are very close. Therefore, as shown in Figure 4.16(c), a common linear fitting on all tested data points of the four waters is capable to determine the relationship between the characteristic frequency and the disinfectant concentration, which is expressed in Eq. (4-7). The average linearity error of 4.19% can be obtained between the data points of the disinfectants prepared by the four waters and the common linear fitting.

$$F_{char\,(tap)} = B_{0\,(tap)} \times Conc + B_{1\,(tap)} \qquad (4\text{-}3)$$

$$F_{char\,(Nes)} = B_{0\,(Nes)} \times Conc + B_{1\,(Nes)} \qquad (4\text{-}4)$$

$$F_{char\,(Das)} = B_{0\,(Das)} \times Conc + B_{1\,(Das)} \qquad (4\text{-}5)$$

$$F_{char\,(D.I.)} = B_{0\,(D.I.)} \times Conc + B_{1\,(D.I.)} \qquad (4\text{-}6)$$

$$F_{char\,(all\ waters)} = B_{0\,(common)} \times Conc \qquad (4\text{-}7)$$

$F_{char\,(water\ type)}$ is the frequency at the characteristic points (i.e., the characteristic frequency) obtained from the linear fitting plot of logarithm real permittivity vs logarithm frequency at low frequency and logarithm real permittivity baseline at a high frequency where real permittivity is around 80 ~ 100 (each high-frequency permittivity values were used to calculate each characteristic frequency); *Conc* is the disinfectant concentration; $B_{0(water\ type)}$ is the slope of each linear fitting of the data points of the characteristic frequency vs the concentration prepared by the four waters, respectively. $F_{char\,(all\ water)}$ is the delta characteristic frequency of all four waters which is calculated by each characteristic frequency at different concentrations subtracting the characteristic frequency of each pure water. $B_{0(common)}$ is the slope of the common linear fitting of all the data points of the characteristic frequency vs the concentration prepared by (all) four waters.

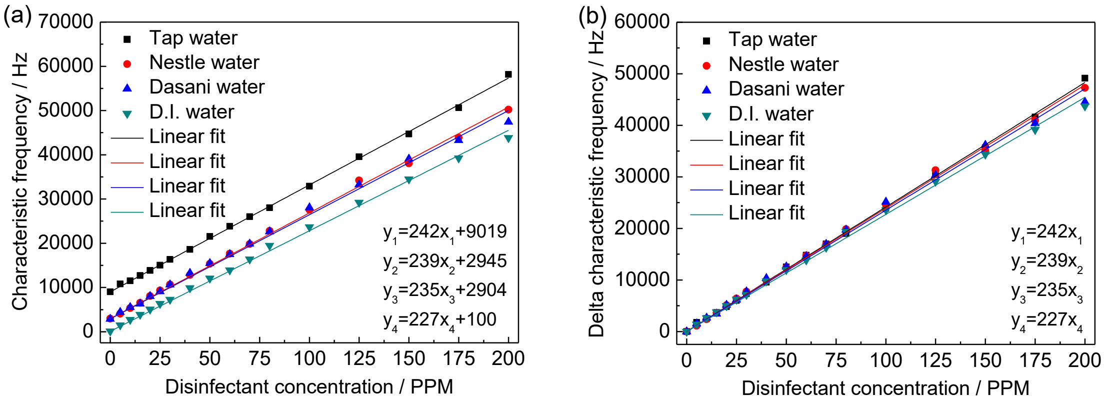

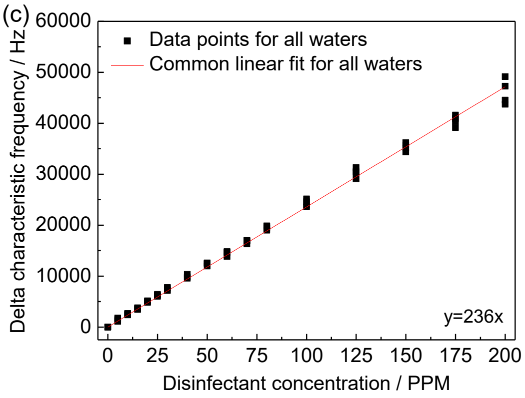

Figure 4.16 Characteristic frequency vs disinfectant concentration for four waters and the linear fittings (a); and the delta characteristic frequency (after subtracting the intercept of each pure water) vs disinfectant concentration for four waters and the linear fittings (b); and a common linear fitting of the data points of all waters (c).

4.4 Calculations to eliminate the influence of water quality issues

As is obtained in Section 4.3, a linear fitting is capable to determine/predicting the relationship between the characteristic frequency and the disinfectant concentration with an average linearity error of 4.19%. The error for each data point is calculated from the value (in PPM) of the data point subtracting the value of the linear fitting (in PPM) and then, divided by the value of each data point (in PPM) in the unit of %. The average error is calculated from the errors of all data points of the disinfectants in different concentrations prepared by four waters. However, it has not been considered that the water quality influences the fitting slope values of the logarithm permittivity vs the logarithm frequency in the linear fitting range. For all data points prepared by the four waters, a fitting slope value modification method can be used to eliminate/mitigate the influence of the water quality issue and further decrease the average (prediction) error. The modification method is described as follows: the characteristic frequencies of the disinfectants prepared by each water are multiplied by a linear fitting slope value of each pure water with an index of times (from -4 to 3 in integers).

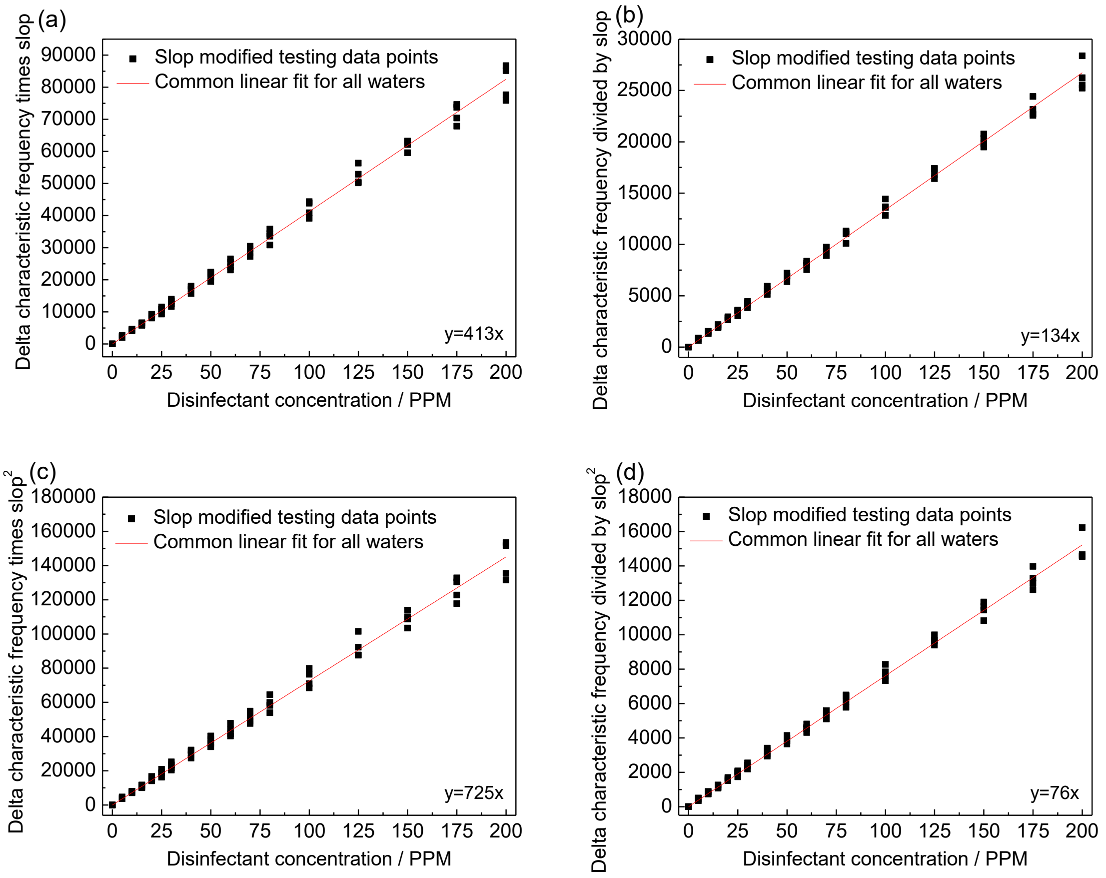

Figure 4.17 Modifications by the fitting slope value of the real permittivity spectrums of each pure water on the delta characteristic frequency vs the concentration (data points) to eliminate the influence of the water quality issue and the linear fittings on the delta characteristic frequency (data points). (a) A linear fitting on all data points of the delta characteristic frequency times the slope value of each pure water; (b) a linear fitting of the delta characteristic frequency divided by the slope value of each pure water; (c) a linear fitting of the delta characteristic frequency times the square of the slope value of each pure water; and (d) a linear fitting of the delta characteristic frequency divided by the square of the slope of each pure water. Linear fittings are all calculated by the least square method.

After the modification by different modification indexes, the slope value modified data points and the fittings are shown in Figure 4.17. Based on the calculated data points and the fittings in Figure 4.17, the average errors modified by different modification indexes are calculated and shown in Figure 4.18 and Table 4.6. The smallest average error between the modified characteristic frequency and the linear fitting is 4.08% after the slope value modification of each pure water with the index of -1, which implies that the delta characteristic frequency (data points) of each water should be divided by the slope value of the real permittivity spectrum of each water. In summary, the slope value modification of each pure water is proved to be an effective method to decrease the average error of the disinfectant sensing from 4.19% to 4.08% in the concentration range of 0 - 200 PPM.

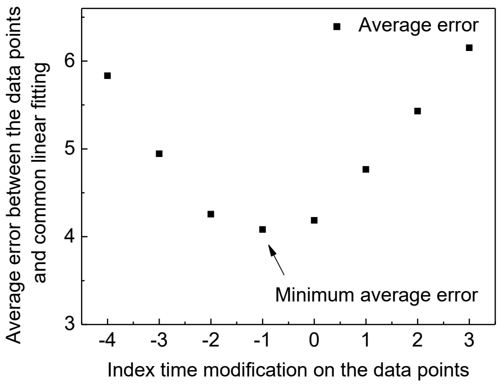

Figure 4.18 Average error (PPM/PPM in %) between the delta characteristic frequency vs the concentration (data points) modified by an index time of the slope value of each pure water and their linear fitting (a). The smallest average error (4.08 %) of the linear fitting can be found for the delta characteristic frequency data points modified by the slope value of each pure water with the index of -1.

Table 4.6 The average error (PPM/PPM) between the delta characteristic frequency data points (after subtracting the intercept of each pure water) modified by index times of the slope value of each pure water and the common linear fitting. The smallest average error of the linear fitting is underlined. (Note that the fitting slope value of D.I. water is picked up at 5 PPM instead of that in pure D.I. water.)

Delta characteristic frequency modified by index times of the slope value of each pure water (for D.I. water, the concentration of 5 PPM is chosen)	Average error (PPM/PPM) between the data points and the common linear fitting / %
-4	5.83
-3	4.94
-2	4.26
-1	4.08
0	4.19
1	4.76
2	5.43
3	6.15

4.5 Comparison between the measured and the calculated dielectric permittivity spectrums of the disinfectants and discussions

The measured capacitance/real permittivity and the capacitance/real permittivity of the dielectric solution might be different due to the existence and influence of the electrode polarization (EP) at low frequency. The study in this section aims to discover if the measured real permittivity can reflect the real permittivity of the dielectric solutions/disinfectants in a wide frequency range. It is known that, at low frequency, the EP plays a role to influence the dielectric sensing of the aqueous solutions. The EP is based on the migration of the ions to the electrodes and the formation of the ionic double layers close to the electrodes under an electrical potential. The occurrence of the EP affects the reading of the capacitance/real permittivity by forming additional capacitance layers close to the electrodes, making the tested solution a multi-layer capacitance medium in a series model. Based on the described scenario, to discover the real dielectric permittivity of the disinfectants, we developed an equation among three terms, i.e., the measured total capacitance, the capacitance of the ionic double layers, and the real capacitance of the dielectric solutions/disinfectants. Some discussions were conducted based on the calculations and analysis of the constants of the equation.

4.5.1 Measured dielectric spectrums at different electrode distances

Figure 4.19 shows the measured dielectric real permittivity and loss spectrums of the disinfectants prepared by the tap water tested by the probe with the changeable electrode distance from 2 mm to 5 mm in a wide frequency range from 0.1 Hz to 4 MHz. All the permittivity and loss spectrums tested by the different electrode distances show identical trends. At low frequency (lower than 5 Hz), the permittivity spectrums show the spectrum stage with an upper limit of the permittivity of the disinfectants in all concentrations. And the loss spectrums tested by the different electrode distances at low frequency are close to zero. From the low frequency of 5 Hz to 100 Hz, the permittivity spectrums of the disinfectants in different concentrations decrease and are gradually diverged from the single-stage value. And the loss spectrums are still in small values and gradually increase. At a frequency higher than 100 Hz, the trends of both the real permittivity and loss spectrums are identical to the spectrums analyzed in Figure 4.7 and Figure 4.8. The reason for the occurrence of the permittivity stage at low frequency is probably that the density of the reorientation of the ionic dipoles in the disinfectants reaches saturation and is balanced with the thermal vibration of the water molecules. When the density of the reorientated ionic dipoles cannot get even higher at the low frequency (lower than 5 Hz), the saturation status is independent of the disinfectant concentration.

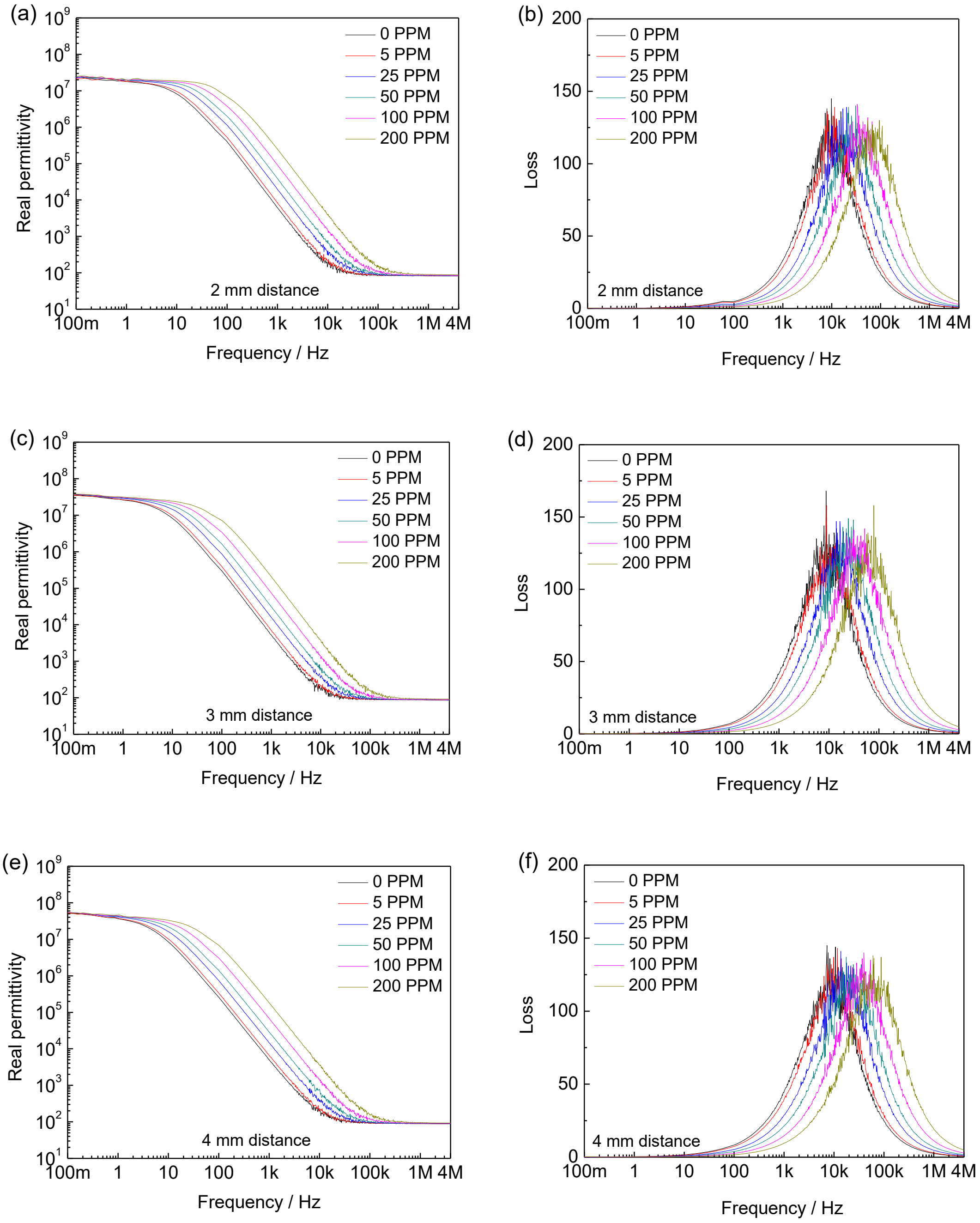

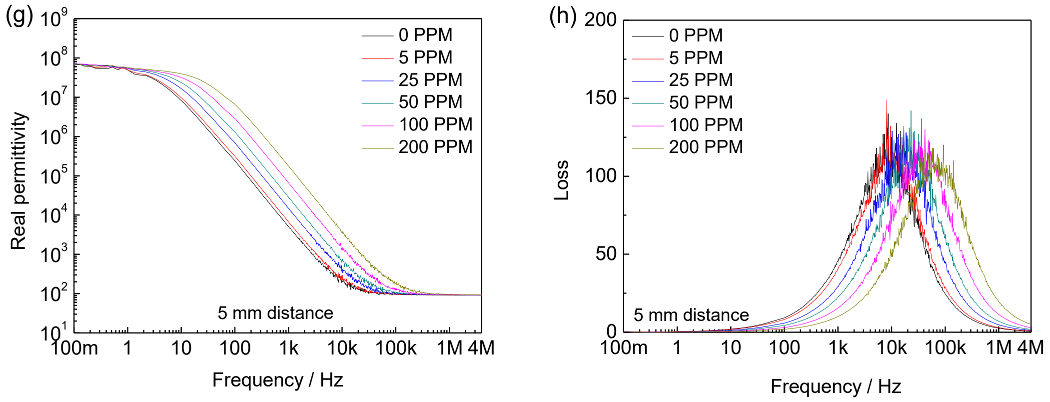

Figure 4.19 Dielectric real permittivity and loss spectrums of the disinfectants (0-200 PPM) prepared by the tap water tested by a probe with the changeable/different electrode distances from 2 mm to 5 mm at a wide frequency range from 0.1 Hz to 4 MHz. (a) permittivity and 2 mm distance; (b) loss and 2 mm distance; (c) permittivity and 3 mm distance; (d) loss and 3 mm distance; (e) permittivity and 4 mm distance; (f) loss and 4 mm distance; (g) permittivity and 5 mm distance; (h) loss and 5 mm distance.

Figure 4.20 shows the imaginary permittivity spectrums of the disinfectants prepared by the tap water tested by the probe with different electrode distances from 2 mm to 5 mm in a wide frequency range from 0.1 Hz to 4 MHz.

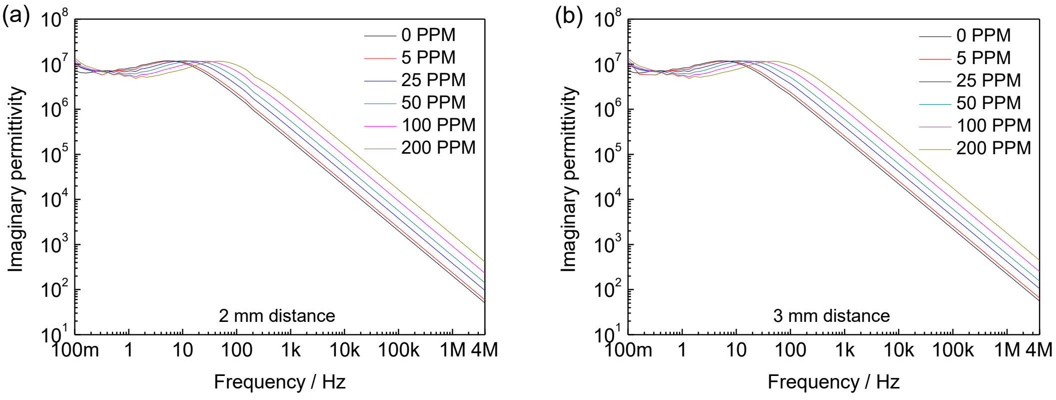

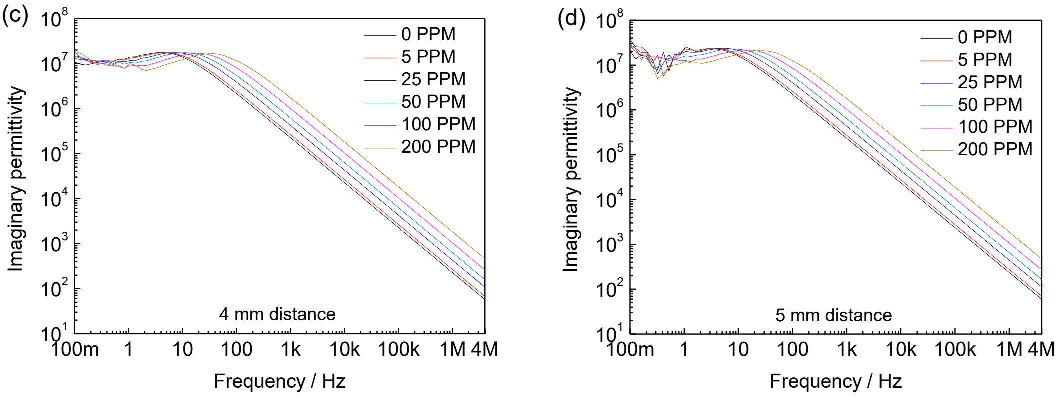

Figure 4.20 Imaginary permittivity spectrums of the disinfectants (0-200 PPM) prepared by the tap water tested by a probe with the changeable/different electrode distances from 2 mm to 5 mm at a wide frequency range from 0.1 Hz to 4 MHz. (a) 2 mm distance; (b) 3 mm distance; (c) 4 mm distance; (d) 5 mm distance.

At a frequency higher than 100 Hz, the trends of the spectrums are identical to the spectrums analyzed in Figure 4.9. However, interestingly, at a frequency lower than 100 Hz, the imaginary permittivity stops increasing where an upper stage with a continuously shaking spectrum is formed. The trends of the spectrums tested in the different electrode distances are identical. The trend at low frequency implies that the conductivity begins to decrease when decreasing frequency from 100 Hz. The reason is probably that thermal vibration plays an important role to impede the long-term migration of the ions in the solution and the ions having a very close distance to the electrodes can migrate and attach to the electrodes to contribute to the conductivity and the imaginary permittivity. Hence, the phenomenon is independent of the electrode distance. Interestingly, at low frequency, the imaginary permittivity seems also independent of the ion/disinfectant concentration, which could not be properly explained.

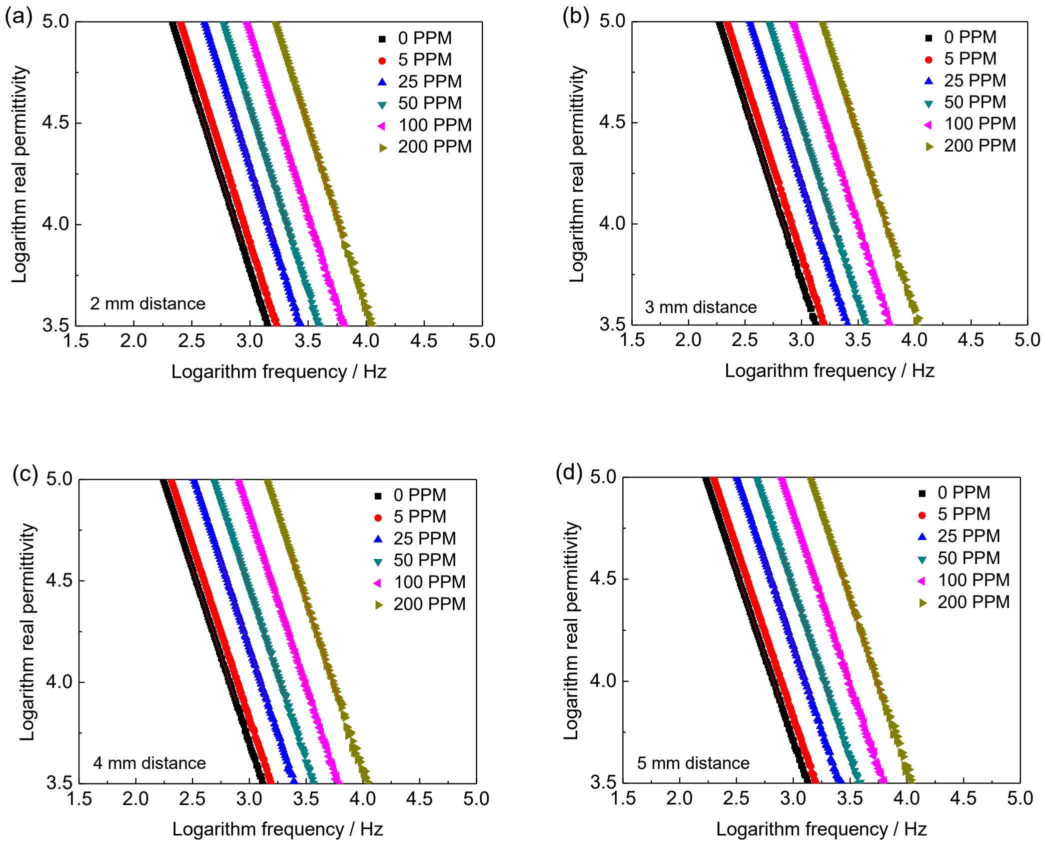

Figure 4.21 Linear fittings of the data points of the logarithm real permittivity vs logarithm frequency of the NaClO disinfectant solutions in different concentrations tested by the probe with different electrode distances from 2 mm to 5 mm. The linear fitting range is from the permittivity of 3.90 to 4.65. (a) 2 mm distance; (b) 3 mm distance; (c) 4 mm distance; (d) 5 mm distance.

Linear fittings of the data points of the logarithm real permittivity vs logarithm frequency of the disinfectant solutions in different concentrations are measured by the probe with different electrode distances from 2 mm to 5 mm, as shown in Figure 4.21. The (common) linear fitting range from the permittivity of 3.90 to 4.65, which has been determined in Table 4.1, is used for all the linear fittings.

Following the calculation methodology illustrated in Figure 4.4 in Section 4.2, the characteristic frequencies of the disinfectants in different concentrations prepared by the tap water measured by the probe with different electrode distances are calculated from the linear fittings of the linear portion of the logarithm real permittivity spectrums at low frequency and the constant real permittivity at high frequency.

Figure 4.22(a) shows the linear relationship between the characteristic frequency and the disinfectant concentration prepared by the tap water measured by the probe with different electrode distances. And the linear fittings have also been expressed by Eq. (4-3) and Figure 4.22(a). The linear fittings on the data points measured by the probe with four different distances are also shown in Figure 4.22(a). Data points of the delta characteristic frequency vs disinfectant concentration are plotted in Figure 4.22(b). In the figure, a slight random difference in the fitting slopes measured by the four distances can be observed. However, the slopes of the fittings do not vary much, and a common linear fitting can be used to fit all the measured data points, as shown in Figure 4.22(c).

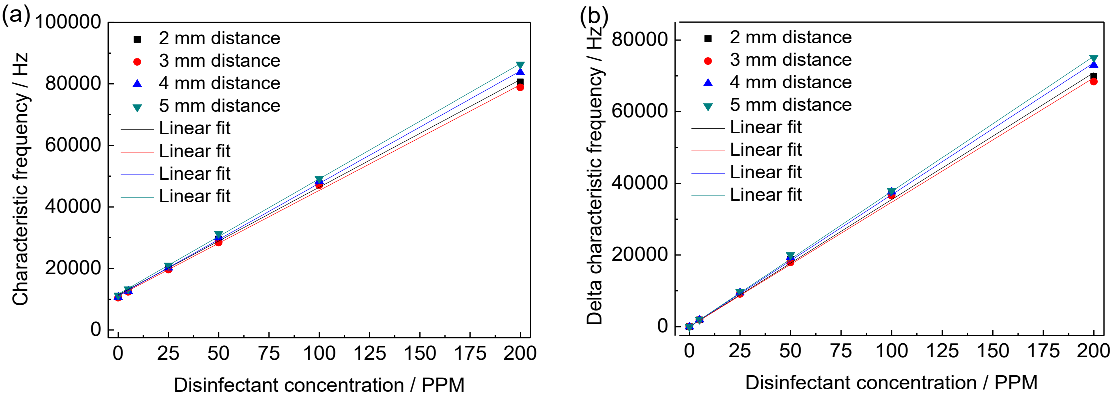

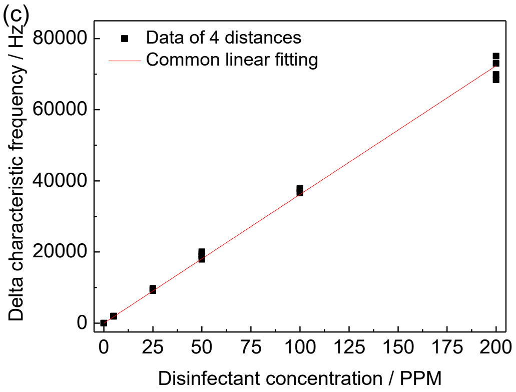

Figure 4.22 Characteristic frequency vs disinfectant concentration tested by the probe with different electrode distances from 2 mm to 5 mm and the linear fittings (a); the delta characteristic frequency (after subtracting the intercept of each pure water) vs disinfectant concentration tested by the probe with four different electrode distances (b); a common linear fitting of the data points tested by the probe with four different electrode distances (c).

In Table 4.7, the characteristic frequencies of the disinfectants measured by the probe with the four different electrode distances and the fitting results and the standard deviations, concentration detection sensitivity, and linearity errors are summarized. The linearity error decreases with increasing the electrode distance. The smallest linearity error of 1.59% can be obtained by the probe with an electrode distance of 5 mm. The linearity error of 3.68% between the data points and the common linear fitting is the highest compared to the linearity error for each electrode distance. In summary, a longer electrode distance is preferred to be used, but the distance should not be too long to have a very large/influencing edge effect.

Table 4.7 Characteristic frequencies of the disinfectants tested by the probe with four electrode distances and the calculated standard deviations, sensitivity, and linearity errors.

		Characteristic frequency / Hz				Common fitting for 4 distances / Hz	Standard deviation for 4 distances / Hz
Distance / mm		2	3	4	5		
Concentration / PPM	5	1919	1919	1943	2008	1809	142.6
	25	9439	9133	9477	9767	9047	164.8
	50	18809	17898	19319	20053	18094	1213.5
	100	36809	36553	37637	37878	36188	1170.1
	200	69878	68361	72982	75076	72376	2739.2
Sensitivity / Hz/PPM		354.5	347.3	368.3	377.4	361.9	/
Linearity error		3.18%	3.15%	2.00%	1.59%	3.68%	/

4.5.2 Discussions on the calculated dielectric permittivity spectrums of the disinfectants

4.5.2.1 Theory

Based on the influence of the EP on the measured capacitance mentioned above, a model of the multi-layer capacitance in a series configuration is developed. The capacitance measured by the probe, *C*, can be expressed by the sum of the capacitances of the dielectric solution/disinfectant and the ionic double layers, which is expressed as follows:

$$\frac{1}{C}=\frac{1}{C_R}+\frac{1}{C_+}+\frac{1}{C_-}=\frac{d-\Delta}{\varepsilon_R\cdot A}+\frac{2}{C_+}=\frac{1}{\varepsilon_0\varepsilon_r A}\cdot d-\frac{1}{\varepsilon_0\varepsilon_r A}\cdot\Delta+\frac{2}{C_+}\quad\text{(4-7)}$$

where C_+ and C_- are the capacitances of the ionic double layers which are close to the electrodes, respectively; ε_R is the dielectric real permittivity of the disinfectant between the electrodes, where $\varepsilon_R = \varepsilon_0\varepsilon_r$; *d* and *A* are the distance between the paralleled electrodes and the area of the electrodes, respectively; Δ is the thickness of the ionic double layers; thus, the thickness of the measured disinfectant can be expressed as Δ-*d*.

It can be analyzed that, $\frac{1}{\varepsilon_0\varepsilon_r A}$, Δ, and C_+, are constants at a (selected) frequency and a constant disinfectant concentration. *d* can be considered as a variable. Hence, we can assume that:

$$a=\frac{1}{\varepsilon_0\varepsilon_r A}\quad\text{(4-8)}$$

$$b = \frac{2}{C_+} - \frac{\Delta}{\varepsilon_0 \varepsilon_r A} = \frac{2}{C_+} - a\Delta \quad \text{(4-9)}$$

Thus, Eq. (4-7) can be rewritten as:

$$\frac{1}{C} = a \cdot d + b \quad \text{(4-10)}$$

where a and b are constants at a (selected) frequency and a constant disinfectant concentration.

From Eq. (4-10), it reveals that, by measuring the capacitances of the disinfectants with different distances of the electrodes, the constants, a, and b, can be calculated at different frequencies and different disinfectant concentrations, respectively. Moreover, the capacitance contributions from both the disinfectant and the ionic double layers can be separated. Therefore, the calculated relative real permittivity of the disinfectant, ε_r, which has a direct relationship with a, can be directly calculated, as shown in Eq. (4-8). The calculated results and the further comparisons between the calculated and the measured real permittivity will be discussed later.

4.5.2.2 Results and discussions

At different frequencies, a and b can be calculated from the linear fittings of the data points of $1/C$ vs d, respectively. Figure 4.23 and Table 4.8 show the linear fittings of the measured data points of $1/C$ vs d for different disinfectant concentrations at different frequencies ranging from 0.1 Hz to 4 MHz. As shown in Eq. (4-9), the fitting slope value, i.e., a, is inversely proportional to ε_r. Therefore, the trend of the fitting slope when increasing disinfectant concentration can reflect the trend of ε_r. At the low frequencies from 0.1 Hz to 1 Hz, the fittings are very close to each other, and their slopes are negative values and very small for all disinfectant concentrations. At the frequencies from 4 Hz to 5 kHz, the fitting slope decreases with increasing disinfectant concentration. However, from the frequency of 10 kHz, this trend of the slope value when increasing disinfectant concentration begins to weaken when the frequency increases. Until the frequency increases to 400 kHz, the slope values remain almost the same when the disinfectant concentration increases. At the frequencies from 1 MHz to 4 MHz, the fittings for different concentrations are almost the same. Table 4.9 shows the intercept (i.e., *b*) values of the linear fittings of the data points of 1/*C* vs *d*. From 0.1 Hz to 9 Hz, *b* values are positive. But, from 37 Hz to 2 kHz, b values turn negative. However, from 10 kHz to 4 MHz, *b* values turn positive. The value change of a and b and their influences will be further discussed next.

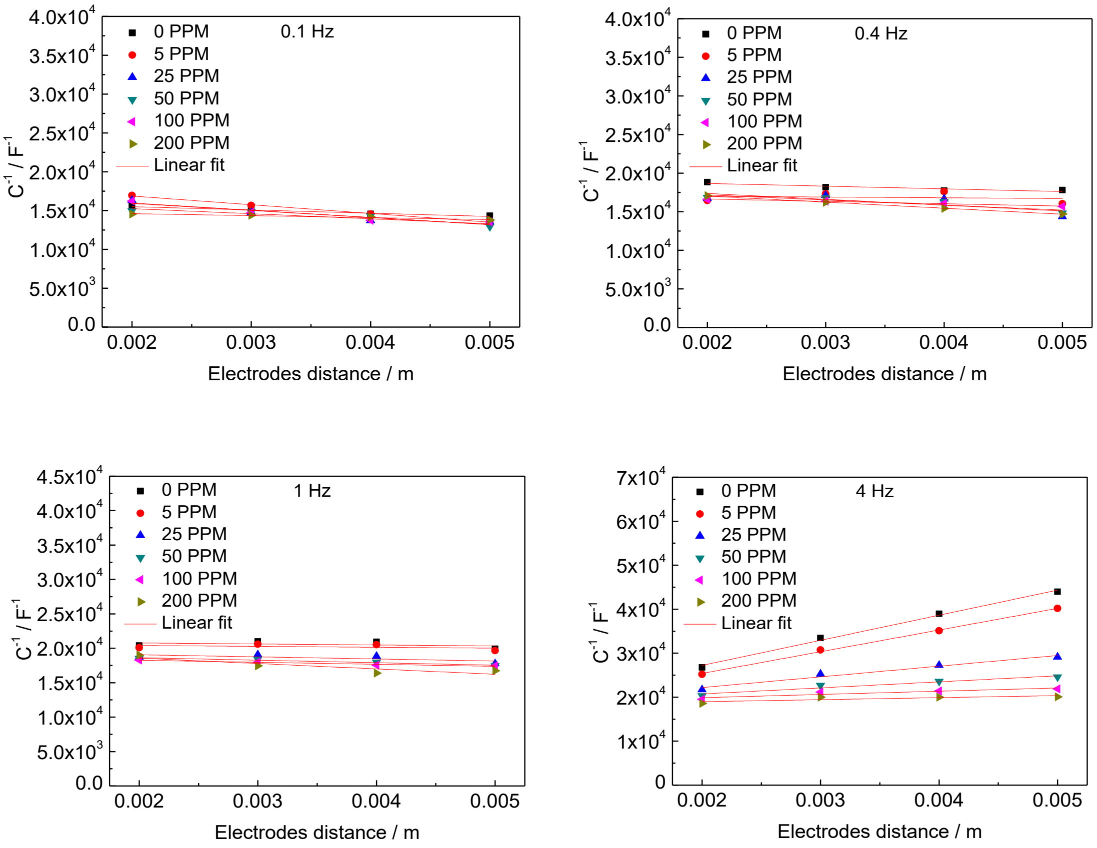

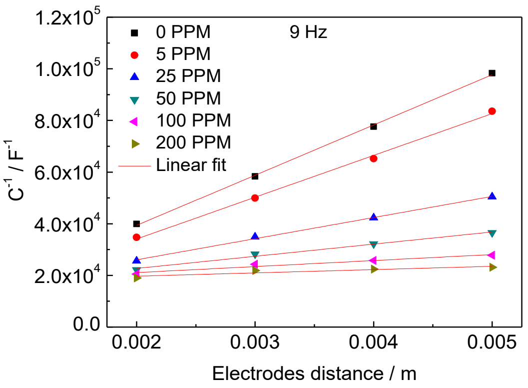
9 Hz
■ 0 PPM
● 5 PPM
▲ 25 PPM
▼ 50 PPM
◀ 100 PPM
▶ 200 PPM
Linear fit
C^{-1} / F^{-1}
0.0
$2.0x10^4$
$4.0x10^4$
$6.0x10^4$
$8.0x10^4$
$1.0x10^5$
$1.2x10^5$
0.002
0.003
0.004
0.005
Electrodes distance / m

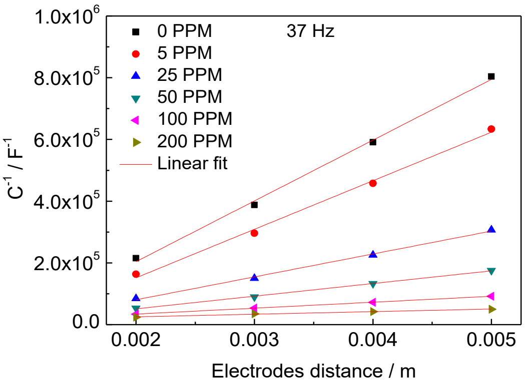
37 Hz
■ 0 PPM
● 5 PPM
▲ 25 PPM
▼ 50 PPM
◀ 100 PPM
▶ 200 PPM
Linear fit
C^{-1} / F^{-1}
0.0
$2.0x10^5$
$4.0x10^5$
$6.0x10^5$
$8.0x10^5$
$1.0x10^6$
0.002
0.003
0.004
0.005
Electrodes distance / m

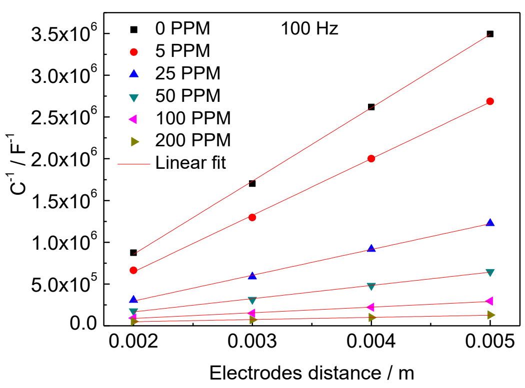
100 Hz
■ 0 PPM
● 5 PPM
▲ 25 PPM
▼ 50 PPM
◀ 100 PPM
▶ 200 PPM
Linear fit
C^{-1} / F^{-1}
0.0
$5.0x10^5$
$1.0x10^6$
$1.5x10^6$
$2.0x10^6$
$2.5x10^6$
$3.0x10^6$
$3.5x10^6$
0.002
0.003
0.004
0.005
Electrodes distance / m

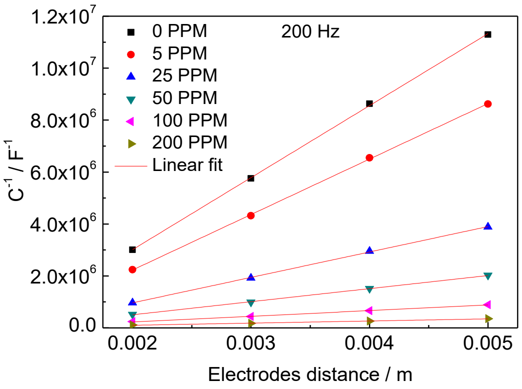
200 Hz
■ 0 PPM
● 5 PPM
▲ 25 PPM
▼ 50 PPM
◀ 100 PPM
▶ 200 PPM
Linear fit
C^{-1} / F^{-1}
0.0
$2.0x10^6$
$4.0x10^6$
$6.0x10^6$
$8.0x10^6$
$1.0x10^7$
$1.2x10^7$
0.002
0.003
0.004
0.005
Electrodes distance / m

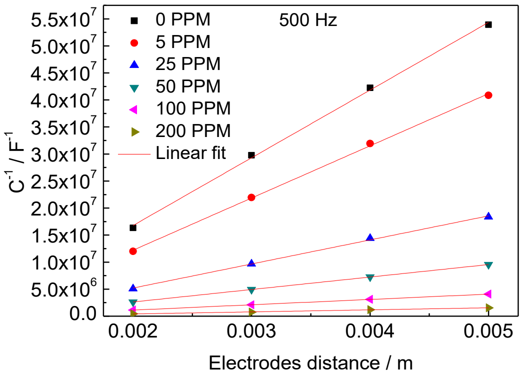
500 Hz
■ 0 PPM
● 5 PPM
▲ 25 PPM
▼ 50 PPM
◀ 100 PPM
▶ 200 PPM
Linear fit
C^{-1} / F^{-1}
0.0
$5.0x10^6$
$1.0x10^7$
$1.5x10^7$
$2.0x10^7$
$2.5x10^7$
$3.0x10^7$
$3.5x10^7$
$4.0x10^7$
$4.5x10^7$
$5.0x10^7$
$5.5x10^7$
0.002
0.003
0.004
0.005
Electrodes distance / m

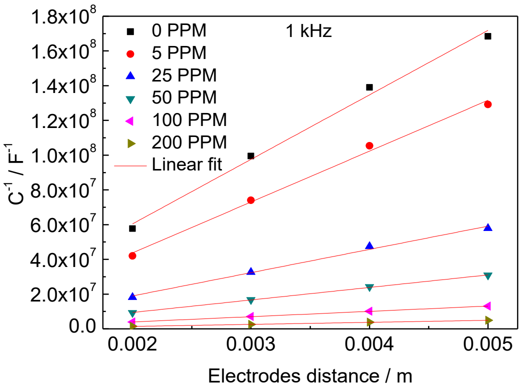
1 kHz
■ 0 PPM
● 5 PPM
▲ 25 PPM
▼ 50 PPM
◀ 100 PPM
▶ 200 PPM
Linear fit
C^{-1} / F^{-1}
0.0
$2.0x10^7$
$4.0x10^7$
$6.0x10^7$
$8.0x10^7$
$1.0x10^8$
$1.2x10^8$
$1.4x10^8$
$1.6x10^8$
$1.8x10^8$
0.002
0.003
0.004
0.005
Electrodes distance / m

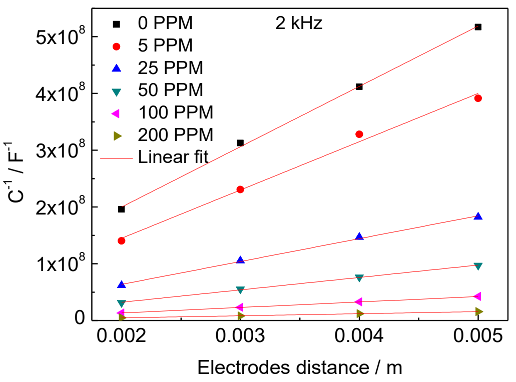
2 kHz
■ 0 PPM
● 5 PPM
▲ 25 PPM
▼ 50 PPM
◀ 100 PPM
▶ 200 PPM
Linear fit
C^{-1} / F^{-1}
0
$1x10^8$
$2x10^8$
$3x10^8$
$4x10^8$
$5x10^8$
0.002
0.003
0.004
0.005
Electrodes distance / m

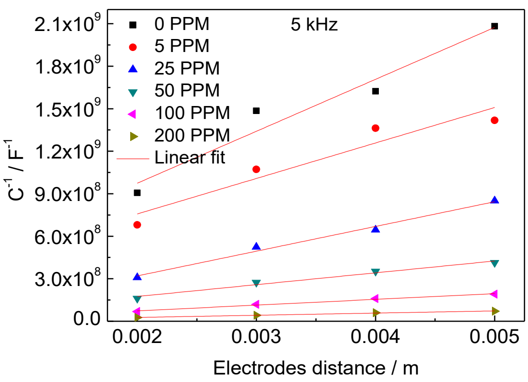
5 kHz
■ 0 PPM
● 5 PPM
▲ 25 PPM
▼ 50 PPM
◀ 100 PPM
▶ 200 PPM
Linear fit
C^{-1} / F^{-1}
0.0
$3.0x10^8$
$6.0x10^8$
$9.0x10^8$
$1.2x10^9$
$1.5x10^9$
$1.8x10^9$
$2.1x10^9$
0.002
0.003
0.004
0.005
Electrodes distance / m

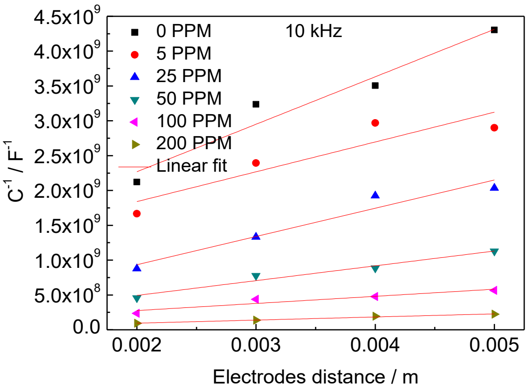
10 kHz
0 PPM
5 PPM
25 PPM
50 PPM
100 PPM
200 PPM
Linear fit
C-1 / F-1
4.5x10^9
4.0x10^9
3.5x10^9
3.0x10^9
2.5x10^9
2.0x10^9
1.5x10^9
1.0x10^9
5.0x10^8
0.0
0.002
0.003
0.004
0.005
Electrodes distance / m

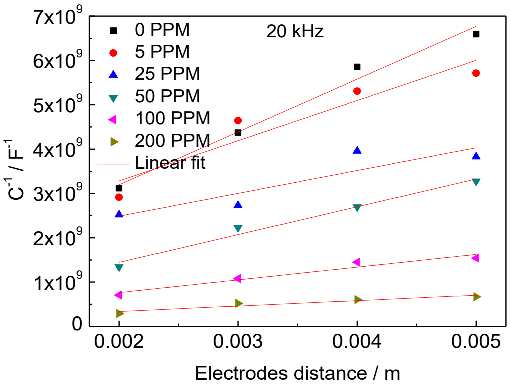
20 kHz
0 PPM
5 PPM
25 PPM
50 PPM
100 PPM
200 PPM
Linear fit
C-1 / F-1
7x10^9
6x10^9
5x10^9
4x10^9
3x10^9
2x10^9
1x10^9
0
0.002
0.003
0.004
0.005
Electrodes distance / m

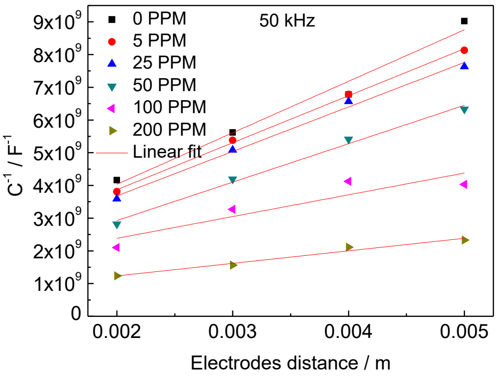
50 kHz
0 PPM
5 PPM
25 PPM
50 PPM
100 PPM
200 PPM
Linear fit
C-1 / F-1
9x10^9
8x10^9
7x10^9
6x10^9
5x10^9
4x10^9
3x10^9
2x10^9
1x10^9
0
0.002
0.003
0.004
0.005
Electrodes distance / m

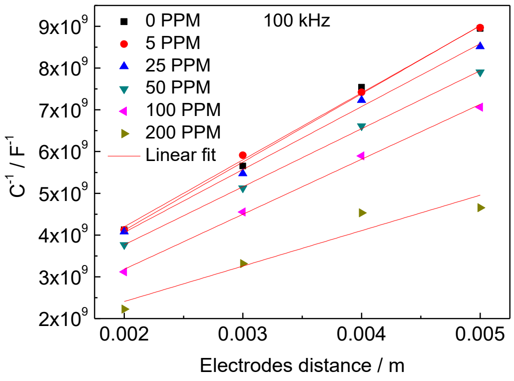
100 kHz
0 PPM
5 PPM
25 PPM
50 PPM
100 PPM
200 PPM
Linear fit
C-1 / F-1
9x10^9
8x10^9
7x10^9
6x10^9
5x10^9
4x10^9
3x10^9
2x10^9
0.002
0.003
0.004
0.005
Electrodes distance / m

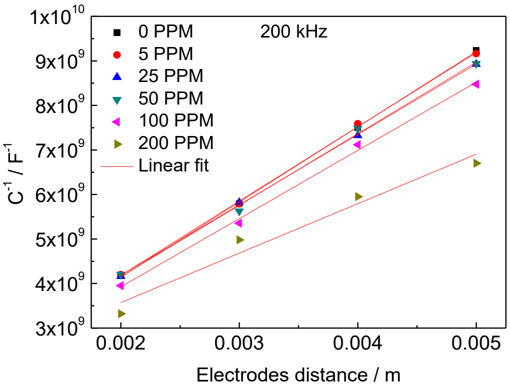
200 kHz
0 PPM
5 PPM
25 PPM
50 PPM
100 PPM
200 PPM
Linear fit
C-1 / F-1
1x10^10
9x10^9
8x10^9
7x10^9
6x10^9
5x10^9
4x10^9
3x10^9
0.002
0.003
0.004
0.005
Electrodes distance / m

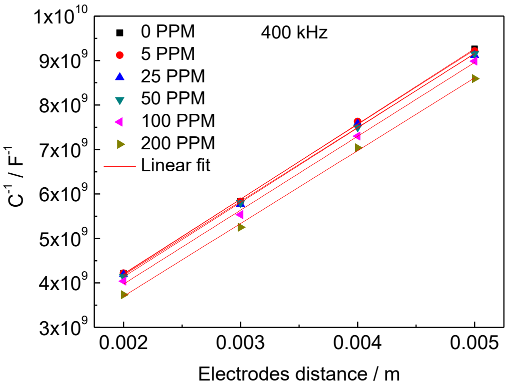
400 kHz
0 PPM
5 PPM
25 PPM
50 PPM
100 PPM
200 PPM
Linear fit
C-1 / F-1
1x10^10
9x10^9
8x10^9
7x10^9
6x10^9
5x10^9
4x10^9
3x10^9
0.002
0.003
0.004
0.005
Electrodes distance / m

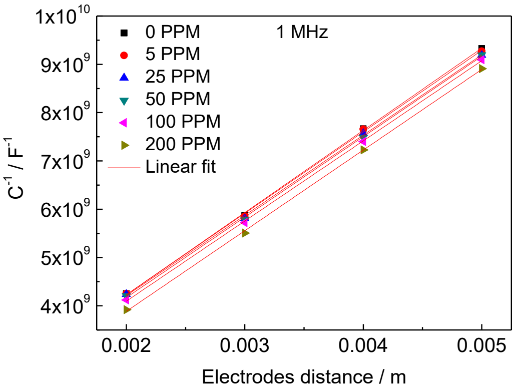
1 MHz
0 PPM
5 PPM
25 PPM
50 PPM
100 PPM
200 PPM
Linear fit
C-1 / F-1
1x10^10
9x10^9
8x10^9
7x10^9
6x10^9
5x10^9
4x10^9
0.002
0.003
0.004
0.005
Electrodes distance / m

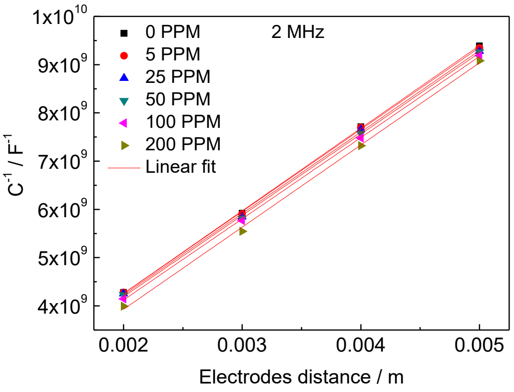
2 MHz
0 PPM
5 PPM
25 PPM
50 PPM
100 PPM
200 PPM
Linear fit
C-1 / F-1
1x10^10
9x10^9
8x10^9
7x10^9
6x10^9
5x10^9
4x10^9
0.002
0.003
0.004
0.005
Electrodes distance / m

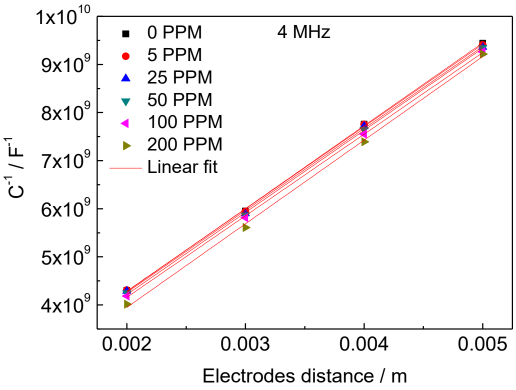

Figure 4.23 Linear fittings of the data points of one over the measured capacitance, 1/C, vs the electrode distance of the probe at different frequencies. (a) 0.1 Hz; (b) 0.4 Hz; (c) 1 Hz; (d) 4 Hz; (e) 9 Hz; (f) 37 Hz; (g) 100 Hz; (h) 200 Hz; (i) 500 Hz; (j) 1 kHz; (k) 2 kHz; (l) 5 kHz; (m) 10 kHz; (n) 20 kHz; (o) 50 kHz; (p) 100 kHz; (q) 200 kHz; (r) 400 kHz; (s) 1 MHz; (t) 2 MHz; (u) 4 MHz.

Table 4.8 Slope (i.e., a) values of the linear fittings of 1/C vs electrode distance.

		Disinfectant concentration / PPM					
		0	5	25	50	100	200
Frequency	0.1 Hz	-4.19E+05	-1.12E+06	-9.33E+05	-6.53E+05	-9.08E+05	-2.54E+05
	0.4 Hz	-3.51E+05	-9.87E+04	-7.56E+05	-6.55E+05	-3.06E+05	-7.85E+05
	1 Hz	-1.46E+05	-1.30E+05	-3.03E+05	-3.64E+05	-2.94E+05	-7.82E+05
	4 Hz	5.71E+06	4.93E+06	2.43E+06	1.38E+06	7.36E+05	4.60E+05
	9 Hz	1.94E+07	1.62E+07	8.18E+06	4.71E+06	2.33E+06	1.27E+06
	37 Hz	1.97E+08	1.57E+08	7.42E+07	4.10E+07	1.93E+07	8.43E+06
	100 Hz	8.78E+08	6.78E+08	3.09E+08	1.58E+08	6.79E+07	2.60E+07
	200 Hz	2.77E+09	2.14E+09	9.79E+08	5.05E+08	2.17E+08	8.19E+07
	500 Hz	1.25E+10	9.65E+09	4.45E+09	2.31E+09	9.86E+08	3.77E+08
	1 kHz	3.71E+10	2.93E+10	1.34E+10	7.21E+09	3.05E+09	1.17E+09
	2 kHz	1.06E+11	8.51E+10	4.03E+10	2.19E+10	9.65E+09	3.65E+09
	5 kHz	3.67E+11	2.50E+11	1.75E+11	8.36E+10	4.07E+10	1.53E+10
	10 kHz	6.82E+11	4.28E+11	4.06E+11	2.13E+11	1.02E+11	4.46E+10
	20 kHz	1.19E+12	9.07E+11	5.15E+11	6.27E+11	2.87E+11	1.22E+11
	50 kHz	1.57E+12	1.44E+12	1.36E+12	1.17E+12	6.65E+11	3.84E+11
	100 kHz	1.64E+12	1.60E+12	1.51E+12	1.39E+12	1.32E+12	8.49E+11
	200 kHz	1.69E+12	1.67E+12	1.58E+12	1.61E+12	1.53E+12	1.11E+12
	400 kHz	1.69E+12	1.68E+12	1.66E+12	1.67E+12	1.66E+12	1.64E+12
	1 MHz	1.70E+12	1.69E+12	1.66E+12	1.67E+12	1.66E+12	1.67E+12
	2 MHz	1.71E+12	1.70E+12	1.69E+12	1.69E+12	1.68E+12	1.70E+12
	4 MHz	1.72E+12	1.71E+12	1.70E+12	1.71E+12	1.70E+12	1.74E+12

Table 4.9 Intercept (i.e., b) values of the linear fittings of 1/C vs electrode distance.

		Disinfectant concentration / PPM					
		0	5	25	50	100	200
Frequency	0.1 Hz	1.63E+04	1.91E+04	1.78E+04	1.66E+04	1.77E+04	1.51E+04
	0.4 Hz	1.94E+04	1.72E+04	1.89E+04	1.85E+04	1.73E+04	1.86E+04
	1 Hz	2.11E+04	2.07E+04	1.97E+04	1.94E+04	1.88E+04	2.01E+04
	4 Hz	1.58E+04	1.56E+04	1.73E+04	1.80E+04	1.84E+04	1.81E+04
	9 Hz	4.66E+02	1.71E+03	9.69E+03	1.33E+04	1.64E+04	1.72E+04
	37 Hz	-1.90E+05	-1.63E+05	-6.80E+04	-3.09E+04	-4.51E+03	8.35E+03
	100 Hz	-9.00E+05	-7.10E+05	-3.21E+05	-1.50E+05	-4.79E+04	-3.39E+03
	200 Hz	-2.53E+06	-2.04E+06	-9.93E+05	-5.05E+05	-2.01E+05	-6.18E+04
	500 Hz	-8.27E+06	-7.10E+06	-3.70E+06	-1.99E+06	-8.49E+05	-3.36E+05
	1 kHz	-1.38E+07	-1.49E+07	-7.83E+06	-4.99E+06	-2.14E+06	-9.34E+05
	2 kHz	-1.27E+07	-2.53E+07	-1.69E+07	-1.16E+07	-5.92E+06	-2.57E+06
	5 kHz	2.41E+08	2.56E+08	-2.91E+07	7.56E+06	-8.10E+06	-3.50E+06
	10 kHz	9.06E+08	9.84E+08	1.21E+08	6.81E+07	7.11E+07	5.49E+06
	20 kHz	8.13E+08	1.47E+09	1.46E+09	1.90E+08	1.89E+08	9.39E+07
	50 kHz	8.87E+08	9.96E+08	9.58E+08	5.76E+08	1.05E+09	4.67E+08
	100 kHz	8.44E+08	9.89E+08	1.05E+09	9.87E+08	5.46E+08	7.09E+08
	200 kHz	7.68E+08	8.47E+08	1.03E+09	9.44E+08	8.61E+08	1.35E+09
	400 kHz	8.13E+08	8.51E+08	8.54E+08	7.86E+08	6.54E+08	4.27E+08
	1 MHz	8.26E+08	8.57E+08	8.87E+08	8.39E+08	7.77E+08	5.46E+08
	2 MHz	8.33E+08	8.57E+08	8.48E+08	8.19E+08	7.55E+08	5.22E+08
	4 MHz	8.32E+08	8.65E+08	8.53E+08	8.01E+08	7.65E+08	4.71E+08

The aim to calculate the real permittivity of the disinfectants is to get rid of the EP influence caused by the ionic double layers close to the electrodes of the probe and obtain the true real permittivity of the disinfectants/solutions. In Figure 4.24, the measured real permittivity spectrums of the disinfectants in different concentrations prepared by the tap water are exhibited in solid curves, which are the same as the real permittivity spectrums in Figure 4.19. After the calculation by Eq. (4-8), the calculated data points of the real permittivity are shown in Figure 4.24 and Table 4.10.

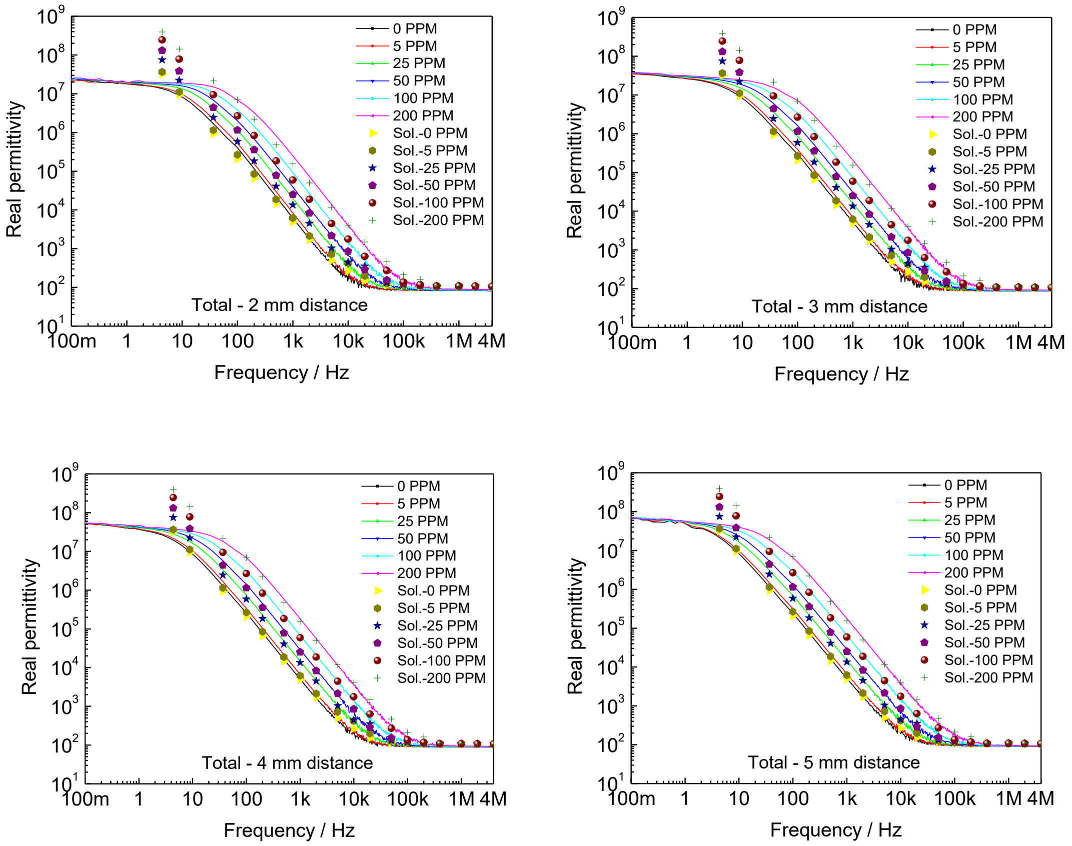

Figure 4.24 Comparison between the measured real permittivity and the real permittivity of the solution (after the calculation). At a frequency higher than 37 Hz, the real permittivity of the solution is very close to the measured real permittivity. However, at a frequency lower than 37 Hz, the calculated permittivity could not show reasonable results.

Comparing the calculated real permittivity to the measured real permittivity of the disinfectants, it is observed that, in a large frequency range from 37 Hz to 4 MHz, the values of the calculated real permittivity are very close to the measured permittivity (in the solid curves) at all disinfectant concentrations. The results reveal that, in the frequency range higher than 37 Hz, the EP influence on the disinfectant sensing is very small and the measured real permittivity can reflect the true real permittivity of the disinfectants. Moreover, as shown in Figures 4.24(a), 4.24(b), 4.24(c), 4.24(d), comparing the real permittivity measured by the probe with the four different electrode distances, *d*, (2mm - 5mm), it seems that, by increasing *d*, the true/calculated real permittivity is much closer to the measured real permittivity. When *d* increases to 4mm and 5mm, as shown in Figure 4.24(d), the measured real permittivity is almost the same as the true/calculated real permittivity in the frequency range higher than 37 Hz. However, when *d* gets even larger, the edge effect of the electrodes will influence the measurements. Hence, 4mm and 5mm of *d* are preferred to be selected for the dielectric measurements of the disinfectant. However, at a frequency lower than 37 Hz, the calculated permittivity could not show reasonable results, due to that, the negative slope values are obtained. It is impossible to get the negative values of the real permittivity. The reason is not clear. In summary, in the frequency range higher than 37 Hz, the measured real permittivity can reflect the true real permittivity of the disinfectants and the preferred electrode distance, *d*, for better-measured results is 4mm and 5mm.

Table 4.10 Calculated real permittivity of the dielectric solutions/disinfectants.

		Disinfectant concentration / PPM					
		0	5	25	50	100	200
Frequency	0.1 Hz	-4.31E+08	-1.61E+08	-1.94E+08	-2.77E+08	-1.99E+08	-7.10E+08
	0.4 Hz	-5.14E+08	-1.83E+09	-2.39E+08	-2.76E+08	-5.91E+08	-2.30E+08
	1 Hz	-1.24E+09	-1.39E+09	-5.95E+08	-4.96E+08	-6.15E+08	-2.31E+08
	4 Hz	3.17E+07	3.67E+07	7.44E+07	1.31E+08	2.45E+08	3.93E+08
	9 Hz	9.29E+06	1.12E+07	2.21E+07	3.84E+07	7.76E+07	1.42E+08
	37 Hz	9.18E+05	1.15E+06	2.43E+06	4.40E+06	9.38E+06	2.14E+07
	100 Hz	2.06E+05	2.67E+05	5.85E+05	1.14E+06	2.66E+06	6.95E+06
	200 Hz	6.52E+04	8.46E+04	1.85E+05	3.58E+05	8.34E+05	2.21E+06
	500 Hz	1.44E+04	1.87E+04	4.06E+04	7.83E+04	1.83E+05	4.79E+05
	1 kHz	4.87E+03	6.17E+03	1.35E+04	2.51E+04	5.93E+04	1.54E+05
	2 kHz	1.70E+03	2.12E+03	4.49E+03	8.26E+03	1.87E+04	4.95E+04
	5 kHz	4.93E+02	7.21E+02	1.04E+03	2.16E+03	4.44E+03	1.18E+04
	10 kHz	2.65E+02	4.22E+02	4.45E+02	8.50E+02	1.77E+03	4.05E+03
	20 kHz	1.52E+02	1.99E+02	3.51E+02	2.88E+02	6.29E+02	1.48E+03
	50 kHz	1.15E+02	1.26E+02	1.33E+02	1.54E+02	2.72E+02	4.71E+02
	100 kHz	1.11E+02	1.13E+02	1.20E+02	1.30E+02	1.37E+02	2.13E+02

	200 kHz	1.07E+02	1.08E+02	1.14E+02	1.13E+02	1.18E+02	1.63E+02
	400 kHz	1.07E+02	1.08E+02	1.09E+02	1.08E+02	1.09E+02	1.10E+02
	1 MHz	1.06E+02	1.07E+02	1.09E+02	1.08E+02	1.09E+02	1.08E+02
	2 MHz	1.06E+02	1.06E+02	1.07E+02	1.07E+02	1.07E+02	1.06E+02
	4 MHz	1.05E+02	1.06E+02	1.06E+02	1.06E+02	1.07E+02	1.04E+02

To investigate the fundamentals of the influence of the ionic double layers, the spectrums of the capacitance of the ionic double layers per unit area, C_0, and the intercept divided by the slope value, b/a, are calculated and analyzed, respectively.

C_0 can be represented as:

$$C_0 = \frac{C_+}{A} \quad \text{(4-11)}$$

b/a spectrums at different disinfectant concentrations can be expressed as:

$$\frac{b}{a} = \frac{2\varepsilon_0\varepsilon_r A}{C_+} - \Delta = \frac{2\varepsilon_0\varepsilon_r}{C_0} - \Delta \quad \text{(4-12)}$$

C_0 represents the capacitance density of the ionic double layers formed close to the electrodes. b/a represents the overall influence of the capacitance density of the ionic double layers and the thickness of the ionic double layers, i.e., Δ. From Figures 4.25(a), 4.25(b), and Table 4.11, in the frequency range higher than 37 Hz, C_0 is almost a very small constant value. However, in the frequency range lower than 37 Hz, C_0 almost reaches another constant value of about 0.2 F/m^2, which means that a large charge of the ionic double layers is formed. To describe the two different capacitance stages between the low frequency and the high frequency is that the behavior of the ionic double layers corresponding to the AC electric field changes from a lower frequency behavior to a high-frequency behavior. The reason is unclear.

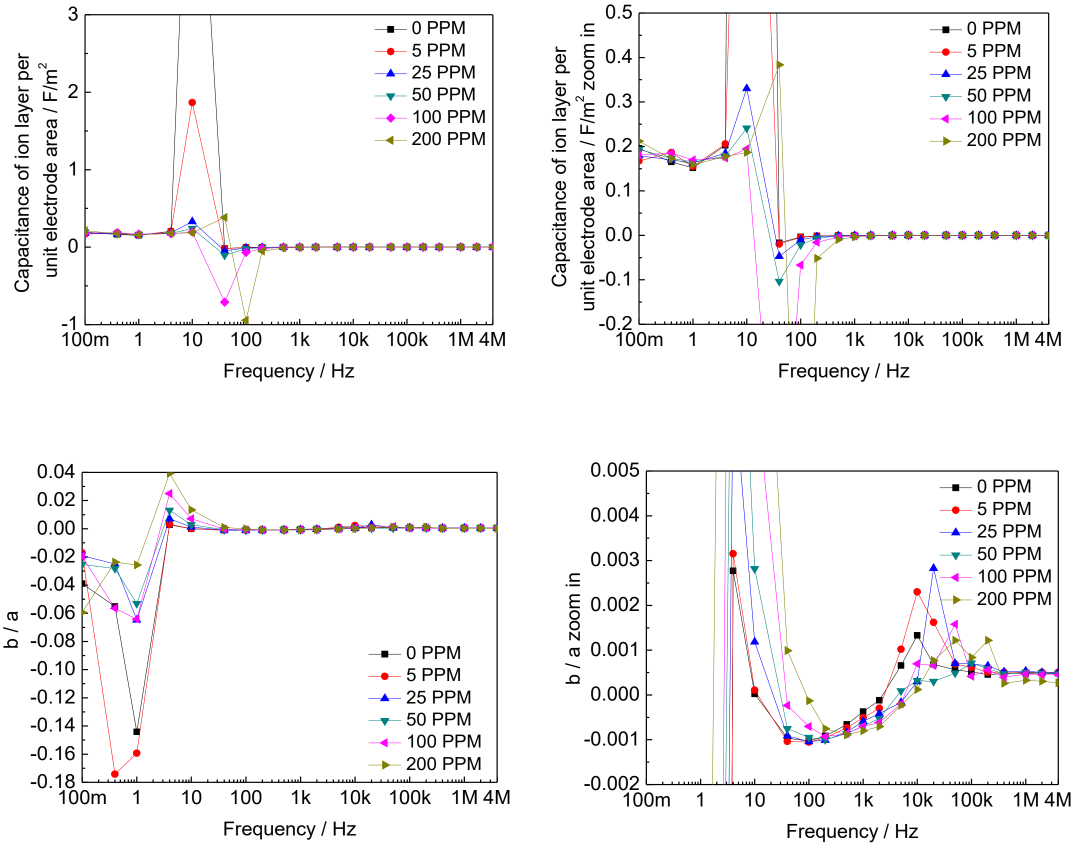

Figure 4.25 Capacitance spectrums of the ionic double layer per unit electrode area (a); zoom in figure (b); and b/a spectrums (which are related to C_0 and Δ) in different concentrations of the dielectric solutions/disinfectants (c); zoom in figure (d).

Table 4.11 The capacitance of the ionic double layer per unit electrode area (F/m^2) in different concentrations of the disinfectants.

		Disinfectant concentration / PPM					
		0	5	25	50	100	200
		C_0 / F•m^{-2}					
Frequency	0.1 Hz	1.96E-01	1.67E-01	1.79E-01	1.93E-01	1.80E-01	2.12E-01
	0.4 Hz	1.65E-01	1.86E-01	1.70E-01	1.73E-01	1.85E-01	1.72E-01
	1 Hz	1.52E-01	1.55E-01	1.63E-01	1.65E-01	1.70E-01	1.59E-01
	4 Hz	2.02E-01	2.06E-01	1.85E-01	1.78E-01	1.74E-01	1.77E-01
	9 Hz	6.87E+00	1.87E+00	3.30E-01	2.41E-01	1.95E-01	1.87E-01
	37 Hz	-1.69E-02	-1.96E-02	-4.71E-02	-1.03E-01	-7.10E-01	3.83E-01
	100 Hz	-3.56E-03	-4.51E-03	-9.97E-03	-2.13E-02	-6.68E-02	-9.44E-01
	200 Hz	-1.26E-03	-1.56E-03	-3.22E-03	-6.33E-03	-1.59E-02	-5.18E-02
	500 Hz	-3.87E-04	-4.50E-04	-8.66E-04	-1.61E-03	-3.77E-03	-9.52E-03

	1 kHz	-2.31E-04	-2.15E-04	-4.09E-04	-6.41E-04	-1.50E-03	-3.43E-03
	2 kHz	-2.52E-04	-1.27E-04	-1.90E-04	-2.76E-04	-5.41E-04	-1.25E-03
	5 kHz	1.33E-05	1.25E-05	-1.10E-04	4.23E-04	-3.95E-04	-9.13E-04
	10 kHz	3.53E-06	3.25E-06	2.64E-05	4.70E-05	4.50E-05	5.83E-04
	20 kHz	3.93E-06	2.18E-06	2.20E-06	1.68E-05	1.70E-05	3.41E-05
	50 kHz	3.61E-06	3.21E-06	3.34E-06	5.56E-06	3.04E-06	6.85E-06
	100 kHz	3.79E-06	3.23E-06	3.05E-06	3.24E-06	5.86E-06	4.51E-06
	200 kHz	4.17E-06	3.78E-06	3.11E-06	3.39E-06	3.72E-06	2.37E-06
	400 kHz	3.94E-06	3.76E-06	3.75E-06	4.07E-06	4.89E-06	7.49E-06
	1 MHz	3.88E-06	3.73E-06	3.61E-06	3.81E-06	4.12E-06	5.86E-06
	2 MHz	3.84E-06	3.73E-06	3.77E-06	3.91E-06	4.24E-06	6.13E-06
	4 MHz	3.85E-06	3.70E-06	3.75E-06	4.00E-06	4.18E-06	6.79E-06

From Figures 4.25(c), 4.25(d), and Table 4.12, in the frequency range higher than 37 Hz, the trend of b/a can be observed, where the frequency range can be further separated into two ranges. From 37 Hz to 2 kHz, b/a is a negative value for the disinfectants in different concentrations. From 10 kHz to 4 MHz, b/a is a positive value for the disinfectants in different concentrations. However, in the frequency range lower than 37 Hz, the b/a value is highly unstable. The reason for the unstable low-frequency values is not clear. The influence of both C_0 and Δ of the ionic double layers will be discussed next.

Table 4.12 Calculated b/a (which is related to C_0 and Δ of the ionic double layer) in different concentrations of the disinfectants.

		Disinfectant concentration / PPM					
		0	5	25	50	100	200
		b/a					
Frequency	0.1 Hz	-3.90E-02	-1.70E-02	-1.91E-02	-2.53E-02	-1.95E-02	-5.94E-02
	0.4 Hz	-5.51E-02	-1.74E-01	-2.50E-02	-2.82E-02	-5.65E-02	-2.37E-02
	1 Hz	-1.44E-01	-1.59E-01	-6.48E-02	-5.32E-02	-6.41E-02	-2.58E-02
	4 Hz	2.77E-03	3.16E-03	7.13E-03	1.31E-02	2.50E-02	3.92E-02
	9 Hz	2.39E-05	1.06E-04	1.18E-03	2.82E-03	7.06E-03	1.35E-02
	37 Hz	-9.64E-04	-1.04E-03	-9.16E-04	-7.54E-04	-2.34E-04	9.90E-04
	100 Hz	-1.03E-03	-1.05E-03	-1.04E-03	-9.48E-04	-7.05E-04	-1.30E-04
	200 Hz	-9.14E-04	-9.57E-04	-1.01E-03	-1.00E-03	-9.30E-04	-7.54E-04
	500 Hz	-6.60E-04	-7.36E-04	-8.31E-04	-8.62E-04	-8.61E-04	-8.92E-04
	1 kHz	-3.73E-04	-5.08E-04	-5.84E-04	-6.92E-04	-7.01E-04	-7.98E-04
	2 kHz	-1.19E-04	-2.97E-04	-4.19E-04	-5.30E-04	-6.13E-04	-7.03E-04
	5 kHz	6.58E-04	1.02E-03	-1.66E-04	9.05E-05	-1.99E-04	-2.29E-04

10 kHz	1.33E-03	2.30E-03	2.98E-04	3.20E-04	6.94E-04	1.23E-04
20 kHz	6.83E-04	1.62E-03	2.83E-03	3.03E-04	6.56E-04	7.69E-04
50 kHz	5.63E-04	6.93E-04	7.04E-04	4.90E-04	1.58E-03	1.22E-03
100 kHz	5.16E-04	6.17E-04	6.97E-04	7.10E-04	4.15E-04	8.35E-04
200 kHz	4.55E-04	5.08E-04	6.51E-04	5.88E-04	5.62E-04	1.22E-03
400 kHz	4.81E-04	5.07E-04	5.15E-04	4.70E-04	3.94E-04	2.61E-04
1 MHz	4.85E-04	5.09E-04	5.33E-04	5.04E-04	4.68E-04	3.27E-04
2 MHz	4.86E-04	5.04E-04	5.02E-04	4.86E-04	4.49E-04	3.06E-04
4 MHz	4.83E-04	5.06E-04	5.00E-04	4.69E-04	4.51E-04	2.71E-04

From Figures 4.25(c), 4.25(d), and Table 4.12, by analysis of Eq. (4-12), at the low-frequency range from 37 Hz to 2 kHz, the relation between *C₀* and Δ can be experimentally found below:

$$C_0 \cdot \Delta > 2\varepsilon_0\varepsilon_r = constant \qquad (4\text{-}13)$$

At the high-frequency range from 10 kHz to 4 MHz, another relation between *C₀* and Δ can be experimentally found below:

$$C_0 \cdot \Delta < 2\varepsilon_0\varepsilon_r = constant \qquad (4\text{-}14)$$

In the frequency range from 37 Hz to 4 MHz, when the frequency increases from low to high, the value of $C_0 \cdot \Delta$ gradually decreases from larger than $+2\varepsilon_0\varepsilon_r$ to lower than $-2\varepsilon_0\varepsilon_r$. Therefore, either the capacitance, the thickness, or both, of the ionic double layers changes when frequency increases. A further elaborately designed experiment is probably needed to classify which parameter of the ionic double layers changes with the testing frequency.

In summary, in this section, in the frequency range higher than 37 Hz, the measured real permittivity can reflect the true real permittivity of the disinfectants and the preferred electrode distance, *d*, for better-measured results is 4mm and 5mm. In the frequency range lower than 37 Hz, unclear results/phenomena are exhibited. The good disinfectant sensing frequency can be chosen from 100 Hz to 4 MHz to obtain preferable sensing of the disinfectants by using the newly developed dielectric sensing methodology.

4.6 Sensing stability of the delta characteristic frequencies at different disinfectant concentrations

The sensing accuracy needs to be studied for the newly developed dielectric sensing methodology to detect the concentration of the disinfectant. The sensing stability of the (calculated) delta characteristic frequencies at five different disinfectant concentrations is analyzed in this section.

4.6.1 Repeatability measurements on dielectric spectrums at different disinfectant concentrations

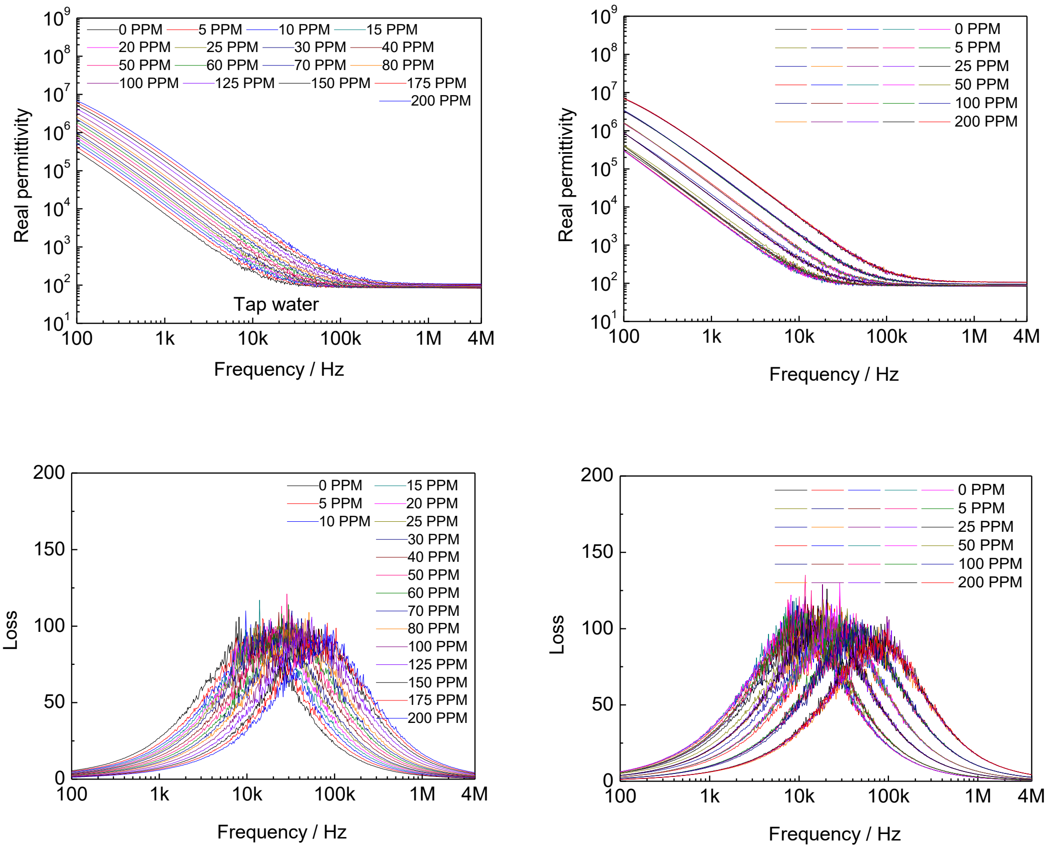

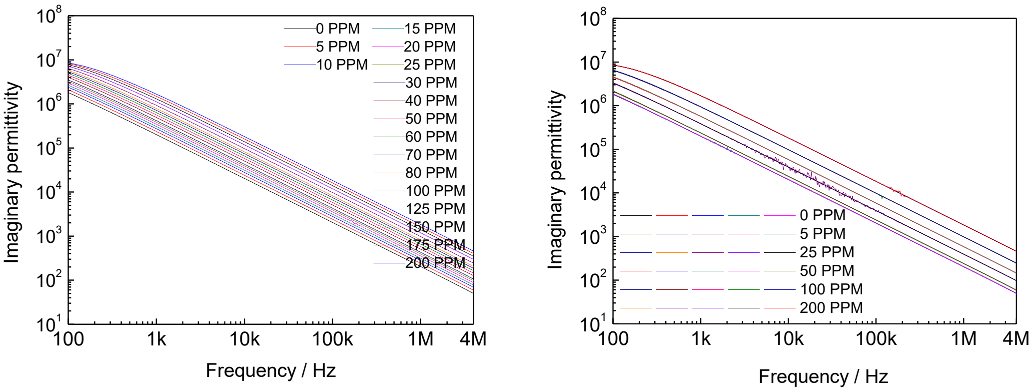

Figure 4.26 Real permittivity, dielectric loss, imaginary permittivity vs frequency spectrums (100 Hz - 4MHz) of the disinfectants in different concentrations (0, 5, 25, 50, 100, 200 PPM) prepared by the tap water and five-time repeatability results. (a) The real permittivity of all concentrations; (b) real permittivity of five-time tests; (c) loss of all concentrations; (d) loss of five-time tests; (e) imaginary permittivity of all concentrations; (f) imaginary permittivity of five-time tests.

Figure 4.26 shows the frequency dependence of the real dielectric permittivity, dielectric loss, and imaginary permittivity of the NaClO disinfectants prepared by the tap water, respectively. As shown in Figures 4.26(a), 4.26(c), 4.26(e), for the disinfectants measured at low frequency, when the NaClO concentration increases, the real permittivity, and the imaginary permittivity increase, respectively, and the peak of the dielectric loss shifts to the high frequency. The trends of the spectrums of the real permittivity, loss, and imaginary permittivity of the disinfectant when increasing the disinfectant concentration are the same as the trends of the measured spectrums described in detail in Section 4.3.1.

Figures 4.26(b), 4.26(d), 4.26(f), show the five-time repeatability spectrums of the real permittivity, dielectric loss, and imaginary permittivity, of the NaClO disinfectants in five (selected) different concentrations prepared by the tap water, respectively. It is found that the repeatability of the five-time measurements is almost identical for all three dielectric property spectrums. Therefore, the repeatability results roughly reveal that the continuous dielectric sensing of the disinfectants is reliable/stable.

4.6.2 Calculations of the standard deviations of the characteristic frequencies at different disinfectant concentrations

Figure 4.27 shows the linear fittings of the linear portion of the five-time measurement results of the real permittivity spectrums of the disinfectants prepared by the tap water, respectively. Following the calculation methodology illustrated in Figure 4.4 in Section 4.2, the characteristic frequencies of the disinfectants in five different concentrations prepared by the tap water are calculated.

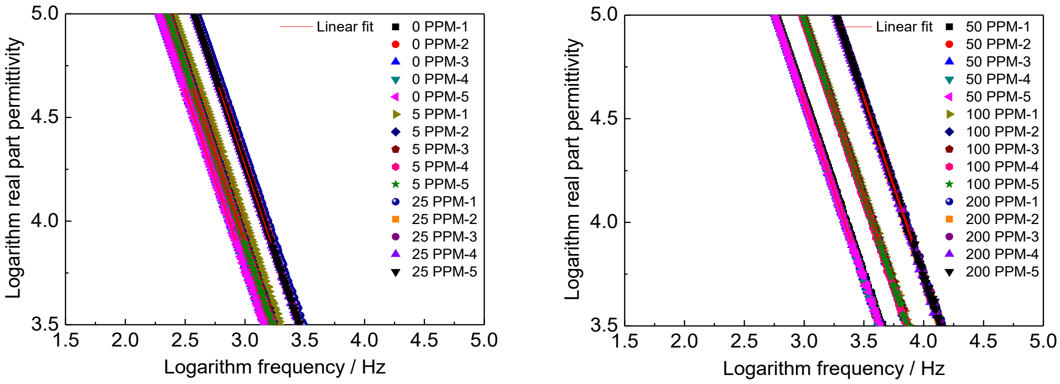

Figure 4.27 Linear fittings of the five-time measurement results of the logarithm real permittivity vs logarithm frequency of the NaClO disinfectants in different concentrations prepared by the tap water. The fitting range is from the permittivity of 3.90 to 4.65. (a) 0, 5, 25 PPM; (b) 50, 100, 200 PPM.

Figure 4.28 shows the calculated characteristic frequency vs disinfectant concentration of the disinfectants in five different concentrations prepared by the tap water. The data points of the characteristic frequency vs NaClO concentration of the disinfectants in five different concentrations can be found in Figure 4.28(a) and the calculated values of the characteristic frequencies are shown in Table 4.13. Figure 4.28(b) shows the data points of the delta characteristic frequency vs NaClO concentration of the disinfectants in five different concentrations. It is found that the data points in each NaClO concentration are very close/almost identical. A good linear fitting of the average values of the data points of the characteristic frequencies of the disinfectants in five different concentrations is shown in Figure 4.28(c). From Figure 4.28(c), the standard deviations of the disinfectants in different concentrations are marked. The average values of the characteristic frequencies and the standard deviations are shown in Table 4.13. It reveals that the standard deviations of the disinfectants are small compared to the average values of the characteristic frequencies, which means that a good sensing accuracy can be achieved. For example, for the detection of the concentration of 5 PPM, the sensing accuracy is about 0.39 PPM. For the detection of the concentration of 25 PPM, which implies the standard safety concentration for the disinfection of the fresh produce, the sensing accuracy is about 1.19 PPM. For the detection of the high concentration of 100 PPM, the sensing accuracy is about 2.07 PPM. Hence, the disinfectant sensing accuracy (relatively) increases with the increase of the disinfectant concentration. In summary, the sensing accuracy is good for the in-situ, continuous detection of the NaClO disinfectant in tap water.

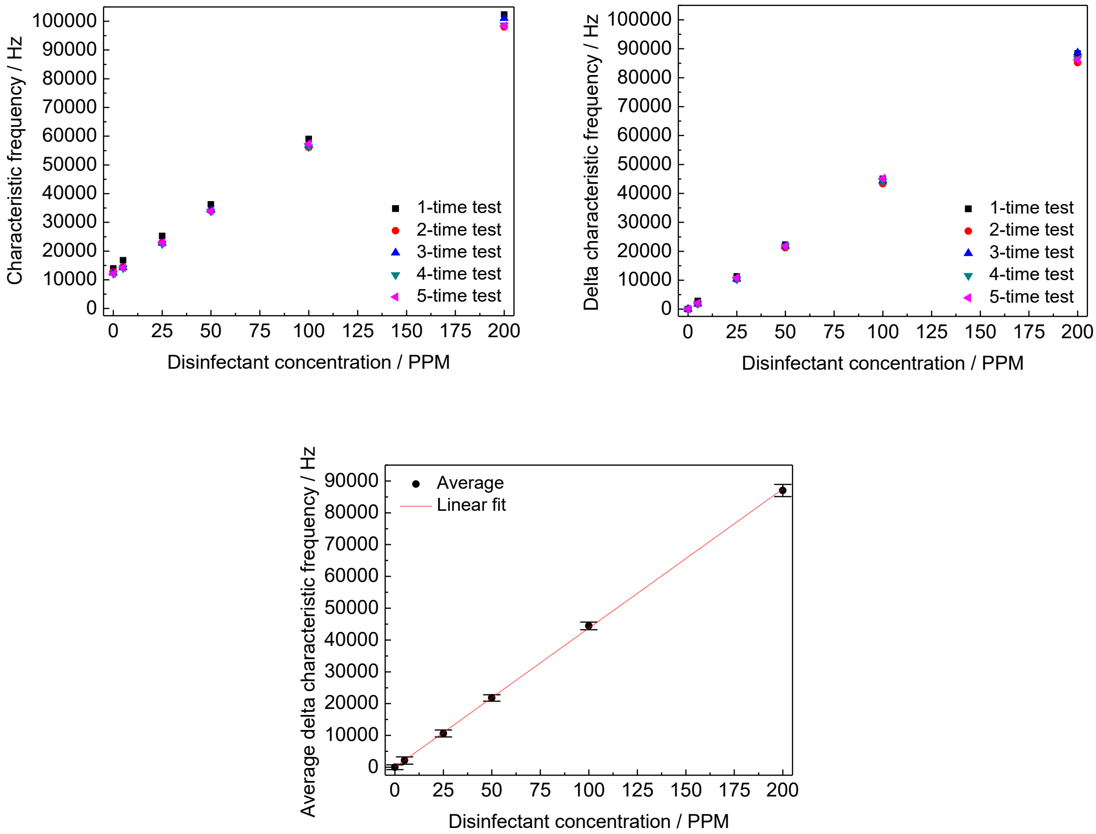

Figure 4.28 Five-time measurement data points of the characteristic frequency vs disinfectant concentration (a); five-time measurement data points of the delta characteristic frequency (after subtracting the intercept of each pure water) vs disinfectant concentration (b); and the average values of the data points of the delta characteristic frequency vs disinfectant concentration with error bars and the linear fitting (c).

Table 4.13 Calculated characteristic frequencies of the five-time measurements on real permittivity spectrums at the NaClO disinfectant concentration of 5, 25, 50, 100, 200 PPM prepared by the tap water. Average values and standard deviations are calculated.

		Disinfectant concentration					
		0 PPM	5 PPM	25 PPM	50 PPM	100 PPM	200 PPM
Characteristic frequency / Hz	Measurement 1	13959	16830	25249	36248	59044	102334
	Measurement 2	12769	14554	23045	33999	56111	97985
	Measurement 3	12406	14258	22824	34283	56830	101082

	Measurement 4	12124	14052	22460	33851	56277	98658
	Measurement 5	12132	14238	22931	33924	57359	98358
	Average	12678	14787	23302	34461	57124	99684
	Standard deviation	763	1157	1110	1012	1180	1915
Sensing accuracy / PPM		/	0.39	1.19	1.47	2.07	3.84

4.7 Influence of the soil and sand on dielectric spectrums of the disinfectant

During the disinfection and wash processes of the fresh produce, a very little amount of the dirt/topsoil probably can be brought to/mixed with the disinfectant aqueous solution. The mixing of the topsoil might influence the sensing accuracy of the concentration of the disinfectant. However, the patent which has been filed previously does not illustrate the potential influence of mixed substances such as air or soil which are considered low permittivity materials (1 for the air and about 3~7 for the different soils and sand). Therefore, as the new dielectric analysis and calculation methodology has been developed, it is very necessary to study the possible influence of the soil mixing issue (and the air mixing issue is the same).

4.7.1 Permittivity equation of the disinfectant mixing with the soil

The permittivity (spectrum) of the disinfectant mixing with the substances (soil for instance) at a (specific) disinfectant concentration prepared by one type of water, $\varepsilon_{r\,(mix,\,water\,type,\,conc)}$, can be expressed as follows:

$$\varepsilon_{r(mix,water\ type,conc)} = \varepsilon_{r(dis,water\ type,conc)}^{1-\varphi} \cdot \varepsilon_{r(sub,water\ type,conc)}^{\varphi} \qquad (4\text{-}15)$$

where φ is the volume percentage of the substance; thus, 1-φ is the volume percentage of the disinfectant after mixing with the substance; $\varepsilon_{r(dis,\ water\ type,\ conc)}$ is the permittivity of the disinfectant without mixing with the substance at a disinfectant concentration prepared by one type of water; $\varepsilon_{r(sub,\ water\ type,\ conc)}$ is the permittivity of the substance mixed with the disinfectant prepared by one type of water.

Take the logarithm of both sides:

$$lg\varepsilon_{mix,water\ type,conc} = (1-\varphi)\cdot \lg\varepsilon_{r(dis,water\ type,conc)} + \varphi \cdot lg\varepsilon_{r(sub,water\ type,conc)} \quad (4\text{-}16)$$

Eq. (4-16) is valid in the frequency range from low (about 10 Hz) to high (4 MHz) according to Figure 4.4 and Figure 4.19. Since the characteristic frequency in the proposed methodology is calculated based on the two frequency ranges of the linear lines/curves of the permittivity spectrum in both logarithm scales of the permittivity and the frequency, Eq. (4-16) reveals that the influence of the mixed substances is linearly affecting the permittivity of the disinfectant. In other words, the permittivity spectrum shifts proportionally in the figure in logarithm scales of both the permittivity and the frequency. As a result, the calculated characteristic frequencies for different disinfectant concentrations do not change with the mixing of the substance (such as the soil). Therefore, theoretically, mixing with either the soil or the air (in a little volume percentage) would not influence the sensing reliability/accuracy by using the newly developed dielectric calculation methodology. Experiment results of the disinfectants mixing with the sand/soils will be analyzed and discussed in the next section.

4.7.2 Experiment results and discussion

Figure 4.29 shows the frequency dependence of the real dielectric permittivity on the tap water mixed with the sand and topsoil in mixing ratios (w/v) of 0%, 0.025%, 0.25%, and 2.5%, respectively. As shown in Figure 4.29(a), for the tap water mixed with each ratio of the sand/topsoil, the real permittivity decreases with the frequency increases until the permittivity decreases to a constant value of about 80 where a dielectric relaxation of the disinfectant ions occurs. Moreover, when the mixing ratio of the topsoil increases, the real permittivity increases in the low-frequency range. But, it seems that when the mixing ratio of the sand increases, the real permittivity spectrum will not change. As shown in Figure 4.29(b), the loss peak shifts to a high frequency when the mixing ratio of the topsoil increases. But, when the mixing ratio of the sand increases, the loss spectrum of the tap water will not change. In the case of the imaginary permittivity, as shown in Figure 4.29(c), a similar trend can be found that the spectrum increases with increasing the mixing ratio of the topsoil. But, it also seems that the mixing of the sand could not influence the imaginary spectrum of the tap water. In summary, a little large amount of the soil (i.e., 0.25% and above) mixing with the tap water could influence the dielectric spectrums of the tap water. However, mixing with the sand (i.e., 0.025% - 2.5%) or a very little amount of the topsoil (0.025%) barely influences the dielectric spectrums of the tap water.

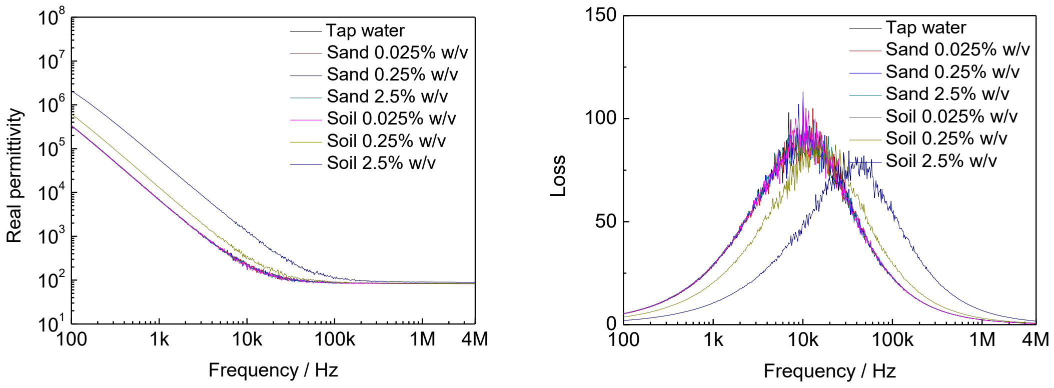

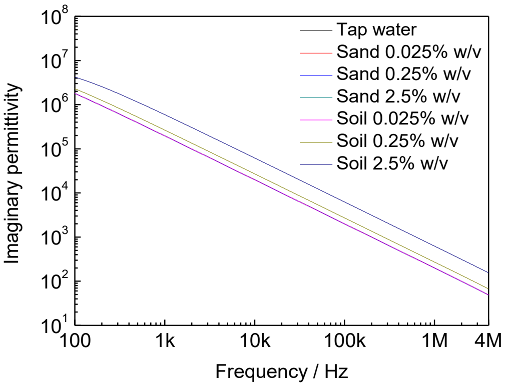

Figure 4.29 Frequency dependence of the real part dielectric permittivity on tap water mixed with the sand and topsoil in mixing ratios (w/v) of 0%, 0.025%, 0.25%, and 2.5%, respectively.

Figure 4.30 shows the linear fittings of the linear portion of the real permittivity spectrums of the tap water mixed with different masses of sand and topsoil. Following the calculation methodology illustrated in Figure 4.4 in Section 4.2, the characteristic frequency of the tap water mixed with the sand and topsoil is calculated from the point of the intersection of the extension line of the linear fittings of the logarithm real permittivity spectrums at low frequency and the extension line of the constant real permittivity at high frequency, respectively.

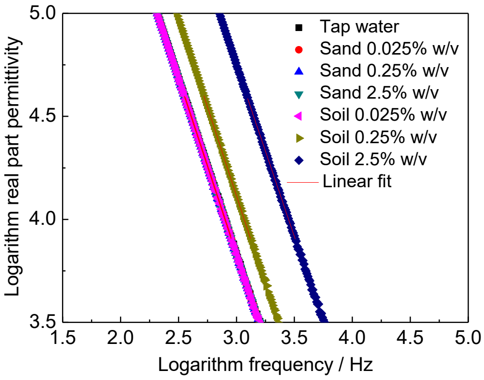

Figure 4.30 Linear fittings of the data points of the logarithm real permittivity vs logarithm frequency of the tap water mixed with different ratios of the sand and topsoil. The linear fitting range is from the permittivity of 3.90 to 4.65.

Figure 4.31 shows the characteristic frequency vs the mixing ratio (w/v) of the sand and topsoil in the tap water. From Figure 4.31(a), it is found that the characteristic frequency is independent of the mixing ratio of the sand in the tap water. The possible reason is that the sand does not contain organic matter and there is barely a dissolution of salts in the tap water. From Figure 4.31(b), it is revealed that the characteristic frequency of the tap water mixed with a small mass of the topsoil (i.e., 0.025%) is almost not influenced compared to that of the tap water (i.e., 0%). These results are identical to the theoretical analysis based on Eq. (4-16) in Section 4.7.1. However, when the mixing ratio of the topsoil increases to 0.25% (w/v), a substantial increase in the characteristic frequency can be observed. The possible reason is that the topsoil contains a considerable mass of organic matter and salts, which could be partially dissolved in the disinfectant/water and influence its characteristic frequency. Which content (organic matter and salts) contribute more is unknown. When the mixing ratio increases to 2.5% (w/v), a significant increase in the characteristic frequency can be observed. In the applications of disinfection of the fresh produce, as shown in Figure 1.3 in Section 1.3.1, the prewash process could get rid of a big portion of the topsoil which is attached to the fresh produce. And the disinfection and wash processes are the major processes after the prewash process, where the sensors are supposed to be placed. Therefore, very little organic matter is dissolved in the water during the disinfection and wash processes of the fresh produce. It can be concluded that, when mixing with a very little mass of the organic matter (i.e., no more than 0.025%) or a relatively larger amount of the sand in the tap water/disinfectant during the disinfection and wash processes, the detection of the disinfectant in the tap water cannot be influenced. Similarly, by analogy, it is also applicable to mix the air (in a small volume percentage) in the disinfectant without varying the sensing result/accuracy. Therefore, it is not necessary to conduct an adjustment on the dielectric sensing of the disinfectant during the disinfection and wash processes of the fresh produce when a very little mass of the topsoil is possibly mixed with the tap water.

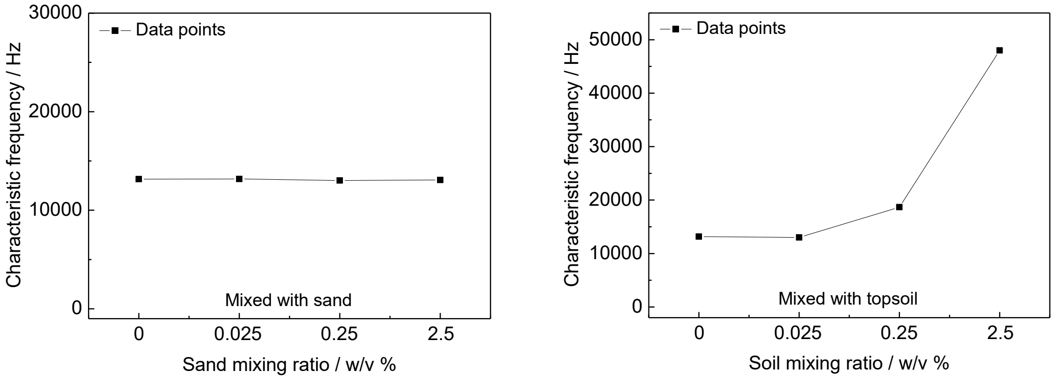

Figure 4.31 The characteristic frequency vs mixing ratio (w/v) of the sand (a), and topsoil (b) in the tap water.

4.8 Conclusions

1. A new dielectric sensing and analysis methodology was developed to rapidly detect disinfectants in water. This dielectric sensing method was based on the determination of a characteristic frequency, which changes with the disinfectant concentration in water. This dielectric sensing method has many advantages, such as time-saving, inexpensive, simple handling, and long-time durability, over other sensing technologies.

2. A linear relation between the characteristic frequency and NaClO disinfectant concentration in water in the range from 0 to 200 PPM was found.

3. Water quality influence on disinfectant concentration sensing was studied. A modification method was used to eliminate/mitigate the influence of water quality issues.

4. Electrode polarization effect on the dielectric sensing methodology was very small. The measured real permittivity spectrum in a wide frequency range was able to reflect the real permittivity of the disinfectants.

5. Soil influence on the dielectric sensing of the disinfectants was theoretically and experimentally studied. Compared with dielectric sensing at a single frequency, the sensing stability of the disinfectant mixing with the soil was more reliable. This sensing methodology has a potential application in real-time in-situ detection on disinfectant concentration for disinfection and wash processes of fresh produce production.

Chapter 5 Conclusions

1. A novel low-cost, in-situ, wireless sensor platform – MSP sensor with a dimension of 13.5 mm × 4.5 mm × 30 μm coated by a thin layer of water-sensitive polymers, CNF, and crosslinked PVA, respectively, was developed.

2. The crosslinked PVA-MSP humidity sensor had both water-resistant capability and high humidity sensing sensitivity. A fundamental study was carried out to optimize the GA/PVA ratio to obtain the crosslinked PVA film with the best match of water-resistant capability and water absorption ability.

3. The sensor signal, i.e., the resonant frequency of the sensor, is linearly dependent on RH. The change in the resonant frequency of the sensor is also linearly dependent on the thickness of the PVA layer. Moreover, the long-time stability of the sensor with the crosslinked PVA layer was improved compared with those of the sensors with the non-crosslinked PVA layer and with the CNF layer. Further, good stability was obtained during a 20-day test. Besides, the sensor can work in an environment that was directly exposed to water.

4. A high dielectric permittivity core-shell BTO-SiO_2 ceramics humidity sensor was developed. The sensor based on capacitance/effective permittivity change corresponding to humidity change has the potential to be used to develop a passive wireless LC humidity resonant sensor to be used in agricultural applications.

5. The ceramics sensor has a long-time humidity testing stability. It is theoretically analyzed and experimentally verified that the ceramics sensor with flat surface electrodes can be used without any influence from the soils at any frequency in the tested humidity range.

6. A new dielectric sensing and analysis methodology was developed to rapidly detect

disinfectants in water. This dielectric sensing method was based on the determination of a characteristic frequency, which changes with the disinfectant concentration in water. This dielectric sensing method has many advantages, such as time-saving, inexpensive, simple handling, and long-time durability, over other sensing technologies.

7. A linear relation between the characteristic frequency and NaClO disinfectant concentration in water in the measurement range was found. Water quality influence on disinfectant concentration sensing was studied.

8. Soil influence on the dielectric sensing of the disinfectants was theoretically and experimentally studied. Compared with dielectric sensing at a single frequency, the sensing stability of the disinfectant mixing with the soil was more reliable. This sensing methodology has a potential application in real-time in-situ detection on disinfectant concentration for disinfection and wash processes of fresh produce production.

Chapter 6 Future work

In Chapter 2, homemade coils are used and connected to a precision impedance analyzer for wirelessly interrogating with the polymer-MSP humidity sensors. There are some issues worth to be studied. First, a small, convenient, handheld interrogating device needs to be developed to replace the current sensing modules with a relatively large size, which can support field measurements. Second, although the homemade coils are used for wirelessly sensing and it is also known that the 1-inch MSP sensor/strip can achieve more than a 1-meter wireless sensing distance in the application of the anti-theft purpose in stores and supermarkets, the wireless sensing distance of the polymer-MSP sensors could be optimized in the future work to balance the strength of the sensing signal and the wireless sensing distance. Future researchers may optimize the configuration of the wireless detection coils to enhance the wireless sensing signal. Finally, the effective wireless sensing distance of the polymer-MSP sensors can be maximized.

In Chapter 3, the humidity sensing performance of the main sensing module, i.e., the high permittivity core-shell BTO-SiO_2 ceramics humidity capacitor/sensor with flat surface electrodes has been comprehensively studied. However, the mechanism of the change of the dielectric property spectrums corresponding to the humidity change has been found different from the typical mechanism and is currently not understood. Therefore, in future work, the study probably should focus on the finding of the mechanism of the dielectric property change with the humidity. Some material characterization techniques, such as XRD and TEM, are probably required for a better understanding of the microstructure and the sensing mechanism of the material.

In Chapter 4, based on the influence of the EP on the measured capacitance, a model (i.e., Eq. (4-7)) of the multi-layer capacitance in series configuration has been developed for a better understanding of the ionic double layer and its influence on the total capacitance. It is found in the experiment that, in the frequency range from 37 Hz to 4 MHz, when frequency increases from low to high, the value of $C_0 \cdot \Delta$ gradually decreases from larger than $+2\varepsilon_0\varepsilon_r$ to lower than $-2\varepsilon_0\varepsilon_r$. Therefore, an issue is found that either the capacitance, the thickness, or both, of the ionic double layers changes, when frequency increases. In future work, a further elaborately designed experiment is probably needed to classify which parameter (C_0 and Δ) of the ionic double layers changes with the testing frequency. It is proposed that a probe with a changeable distance of the electrodes, where the minimum electrode distance could be adjusted down to 100 μm, should be manufactured to meet the high requirements of parallelism and surface roughness of the electrodes for reliable measurements. This approach is temporarily very difficult to process based on the current experiment equipment.

References

[1] N. Johnson, C. Revenga, J. Echeverria. Managing water for people and nature. Science 292.5519(2001):1071-1072.

[2] I.A. Shiklomanov. Comprehensive assessment of the freshwater resources and water availability in the world: assessment of water resources and water availability in the world. Geneva (Switzerland): World Meteorological Organization (1997).

[3] H. Yin, Y. Cao, B. Marelli, X. Zeng, A.J. Mason, C. Cao. Soil sensors and plant wearables for smart and precision agriculture. Advanced Materials 33.20(2021):2007764.

[4] N. Zhang, M. Wang, N Wang. Precision agriculture-a worldwide overview. Computers and electronics in agriculture 36(2002):113-132.

[5] R. Bogue. Sensors key to advances in precision agriculture. Sensor Review (2017).

[6] K. Noborio. Measurement of soil water content and electrical conductivity by time domain reflectometry: a review. Computers and electronics in agriculture 31.3(2001):213-237.

[7] A. Allende, M.V. Selma, F. López-Gálvez, R. Villaescusa, M.I. Gil. Role of commercial sanitizers and washing systems on epiphytic microorganisms and sensory quality of fresh-cut escarole and lettuce. Postharvest Biology and Technology 49.1(2008):155-163.

[8] S.B. Jones, J.M. Wraith, and D. Or. Time domain reflectometry measurement principles and applications. Hydrological Processes 16.1(2002):141-153.

[9] D.A. Robinson, S.B. Jones, J.M. Wraith, D. Or, S.P. Friedman. A review of advances in dielectric and electrical conductivity measurement in soils using time domain reflectometry. Vadose Zone Journal 2.4(2003):444-475.

[10] E. Veldkamp, J.J. O'Brien. Calibration of a frequency domain reflectometry sensor for

humid tropical soils of volcanic origin. Soil Science Society of America Journal 64.5(2000):1549-1553.

[11] A. Robert. Dielectric permittivity of concrete between 50 MHz and 1 GHz and GPR Measurements for building materials evaluation. Journal of applied geophysics 40(1998):89-94.

[12] S. Fityus, T. Wells, W. Huang. Moisture content measurement in expansive soils using the neutron probe. Geotechnical Testing Journal 34(2011):1-10.

[13] F.S. Zazueta, J. Xin. Soil Moisture Sensors. Florida Cooperative Extension Service, Bulletin 292, Inst. Food and Agricultural Sciences, University of Florida, Gainesville, 1994.

[14] B.R. Scanlon, B.J. Andraski, J. Bilskie. 3.2. 4 Miscellaneous methods for measuring matric or water potential. Methods of Soil Analysis 643-670, 2002.

[15] F. Shuai, D.G. Fredlund. Use of a new thermal conductivity sensor to measure soil suction. Advances in unsaturated geotechnics. Geotechnical Spec. Publ. 99. Proc. of Sessions in Geo-Denver 1-12, 2000.

[16] M. Persson, J.M. Wraith, T. Dahlin. A Small-Scale Matric Potential Sensor Based on Time Domain Reflectometry. Soil Science Society of American Journal 70(2006):533-536.

[17] O.W. Israelsen. Water-holding capacity of irrigated soils. Utah Agricultural College Experiment Station, 1922.

[18] N.C. Brady, R.R. Weil, R.R. Weil. The nature and properties of soils. Upper Saddle River, NJ: Prentice Hall, Vol 13, 2008.

[19] M. Bittelli. Measuring soil water potential for water management in agriculture: A review. Sustainability 2.5(2010)1226-1251.

[20] S.A. Imam, A. Choudhary, V.K. Sachan. Design issues for wireless sensor networks and smart humidity sensors for precision agriculture: A review. 2015 International Conference on Soft Computing Techniques and Implementations (ICSCTI). IEEE, 2015:181-187.

[21] V.S. Palaparthy, M.S. Baghini, D.N. Singh. Review of polymer-based sensors for agriculture-related applications. Emerging Materials Research 2.4(2013):166-180.

[22] Z. Chen, C. Lu. Humidity sensors: a review of materials and mechanisms. Sensor letters 3.4(2005):274-295.

[23] H. Farahani, R. Wagiran, M.N. Hamidon. Humidity sensors principle, mechanism, and fabrication technologies: a comprehensive review. Sensors 14.5(2014):7881-7939.

[24] W.F. Fett. Factors affecting the efficacy of chlorine against Escherichia coli O157:H7 and Salmonella on alfalfa seed. Food Microbiology 19,2-3(2002):135-149.

[25] W.F. Fett. Reduction of Escherichia coli O157:H7 and Salmonella spp. on laboratory-inoculated mung bean seed by chlorine treatment. Journal of Food Protection 65,5(2002):848-852.

[26] R.E. Wilson, I. Stoianov, D. O’Hare. Continuous chlorine detection in drinking water and a review of new detection methods. Johnson Matthey Technology Review 63.2(2019):103-118.

[27] U. Pinkernell, B. Nowack, H. Gallard, U.V. Gunten. Methods for the photometric determination of reactive bromine and chlorine species with ABTS. Water Research 34.18(2000):4343-4350.

[28] H. Yu, L. Zheng. Manganese dioxide nanosheets as an optical probe for photometric determination of free chlorine. Microchimica Acta 183.7(2016):2229-2234.

[29] M. Szili, I. Kasik, V. Matejec, G. Nagy, B. Kovacs. Poly (luminol) based sensor array for determination of dissolved chlorine in water. Sensors and Actuators B: Chemical 192(2014):92-98.

[30] Y.T. Chang, K.C. Lin, S.M. Chen. Preparation, characterization and electrocatalytic properties of poly (luminol) and polyoxometalate hybrid film modified electrodes. Electrochimica acta 51.3(2005):450-461.

[31] A. Kraft, M. Stadelmann, M. Wünsche, M. Blaschke. Electrochemical destruction of organic substances in deionized water using diamond anodes and a solid polymer electrolyte. Electrochemistry communications 8.1(2006):155-158.

[32] C.L. Gopu, A.S. Krishna, K. Sreenivasan. Fluorimetric detection of hypochlorite using albumin stabilized gold nanoclusters. Sensors and Actuators B: Chemical 209(2015):798-802.

[33] Y. Yan, S. Wang, Z. Liu, H. Wang, D. Huang. CdSe-ZnS quantum dots for selective and sensitive detection and quantification of hypochlorite. Analytical chemistry 82.23(2011):9775-9781.

[34] M. Xue, L. Zhang, M. Zou, C. Lan, Z. Zhan, S. Zhao. Nitrogen and sulfur co-doped carbon dots: a facile and green fluorescence probe for free chlorine. Sensors and Actuators B: Chemical 219(2015):50-56.

[35] M. Sun, H. Yu, H. Zhu, F. Ma, S. Zhang, D. Huang, S. Wang. Oxidative cleavage-based near-infrared fluorescent probe for hypochlorous acid detection and myeloperoxidase activity evaluation. Analytical chemistry 86.1(2014):671-677.

[36] N.A. Dimmock, D. Midgley. Modified amperometric membrane probes for determining free and total residual chlorine in saline cooling waters. Water Research 13.12(1979):1317-

1327.

[37] A. Kraft. Electrochemical water disinfection: a short review. Platinum metals review 52.3(2008):177-185.

[38] O. Ordeig, R. Mas, J. Gonzalo, F.J.D. Campo, F.J. Muñoz, C. de Haro. Continuous detection of hypochlorous acid/hypochlorite for water quality monitoring and control. Electroanalysis: An International Journal Devoted to Fundamental and Practical Aspects of Electroanalysis 17.18(2005):1641-1648.

[39] R. Olivé-Monllau, J. Orozco, C. Fernández-Sánchez, M. Baeza, J. Bartrolí, C. Jimenez-Jorquera, F. Céspedes. Flow injection analysis system based on amperometric thin-film transducers for free chlorine detection in swimming pool waters. Talanta 77.5(2009):1739-1744.

[40] J. Muñoz, F. Céspedes, M. Baeza. Modified multiwalled carbon nanotube/epoxy amperometric nanocomposite sensors with CuO nanoparticles for electrocatalytic detection of free chlorine. Microchemical Journal 122(2015):189-196.

[41] J.V. Macpherson. A practical guide to using boron doped diamond in electrochemical research. Physical Chemistry Chemical Physics 17.5(2015):2935-2949.

[42] T. Yano, D.A. Tryk, K. Hashimoto, A. Fujishima. Electrochemical behavior of highly conductive boron-doped diamond electrodes for oxygen reduction in alkaline solution. Journal of the Electrochemical Society 145.6(1998):1870-1876.

[43] C. Heim, M.U. Vivanco, M. Rajab, E. Müller, T. Letzel, B. Helmreich. Rapid inactivation of waterborne bacteria using boron-doped diamond electrodes. International journal of environmental science and technology 12.10(2015):3061-3070.

[44] C. Karuwan, T. Mantim, P. Chaisuwan, P. Wilairat, K. Grudpan, P. Jittangprasert, D. Nacapricha. Pulsed amperometry for anti-fouling of boron-doped diamond in electroanalysis of β-agonists: application to flow injection for pharmaceutical analysis. Sensors 6.12(2006):1837-1850.

[45] R.E. Wilson, I. Stoianov, D. O'Hare. Biofouling and in situ electrochemical cleaning of a boron-doped diamond free chlorine sensor. Electrochemistry Communications 71(2016):79-83.

[46] P.O. Kane, J.M. Young. The design of electrochemical probes for oxygen and chlorine and their applications in process control analysis. Journal of Electroanalytical Chemistry and Interfacial Electrochemistry 75.1(1977):255-267.

[47] Z. Sheng. Development of Magnetostrictive Fe-Co-B Alloys for High-frequency Sensors and Magnetoelectric Composites. Doctoral dissertation, Auburn University, 2015.

[48] L.D. Landau, E.M. Lifshitz. Theory of Elasticity. Pergamon Press, Oxford, 1986.

[49] F.T. Calkins, A.B. Flatau, M.J. Dapino. Overview of magnetostrictive sensor technology. Journal of Intelligent Material Systems and Structures 18.10(2007):1057-1066.

[50] K. Zhang, L. Zhang, L. Fu, S. Li, H. Chen, Z.Y. Cheng. Magnetostrictive resonators as sensors and actuators. Sensors and Actuators A: Physical 200(2013):2-10.

[51] Y. Chai, S. Li, S. Horikawa, M.K. Park, V. Vodyanoy, B.A. Chin. Rapid and sensitive detection of Salmonella Typhimurium on eggshells by using wireless biosensors. Journal of food protection 75.4(2012):631-636.

[52] Y. Chai, H.C. Wikle, Z. Wang, S. Horikawa, S. Best, Z.Y. Cheng, B.A. Chin. Design of a surface-scanning coil detector for direct bacteria detection on food surfaces using a

magnetoelastic biosensor. Journal of Applied Physics 114.10(2013):104504.

[53] Y. Chai, S. Horikawa, S. Li, H.C. Wikle, B.A. Chin. A surface-scanning coil detector for real-time, in-situ detection of bacteria on fresh food surfaces. Biosensors and Bioelectronics 50(2013):311-317.

[54] Y. Chai, S. Horikawa, H.C. Wikle, Z. Wang, B.A. Chin. Surface-scanning coil detectors for magnetoelastic biosensors: A comparison of planar-spiral and solenoid coils. Applied Physics Letters 103.17(2013):173510.

[55] Y. Chai, S. Horikawa, J. Hu, I.H. Chen, J. Hu, J.M. Barbaree, B.A. Chin. In-situ detection of multiple pathogenic bacteria on food surfaces. In Sensing for Agriculture and Food Quality and Safety VII, International Society for Optics and Photonics, 2015.

[56] S. Li, Y. Chai, B.A. Chin. High throughput pathogen screening for food safety using magnetoelastic biosensors. In Sensing for Agriculture and Food Quality and Safety VII, International Society for Optics and Photonics, 2015.

[57] P. Chen, Q. Jiang, S. Horikawa, S. Li. Magnetoelastic-sensor integrated microfluidic chip for the measurement of blood plasma viscosity. Journal of the Electrochemical Society 164.6(2017):B247.

[58] Y. Liu, S. Horikawa, I.H. Chen, S. Du, H.C. Wikle, S.J. Suh, B.A. Chin. Highly sensitive surface-scanning detector for the direct bacterial detection using magnetoelastic (ME) biosensors. In Sensing for Agriculture and Food Quality and Safety IX, International Society for Optics and Photonics, 2017.

[59] C.A. Grimes, D. Kouzoudis, E.C. Dickey, D. Qian, M.A. Anderson, R. Shahidain, L. Green. Magnetoelastic sensors in combination with nanometer-scale honeycombed thin film

ceramic TiO2 for remote query measurement of humidity. Journal of Applied Physics 87.9(2000):5341-5343.

[60] M.A. Fonseca, J.M. English, M. Von Arx, M.G. Allen. Wireless micromachined ceramic pressure sensor for high-temperature applications. Journal of Microelectromechanical Systems 11.4(2002):337-343.

[61] C. Li, Q. Tan, P. Jia, W. Zhang, J. Liu, C. Xue, J. Xiong. Review of research status and development trends of wireless passive LC resonant sensors for harsh environments. Sensors 15.6(2015):13097-13109.

[62] Q.A. Huang, L. Dong, L.F. Wang. LC passive wireless sensors toward a wireless sensing platform: status, prospects, and challenges. Journal of Microelectromechanical Systems 25.5(2016):822-841.

[63] R. Nopper, R. Niekrawietz, L. Reindl. Wireless readout of passive LC sensors. IEEE Transactions on Instrumentation and Measurement 59.9(2009):2450-2457.

[64] T. Nenov, S.P. Yordanov. Ceramic sensors: technology and applications. CRC Press, 1996.

[65] S. Akbar, P. Dutta, C. Lee. High-temperature ceramic gas sensors: a review. International journal of applied ceramic technology 3.4(2006):302-311.

[66] J. Xu, Q. Pan, Z. Tian. Grain size control and gas sensing properties of ZnO gas sensor. Sensors and Actuators B: Chemical 66.1-3(2000):277-279.

[67] J.S.G.D. Santos-Alves, R.F. Patier. The environmental control of atmospheric pollution. The framework directive and its development. The new European approach. Sensors and Actuators B: Chemical 59(1999):69-74.

[68] A. Haeusler, J.U. Meyer. A novel thick film conductive type CO2 sensor. Sensors and Actuators B: chemical 34(1996):388-395.

[69] T. Doll, J. Lechner, I. Eisele, K.D. Schierbaum, W. Gopel. Ozone detection in the ppb range with work function sensors operating at room temperature. Sensors and Actuators B: Chemical, 34(1996):506-510.

[70] S.J. Jung, H. Yanagida. The characterization of a CuO/ZnO heterocontact-type gas sensor having selectivity for CO gas. Sensors and Actuators B: Chemical 37(1996):55-60.

[71] H. Zhu, T.C. Lo, R. Lenigk, R. Renneberg. Fabrication of a novel oxygen sensor with CMOS compatible processes. Sensors and Actuators B: Chemical, 46.2(1998):155-159.

[72] G. Korotchenkov, V. Brynzari, S. Dmitriev. SnO2 films for thin film gas sensor design. Materials Science and Engineering: B 63.3(1999):195-204.

[73] D. Mardare, N. Cornei, C. Mita, D. Florea, A. Stancu, V. Tiron, C. Adomnitei. Low temperature TiO2 based gas sensors for CO2. Ceramics International 42.6(2016):7353-7359.

[74] I. Alessandri, E. Comini, E. Bontempi, G. Faglia, L.E. Depero, G. Sberveglieri. Cr-inserted TiO2 thin films for chemical gas sensors. Sensors and Actuators B: Chemical 128.1(2007):312-319.

[75] E. Traversa. Ceramic sensors for humidity detection: the state-of-the-art and future developments. Sensors and Actuators B: Chemical 23.2-3(1995):135-156.

[76] T.A. Blank, L.P. Eksperiandova, K.N. Belikov. Recent trends of ceramic humidity sensors development: A review. Sensors and Actuators B: Chemical 228(2016):416-442.

[77] J. Wang, X.H. Wang, X.D. Wang. Study on dielectric properties of humidity sensing nanometer materials. Sensors and Actuators B: Chemical 108(2005):445-449.

[78] H.Y. Wang, Y.Q. Wang, Q.F. Hu, X.J. Li. Capacitive humidity sensing properties of SiC nanowires grown on silicon nanoporous pillar array. Sensors and Actuators B: Chemical 166(2012):451-456.

[79] T.L. Yeo, T. Sun, K.T.V. Grattan. Fibre-optic sensor technologies for humidity and moisture measurement. Sensors and Actuators A: Physical 144.2(2008):280-295.

[80] C.H. Lin, C.H. Chen. Sensitivity enhancement of capacitive-type photoresistor-based humidity sensors using deliquescent salt diffusion method. Sensors and Actuators B: Chemical, 129.2(2008):531-537.

[81] L.L. Wang, H.Y. Wang, W.C. Wang, K. Li, X.C. Wang, X.J. Li. Capacitive humidity sensing properties of ZnO cauliflowers grown on silicon nanoporous pillar array. Sensors and Actuators B: Chemical 177(2013):740-744.

[82] Q. Qi, T Zhang, Q. Yu, R. Wang, Y. Zeng, L. Li, H. Yang, Properties of humidity sensing ZnO nanorods-base sensor fabricated by screen-printing. Sensors and Actuators B: Chemical 133.2(2008):638-643.

[83] Y. Deng. Magnetoresistive and Magnetostrictive Sensors for the Mobile Era. Stanford University, ProQuest Dissertations Publishing, 2020, 28241741.

[84] S. Li. Development of novel acoustic wave biosensor platforms based on magnetostriction and fabrication of magnetostrictive nanowires. Dissertation, Auburn University, 2007.

[85] L. Greenspan. Humidity fixed points of binary saturated aqueous solutions. Journal of research of the National Bureau of Standards. Section A, Physics and chemistry, 81.1(1977): 89.

[86] M Parit, H Du, X Zhang, C Prather, M Adams, Z Jiang. Polypyrrole and cellulose nanofiber based composite films with improved physical and electrical properties for electromagnetic shielding applications. Carbohydrate Polymers 240(2020):116304.

[87] L. Bo, P. Wang, Y. Semenova, G. Farrell. Optical microfiber coupler based humidity sensor with a polyethylene oxide coating. Microwave and Optical Technology Letters 57.2(2015):457-460.

[88] L.H. Chen, T. Li, C.C. Chan, R. Menon, P. Balamurali, M. Shaillender, B. Neu, X.M. Ang, P. Zu, W.C. Wong, K.C. Leong. Chitosan based fiber-optic Fabry–Perot humidity sensor. Sensors and Actuators B: Chemical 169(2012): 167-172.

[89] L. Kosuru, A. Bouchaala, N. Jaber, M.I. Younis. Humidity detection using metal organic framework coated on QCM. Journal of Sensors, 2016.

[90] G.A. Eyebe, B. Bideau, N. Boubekeur, E. Loranger, F. Domingue. Environmentally-friendly cellulose nanofibre sheets for humidity sensing in microwave frequencies. Sensors and Actuators B: Chemical 245(2017):484-492.

[91] T. Abitbol, A. Rivkin, Y. Cao, Y. Nevo, E. Abraham, T. Ben-Shalom, O. Shoseyov. Nanocellulose, a tiny fiber with huge applications. Current opinion in biotechnology 39(2016):76-88.

[92] D.J. Gardner, G.S. Oporto, R. Mills, M.A.S.A. Samir. Adhesion and surface issues in cellulose and nanocellulose. Journal of Adhesion Science and Technology 22.5-6(2008):545-567.

[93] D. Klemm, F. Kramer, S. Moritz, T. Lindström, M. Ankerfors, D. Gray, A. Dorris. Nanocelluloses: a new family of nature-based materials. Angewandte Chemie International

Edition 50.24(2011):5438-5466.

[94] A.I. Yusra, H. Juahir, N.N.A. Firdaus, A.H. Bhat, A. Endut, H.A. Khalil, G. Adiana. Controlling of green nanocellulose fiber properties produced by chemo-mechanical treatment process via SEM, TEM, AFM and image analyzer characterization. Journal of Fundamental and Applied Sciences 10.1S(2018):1-17.

[95] P. Zhu, H. Ou, Y. Kuang, L. Hao, J. Diao, G. Chen. Cellulose Nanofiber/Carbon Nanotube Dual Network-Enabled Humidity Sensor with High Sensitivity and Durability. ACS Applied Materials & Interfaces 12.29(2020):33229-33238.

[96] S.J. Peters, T.S. Rushing, E.N. Landis, T.K. Cummins. Nanocellulose and microcellulose fibers for concrete. Transportation Research Record 2142.1(2010):25-28.

[97] E.M. Amin, N.C. Karmakar, B. Winther-Jensen-Polyvinyl-alcohol (PVA)-based RF humidity sensor in microwave frequency. Progress in Electromagnetics Research B 54(2013):149-166.

[98] T. Venugopalan, T.L. Yeo, T. Sun, K.T. Grattan. LPG-based PVA coated sensor for relative humidity measurement. IEEE Sensors Journal 8(2008):1093-1098.

[99] M. Penza, V.I. Anisimkin. Surface acoustic wave humidity sensor using polyvinyl-alcohol film. Sensors and Actuators A: Physical 76(1999):162-166.

[100] H.S. Mansur, C.M. Sadahira, A.N. Souza, A.A. Mansur. FTIR spectroscopy characterization of poly (vinyl alcohol) hydrogel with different hydrolysis degree and chemically crosslinked with glutaraldehyde. Materials Science and Engineering C 28(2008):539-548.

[101] B. Bolto, T. Tran, M. Hoang, Z. Xie. Crosslinked poly(vinyl alcohol) membranes.

Progress in Polymer Science 34(2009):969-981.

[102] K.C.S. Figueiredo, T.L.M. Alves, C.P. Borges. Poly(vinyl alcohol) films crosslinked by glutaraldehyde under mild conditions. Journal of applied polymer science 111(2009) 3074-3080.

[103] K.J. Kim, S.B. Lee, N.W. Han. Effects of the degree of crosslinking on properties of poly (vinyl alcohol) membranes. Polymer journal 25 (1993) 1295-1302.

[104] C.H. Zhang, F. Yang, W.J. Wang, B. Chen. Preparation and characterization of hydrophilic modification of polypropylene non-woven fabric by dip-coating PVA (polyvinyl alcohol). Separation and Purification Technology 61 (2008) 276-286.

[105] C.K. Yeom, K.H. Lee. Pervaporation separation of water-acetic acid mixtures through poly(vinyl alcohol) membranes crosslinked with glutaraldehyde. Journal of membrane science 109 (1996) 257-265.

[106] P.M. Faia, C.S. Furtado, A.J. Ferreira. Humidity sensing properties of a thick-film titania prepared by a slow spinning process. Sensors and Actuators B: Chemical 101.1-2(2004):183-190.

[107] T.C. Kaspar, W.L. Bland. Soil temperature and root growth. Soil Science 154.4(1992):290-299.

[108] K.S. Pregitzer, J.S. King, A.J. Burton, S.E. Brown. Responses of tree fine roots to temperature. New Phytologist 147.1(2000):105-115.

[109] C.S. Walker. Capacitance, inductance, and crosstalk analysis. Artech House on Demand, 1990.

[110] J.D. Kraus. Electromagnetics. McGraw-Hill, New York, 1984.

[111] U.C. Chung, C. Elissalde, S. Mornet, M. Maglione, C. Estournes. Controlling internal barrier in low loss BaTiO3 supercapacitors. Applied Physics Letters, 94.7(2009): 072903.

[112] D.S. Tucker, C.W. Hill, X. Zhou, G. Thompson, B. Ma, Z. Chang. High permittivity behavior and microstructure in a two-phase barium-silicon titanate. Materialia, 1(2018): 46-51.

[113] T. Seiyama, N. Yamazoe, H. Arai. Ceramic humidity sensors. Sensors and Actuators, (1983): 85-96.

[114] M. Li, D.F. Zhang, W.Y. Wang, G. Wang and X.L. Chen. The effects of grain boundary response and electrode contact response on the dielectric properties of CaCu3Ti4O12. Journal of Physics D: Applied Physics 43.29(2010):295405.

[115] M. Li. Study of the humidity-sensing mechanism of CaCu3Ti4O12. Sensors and Actuators B: Chemical 228(2016):443-447.

[116] A.I. Zia, M.S.A. Rahman, S.C. Mukhopadhyay, P.L. Yu, I.A. Bahadly, C.P. Gooneratne, J. Kosel, T.S. Liao. Technique for rapid detection of phthalates in water and beverages. Journal of Food Engineering 116(2013):515-523.

[117] W. Guo, X. Zhu, H. Liu, R. Yue, S. Wang. Effects of milk concentration and freshness on microwave dielectric properties. Journal of Food Engineering 99.3(2010):344-350.

[118] M.A. Centanni. Method and apparatus for measuring chemical concentration in a fluid. U.S. Patent No. 6,844,742, 2005.